Microfluidic Fuel Cells

by

Erik Kjeang

M.Sc., Umeå University, 2004

A Dissertation Submitted in Partial Fulfillment
of the Requirements for the Degree of

DOCTOR OF PHILOSOPHY

in the Department of Mechanical Engineering

University of Victoria

Supervisory Committee

Microfluidic Fuel Cells

by

Erik Kjeang
M.Sc., Umeå University, 2004

Supervisory Committee

Dr. David Sinton, Department of Mechanical Engineering
Supervisor

Dr. Ned Djilali, Department of Mechanical Engineering
Supervisor

Dr. Peter Oshkai, Department of Mechanical Engineering
Departmental Member

Dr. David A. Harrington, Department of Chemistry
Outside Member

Dr. Shelley D. Minteer, Department of Chemistry, Saint Louis University
External Examiner

Abstract

Supervisory Committee
Dr. David Sinton, Department of Mechanical Engineering
Supervisor
Dr. Ned Djilali, Department of Mechanical Engineering
Supervisor
Dr. Peter Oshkai, Department of Mechanical Engineering
Departmental Member
Dr. David A. Harrington, Department of Chemistry
Outside Member
Dr. Shelley D. Minteer, Department of Chemistry, Saint Louis University
External Examiner

Microfluidic fuel cell architectures are presented in this thesis. This work represents the mechanical and microfluidic portion of a microfluidic biofuel cell project. While the microfluidic fuel cells developed here are targeted to eventual integration with biocatalysts, the contributions of this thesis have more general applicability. The cell architectures are developed and evaluated based on conventional non-biological electrocatalysts. The fuel cells employ co-laminar flow of fuel and oxidant streams that do not require a membrane for physical separation, and comprise carbon or gold electrodes compatible with most enzyme immobilization schemes developed to date. The demonstrated microfluidic fuel cell architectures include the following: a single cell with planar gold electrodes and a grooved channel architecture that accommodates gaseous product evolution while preventing crossover effects; a single cell with planar carbon electrodes based on graphite rods; a three-dimensional hexagonal array cell based on multiple graphite rod electrodes with unique scale-up opportunities; a single cell with porous carbon electrodes that provides enhanced power output mainly attributed to the increased active area; a single cell with flow-through porous carbon electrodes that provides improved performance and overall energy conversion efficiency; and a single cell with flow-through porous gold electrodes with similar capabilities and reduced ohmic resistance.

As compared to previous results, the microfluidic fuel cells developed in this work show improved fuel cell performance (both in terms of power density and efficiency). In addition, this dissertation includes the development of an integrated electrochemical velocimetry approach for microfluidic devices, and a computational modeling study of strategic enzyme patterning for microfluidic biofuel cells with consecutive reactions.

Table of Contents

Acknowledgments

I would like to express my greatest appreciation to my supervisors, Dr. David Sinton and Dr. Ned Djilali, for their excellent support and guidance throughout all aspects of my research. It has been a true privilege to work with them and share their combined expertise and experience essential to this dissertation.

I would also like to thank all my other coworkers within the biofuel cell project: Dr. Alexandre G. Brolo, Dr. David B. Levin, Dr. Manuel Marechal, Amanda Finn, Robert Sacci, Meikun Fan, Dan Sanderson, David Harrison, Jonathan McKechnie, and most of all, Dr. David A. Harrington, the chair of the biofuel cell project, for effectively acting as a 'third supervisor' and great mentor in the field of electrochemistry.

I would like to thank all my colleagues at the Department of Mechanical Engineering, and all past and present members of the microfluidics group and the CFCE group, in particular Marc Secanell and Ron Songprakorp for sharing joy and frustration in our graduate office, and undergraduate students Jesse Musial, Brent Proctor and Raphaelle Michel who worked under my supervision.

I would also like to acknowledge financial support from the Natural Science and Engineering Research Council of Canada (NSERC), Angstrom Power Inc., and Bengt Ingeströms Stipendiefond.

Finally, I would like to express my gratitude and love to my family in Sweden for their endless support and care regardless of how far away from home I may go, and to my kiwi girlfriend Nicky Collins who has contributed tremendously to my quality of life and wellbeing as a graduate student in Canada.

Dedication

This dissertation is dedicated to Dr. Mohammad R. Golriz, who was my graduate supervisor during my Master’s degree at Umeå University in Sweden and Carleton University in Ottawa, Canada. It was Dr. Golriz who brought me to where I am today, and without his inspiration and enthusiasm I would never have started my doctoral studies. Many thanks, Mohammad, for your continuous support and guidance.

Organization

This dissertation has the following organization: Chapter 1 provides an introduction, including the overall objectives, motivation of the work, an overview of previous research, and specific objectives of this dissertation based on current research trends. The bulk of the work presented in this thesis is contained in the Appendices. Each Appendix (A-G) includes a complete scientific journal publication. These seven peer-reviewed journal papers are either published, in press, or currently under review. Chapter 2 summarizes each one of them and explains how they are connected in order to meet the objectives of this thesis. Finally, Chapter 3 provides a brief summary of the overall contributions, conclusions, and suggested future work.

Chapter 1

Introduction

1.1 Aims and Motivation

1.1.1 Objective

The objective of this work is to develop novel fuel cell architectures that provide enhanced power output and efficiency. Specifically, the objectives are to develop microfluidic fuel cell architectures based on co-laminar flow of fuel and oxidant solutions in a membraneless configuration, and to evaluate their performance using traditional electrocatalysts and project their capability towards the integration of biocatalytic electrodes.

This dissertation represents the mechanical and microfluidic components of a collaborative strategic project in the Institute for Integrated Energy Systems (IESVic) at the University of Victoria. The overall objective of the collaborative project is to *marry the forefront methods of molecular biology and microfluidic technology to develop practical biofuel cell systems with novel architectures that result in advanced functionality*. The IESVic biofuel cell initiative is a multidisciplinary collaborative effort that brings together faculty and researchers within the Department of Chemistry, Department of Biology and Department of Mechanical Engineering, and combines their expertise in the fields of electrochemistry, polymer science, surface chemistry, molecular biology, fuel cell technology, microfluidics, microfabrication, and transport phenomena. To put the objectives of this dissertation in this larger context, a general overview of fuel cells for portable power applications is provided in Section 1.1.2, followed by an overview of current biofuel cell technologies in Section 1.1.3. As the contributions from this dissertation apply more generally to the field of microfluidic fuel cells, a detailed literature review of these technologies is provided in Section 1.2.

1.1.2 Overview of Fuel Cells for Portable Power

Many different types of fuel cells are currently under development, with a variety of targeted applications ranging from miniature power supplies to large-scale combined heat and power plants. With the exception of limited small scale commercialization of some stationary units, most of these fuel cells have not yet gone beyond the field trials stage. Small fuel cells for portable electronic equipment are considered rather close-to-market for a number of reasons [1]: it is unlikely that the technical development of batteries will keep pace with the accelerating power demands; small, microstructured fuel cells enable higher overall energy density than batteries; and the market for portable electronics has an inherently higher cost tolerance. There are still some technical challenges, though, related to small fuel cell development. Hydrogen-based fuel cells require hydrogen storage units that are currently too bulky for portable device applications, and alcohol-based fuel cells, with compact fuel storage solutions, suffer from reduced cell voltage due to slow electrochemical kinetics and fuel crossover from anode to cathode.

1.1.3 Overview of Biofuel Cells

Fuel cells that utilize biological catalysts are collectively termed biofuel cells [2-4]. There is a common misunderstanding that biofuel cells are named as such because they use biological fuels, which is ambiguous since the same fuel (e.g. methanol) can be produced from both biological and non-biological sources. A biofuel cell mimics electrochemical processes occurring in nature to harvest a useful electrical current, without the use of precious electrocatalysts such as platinum. The oxidative metabolism of ethanol in the human liver, principally catalyzed by the alcohol and aldehyde dehydrogenase enzymes, exemplifies a bioanodic process. There are two main categories of biofuel cells; microbial biofuel cells and enzymatic biofuel cells. Oxidoreductases (redox enzymes), separated and purified from suitable organisms, exhibit superior catalytic turnover rates compared to the more complex biocatalytic microbes [5]. Oxidoreductases have many advantages in relation to conventional catalysts: enzymes can be produced by low-cost, renewable fermentation; the optimum temperature for enzyme activity is near-ambient; the inherent electrochemical overpotentials are generally low; the biocatalytic enzymes are available for a variety of fuels and oxidants; and perhaps most importantly, each individual enzyme is specific to a particular substrate. The specificity of enzyme catalysis introduces a wide range of additional benefits: fuel and oxidant streams can be combined in a single manifold; no proton exchange membrane is needed; sealing and manifolding as well as fluid delivery requirements are greatly reduced; and fuel crossover is eliminated. Full exploitation of these advantages would allow extremely cost competitive and efficient units.

Conventionally, biocatalytic enzymes are placed in a two-compartment electrochemical cell containing buffered solution with concentrated substrate and oxidant in the anolyte and catholyte compartments, respectively. These compartments are generally separated by an ion-exchange membrane or a salt bridge [2]. Each compartment also includes a redox couple acting as a diffusional electron mediator (cofactor), which is necessary for efficient catalyst utilization. Palmore et al. [6] introduced NAD as a cofactor in state-of-the-art bioanodes reaching an open-circuit potential of 0.8 V versus a conventional Pt cathode and a maximum power density of 0.67 mW cm^{-2}. The rate of electron transfer is generally confined by the rate of diffusion of these redox species and the ion permeability of the membrane that separates the two compartments [4]. Moreover, enzymes in solution are only stable for a few days. Recently, several novel methodologies have been developed for the functionalization of electrode surfaces and immobilization of active enzymes in order to improve electron transfer characteristics and stability: covalent polymer tethering of cofactor units to multilayered enzyme array assemblies; cross-linking of affinity complexes formed between redox enzymes and immobilized cofactors on functionalized conductive supports; and non-covalent coupling by hydrophobic/hydrophilic or affinity (e.g. antigen-antibody) interactions [7]. Minteer's group [8-10] created a biocatalytic anode through encapsulation of alcohol dehydrogenase enzymes in a modified Nafion matrix, which was shown to be kinetically limited by the diffusion of the NADH cofactor within the membrane structure [9]. Despite this limitation, improved power densities ranging from 1.16 to 2.04 mW cm^{-2} were obtained using an electrochemical cell with a Pt cathode [8]. A Nafion-immobilized biocathode based on bilirubin oxidase enzyme was also developed to complement the bioanode [10]. This pair of bioelectrodes was inserted in an electrochemical cell, and the performance was analyzed using buffered ethanol/NAD$^+$ anolyte and air-saturated catholyte with and without a membrane separator. The complete biofuel cell initially produced 0.83 mW cm^{-2} with the half-cells separated by a membrane, which was reduced to 0.39 mW cm^{-2} after removal of the membrane. The reduced performance of the membraneless configuration was attributed to incomplete specificity of the system. Enzymes encapsulated in a modified Nafion matrix are expected to have a lifetime of more than 90 days [10], though the lifetime of the biofuel cell was reduced to about 30 days due to degradation of the cathodic redox mediator.

Encapsulation of enzymes in polymer matrices results in an unorganized immobilization pattern that may degrade the kinetics. Willner and Katz [7] emphasize the advantage of organizing proteins in ordered and defined nanostructures with the immobilized cofactor aligned and oriented with the conductive support structure. Unprecedented electrical conductivity was demonstrated using Au nanoparticles functionalized with the FAD and PQQ cofactors for reconstitution of apo-glucose oxidase and apo-glucose dehydrogenase enzymes, respectively, on an Au electrode surface [11, 12]. Heller’s team reported a complete biofuel cell powered by glucose/oxygen with redox hydrogel-wired biocatalytic anode and cathode [13] in a compartment-less configuration [14], exhibiting the highest open-circuit voltage to date (0.88 V). This voltage is higher than the equivalent for platinum, but corresponded to a relatively low power density (0.35 mW cm^{-2}). They also demonstrated the capability of operation in a biological environment by insertion of bioelectrocatalyst-coated carbon fibers into a grape [15], and compatibility with physiological conditions [16, 17]. Similarly constructed biofuel cell electrodes have also been tested in serum [18, 19], albeit with reduced power output and stability caused by deactivation of the enzyme by urate [20].

The performance of current bioanodes and biocathodes must be improved in order for biofuel cells to reach their full potential and become competitive on the small fuel cells market. Improved immobilization and redox mediation schemes, more efficient wiring, and improved alignment and orientation would increase both stability and current density. Another possible avenue would be to identify and develop new enzyme proteins with higher turnover rates by genetic engineering. Early applications will likely focus on applications where the specific advantages of biocatalysis are required. For example, biofuel cells are promising candidates for certain biochemical applications related to lab-on-chip technologies or micro total analysis systems since they can use solutions available in those applications to generate power on-chip. Given their compatibility with physiological conditions, biofuel cells are also considered promising for low-power *in vivo* biomedical applications such as self-powered glucose sensors and power supplies for prosthetic valve actuators as well as skin-patch-based power sources for receiver-amplifier-transmitter units and miniaturized drug delivery systems. Glucose monitoring devices based on microfluidic nanoliter-sample fluid delivery systems, in conjunction with enzyme microcells equipped with electrically wired glucose oxidase for coulometric glucose measurements, are now available off-the-shelf (Abbott Laboratories, Abbott Park, IL). Implantable biofuel cells have effectively unlimited energy capacity when utilizing blood-supplied glucose and oxygen available in the subcutaneous interstitial fluid. The combination of inexpensive microfabrication, low-cost enzymatic catalyst, and the absence of precious metals and other expensive components, would enable integrated biofuel cell units that can be disposed of and replaced at the end of their lifetime. Pending the success of these specialized applications, biofuel cells may be scaled up to meet the power and lifetime requirements of more wide-spread applications.

The current densities of biocatalytic electrodes using enzymes immobilized in redox hydrogels are frequently controlled by the diffusive transport of reactant from the bulk solution to the active polymer matrix, for both glucose bioanodes [17, 21] and oxygen biocathodes [14, 22, 23]. Moreover, biocathodes based on bilirubin oxidase or laccase enzymes have outperformed platinum in terms of reduced overpotential and enhanced activity towards oxygen reduction [14, 22, 23]. Biofuel cells stand to benefit from development of microfluidic fuel cell technologies through (i) enhancing convective mass transport, enabling the enzymatic turnover rates to reach their full capability without the constraints associated with pure diffusional transport, and (ii) harnessing the high surface to volume ratio inherent to microstructured devices to promote the surface-based electrochemical reactions catalyzed by the immobilized enzymes.

1.2 Review of Microfluidic Fuel Cells

1.2.1 Definition and Fundamentals

Microfluidic fuel cells, sometimes called laminar flow-based fuel cells or membraneless fuel cells, describes a group of fuel cells capable of operation within the framework of a microfluidic chip. A microfluidic fuel cell is defined as a fuel cell with fluid delivery and removal, reaction sites and electrode structures all confined to a microfluidic channel. This type of fuel cell operates without a physical barrier, such as a membrane, to separate the anode and the cathode, and can use both metallic and biological catalysts. In the most common configuration, a microfluidic fuel cell utilizes the laminar flow characteristics of microfluidic flows at low Reynolds numbers to delay convective mixing of fuel and oxidant. Two aqueous streams, one containing the fuel (anolyte) and one containing the oxidant (catholyte), are allowed to flow side-by-side down a single microfluidic channel. The anolyte and catholyte also contain supporting electrolyte that facilitates ionic transport within the streams, thereby eliminating the need for a separate electrolyte. Mixing of the two streams occurs by transverse diffusion only, and is restricted to an interfacial width at the center of the channel. The mixing width can be controlled by modification of channel dimensions and flow rate [24], and the electrodes are integrated on the walls of the manifold with sufficient separation from the co-laminar inter-diffusion zone in order to prevent fuel crossover. The position and orientation of the electrodes also influences fuel utilization as well as ohmic resistance in the channel.

The microfluidic fuel cell design avoids many of the issues encountered in polymer electrolyte membrane-based fuel cells, for example humidification, membrane degradation, and fuel crossover. The co-laminar configuration also allows the composition of the anolyte and catholyte streams to be chosen independently, thus providing an opportunity to improve reaction rates and cell voltage. In addition to compactness, miniaturization of fuel cells has a further advantage: since electrochemical reactions are surface-based, the performance of the fuel cell benefits from a high surface-to-volume ratio, which scales as the inverse of the characteristic length. The most prominent benefit related to microfluidic fuel cells, however, is the economical aspect. Microfluidic fuel cells can be manufactured by inexpensive, well-established micromachining and microfabrication methods and the cost associated with the membrane, which is significant for most other fuel cells, is eliminated. In addition, microfluidic fuel cells are normally operated at room temperature and require no auxiliary humidification, water management, or cooling systems. Before it is possible to capitalize on the advantages of microfluidic fuel cells, however, significant progress is required in terms of energy density and fuel utilization.

Since the invention by Choban et al. in 2002 [25], the field of microfluidic fuel cells has generated an array of scientific publications and the technology is now being developed commercially by a recent start-up company (INI Power Systems, Morrisville, NC) with core technology licensed from the University of Illinois at Urbana-Champaign.

1.2.2 Microfluidic Fuel Cell Developments

Proof-of-concept microfluidic fuel cells have been demonstrated based on hydrogen [26-28], methanol [29-31], formic acid [32-36], hydrogen peroxide [37] and vanadium redox species [38] as fuel. The majority of these devices employed a Y- or T-shaped microfluidic channel design featuring two aqueous co-laminar streams with fuel and oxidant dissolved in a supporting electrolyte and electrodes on opposite channel walls parallel to the inter-diffusion zone. The power density of these fuel cells was predominantly restricted by the rate of mass transport to the active sites, typically in the cathodic half-cell, and the overall system performance suffered from low fuel utilization. The all-liquid nature of most microfluidic fuel cells enables the use of an external reference electrode to characterize individual half-cells and measure ohmic resistance *in situ* during fuel cell operation. Using this experimental approach, the overall cathodic mass transport limitation of dissolved oxygen-based systems was unambiguously verified [30]. For early devices using formic acid in the anodic stream and dissolved oxygen in the cathodic stream, the maximum power density levels achieved were only about 0.2 mW cm^{-2} [34, 35], primarily constrained by the low solubility of oxygen in the aqueous electrolyte (2-4 mM). Similar power densities were obtained using dissolved hydrogen as fuel [26]. The combination of gaseous reactants and poly(dimethylsiloxane) (PDMS) material provides an interesting opportunity for microfluidic fuel cell fabrication and design, attributed to the relatively high gas permeability of PDMS. This feature enables gaseous reactant supply through thin layers of PDMS to a pair of electrodes separated by an electrolyte channel [27, 28]. The power output of the device (0.7 mW cm^{-2}) was restricted by the permeation rate of hydrogen through the polymer and oxygen crossover. Cohen et al. [26] demonstrated that the open circuit potential of a hydrogen/oxygen fuel cell could be raised well beyond the standard cell potential of 1.23 V by implementation of an alkaline dissolved hydrogen stream and an acidic dissolved oxygen stream in a co-laminar microfluidic fuel cell. The media flexibility was also explored by Kenis' group by operating a methanol/oxygen fuel cell under all-acidic, all-alkaline, and mixed-media conditions [29]. In contrast to membrane-based fuel cells, the microfluidic fuel cell design eliminated the issue of membrane clogging by carbonates formed in alkaline media. The methanol/oxygen fuel cell produced a room-temperature peak power density of 5 mW cm^{-2} at 1.0 V cell voltage under mixed-media conditions (alkaline anolyte and acidic catholyte), compared to 2.4 and 2.0 mW cm^{-2} for all-acidic and all-alkaline conditions, respectively. Operation under mixed-media conditions, however, causes exothermic neutralization of OH^- and H^+ at the co-laminar flow interface with reduced ionic strength as a result. Hasegawa et al. [37] used the mixed-media approach to operate a microfluidic fuel cell on hydrogen peroxide as both fuel *and* oxidant, in alkaline and acidic media, respectively. This fuel cell produced relatively high power densities, but the electrochemical reactions required net consumption of supporting electrolyte, which has a negative effect on both overall energy density and cell resistance via reduced ionic conductivity. An acidic hydrogen peroxide solution was also employed as the oxidant in a laser-micromachined microfluidic fuel cell device [33] with power densities up to 2 mW cm^{-2}, partially restricted by instabilities caused by oxygen evolution from hydrogen peroxide decomposition. Two methods to stabilize the co-laminar liquid-liquid interface have recently been proposed; a liquid-liquid interface less susceptible to mixing was provided by magnetic techniques [39], or by adding a third stream containing a blank electrolyte to further separate the anolyte and catholyte streams [32].

One way to address the oxygen solubility limitation is to integrate an air-breathing porous cathode structure that allows gaseous oxygen transport from the ambient air, a source of oxygen that has significantly higher diffusivity and concentration than dissolved oxygen. Jayashree et al. [36] introduced the first microfluidic fuel cell with integrated air-breathing cathode, using a graphite plate anode covered with palladium black nanoparticles and a porous carbon paper cathode covered with platinum black nanoparticles. The air-breathing cell architecture requires a blank cathodic electrolyte stream (without dissolved oxidant) to provide sufficient separation between the inter-diffusion zone and the cathode, and to facilitate ionic transport to the cathodic reaction sites. A peak power density of 26 mW cm^{-2} was achieved with 1 M formic acid in 0.5 M sulfuric acid anolyte and a blank 0.5 M sulfuric acid catholyte flowing at 0.3 mL min^{-1} per stream. The air-breathing cell architecture was also evaluated using methanol [31], a fuel that enables higher overall energy density than formic acid. Despite the modest power densities obtained with 1 M methanol fuel (17 mW cm^{-2}), this study demonstrated significantly improved reaction kinetics for both methanol oxidation and oxygen reduction by switching from an acidic to an alkaline supporting electrolyte. The air-breathing cells also enabled significantly higher coulombic fuel utilization than the cells based on dissolved oxygen, up to a maximum 33% per single pass at 0.1 mL min^{-1} [36]. However, in the context of microfluidic fuel cells, the air-breathing feature reduces the flexibility of scale-up by three-dimensional stacking of individual cells, and requires a recirculation scheme to acquire practical fuel utilization and overall energy conversion efficiency.

The use of alternative oxidants soluble at higher concentrations than dissolved oxygen provides another avenue towards improved performance of typically mass-transfer limited microfluidic fuel cells. An all-vanadium microfluidic fuel cell design based on soluble vanadium redox species was introduced [38]. Vanadium redox fuel cells utilize two different aqueous vanadium redox couples, V^{2+}/V^{3+} and VO^{2+}/VO_2^{+}, as fuel and oxidant, respectively, dissolved in dilute sulfuric acid. This combination of redox pairs offers several advantages for microfluidic fuel cell operation: they provide well-balanced electrochemical half-cells in terms of reaction rates and transport characteristics; they have high solubility and enable relatively high redox concentrations; they have a large difference in formal redox potentials resulting in a high open-circuit voltage (up to ~1.7 V at uniform pH); and the reactions are facilitated by bare carbon electrodes without precious metal catalysts. Excluding the works presented in this thesis, the highest power density of the microfluidic fuel cells reported to date was 38 mW cm^{-2}. This performance was achieved using the vanadium redox system at 1.5 mL min^{-1} flow rate [38]. The fuel utilization at this flow rate was however limited to ~0.1%, and the energy density of such a fuel cell system would ultimately be limited by the solubility of the vanadium redox species.

Mathematical and computational modeling is an important tool in the analysis of the transport phenomena and electrochemical reactions that take place inside a microfluidic fuel cell. This area was first demonstrated by Bazylak et al. [40] using computational modeling to analyze microfluidic fuel cells with different cross-sectional channel geometries and electrode configurations. It was found that a high aspect ratio (width/height) channel geometry with electrodes placed orthogonally to the co-laminar flow interface on the top and bottom walls would enable significantly improved fuel utilization and reduced inter-diffusional mixing width. A similar computational model was developed by Chang et al. [41, 42], extended with Butler-Volmer electrochemical reaction kinetics, with the capability of predicting complete polarization curves. The results obtained for a dissolved oxygen-based cell confirmed the cathodic mass transport limitation and they recommended high aspect ratio channels or a thicker cathode catalyst layer to improve the performance. This work was complemented by an in-depth theoretical study of the cathode kinetics of the same fuel cell [43], and a Butler-Volmer model of the hydrogen peroxide fuel cell [44]. No modeling efforts to date have been applied to the air-breathing microfluidic fuel cell architecture or the vanadium redox system.

Overall, the development of co-laminar microfluidic fuel cells to date has been tremendous, given that it is a relatively new invention. Research so far has resulted in operational devices with promising performance in terms of power density and open-circuit voltage, but little has been done in order to design practical, efficient and competitive devices with high energy density and high fuel utilization. The most prominent constraint identified for current microfluidic fuel cells is their low energy density, defined as energy output per system volume or mass. The core physics of the co-laminar flow configuration require that both streams are liquid and contain an electrolyte. Although reactants may be added to the system at high concentration, the energy density of all devices presented hitherto has been low compared to other microstructured fuel cells due to the impractical single-pass use of liquid electrolyte without any form of recirculation or recycling. The implementation of a recirculation system for the electrolyte is a challenging task due to the space constraints and inevitable mixing/contamination issues. Moreover, although fuel utilization data (excluding the present work) up to 33% per single pass have been presented, the fuel utilization at practical flow rates and useful cell voltages has generally been below 10%. In addition, there is a lack of engineering solutions for important functions such as the integration of fuel and oxidant storage, waste handling, and low-power microfluidics-based fluid delivery (normally driven by a syringe pump via external tubing) using integrated micropumps and microvalves.

The power output of a single planar microfluidic fuel cell is inadequate for most practical applications. The feasibility of enlarging a single planar cell, i.e. increasing the geometrical area of electrodes and microchannel, is limited by structural constraints, increased crossover, and increased ohmic losses if the average distance between anodic and cathodic active sites becomes large. In order to produce adequate power, multiple independent planar cells could be accommodated on a single plane, and then these planes could be stacked as in typical PEM fuel cells. The volumetric power density of such devices would however be limited by the volume of the sealing and structural elements separating the cells. In traditional PEM fuel cell stacks, which are limited by similar issues [45], the bi-polar plates serve as structural and electrical components. The inherent advantage of non-planar electrode–electrolyte interfaces has been recognized and demonstrated for such cells using, for example, waved membrane-electrode assemblies [45]. In contrast, the microfluidic fuel cells presented to date contain mostly non-participating structural material such as glass or PDMS. The scale-up of microfluidic fuel cell technology in a volumetrically efficient manner remains a challenge.

1.2.7 Microfluidic Biofuel Cell Developments

The immobilization of enzymes on conductive supports enables integrated microfluidic biofuel cell designs. Biofuel cells with non-selective electrochemistry, i.e. cells using diffusional redox mediators, can utilize the co-laminar microfluidic fuel cell design previously described, which also enables the tailoring of independent anolyte and catholyte compositions for optimum enzymatic activity and stability. Full selectivity of both anodic and cathodic half-cells (i.e. co-immobilized redox relays and enzymes based on suitable immobilization schemes with electronic coupling) allows microfluidic biofuel cell operation in a single, combined fuel and oxidant channel with mixed reactants. A microfluidic system would also be favourable for stability studies since the reactant concentrations can be kept constant by continuous flow. The number of microfluidic biofuel cells presented to date is very limited. Togo et al. [46] developed a microfluidic bioanode based on vitamin K_3-mediated glucose oxidation by the glucose dehydrogenase enzyme. The bioanode was immobilized inside a fluidic chip containing a PDMS-coated conventional platinum cathode. The flow cell produced 32 μW cm^{-2} at 0.29 V when an air-saturated pH 7-buffered fuel solution containing 5 mM glucose and 1 mM NAD^+ was introduced at 1 mL min^{-1} flow rate. The current density of the proof-of-concept cell declined by 50% over 18 hours of continuous operation, probably due to swelling effects. This report was preceded by an earlier contribution from Minteer's group; a microchip-based bioanode with NAD-dependent alcohol dehydrogenase enzymes immobilized in a tetrabutylammonium bromide treated Nafion membrane [9]. The bioanode was assembled on a glass substrate under a PDMS microchannel that was used to deliver the fuel solution containing ethanol and NAD^+ in phosphate buffer. When operated versus an external platinum cathode, the microfluidic bioanode produced an open-circuit voltage of 0.34 V and a maximum current density of 53 μA cm^{-2}, expected to be limited by the rate of diffusion of NADH within the membrane. To the author's knowledge, Minteer's group is continuing this research towards an integrated microfluidic fuel cell based on their unique enzyme immobilization technique. This technology is currently licensed to Akermin, Inc. of St Louis, MO, under the trademark "stabilized enzyme biofuel cells", which is considered state-of-the-art microfluidic biofuel cell technology in terms of both power density and stability.

Chapter 2

Summary of Contributions

The main contributions in this dissertation are contained in the seven journal papers provided in Appendix A-G. This chapter summarizes these contributions and explains how they are connected towards the overall objective of this work.

2.1 Integrated Electrochemical Velocimetry for Microfluidic Devices

Most microfluidic velocimetry techniques require optomechanical supporting infrastructure that is substantial with respect to both cost and size, and incompatible with on-chip integration. The primary objective of this study was to demonstrate an advanced integrated electrochemical velocimetry methodology for microfluidic devices with direct electrical output. A second more project-focused objective of this study was to fabricate and integrate microfluidics with patterned electrodes and obtain quantitative electrochemical measurements in the microfluidic environment.

The proposed methodology was based on amperometric monitoring of the transport-limited reduction rate of a reversible redox species at an embedded microband working electrode. Three microband electrodes, including working, counter and reference electrodes, were all integrated on-chip for complete miniaturization of the sensor. Experimental results were complemented by a theoretical framework including a full 3D electrochemical model as well as empirical mass transfer correlations and scaling laws.

When the sensor was operated in the convective/diffusive transport controlled mode, the output signal exhibited a predictable function of velocity in two distinct regimes: (i) in the low velocity regime, the signal was directly proportional to flow rate; and (ii) in the high velocity regime, the signal scaled as the cube root of the mean velocity. The proposed velocimetry technique is applicable to all practicable pressure-driven laminar flows in microchannels with known cross-sectional geometry.

Overall, this study provided preliminary testing and evaluation of microfluidic electrochemical cells, experimental setup and *in situ* measurements for future microfluidic fuel cell devices. This work also included the development of a complete microfabrication procedure of micropatterned gold electrodes integrated on the walls of microfluidic networks that could be implemented for microfluidic biofuel cells with enzymes immobilized on gold.

For further information, the reader is directed to Appendix A or [47].

2.2 Hydrogen Peroxide as an Oxidant for Microfluidic Fuel Cells

The performance of microfluidic fuel cells can be improved by employing aqueous oxidants that are soluble at higher concentrations than dissolved oxygen. Like common fuels such as methanol and formic acid, hydrogen peroxide is available at high concentrations and has high solubility in aqueous media, enabling balanced half-cell configurations. In this study, a novel microfluidic fuel cell design was developed with the goal of harnessing these advantages. As fuel cell performance critically depends on both electrode and channel architecture, several different prototype cells were developed and results compared. High-surface area electrodeposited platinum and palladium electrodes were evaluated both *ex situ* and *in situ* for the combination of direct H_2O_2 reduction and oxygen reduction via the decomposition reaction. Oxygen gas bubbles produced at the fuel cell cathode introduced an unsteady two-phase flow component that, if not controlled, resulted in perturbed co-laminar flow and reduced fuel cell performance. A grooved channel design was developed in this study that restricted gas bubble growth and transport to the vicinity of the cathodic active sites, thereby enhancing the rate of oxygen reduction, and limiting fuel and oxidant crossover. The proof-of-concept H_2O_2-based microfluidic fuel cell produced power densities up to 30 mW cm^{-2} and a maximum current density of 150 mA cm^{-2}, when operated on 2 M H_2O_2 oxidant together with formic acid-based fuel.

Using the microfabrication methodology developed in the previous contribution, this study provided hands-on experience of microfluidic fuel cell fabrication and experimental evaluation in a co-laminar flow configuration. It also provided the opportunity to develop a creative solution for microfluidic fuel cell systems constrained by gaseous reaction products or decomposition that may otherwise lead to crossover problems and reduced performance.

For further information, the reader is referred to Appendix B or [48].

2.3 Planar and Three-Dimensional Microfluidic Fuel Cell Architectures Based on Graphite Rod Electrodes

The objective of this contribution was to develop membraneless microfluidic fuel cell architectures employing low-cost graphite rod electrodes. Commonly employed as mechanical pencil refills, graphite rods are inexpensive and serve effectively as both electrode and current collector for the combined all-vanadium fuel/oxidant system. In contrast to film-deposited electrodes, the geometry and mechanical properties of graphite rods enable unique three-dimensional microfluidic fuel cell architectures. Planar microfluidic fuel cells employing graphite rod electrodes were first developed, incorporating a typical microfluidic fuel cell geometry that permitted fuel cell performance comparisons and the evaluation of graphite rods as electrodes. The planar cells produced a peak power density of 35 mW cm^{-2} at 0.8 V using 2 M vanadium solutions, and provided steady operation at flow rates spanning four orders of magnitude. Numerical simulations and empirical scaling laws were also developed to provide insight into the measured performance and graphite rods as fuel cell electrodes. This contribution also demonstrated the first three-dimensional microfluidic fuel cell architecture with multiple electrodes. The proposed fuel cell architecture, consisting of a hexagonal array of graphite rods, enables scale-up/integration of microfluidic fuel cell technology as well as power conditioning flexibility beyond that of the traditional fuel cell stack. When provided the same flow rate as the planar cell, the array cell generated an order of magnitude higher power output. The array architecture also enabled unprecedented levels of single pass fuel utilization, up to 78% per single pass.

Overall, this contribution demonstrated both planar and three-dimensional microfluidic fuel cell architectures based on graphite rod electrodes. In the context of the biofuel cell project, the vanadium redox system provided a practical model system for experimental prediction of the appropriateness of these fuel cell architectures for biofuel cell application. Given that most enzyme immobilization schemes are compatible with carbon substrates, the graphite rod-based fuel cell architectures would be viable for microfluidic biofuel cells, however the planar surface morphology and relatively large diameter of graphite rods may not be ideal in terms of surface to volume ratio and associated power density of such a device.

For further information, the reader is directed to Appendix C or [49].

2.4 High-Performance Microfluidic Vanadium Redox Fuel Cell

The objective of this contribution was to investigate the performance benefits associated with the integration of porous electrodes in a microfluidic fuel cell. Towards this end, a new microfluidic fuel cell was developed with high-surface area porous carbon electrodes and high aspect ratio channel. This fuel cell also employed the vanadium redox system as fuel and oxidant. The fuel cell exhibited a peak power density of 70 mW cm^{-2} at room temperature, significantly higher than all previously reported microfluidic fuel cells. Efficient low flow rate operation essentially free from crossover was also established with single pass fuel utilization levels up to 55%. In the low flow rate regime, the power generated by the fuel cell was primarily controlled by transport from the bulk fluid, independent of electrode structure and porosity. At medium to high flow rates, however, fuel cell performance was controlled by a combination of factors including convective/diffusive transport, electrochemical kinetics, ohmic resistance, and active area. When compared to the planar fuel cell architecture based on graphite rods, the device with high-surface area porous electrodes generated up to 72% higher power density. The improved performance is attributed to the increased active area (20-30 times higher than the corresponding planar area) and improved transport characteristics facilitated by partial flow inside the top portion of the porous electrodes, although the penetration depth of the porous medium and associated utilization of available active area was limited.

The porous electrode fuel cell design facilitated cost-effective and rapid fabrication, and would be applicable to most microfluidic fuel cell architectures and fuel/oxidant combinations (with electrocatalyst addition). The redox hydrogel enzyme immobilization technique developed by Heller's group [13] would be compatible with this microfluidic fuel cell design, provided the similarity of the porous carbon material employed here and the fibrous carbon used as substrates for the redox hydrogels.

For additional information, the reader is referred to Appendix D or [50].

2.5 A Microfluidic Fuel Cell with Flow-Through Porous Electrodes

Microfluidic fuel cells have additional characteristics that have yet to be exploited through creative fuel cell design. Specifically, the reactants, products and electrolyte are all in the same liquid phase, and the reaction zones are simple solid-liquid interfaces. These characteristics provide potential for a variety of three-dimensional fuel cell architectures. In this contribution, a microfluidic fuel cell incorporating flow-through porous electrodes was developed, resulting in high active surface area and highly three-dimensional reaction zones. The proposed microfluidic fuel cell had two unique features as compared to the previous microfluidic fuel cell with porous electrodes [50]: (i) hydrophilic electrode treatment that promotes liquid saturation of the porous electrode; and (ii) a three-dimensional flow-through architecture that improves utilization of the active area through enhanced transport. The flow-through design is based on cross-flow of fuel and oxidant solutions through the electrodes into an orthogonally arranged co-laminar exit channel, where the waste solutions provide ionic charge transfer in a membraneless configuration. The flow-through architecture enables uniformly distributed flow at low mean velocity directly through the porous electrode and provides enhanced rates of convective/diffusive transport without substantially increasing the parasitic loss required to drive the flow. Improved performance as compared to previous microfluidic fuel cells was demonstrated using the all-vanadium redox system, including power densities at room temperature up to a remarkable 131 mW cm^{-2}. In addition, the flow-through architecture enabled unprecedented levels of overall energy conversion efficiency as relatively high levels of fuel utilization and cell voltage were achieved concurrently. When operated at 1 µL min^{-1} flow rate, the fuel cell produced 20 mW cm^{-2} at 0.8 V combined with an active fuel utilization of 94%. Finally, this contribution demonstrated *in situ* fuel and oxidant regeneration by running the flow-through architecture fuel cell in reverse.

This contribution is anticipated to have a significant impact on the development of microfluidic fuel cells, given the high performance levels of the relatively un-optimized device. The flow-through fuel cell architecture has tremendous potential for biofuel cell implementation. The performance levels demonstrated in this contribution were largely restricted by ohmic resistance, but since the overall ohmic resistance is proportional to the current density, this limitation would not be experienced by biofuel cells.

For more information, please refer to Appendix E or [51].

2.6 An Alkaline Microfluidic Fuel Cell Based on Formic Acid and Hypochlorite Bleach

The objective of this contribution was to identify and demonstrate an alternative all-liquid fuel and oxidant combination that enables high energy density while maintaining the advantages of the microfluidic fuel cell architecture with flow-through porous electrodes. The new fuel and oxidant combination was subject to the following restrictions: all reactants and products must be available and stable at high concentration in the liquid phase; the reactants must provide at least two electrons per molecule; spontaneous and/or electrochemically activated decomposition into gaseous products must be prevented; the fuel and oxidant may not react vigorously upon mixing; and if the anodic and cathodic supporting electrolytes are different, the fuel and oxidant species must be stable in both electrolytes. A unique anodic half-cell was demonstrated based on alkaline formate that utilized carbonate absorption to prevent gaseous CO_2 formation. This work also demonstrated a cathodic half-cell based on sodium hypochlorite solution, commonly known as hypochlorite bleach, which is also unique in a fuel cell environment. Both half-cells provided high current densities at relatively low overpotentials and were completely free of gaseous components. The proof-of-concept all-liquid microfluidic fuel cell incorporating the flow-through porous electrode architecture previously developed for the all-vanadium redox system produced power densities up to 52 mW cm^{-2} at room temperature using 5% formic acid fuel and 5% sodium hypochlorite oxidant. It also demonstrated the capability of combining high power density with high single-pass fuel utilization at practical cell voltages. Unlike the all-vanadium redox system, both formic acid and hypochlorite are available and stable in the liquid phase at high concentration, which facilitates a unique microfluidic fuel cell system with high overall energy density.

The overall purpose of this contribution was to verify the fuel/oxidant flexibility of the flow-through architecture fuel cell, and to further support this novel fuel cell concept beyond the solubility limitation of the vanadium redox species. Another key contribution of this work was the electrodeposition methodology developed to obtain high-surface area porous gold electrodes with uniform coating and reduced overall ohmic resistance. In a biofuel cell context, this feature broadens the application of the flow-through architecture by the additional compatibility with gold-supported enzyme immobilization schemes.

For more information, please refer to Appendix F or [52].

2.7 Strategic Enzyme Patterning for Microfluidic Biofuel Cells

Patterning multiple enzyme electrodes to harness consecutive reactions represents a significant opportunity for biofuel cell technologies, particularly with respect to fuel utilization. The objective of this study was to determine a strategic enzyme patterning strategy that captures this opportunity. Towards this end, a generic computational model of species transport coupled with heterogeneous chemical reactions and Michaelis-Menten enzyme kinetics was established and verified based on typical microchannel geometries. This was the first computational study of microfluidic fuel cell technology, and the results were intended to provide guidelines for the design and fabrication of microfluidic biofuel cells exploiting consecutive reactions. Separated and mixed enzyme patterns in different proportions were analyzed for various Peclet numbers. High fuel utilization was achieved in the diffusion dominated and mixed species transport regimes with separated enzymes arranged in relation to individual turnover rates. However, results indicated that the Peclet number must be above a certain threshold value to obtain satisfying current densities. The mixed transport regime was shown to be particularly attractive while current densities were maintained close to maximum levels. Optimum performance was achieved by mixed enzyme patterning tailored with respect to individual turnover rates, enabling high current densities combined with nearly complete fuel utilization.

This contribution has its main application for microfluidic biofuel cells exploiting consecutive reactions with multiple enzymes. Based on its highly generalized approach, the results are expected to be applicable to most immobilization schemes and cell architectures.

For further information, please refer to Appendix G or [53].

Chapter 3

Conclusions and Future Work

3.1 Conclusions and Contributions

This dissertation was devoted to the development, design and evaluation of microfluidic fuel cell architectures. While the microfluidic fuel cells developed here were targeted to eventual implementation with biocatalysts, the contributions of this thesis have more general applicability. The proposed cell architectures were evaluated based on conventional non-biological electrocatalysts and model electrochemical fuel and oxidant systems. The development was aided primarily by experimentation but also included microfabrication and modeling components: most contributions in this thesis incorporated design, microfabrication implementation, experimental verification, and numerical/analytical justification. Some of these components were carried out in collaboration with other graduate students and undergraduate students under the umbrella of the multidisciplinary IESVic biofuel cell project. Most notably, Jonathan McKechnie provided important input in the microfabrication of several cells, and the use of graphite rod electrodes. The key contributions of this dissertation can be summarized as follows:

(i) An integrated electrochemical velocimetry technique for microfluidic networks with direct electrical output was realized by means of embedded microband electrodes and a redox couple in solution. As demonstrated experimentally and verified theoretically and numerically, a functional relationship between mean velocity and the reductive current drawn from the working electrode was obtained for operation in the transport controlled mode. Two velocity regimes were found: in the high velocity regime, the amperometric signal scales as the cube root of mean velocity, whereas in the low velocity regime, the signal is directly proportional to the flow rate. The proposed velocimetry technique can resolve mean flow velocities for the full range of laminar pressure-driven flow rates in microfluidic channels with known cross-sectional geometry.

(ii) Microfluidic fuel cell operation based on hydrogen peroxide oxidant was demonstrated. A novel microfluidic fuel cell design was developed with a grooved channel geometry that utilizes gas evolution and unsteady two-phase flow characteristics to enhance local transport rates and time-averaged current density, and restricts oxygen bubble growth and expulsion to the channel section directly above the cathode in order to enhance the rate of oxygen reduction and prevent detrimental fuel and oxidant crossover effects.

(iii) Planar and three-dimensional microfluidic fuel cell designs were demonstrated based on graphite rod electrodes. Low-cost graphite rods, available as mechanical pencil refills, provided both reaction sites and current collectors for the combined all-vanadium fuel and oxidant system without additional catalyst requirements. Planar single cells, comparable to existing fuel cell designs, were manufactured and evaluated experimentally to confirm the viability of the proposed graphite rod electrodes. The proof-of-concept three-dimensional microfluidic fuel cell architecture, based on a hexagonal array of graphite rods, produced an order of magnitude more power than the planar cell at similar flow rates. Furthermore, highly efficient array cell operation was demonstrated at low to moderate flow rates, achieving unique levels of fuel utilization per single pass. The array cell, with multiple anodes and cathodes, provides additional power conditioning flexibility in series and/or parallel configurations, as well as unique scalability by vertical expansion without additional fluid manifold requirements or performance loss.

(iv) A microfluidic vanadium redox fuel cell employing porous electrodes with high active surface area was also demonstrated. Operation at high flow rate resulted in unprecedented peak power densities, up to 72% higher than with planar electrodes, and operation at low flow rate resulted in high overall fuel utilization without crossover effects. The improved performance is attributed to the increased active area and improved transport characteristics facilitated by partial flow within the top portion of the porous electrodes. This work projects that the integration of similar high-surface area porous electrodes or catalyst supports would boost the performance of most other microfluidic fuel cell architectures including biofuel cells. In particular, the integration of electrode features with characteristic length scale on the order of 10 µm (about one order of magnitude smaller than the channel dimension) enables substantially increased active area combined with enhanced transport characteristics, and reduces transport limitations.

(v) A microfluidic fuel cell architecture incorporating flow-through porous electrodes was presented. In contrast to previous work, the flow-through architecture was designed to direct the flow of fuel and oxidant solutions uniformly through the porous electrode structures prior to combination of the waste streams in a co-laminar format. This strategy achieved utilization of the full depth of the porous electrode and associated active area, and provided enhanced species transport from the bulk to the active sites. Performance levels were demonstrated that are unprecedented to date in microfluidic fuel cells: two to four times higher power density than the previously developed cell with porous electrodes, near complete fuel utilization, and high operational cell voltages. The fuel cell also had the capability to combine these three characteristics during steady state operation, resulting in an overall energy conversion efficiency of 60% per single pass. In addition, proof-of-concept *in situ* regeneration of the initial fuel and oxidant species was established by running the fuel cell in reverse. The demonstrated flow-through fuel cell architecture would make an ideal candidate for biofuel cell implementation. The flow-through electrode architecture may also find utility in analytical chip-based electrochemical detection.

(vi) The feasibility of an alkaline formate anode coupled with an alkaline hypochlorite cathode in an all-liquid microfluidic fuel cell architecture with flow-through porous electrodes was demonstrated. Both half-cells were unique in terms of application in a fuel cell. In contrast to the vanadium redox system, formic acid and hypochlorite are both available in liquid form at high concentrations, thereby enabling a microfluidic fuel cell system with high overall energy density. The proof-of-concept formate/hypochlorite microfluidic fuel cell concurrently achieved high power densities and near-complete fuel utilization at relatively high cell voltages, and therefore enabled high overall energy conversion efficiency. The new alkaline formate and hypochlorite fuel cell concept demonstrated here, or either one of its individual half-cells, may also find applications using conventional membrane-based fuel cell designs. Another key contribution was the electrodeposition methodology developed to obtain high-surface area porous gold electrodes. In a biofuel cell setting, this feature broadens the applicability of the flow-through architecture by the additional compatibility with gold-supported enzyme immobilization schemes.

(vii) A strategic enzyme patterning methodology was proposed to provide guidelines for the design and fabrication of microfluidic biofuel cells exploiting consecutive reactions with multiple enzymes. A generic numerical model of species transport coupled with heterogeneous chemical reactions and Michaelis-Menten enzyme kinetics was developed and verified to evaluate different patterning strategies. Optimum overall performance in terms of high current density and near-complete fuel utilization was achieved by a mixed enzyme patterning strategy that accounts for individual enzymatic turnover rates. Based on the highly generalized approach, the results are expected to be applicable to most immobilization schemes and cell architectures.

3.2 Future Work

The central future work component required to meet the overall objective of the IESVic biofuel cell initiative is to integrate a bioanode and/or a biocathode in the proposed microfluidic fuel cell architectures and analyze the performance experimentally. The co-laminar fuel cell configuration enables tailored conditions for optimum enzyme activity and stability in both half cells. Furthermore, the specificity of the enzymes may be measured by comparing data from operation under co-laminar reactant flow to operation under mixed reactant flow. Enzyme immobilization in the redox hydrogels developed by Heller's group [13], or a similar version thereof, is well-suited for the biofuel cell architectures proposed here for several reasons: the electrodes are typically transport limited and have low overpotentials; the immobilization strategy is compatible with both carbon and gold substrates; the thickness of the redox hydrogel film is on the order of 1-10 μm which is similar to the fiber diameter and smaller than the average pore size of the porous electrodes; and it provides a wetted matrix that enables depth-wise reactant transport and utilization of a high enzyme loading and internal active area. The flow-through architecture is particularly well-suited for this type of biofuel cells given its high overall performance demonstrated with the vanadium model system.

The following recipe would make a useful approach for an experimental feasibility study: starting with one electrode (either a bioanode or a biocathode), immobilize an enzyme-containing redox hydrogel on a prefabricated porous carbon electrode, and after drying and stabilizing the film, evaluate the performance by slow scan cyclic voltammetry (CV) in a conventional electrochemical cell containing a buffered fuel or oxidant solution at optimum conditions. Then transfer the same electrode to a prefabricated flow cell and seal the structure. Run a slow scan CV for flow cell operation with the same solution at the same conditions, using the opposite *in situ* electrode as counter electrode and an external reference electrode. Finally, compare the data obtained in the flow cell to the data previously measured in the stationary cell with the same electrode. This approach provides a just comparison as it eliminates the variability associated with the deposition of the hydrogel film, and can be extended to a complete bioanode and biocathode pair that correctly represents a microfluidic *biofuel cell*.

With respect to the individual contributions of this dissertation some additional future work is proposed below:

(i) For the integrated microfluidic redox velocimetry method, it would be useful to investigate alternative redox species that are more practical than the ruthenium hexamine and available at low-cost, and to extend the experimental study with various electrode and channel geometries for further verification of the numerical predictions.

(ii) The performance of hydrogen peroxide-based cathodes, as well as overall fuel cell performance, would further benefit from a catalyst optimization study within the framework of a microfluidic fuel cell, including platinum and palladium nanoparticles and various high-surface area Au electrodes.

(iii) Graphite-rod based fuel cell performance would likely benefit from increasing the concentration and purity level of both supporting electrolyte and vanadium redox species, and by optimizing the rod diameter and characteristic spacing of the array cell. There is also ample opportunity for a numerical modeling extension of this work that includes electrochemical reaction kinetics, as well as a thorough experimental/theoretical electrochemical impedance spectroscopy (EIS) analysis under various operating conditions.

(iv) The performance of the vanadium redox fuel cells with porous electrodes would be enhanced by increasing the concentration and purity level of both supporting electrolyte and vanadium redox species, incorporating highly conductive current collectors, and optimizing the porosity of the carbon electrodes.

(v) Similarly, the performance of the flow-through architecture fuel cell would likely benefit from increasing the concentration of the vanadium redox species, optimizing the microstructure and porosity of the flow-through carbon electrodes, and most importantly, reducing the combined ohmic resistance of the cell. In addition, developing the membraneless regeneration capability towards an integrated microfluidic redox battery could have significant impact.

(vi) The performance of the formate/hypochlorite fuel cell would be further enhanced by reducing the combined ohmic resistance of the cell, specifically the on-chip electrical contact resistance, and by performing a catalyst screening study for hypochlorite reduction to reduce the activation overpotential and enhance the electrochemical kinetics while preventing gas evolution. Alternatively, a modified cell architecture could be developed that accommodates small amounts of gas evolution without compromising the co-laminar flow and transport characteristics associated with the flow-through porous electrodes. Other possible advancements include employing higher fuel and oxidant concentrations in the fuel cell, switching to potassium hydroxide electrolyte and optimizing its concentration, and evaluating other liquid hydrocarbon fuels such as methanol. Although no performance degradation was observed during the proof-of-concept study, a long-term stability test should be performed to analyze the possibility of electrode contamination from the carbonate species. The new alkaline formate and hypochlorite fuel cell concept, or either one of its individual half-cells, may also find applications using conventional membrane-based fuel cell designs with consideration of membrane clogging by carbonates.

(vii) The most appropriate extension of the strategic enzyme patterning study is an experimental verification of the advantages associated with mixed enzyme patterning by implementing some of the proposed patterning strategies in a multi-enzyme microfluidic fuel cell with consecutive reactions. A useful approach for this experimental study would be to employ an array of enzymes that have the same cofactor, such as the methanol or alcohol dehydrogenase, formaldehyde dehydrogenase, and formate dehydrogenase enzymes, which are all NAD-dependent and can be immobilized in the same matrix in different proportions, for complete oxidation of methanol to carbon dioxide.

Bibliography

[1] C.K. Dyer, Journal of Power Sources 106 (2002) 31-34.

[2] R.A. Bullen, T.C. Arnot, J.B. Lakeman, F.C. Walsh, Biosensors & Bioelectronics 21 (2006) 2015-2045.

[3] F. Davis, S.P.J. Higson, Biosensors & Bioelectronics 22 (2007) 1224-1235.

[4] E. Katz, A.N. Shipway, I. Willner. Biochemical Fuel Cells. In W. Vielstich, H.A. Gasteiger,A. Lamm, eds. *Handbook of Fuel Cells - Fundamentals, Technology and Applications* (John Wiley & Sons, Ltd., New York, 2003).

[5] D.H. Park, J.G. Zeikus, Applied and Environmental Microbiology 66 (2000) 1292-1297.

[6] G.T.R. Palmore, H. Bertschy, S.H. Bergens, G.M. Whitesides, Journal of Electroanalytical Chemistry 443 (1998) 155-161.

[7] I. Willner, E. Katz, Angewandte Chemie-International Edition 39 (2000) 1180-1218.

[8] N.L. Akers, C.M. Moore, S.D. Minteer, Electrochimica Acta 50 (2005) 2521-2525.

[9] C.M. Moore, S.D. Minteer, R.S. Martin, Lab on a Chip 5 (2005) 218-225.

[10] S. Topcagic, S.D. Minteer, Electrochimica Acta 51 (2006) 2168-2172.

[11] M. Zayats, E. Katz, R. Baron, I. Willner, Journal of the American Chemical Society 127 (2005) 12400-12406.

[12] M. Zayats, E. Katz, I. Willner, Journal of the American Chemical Society 124 (2002) 14724-14735.

[13] A. Heller, Physical Chemistry Chemical Physics 6 (2004) 209-216.

[14] V. Soukharev, N. Mano, A. Heller, Journal of the American Chemical Society 126 (2004) 8368-8369.

[15] N. Mano, F. Mao, A. Heller, Journal of the American Chemical Society 125 (2003) 6588-6594.

[16] N. Mano, F. Mao, A. Heller, Journal of the American Chemical Society 124 (2002) 12962-12963.

[17] N. Mano, F. Mao, A. Heller, Chembiochem 5 (2004) 1703-1705.

[18] C. Kang, H. Shin, A. Heller, Bioelectrochemistry 68 (2006) 22-26.

[19] F. Gao, Y.M. Yan, L. Su, L. Wang, L.Q. Mao, Electrochemistry Communications 9 (2007) 989-996.

[20] H. Shin, C. Kang, A. Heller, Electroanalysis 19 (2007) 638-643.

[21] N. Mano, F. Mao, A. Heller, Journal of Electroanalytical Chemistry 574 (2005) 347-357.

[22] N. Mano, J.L. Fernandez, Y. Kim, W. Shin, A.J. Bard, A. Heller, Journal of the American Chemical Society 125 (2003) 15290-15291.

[23] N. Mano, V. Soukharev, A. Heller, Journal of Physical Chemistry B 110 (2006) 11180-11187.

[24] R.F. Ismagilov, A.D. Stroock, P.J.A. Kenis, G. Whitesides, H.A. Stone, Applied Physics Letters 76 (2000) 2376-2378.

[25] E.R. Choban, L.J. Markoski, J. Stoltzfus, J.S. Moore, P.J.A. Kenis, Power Sources, pp. 317-320, Cherry Hill, NJ, 2002.

[26] J.L. Cohen, D.J. Volpe, D.A. Westly, A. Pechenik, H.D. Abruna, Langmuir 21 (2005) 3544-3550.

[27] S.M. Mitrovski, L.C.C. Elliott, R.G. Nuzzo, Langmuir 20 (2004) 6974-6976.

[28] S.M. Mitrovski, R.G. Nuzzo, Lab on a Chip 6 (2006) 353-361.

[29] E.R. Choban, J.S. Spendelow, L. Gancs, A. Wieckowski, P.J.A. Kenis, Electrochimica Acta 50 (2005) 5390-5398.

[30] E.R. Choban, P. Waszczuk, P.J.A. Kenis, Electrochemical and Solid State Letters 8 (2005) A348-A352.

[31] R.S. Jayashree, D. Egas, J.S. Spendelow, D. Natarajan, L.J. Markoski, P.J.A. Kenis, Electrochemical and Solid State Letters 9 (2006) A252-A256.

[32] M.H. Sun, G.V. Casquillas, S.S. Guo, J. Shi, H. Ji, Q. Ouyang, Y. Chen, Microelectronic Engineering 84 (2007) 1182-1185.

[33] A. Li, S.H. Chan, N.T. Nguyen, Journal of Micromechanics and Microengineering 17 (2007) 1107-1113.

[34] E.R. Choban, L.J. Markoski, A. Wieckowski, P.J.A. Kenis, Journal of Power Sources 128 (2004) 54-60.

[35] J.L. Cohen, D.A. Westly, A. Pechenik, H.D. Abruna, Journal of Power Sources 139 (2005) 96-105.

[36] R.S. Jayashree, L. Gancs, E.R. Choban, A. Primak, D. Natarajan, L.J. Markoski, P.J.A. Kenis, Journal of the American Chemical Society 127 (2005) 16758-16759.

[37] S. Hasegawa, K. Shimotani, K. Kishi, H. Watanabe, Electrochemical and Solid State Letters 8 (2005) A119-A121.

[38] R. Ferrigno, A.D. Stroock, T.D. Clark, M. Mayer, G.M. Whitesides, Journal of the American Chemical Society 124 (2002) 12930-12931.

[39] R. Aogaki, E. Ito, M. Ogata, Journal of Solid State Electrochemistry 11 (2007) 757-762.

[40] A. Bazylak, D. Sinton, N. Djilali, Journal of Power Sources 143 (2005) 57-66.

[41] M.H. Chang, F. Chen, N.S. Fang, Journal of Power Sources 159 (2006) 810-816.

[42] F.L. Chen, M.H. Chang, M.K. Lin, Electrochimica Acta 52 (2007) 2506-2514.

[43] W.Y. Chen, F.L. Chen, Journal of Power Sources 162 (2006) 1137-1146.

[44] F. Chen, M.-H. Chang, C.-W. Hsu, Electrochimica Acta 52 (2007) 7270-7277.

[45] W.R. Merida, G. McLean, N. Djilali, Journal of Power Sources 102 (2001) 178-185.

[46] M. Togo, A. Takamura, T. Asai, H. Kaji, M. Nishizawa, Electrochimica Acta 52 (2007) 4669-4674.

[47] E. Kjeang, B. Roesch, J. McKechnie, D. Harrington, N. Djilali, D. Sinton, Microfluidics and Nanofluidics 3 (2007) 403-416.

[48] E. Kjeang, A.G. Brolo, D.A. Harrington, N. Djilali, D. Sinton, Journal of the Electrochemical Society 154 (in press)

[49] E. Kjeang, J. McKechnie, D. Sinton, N. Djilali, Journal of Power Sources 168 (2007) 379-390.

[50] E. Kjeang, B.T. Proctor, A.G. Brolo, D.A. Harrington, N. Djilali, D. Sinton, Electrochimica Acta 52 (2007) 4942-4946.

[51] E. Kjeang, R. Michel, N. Djilali, D. Sinton, Manuscript in preparation

[52] E. Kjeang, R. Michel, D. Sinton, N. Djilali, D.A. Harrington, Manuscript in preparation

[53] E. Kjeang, D. Sinton, D.A. Harrington, Journal of Power Sources 158 (2006) 1-12.

Appendix A

Integrated Electrochemical Velocimetry for Microfluidic Devices

Reproduced by permission of Springer

Microfluid Nanofluid (2007) 3:403–416
DOI 10.1007/s10404-006-0128-1

RESEARCH PAPER

Integrated electrochemical velocimetry for microfluidic devices

Erik Kjeang · Bettina Roesch · Jonathan McKechnie · David A. Harrington · Ned Djilali · David Sinton

Received: 27 July 2006 / Accepted: 26 September 2006 / Published online: 6 December 2006

Abstract We present a new electrochemical velocimetry approach with direct electrical output that is capable of complete device-level integration. The steady reduction rate of a reversible redox species at an embedded microband working electrode is monitored amperometrically. Only one working electrode of arbitrary width is required; all three electrodes, including counter and reference electrodes, are integrated on-chip for complete miniaturization of the sensor. Experimental results are complemented by a theoretical framework including a full 3D electrochemical model as well as empirical mass transfer correlations and scaling laws. When the sensor is operated in the convective/diffusive transport controlled mode, the output signal becomes a predictable function of velocity in two distinct regimes: (i) in the low velocity regime, the signal is directly proportional to flow rate, and (ii) in the high velocity regime, the signal scales as the cube root of the mean velocity. The proposed velocimetry technique is applicable to all practicable pressure-driven laminar flows in microchannels with known cross-sectional geometry.

E. Kjeang · J. McKechnie · N. Djilali · D. Sinton (✉)
Department of Mechanical Engineering,
Institute for Integrated Energy Systems (IESVic),
University of Victoria, PO Box 3055, Stn CSC,
Victoria, BC V8W 3P6, Canada
e-mail: dsinton@me.uvic.ca

B. Roesch · D. A. Harrington
Department of Chemistry,
Institute for Integrated Energy Systems (IESVic),
University of Victoria, PO Box 3055, Stn CSC,
Victoria, BC V8W 3P6, Canada

Keywords Microfluidics · Velocimetry · Flow sensor · Redox electrochemistry

1 Introduction

Recent developments in miniaturized total analysis systems and lab-on-chip technologies (Reyes et al. 2002; Auroux et al. 2002) have motivated increased use of electrochemical detection techniques (Nyholm 2005). Applications such as separation of analytes, sorting and sizing of cells and DNA hybridization and quantification all rely on advanced methods for detection. Electrochemical methods are attractive for the small physical dimensions required for capillary electrophoresis (CE) systems: the noise generated actually decreases with electrode surface area and the instrumentation is less expensive than for other detection techniques (Baldwin 2000). Amperometry is the most widely reported CE detection mode (Qiu et al. 2005), combining inherently high selectivity with the high resolution and efficiency achievable with CE separation. This method relies on oxidation or reduction of electrochemically active species by applying a fixed potential to a working electrode (WE) and recording the faradaic current. Requiring only electrical infrastructure, electrochemical detection strategies are appropriate for device-level integration and miniaturization as embedded microelectrodes may be readily incorporated by conventional microfabrication methods.

Microscale flow visualization has played a central role in the development of microfluidic theory and applications (Sinton 2004). Most quantitative visualization techniques developed to date are applied to velocimetry, that is, to measure the mean velocity, flow rate and/or velocity profile. The goal of all these methods is to alter the fluid sufficiently such that its velocity can be measured without disturbing the actual fluid motion. Achieving truly non-intrusive visualization based measurements becomes increasingly challenging as the channel dimensions are reduced. Most visualization methods are either particle based or scalar based. In particle based methods, bulk fluid motion is inferred from the detected velocity of marker particles. Micro-particle image velocimetry (μPIV) is the most mature technique, capable of acquiring high spatial/temporal resolution two-component velocity field data (Meinhart et al. 1999; Santiago et al. 1998). Scalar based methods, collectively termed scalar image velocimetry (SIV), include fluorescence, phosphorescence, photobleaching and photochromic reactions (Sinton 2004). In SIV, molecular tracers are injected into the bulk fluid and the motion is inferred from the observed velocity of the conserved scalar. Both particle- and scalar based visualization techniques require optomechanical supporting infrastructure that is substantial with respect to both cost and size. Although well-suited to research, visualization based velocimetry techniques are not compatible with on-chip integration.

Electrochemical velocimetry has previously been developed to measure flow characteristics in macroscale channels and ducts (Ranz 1958), but the integration of these techniques with microfluidic applications is uncommon. Electrochemical methods are attractive for small channels with laminar flow. A general advantage of electrochemical velocimetry for microfluidic applications is the lack of large scale supporting infrastructure required by other microscale flow visualization techniques (Sinton 2004), which enables flow sensors with minimum footprint. Disadvantages of electrochemical methods include: the requirement of active reacting solutes and/or electrolyte; microfluidics must be designed and fabricated to include the electrode layer and avoid undesired fluid–electrode contact; these methods are not generally applicable to electrokinetic flows; and they do not directly resolve the cross-sectional velocity profile. The latter limitation can be mitigated if the velocity profile may be determined from conventional laminar flow theory given the measured bulk average velocity. The transport-limited current from a microdisc electrode in a flow cell (Booth et al. 1995) or from microelectrodes in cylindrical microholes (Zosel et al. 2003) has previously been shown to correlate with the flow rate. Ayliffe and Rabbitt (2003) developed a convection based flow sensor using electrochemical impedance spectroscopy. Paeschke et al. (1996) placed interdigitated microband electrodes on a silicon wafer microchannel structure and projected that the flow rate could be estimated using redox mediators and potential pulses. Several time-of-flight methods have recently been introduced. Amatore et al. (2004) used paired microband electrodes and a redox couple operating in generator–collector mode to quantify the pressure-driven flow rate in a microchannel. The time delay between generation and collection was measured, and the average velocity was assumed to be equal to the electrode separation divided by the time delay. The streamwise diffusion of the redox species was ignored and the accuracy of the results was not quantified. Other time-of-flight methods presented to date exploit thermal pulses (Yang et al. 1991), temperature-dependent fluorescent dyes (Fu and Li 2006) and electrochemically produced tracers (Wu and Sansen 2002) between upstream and downstream cells. An elegant flow rate measurement technique based on amperometric oxygen sensors was developed by Wu and Ye (2005). Simulation and experimental results show that the response ratio of two thin, closely spaced WEs is related to the flow rate. This approach is independent of initial oxygen concentration, but the results showed limited sensitivity and range.

In this study, we present and demonstrate a novel electrochemical in situ velocimetry approach for microfluidic chip based systems that fully exploits the convective/diffusive transport of a solute redox couple. The amperometric signal from a single, embedded working electrode is analyzed as a direct function of the mean velocity in the channel. The experiments are complemented by a complete theoretical framework employing (i) a full electrochemical model implemented computationally in 3D (including a 2D symmetry assumption with quantified relative error) that combines heterogeneous redox electrochemistry and mass transport theory, (ii) an empirical mass transfer model for sensor operation in the transport controlled mode and (iii) scaling laws that quantify sensor operation in the high and low velocity regimes. We propose the following improvements over existing designs: robust electrochemistry; reduced number of electrodes; case-specific, tailored sensor design; enhanced sensitivity; and extended operational range.

2 Experimental

2.1 Microfabrication

Microfluidic flow cell assemblies were prepared using in-house microfabrication techniques. The base substrate was patterned with microband electrodes according to the following procedure: a thin layer of negative photoresist (SU-8 25; Microchem, Newton, MA) was spin-coated (Specialty Coating Systems, Indianapolis, IN) with ramping at 2,000 rpm/30 s on a pretreated glass substrate followed by a two-step soft bake on covered contact hot plates at 65°C/5 min and 95°C/10 min. A photomask that defines the desired electrode pattern was generated in CAD software and printed by a high-resolution image setter on a transparency. The substrate, placed under the photomask, was then exposed to columnated UV light (Tamarack Sci., Corona, CA) for 30 s, post-exposure baked at 65°C/3 min and 95°C/5 min, and finally, immersed in SU-8 developer liquid (Microchem) to dissolve the unexposed portions of the photoresist. Gold (Sigma-Aldrich, Oakville, Canada) was coated over the whole substrate in a two-stage process: a thin (20 nm) adhesive coating of chromium (Kurt J Lesker, Clairton, PA) was evaporated under vacuum at 0.3–0.6 Å s^{-1}; and then a substantially thicker (150 nm) gold coating was evaporated at 0.6–0.8 Å s^{-1} over the chromium layer. After cooling, the substrate was soaked in an acetone bath for 2 h to lift off the gold-coated photoresist sections, thus revealing the final microband gold electrode structure adhered to the glass substrate (Fig. 1). The top part of the flow cell, containing the 100 µm high and 1 mm wide rectangular channel structure, was fabricated by replica molding in poly(dimethylsiloxane) (PDMS; Dow Corning, Midland, MI), following established soft-lithographic protocols (Duffy et al. 1998). The specific equipment and procedure employed is detailed elsewhere (Coleman et al. 2006). Holes for inlet and outlet tubing were punched in the PDMS prior to assembly. Both surfaces were plasma-treated (Harrick Sci., Pleasantville, NY) for 30 s to yield silanol surface groups that covalently bind glass to PDMS and render hydrophilic channel walls. The PDMS slab was aligned perpendicularly to the microband electrodes on the bottom substrate, leaving the external gold contacts exposed, as illustrated in Fig. 1a. The final flow cell shown in Fig. 1b includes external wires attached to the contacts using silver conductive epoxy (MG Chemicals, Toronto, Canada) and Tygon® flexible tubes for fluid delivery. The channel has a rectangular cross-section: $h = 100$ µm high and $d = 1$ mm wide; the microband electrodes are $w = 500$ µm wide, separated by 500 µm gaps.

2.2 Electrochemistry

Fresh 0.2 M potassium sulfate (K_2SO_4) electrolyte solutions containing 2.5 or 5 mM of each ruthenium hexaammine $[Ru(NH_3)_6^{2+/3+}]$ solute redox species obtained from $Ru(NH_3)_6Cl_2$ and $Ru(NH_3)_6Cl_3$ salts

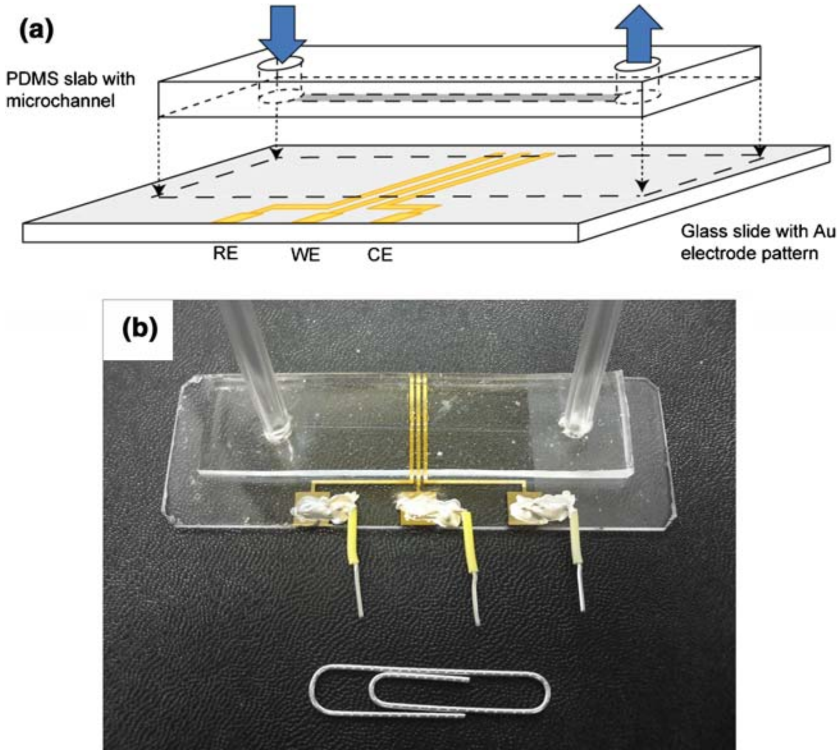

Fig. 1 **a** Schematic diagram of a microfluidic flow cell assembly: plasma-treated, pre-fabricated substrate with micropatterned electrodes, brought into contact with the elastomeric microfluidic channel structure. *RE*, *WE* and *CE* represent reference, working and counter electrodes. **b** Complete flow cell assembly with three embedded Au electrodes on the bottom surface of the channel (running left to right)

(Sigma-Aldrich) were prepared from Millipore Milli-Q water (Millipore, Billerica, MA) and potassium sulfate (K_2SO_4, AnalaR; BDH, Poole, UK) and used within 24 h. Redox couples and supporting electrolytes can be chosen from many tabulations (e.g., Bard et al. 1985), though attention must be paid to possible interferences with the process chemistry of the system. While reversible systems such as $Ru(NH_3)_6^{2+/3+}$, $Fe(CN)_6^{3-/4-}$, ferrocene/ferrocinium or hydroquinone/*p*-benzoquinone are preferred, suitable modeling and calibration such as is done here should also allow less reversible couples to be used. In general, the use of K_2SO_4 supporting electrolyte is preferred to acidic electrolytes in order to achieve maximum separation of the $Ru(NH_3)_6^{2+/3+}$ and the hydrogen redox potentials. All solutions were degassed with argon for 30 min prior to and during the experiments. Steady flow of solution through the microchannel was facilitated by a syringe pump (Harvard Apparatus, Holliston, MA) operating in refill mode, providing a vacuum pressure at the outlet reservoir. The flow cell was mounted inside a custom-made Faraday cage (optional) and driven by a PARSTAT 2263 potentiostat (Advanced Measurement Technology, Oak Ridge, TN). The potential of the integrated WE was controlled in order to maintain operation in the transport dominated regime, and its steady-state amperometric response was recorded. The reference (RE) and counter (CE) electrodes can be placed either internally or externally; although, in the most elegant configuration in terms of miniaturization, all three electrodes are integrated on-chip. As shown in Fig. 1, the RE is positioned upstream of the WE, such that it senses the equilibrium potential of the redox couple ahead of any electrochemical perturbation at the WE. The CE is located downstream of the WE to avoid disturbances in redox concentration from any extraneous electrochemical processes. In the case of external RE and CE, Ag/AgCl (1 M KCl) and platinum mesh electrodes, respectively, were immersed in the inlet reservoir. All active surfaces were cleaned by electrochemical cycling in blank electrolyte from –0.2 to +0.2 V versus the external RE before starting the experiments. In the case of integrated RE, the potentials are quoted relative to the equilibrium potential of the redox pair.

3 Theory

3.1 Electrochemical model

A computational electrochemical model that combines heterogeneous redox electrochemistry and subsequent convective-diffusive transport was developed and implemented in a commercial code. The model yields full 3D concentration field data and accurate predictions of the amperometric signals for both transient and steady-state operational modes. Pressure-driven flow of aqueous solutions in microchannels is typically laminar. For example, the Reynolds number in a channel with hydraulic diameter $D_h \approx 0.2$ mm (as in the flow cell in Fig. 1) results in $Re \approx 10$ for a mean velocity of $U \approx 50$ mm s^{-1}. The continuum assumption is appropriate for liquid flows on this scale, justifying the use of continuous flow theory and established computational fluid dynamics (CFD) methods (Erickson 2005). In this context, conservation of mass and momentum for a Newtonian fluid are described by the continuity and Navier–Stokes equations for incompressible, steady, laminar flow:

$$\nabla \cdot \vec{u} = 0 \tag{1}$$

$$\rho \vec{u} \cdot \nabla \vec{u} = \rho \vec{g} - \nabla p + \mu \nabla^2 \vec{u} \tag{2}$$

No-slip boundary conditions are implemented at the channel walls. Uniform velocity and constant pressure are prescribed at the inlet and outlet, respectively, and the system of equations is implemented and solved computationally using the commercial software package COMSOL Multiphysics 3.2 (COMSOL, Stockholm, Sweden). In the fully developed region, the classical parabolic velocity profile (Poiseuille flow) is obtained.

To simulate electrochemical operation of the flow sensor, the concentration distributions of the solute redox species in the microchannel and the rate of electron-transfer reactions at the embedded electrodes must be addressed. The high concentration of supporting electrolyte leads to several benefits: electromigration of the low-concentration redox species can be ignored, the thickness of the electrical double layer can be assumed negligible relative to other characteristic lengths, activity coefficients may be assumed independent of redox concentration, and the potential drop in the channel can be neglected. The redox reaction

$$\mathrm{Ru(NH_3)_6}^{3+} + e^- \underset{k_{-1}}{\overset{k_1}{\leftrightarrow}} \mathrm{Ru(NH_3)_6}^{2+}$$

has a formal redox potential of $E^{\circ\,\prime} = -0.15$ V versus Ag/AgCl (1 M KCl) (Muzikar and Fawcett 2004). Equal concentrations of the oxidized and reduced species in the presence of a supporting electrolyte ensures that the standard, formal, and equilibrium potentials may be taken to be equal; the overpotential (η) is the departure of the potential from this value.

The forward and backward rate constants show the usual Tafel potential dependence of first-order electrode kinetics (Newman and Thomas-Alyea 2004):

$$\text{Forward:} k_1 = k^\circ \exp\left(-\frac{\beta F \eta}{RT}\right) \tag{3}$$

$$\text{Backward:} k_{-1} = k^\circ \exp\left(\frac{(1-\beta) F \eta}{RT}\right). \tag{4}$$

For modeling purposes, we use the standard rate constant, k° = 1.44 cm s^{-1}, and exponential charge transfer coefficient, β = 0.48, recently reported by Muzikar and Fawcett (2004) for $Ru(NH_3)_6^{2+/3+}$ in 0.02 M perchloric acid on a gold electrode. The rate of the reaction is written as

$$v = k_1 c_{Ru(NH_3)_6{}^{3+}} - k_{-1} c_{Ru(NH_3)_6{}^{2+}}. \tag{5}$$

Note that the concentrations in Eq. 5 are computed at the surface of the WE where the charge transfer takes place. Provided that there is no surface adsorption, the fluxes of the redox species at the WE are equal and opposite, and assuming that the diffusion coefficients are equal (similar sized molecules), the sum of the two concentrations must be constant:

$$c_{Ru(NH_3)_6{}^{3+}} + c_{Ru(NH_3)_6{}^{2+}} = c_{0,Ru(NH_3)_6{}^{3+}} + c_{0,Ru(NH_3)_6{}^{2+}}. \tag{6}$$

Electron exchange between the oxidized and reduced species may also occur in solution, but Eq. 6 remains valid. If the inlet concentrations (c_0) are of the same magnitude, we obtain

$$c_{Ru(NH_3)_6{}^{2+}} = 2c_0 - c_{Ru(NH_3)_6{}^{3+}}. \tag{7}$$

By manipulation of Eqs. 5–7 we can now eliminate one of the redox concentrations, drop the subscript and arrive at

$$v = k_1 c - k_{-1}(2c_0 - c). \tag{8}$$

The local Faradaic current density at the electrode is proportional to the reaction rate:

$$i = -nFv. \tag{9}$$

Total electrical current is obtained by integration of the current density over the electrode surface (S), i.e.,

$$I = \int_S i \mathrm{d}S. \tag{10}$$

In summary, the amperometric signal generated at the WE with applied overpotential η is obtained by combining Eqs. 3–10 into

$$I = \int_S -nFk^\circ \left\{ \exp\left(-\frac{\beta F\eta}{RT}\right) c - \exp\left(\frac{(1-\beta)F\eta}{RT}\right)(2c_0 - c)\right\} \mathrm{d}S. \tag{11}$$

This equation relates the amperometric signal to the redox concentration in the WE proximity, however, it does not provide current as a function of mean velocity or flow rate. The redox concentration near the WE ultimately depends on the flow characteristics and channel geometry by means of the convective diffusion equation for solute species conservation with passive scalar treatment and constant density (Probstein 2003):

$$\frac{\partial c}{\partial t} + \vec{u} \cdot \nabla c = D \nabla^2 c. \tag{12}$$

Here, the source term has been neglected due to the absence of net homogeneous reactions. The diffusion coefficient is assumed to be independent of concentration and equal to D = 9.1 × 10^{-6} cm^2 s^{-1}, determined for $Ru(NH_3)_6^{2+/3+}$ in 0.1 M KCl by rotating disk voltammetry (Marken et al. 1995). Electrochemical reactions (Eq. 8) are applied as boundary conditions confined to the exposed electrode surfaces. All other surfaces are treated as impermeable walls subject to a Neumann condition, with a Dirichlet condition at the inlet and a convective flux condition at the outlet. Temperature effects are negligible, provided that the current generation is low and that the electrodes are situated on glass, which provides an efficient heat sink in hybrid PDMS/glass microfluidic systems (Erickson et al. 2003).

The convective diffusion equation coupled with the electrochemical boundary condition was solved computationally using COMSOL Multiphysics 3.2 on the microchannel domain using the velocity field obtained from decoupled Navier–Stokes simulations. The amperometric signal from the WE is calculated by boundary integration according to Eq. 8. A steady-state solution is sufficient to retrieve the amperometric signal as a function of flow rate, whereas a transient approach is used to analyze the dynamic behaviour and response time. Mesh optimization and convergence were assured in all simulations.

3.2 Mass transfer model

An empirical mass transfer model was developed for sensor operation in the transport controlled regime, based on established heat transfer correlations in conjunction with the heat and mass transfer analogy. The purpose of this analysis is to seek a closed form relationship for the amperometric signal as a function of mean velocity. The rate of a heterogeneous chemical reaction is related to the rate of mass transfer by the Damköhler number (*Da*). For a reversible electrochemical reaction, this dimensionless similarity parameter is defined as

$$Da = v\left(D\frac{\partial c}{\partial y}\bigg|_s\right)^{-1}. \tag{13}$$

For sufficiently large overpotentials, the rate of the electrochemical reaction is much faster than the rate of species diffusion to the surface ($Da >> 1$) and the boundary condition at the WE surface becomes (Probstein 2003)

$$c_s \approx 0. \tag{14}$$

This condition describes the transport controlled regime: all molecules approaching the WE surface react instantaneously and the current is limited by the convective/diffusive transport of reactant. A concentration boundary layer that depends on the flow characteristics will thus develop in the channel, starting at the leading edge of the WE ($x = 0$). To approximate the total flux of reactant to the WE and sequentially the amperometric signal, one can consider the limiting case of internal, fully developed laminar flow between two flat plates with one reacting wall. There is no analytical solution to this mass transfer problem available in the literature, but there is an extensive body of textbook examples available for mathematically similar heat transfer problems. For a particular geometry, the results from convection heat transfer can conveniently be used for convection mass transfer by replacing the Nusselt number (*Nu*) with the Sherwood number (*Sh*) and the Prandtl number (*Pr*) with the Schmidt number (*Sc*) (Incropera and De Witt 1990). The classical Graetz problem (Graetz 1885) of heat transfer describes the temperature profiles in a fully developed tube flow where the wall temperature suddenly changes from one fixed value to another fixed value, taking the thermal entry length into account. The Nusselt numbers are, in principle, infinite at $x = 0$ and decay towards their fully developed value with increasing axial coordinate, x. The equivalent Graetz solution for flow between two heated flat plates with equal and uniform temperature distribution was developed by Nusselt (1923), based on infinite series with tabulated eigenvalues. The following empirical equations for the average Nusselt number in the thermal entry region is found to yield results within ±3% of Nusselt's theoretical solution (Kakac et al. 1987):

$$\bar{Nu} = \begin{cases} 1.849x^{*-1/3} & x^* \leqslant 0.0005 \\ 1.849x^{*-1/3} + 0.6 & 0.0005 \leqslant x^* \leqslant 0.006 \\ 7.541 + 0.0235/x^* & x^* > 0.006 \end{cases} \tag{15}$$

where $x^* = \frac{x}{D_h Re Pr}$ is a dimensionless axial coordinate. Using the heat and mass transfer analogy we obtain

$$\bar{Sh} = \begin{cases} 1.849U^{*1/3} & U^{*-1} \leqslant 0.0005 \\ 1.849U^{*1/3} + 0.6 & 0.0005 \leqslant U^{*-1} \leqslant 0.006 \\ 7.541 + 0.0235U^* & U^{*-1} > 0.006 \end{cases} \tag{16}$$

where we introduced the dimensionless velocity $U^* = \frac{D_h Re Sc}{w} = \frac{UD_h^2}{wD}$. The average mass transfer coefficient for molar flux, $\bar{h}_{MT}$, is obtained from

$$\bar{Sh} = \frac{\bar{h}_{MT} D_h}{D}. \tag{17}$$

The average molar flux based on the logarithmic mean concentration difference is determined by

$$\bar{J}_s = \bar{h}_{MT} \frac{(c_s - c_m)_{x=0} - (c_s - c_m)_{x=w}}{\ln\left[(c_s - c_m)_{x=0}/(c_s - c_m)_{x=w}\right]}. \tag{18}$$

Here, the subscript m indicates bulk mean values. With the boundary condition $c_s = 0$ and bulk mean concentration at $x = 0$ equal to the inlet concentration, we get

$$\bar{J}_s = \bar{h}_{MT} \frac{c_{m,x=w} - c_0}{\ln\left[c_0/c_{m,x=w}\right]}. \tag{19}$$

For the case of constant surface temperature convective heat flux, the bulk mean temperature changes according to (Incropera and De Witt 1990)

$$\frac{(T_s - T_m)_{x=w}}{(T_s - T_m)_{x=0}} = \exp\left(-\frac{Pw}{\dot{m}c_p}\bar{h}_{HT}\right). \tag{20}$$

This equation can be extended to mass transfer upon the implementation of the heat and mass transfer analogy, arriving at

$$\frac{(c_s - c_m)_{x=w}}{(c_s - c_m)_{x=0}} = \exp\left(-\frac{Pw}{UA_c}\bar{h}_{\mathrm{MT}}\right)$$
$$\Rightarrow c_{m,x=w} = c_0 \exp\left(-\frac{Pw}{UA_c}\bar{h}_{\mathrm{MT}}\right). \tag{21}$$

Finally, the total current generated at the WE is given by

$$I = nF\bar{J}_s A = Fdw\bar{h}_{\mathrm{MT}} \frac{c_{m,x=w} - c_0}{\ln\left[c_0/c_{m,x=w}\right]} \tag{22}$$

For a given geometry, Eq. 22 provides an estimate of WE current as a direct function of mean velocity in closed form.

3.3 Scaling laws

Scaling laws for the amperometric signal were derived in two specific regimes: the high U^* regime (high velocity, large hydraulic diameter and small WE width) and the low U^* regime (low velocity, small hydraulic diameter and large WE width).

3.3.1 High U^* regime

Scaling laws for the high U^* regime can be obtained by further simplification of the mass transfer model. To derive a simple power law, two additional assumptions are required: (i) bulk mean properties are equal to the free stream value, and (ii) the Sherwood number previously used for high U^* is valid for all U^* under study. In other terms:

$$c_m = c_0 \tag{23}$$

$$\bar{h}_{\mathrm{MT}} = 1.849 \frac{D}{D_{\mathrm{h}}} U^{*1/3}. \tag{24}$$

Since the concentration difference is now constant, logarithmic mean averaging is not required, and the average molar flux is given by

$$\bar{J}_s = \bar{h}_{\mathrm{MT}}(c_s - c_0). \tag{25}$$

By noting that $c_s = 0$, the total amperometric signal becomes

$$I = nF\bar{J}_s A = -1.849 Fdwc_0 \frac{D}{D_{\mathrm{h}}} U^{*1/3} = -1.849 Fdwc_0 \times \frac{D}{D_{\mathrm{h}}}\left(\frac{UD_h^2}{wD}\right)^{1/3} = -1.849 Fdc_0 \left(\frac{w^2 D^2 U}{D_{\mathrm{h}}}\right)^{1/3}. \tag{26}$$

We now have a functional relationship for the amperometric signal in terms of inlet concentration, geometrical parameters and mean velocity. The current is proportional to inlet concentration, $I \propto c_0$, and scales as $I \propto w^{2/3}$ versus WE width and $I \propto U^{1/3}$ versus mean velocity. For high aspect ratio channel geometries with hydraulic diameter approximated by $D_{\mathrm{h}} \approx 2h$, the current is also proportional to channel width, $I \propto d$, and scales as $I \propto h^{-1/3}$ versus channel height. Furthermore, if we introduce the dimensionless current

$$I^* = \frac{I}{Fdwc_0 D/D_{\mathrm{h}}}, \tag{27}$$

we obtain a linear relationship between I^* and $U^{*1/3}$ for all inlet concentrations and sensor/channel geometries under study:

$$I^* = -1.849 U^{*1/3}. \tag{28}$$

The sensitivity of the amperometric signal to changes in mean velocity is defined as the partial derivative of I with respect to U, which is equal to

$$\frac{\partial I}{\partial U} = -\frac{1.849}{3} Fdc_0 \left(\frac{w^2 D^2}{D_{\mathrm{h}} U^2}\right)^{1/3} \tag{29}$$

at high velocities. Thus, the sensitivity scales as $\frac{\partial I}{\partial U} \propto U^{-2/3}$ versus mean velocity and is proportional to inlet concentration.

3.3.2 Low U^* regime

In the low U^* regime, the operation of the sensor reaches a point where all of the incoming reactant is consumed at the WE, such that the total flux entering the channel is equal to the total flux sensed by the WE:

$$\int_{x=0} cu\,\mathrm{d}A = \int_{\mathrm{WE}} J_s \mathrm{d}A \tag{30}$$

Evaluation of the integrals leads to

$$c_0 U A_c = -I/F \Rightarrow I = -Fc_0 U A_c. \tag{31}$$

Thus, the current is independent of WE width and proportional to each of the following variables at low velocities: inlet concentration, mean velocity and cross-sectional area. The signal is therefore also proportional to flow rate. Eq. 31 can also be written in terms of the dimensionless variables I^* and U^*. For high aspect ratio channels with $D_{\mathrm{h}} \approx 2h$ and $A_c = dh$, we obtain

$$I^* = -\frac{1}{2}U^*. \quad (32)$$

The transition point from the high U^* regime to the low U^* regime is found by setting the I^* variables in Eqs. 28 and 32 equal:

$$-\frac{1}{2}U^* = -1.849U^{*1/3}. \quad (33)$$

By solving this equation, the transition point becomes

$$\begin{aligned} U^{*1/3} &= (2 \times 1.849)^{1/2} = 1.9 \\ U^* &= (2 \times 1.849)^{3/2} = 7.1. \end{aligned} \quad (34)$$

The low U^* solution is thus valid in the range $0 \leq U^* \leq 7.1$. The high U^* solution is applicable to $U^* \geq 7.1$, provided that the flow remains laminar.

The sensitivity in the low U^* regime equals

$$\frac{\partial I}{\partial U} = -Fc_0A_c, \quad (35)$$

which is independent of velocity and proportional to both inlet concentration and cross-sectional area.

4 Results and discussion

Three-dimensional computational simulations based on the electrochemical model were performed for various flow cell geometries and operating conditions to establish an appropriate configuration for velocimetry. The domain, initially the entire microchannel, was reduced significantly by noting that current flows at the upstream RE are negligible and do not perturb the uniform inlet concentrations. Moreover, the reactions occurring at the CE need not be included, since this electrode is placed downstream in relation to the WE and will not influence the amperometric signal. Large aspect ratio geometries offer the possibility of reduced dimensionality, which is advantageous for analysis of results and comparison with theory. Full 3D simulations on the channel geometry of the flow cell in Fig. 1 (10:1 aspect ratio) were compared to 2D simulations in which end effects of the far walls were neglected. It was concluded that the 2D model is adequate for aspect ratios larger than 10:1, with errors less than 2%. Two-dimensional simulations also enabled significantly increased spatial resolution in the two dominant dimensions.

Concentration field data obtained using the 2D steady-state electrochemical model are plotted in Fig. 2. Negative overpotentials reduce $Ru(NH_3)_6^{3+}$, leading to $Ru(NH_3)_6^{3+}$ depletion and $Ru(NH_3)_6^{2+}$ accumulation in the WE proximity. The concentration of the depleted species becomes approximately zero at the WE interface, although the reversibility of the redox couple provides a small shift towards non-zero values. The reduction rate of the $Ru(NH_3)_6^{3+}$ species at the WE depends on the concentration gradient estab-

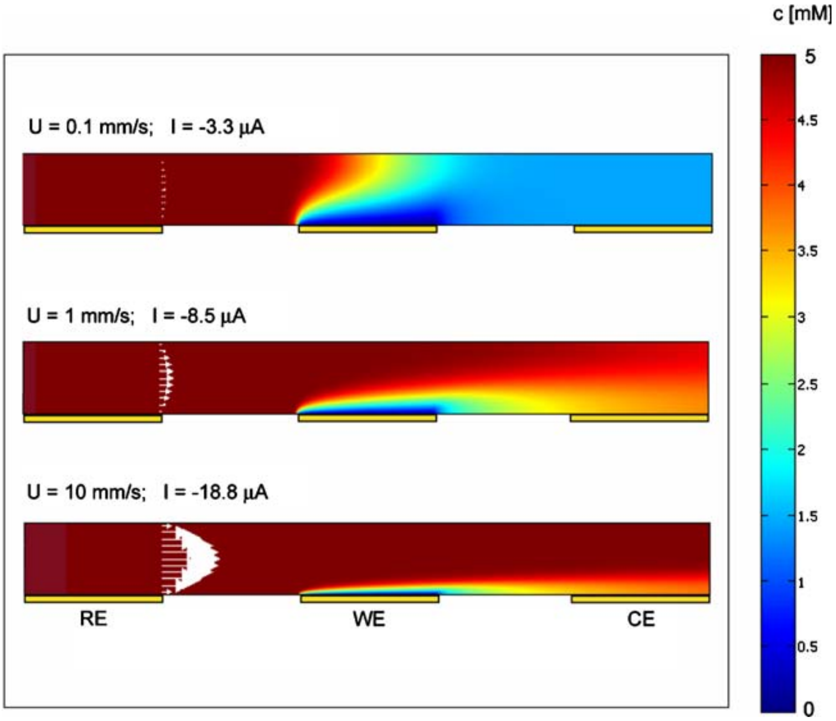

Fig. 2 Computational proof-of-concept: steady-state $Ru(NH_3)_6^{3+}$ concentration distributions obtained from the electrochemical model in the symmetry plane of a flow cell operating at negative WE overpotential. The magnitude of the WE current (*I*) increases with mean velocity (*U*). Conditions: c_0 = 5 mM, η = –0.2 V, *h* = 100 μm, *w* = 500 μm, *d* = 1 mm

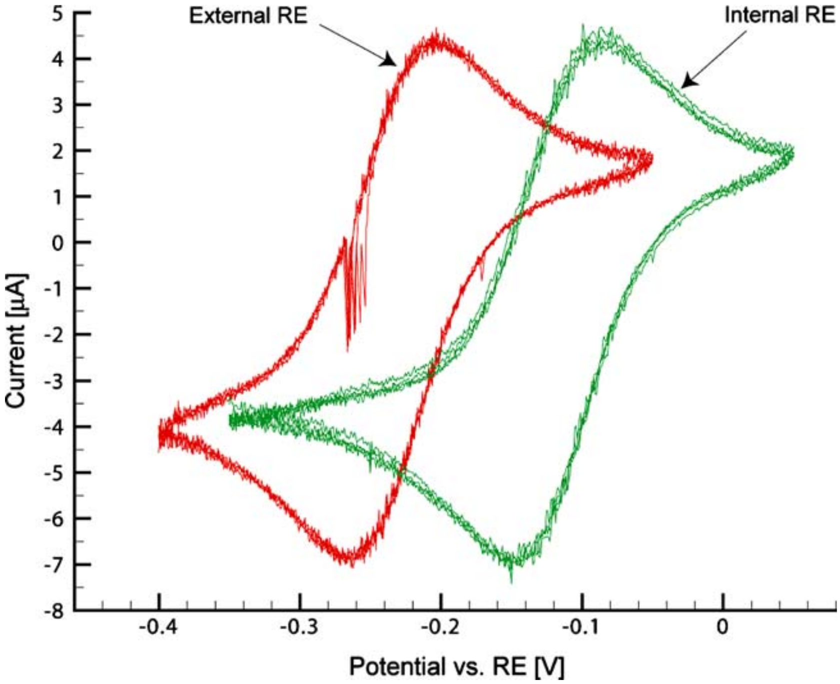

Fig. 3 Experimental cyclic voltammograms. Sweep rate 50 mV s^{-1}. The *external RE* curve shows the potential of the WE in channel controlled vs an off-chip Ag/AgCl reference electrode in the inlet reservoir. The *internal RE* curve shows the potential of the WE in channel controlled vs upstream RE in channel

lished by the flow. Specifically, increased velocity results in reduced concentration boundary layer thickness and increased cross-stream diffusion of reactant. The amperometric signals, obtained by boundary integration of the flux at the WE surface, demonstrate that the magnitude of the current increases with velocity, thus serving as a theoretical proof-of-concept for flow cell design.

The flow sensor could be designed for operation in the rate controlled regime, the transport controlled regime or in a mixed regime. That is, the current drawn from the WE can be limited by either the rate of the chemical reactions or the rate of species transport to the active sites. The transport controlled regime is generally preferred, given that fewer parameters will influence the measured amperometric signal. As shown by the scaling laws in Sect. 3.3, these parameters include inlet concentration of redox species, diffusion coefficient and mean velocity. For the case of fixed inlet concentration and diffusion coefficient, the signal will therefore be a function of velocity only. Operation in the transport controlled regime has other advantages as well: uncertainties in parameters such as rate constant and charge-transfer coefficient are unimportant; mass transfer models (Sect. 3.2) and scaling laws (Sect. 3.3) are appropriate; the response exhibits a higher signal-to-noise ratio; potential loss due to ohmic resistance can be ignored; the signal is independent of minor surface defects; and most importantly, the sensitivity of the amperometric response as a function of flow rate is much higher.

Cyclic voltammograms were generated experimentally for diagnostics of electrode performance. Figure 3 presents the curves obtained at 50 mV s^{-1} scan rate for two separate runs with external and internal RE and CE. These well-defined curves with redox couple oxidation and reduction peaks situated near the formal redox potential confirm that no competing reactions are present and that the reversible behaviour of the redox couple is preserved. The potential shift from external to internal RE curves is close to the expected 0.15 V. A small shift towards more negative potentials is observed for both curves, which is an inherent feature of the micro flow cell configuration not encountered in conventional electrochemical cells. The similarities between the curves for external and internal RE and CE show that the miniaturization of the system via on-chip integration of these electrodes does not mitigate its electrochemical performance. It is also desirable to maintain operation in the transport controlled regime with a lower bound at the characteristic reversible peak separation, 59 mV. Simulation results evaluated at different overpotentials reveal that $|\eta| = 0.2$ V provides 99% overall transport controlled current, suitable for reliable sensor operation with negligible change due to possible variations in electrochemical rate parameters. Competing reactions are generally more likely to be introduced for large overpotentials, resulting in an upper bound for the WE potential.

The dynamic behaviour of the flow sensor was investigated computationally using the transient electrochemical model. Results from a typical case are plotted in Fig. 4. At $t < 0$, there is no overpotential applied to the WE and the fully developed laminar flow is steady at a mean velocity of 1 mm s^{-1}. In this case, the amperometric response is zero due to the cancellation of the forward and backward rate terms when the redox concentrations are equal. As the switch to constant $|\eta| = 0.2$ V is initiated at $t = 0$, a current spike is generated that gradually diminishes with time. On the order of $\tau_e \sim 100$ ms, the amperometric response is fully stabilized at the steady-state value. The response time needed to reach steady-state is even shorter for higher velocities and smaller channel cross-sections. Since inertial effects are relatively insignificant in microfluidic systems, the time scale required to establish steady flows, τ_f, is relatively fast. It can be estimated by balancing unsteady inertial forces with viscous forces for pressure-driven flow (Squires and Quake 2005) according to

$$\tau_f \sim \frac{\rho {D_\mathrm{h}}^2}{\mu} \tag{36}$$

For $h = 100$ μm channels, hydrodynamic steady-state is reached within $\tau_f \sim 10$ ms. The amperometric response to changes in flow dynamics should therefore be smooth with overall response time limited by the stabilization time for the amperometric signal, $\tau_e \sim 100$ ms.

Transient results were obtained experimentally with the potentiostat in reductive amperometric mode, incorporating recurrent overpotential pulses at –0.2 V with 10 s time intervals, with results shown in Fig. 5. Each time the overpotential is switched on, a distinct reduction current spike is generated due to the presence of reactant in the WE proximity. The current is stabilized near the steady-state value after less than 1 s, in agreement with the transient modeling results presented in Fig. 4. After this initial transition period, the current is indeed very stable and the steady-state data are registered at the end of each 10 s interval. The steady-state modeling results (dashed lines in Fig. 5) are in good agreement with the experimentally measured reduction current. In general, the option of applying positive overpotentials and thereby oxidizing the redox pair was found to be less reliable than the operation in reduction mode. The reduction current mode ($\eta < 0$) was therefore applied in all tests.

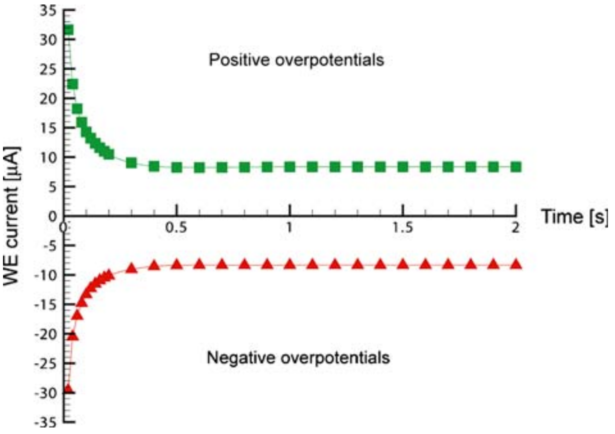

Fig. 4 Dynamic amperometric response obtained using the transient electrochemical model. $|\eta| = 0.2$ V is switched on at $t = 0$. Conditions: $U = 1$ mm s^{-1}, $c_0 = 5$ mM, $h = 100$ μm, $w = 500$ μm, $d = 1$ mm

Steady-state operation is the preferred mode for reliable velocimetry with reproducible data. Experimental data were obtained 10 s after the application of the overpotential to ensure steady operation. The reductive amperometric signals for two different redox concentrations are presented in Fig. 6 as a function of mean velocity. Several aspects of these results are noteworthy. First, the slope of the curves reveals a functional relationship between velocity and measured current, which is the basis of the flow sensor operation. This variation of the output signal is significant through a velocity range of two orders of magnitude. Secondly, the smooth features of the data obtained at 2.5 mM, unobstructed by noise, show that this concentration is sufficiently high for detection of a wide range of velocities. Finally, the experimental results are in good

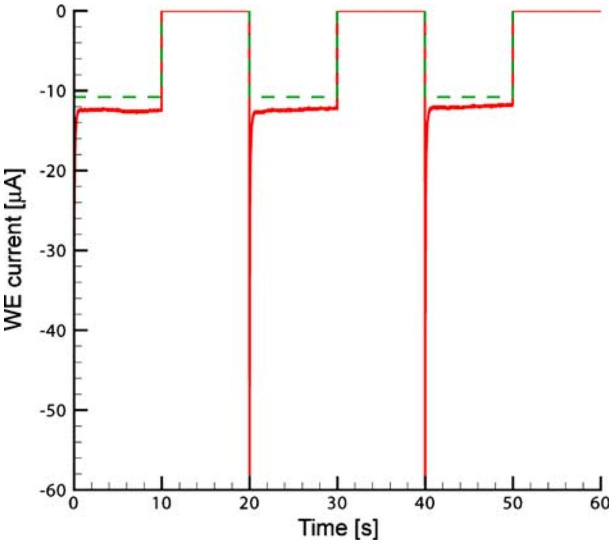

Fig. 5 Amperometric signal obtained experimentally (*solid line*) with recurrent potential pulses applied to the WE. Steady-state modeling results (*dashed line*) are plotted for comparison. Conditions: $U = 2$ mm s^{-1}, $c_0 = 5$ mM, $\eta = -0.2$ V, $h = 100$ μm, $w = 500$ μm, $d = 1$ mm

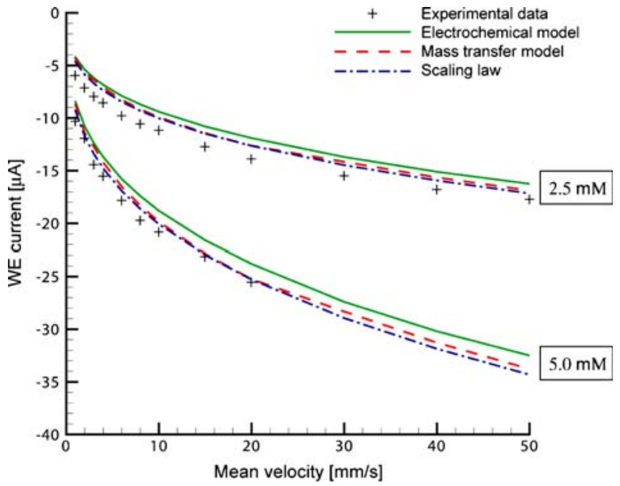

Fig. 6 Amperometric signals determined experimentally (*symbols*) plotted in relation to results from the electrochemical model (*solid lines*), the mass transfer model (*dashed lines*) and the scaling law (*dash-dot lines*). As indicated in the figure, two different inlet concentrations were used: c_0 = 2.5 and c_0 = 5.0 mM. Other conditions: η = –0.2 V, h = 100 μm, w = 500 μm, d = 1 mm

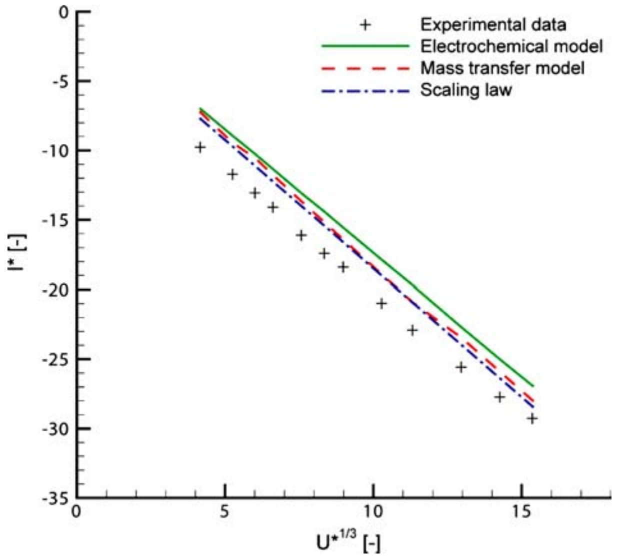

Fig. 7 Normalized amperometric signal (I^*) as a function of the dimensionless velocity parameter $U^{*1/3}$. Conditions: c_0 = 2.5 mM, η = –0.2 V, h = 100 μm, w = 500 μm, d = 1 mm

agreement with the electrochemical model. The small systematic discrepancy of ~10% is expected from uncertainties in diffusion coefficients and cross-sectional channel dimensions. The repeatability of the experiments was found to be very high, provided that the electrode surfaces were free from impurities. For consecutive experimental trials using the same solution, the change was < 1%; whereas the average variation between fully separated trials on different days with different solutions was about 3%.

In relation to the electrochemical model, the mass transfer model uniformly overestimates the current somewhat due to the c_s = 0 assumption and the imposed effect of the non-reacting opposite wall. The difference is yet less than 6% in the entire velocity range considered for this geometry. The results obtained from the high U^* scaling law overshoots up to 10% compared to the electrochemical model because of the additional assumption of $c_{m,x=w} = c_0$. The scaling results are most accurate in the high velocity regime where this assumption is appropriate. Further analysis is provided in Fig. 7, where the data for c_0 = 2.5 mM is plotted in the dimensionless quantities $I^* = \frac{I}{Fdwc_0D/D_\mathrm{h}}$ and $U^{*1/3} = \left(\frac{UD_\mathrm{h}^2}{wD}\right)^{1/3}$, identified through the scaling derivations in Sect. 3.3. The scaled data for different inlet concentrations collapse (omitted from Fig. 7 for clarity), showing that the current is proportional to inlet concentration. All curves are linear with a slope similar to that predicted by the high U^* scaling law in the range shown, confirming that the amperometric signal does indeed scale with velocity to the power of 1/3 ($I \propto U^{1/3}$). In summary, any of the proposed theoretical methods can be used to obtain calibration curves: the electrochemical model is the preferred one, followed by the empirical mass transfer model. The accuracy of the scaling law is satisfactory for quick approximations.

The flexibility of the proposed amperometric velocimetry technique with respect to cross-sectional channel geometry and width of the microband WE is demonstrated in Fig. 8. The technique is applicable to any cross-sectional channel geometry. The computationally obtained curves for different channel heights have similar shapes although the magnitude of the signal for the 25 μm channel is greater, since the concentration gradients generated at a given velocity are larger in thinner channels. Modification of the width of the microband electrodes introduces another degree of freedom for sensor design. Figure 8a shows the effect of increasing WE width from 0.5 to 2.0 mm for 25 and 100 μm high channels. Increasing WE width raises the magnitude of the signal for both channels. On the other hand, if the specific application is constrained w.r.t. planar area, our results indicate that a WE width as small as 0.1 mm is sufficient, although the signal loses some of its strength. Variables I^* and $U^{*1/3}$ provide effective dimensionless scaling for WE current and mean velocity, respectively. It is noteworthy, however, that these variables depend further on the geometry of the WE and the microchannel. The linearity shown in Fig. 8b demonstrates

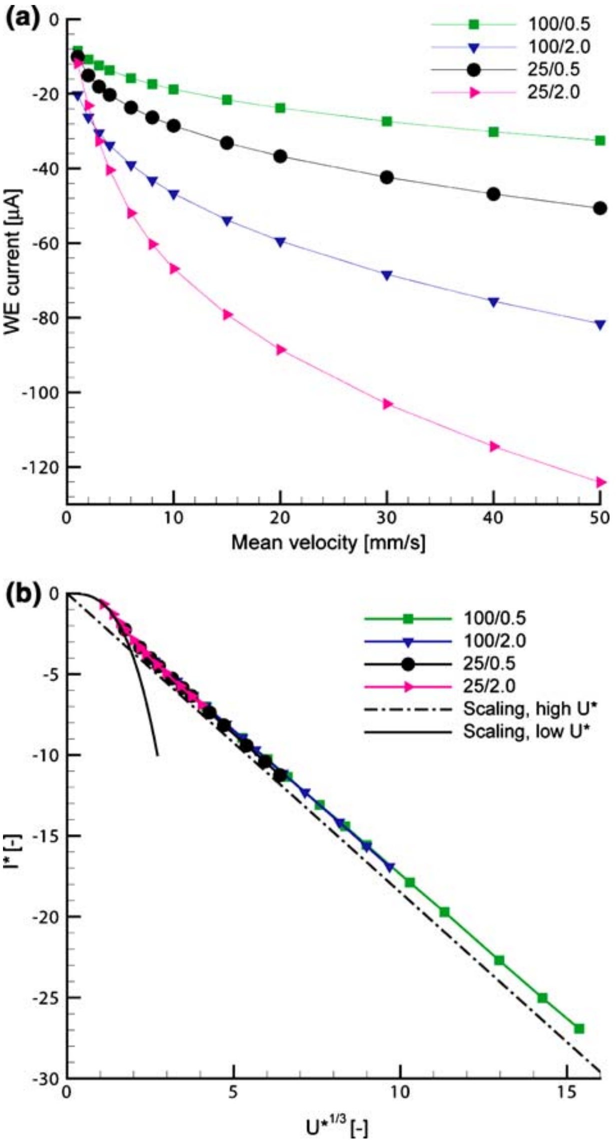

Fig. 8 Real (**a**) and normalized (**b**) amperometric signal as a function of mean velocity and dimensionless velocity parameter $U^{*1/3}$, respectively, obtained using the electrochemical model for selected geometries: the numbers in the legend represent channel height in μm and WE width in mm. The mass transfer scaling laws for high and low U^* are plotted for comparison in (*b*). Other conditions: c_0 = 5 mM, η = –0.2 V, d = 1 mm

the validity of the high U^* scaling law for all geometries under study: the amperometric response scales to the power of 2/3 with WE width ($I \propto w^{2/3}$) and –1/3 with hydraulic diameter ($I \propto D_h^{-1/3}$), or –1/3 with channel height ($I \propto h^{-1/3}$) for high aspect ratio channels. There is, however, one exception: at low U^*, a combination of low U, small D_h and large w causes departure from the general trend. This is the transition to the low U^* regime, in which all the reactant that enters the channel is completely consumed at the WE. The transition occurs at $U^{*1/3}$ = 1.9, equivalent to U^* = 7.1, as determined theoretically in Sect. 3.3. The curves in Fig. 8b also show the validity of the low U^* scaling law below the transition point and that the electrochemical model provides accurate predictions in both regimes.

The sensitivity of the amperometric signal, defined as the change in output current to a change in mean velocity, is of key importance for sensor design. The shape of all calibration curves presented so far indicate that the sensitivity has a maximum for low flow rates. A more detailed study of sensitivity, including both computational and experimental data, is shown in the log-log plot of Fig. 9. The range considered here comprises velocities of four orders of magnitude: from 0.1 to 100 mm s^{-1}. Several conclusions concerning the sensitivity can be drawn from this figure: it remains sufficiently high over the entire range of flow rates; as already mentioned, it is reduced as the velocity increases; it is generally enhanced for thin channels and wide electrodes; it follows the scaling lines at high U^*, confirming that the sensitivity scales with velocity to the power of –2/3 ($\frac{\partial I}{\partial U} \propto U^{-2/3}$); and it reaches a geometry dependent upper bound for low velocities. This upper sensitivity bound is directly related to the transition to the low U^* regime at U^* = 7.1. Within the low U^* regime, the sensitivity is independent of velocity and proportional to cross-sectional area, as shown by the jump between the two low U^* scaling lines. The amperometric signal is therefore proportional to both mean velocity and cross-sectional area,

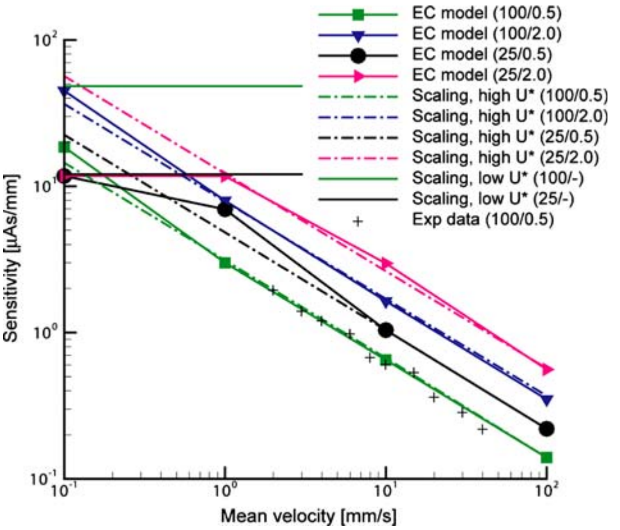

Fig. 9 Selected sensitivity data as a function of mean velocity. Results from the electrochemical model plus experimental data are presented in relation to scaling lines in the high (*dash-dot*) and low (*solid*) U^* regimes. The *numbers in brackets* represent channel height in μm and WE width in mm. Conditions: c_0 = 5 mM, η = –0.2 V, d = 1 mm

as proposed theoretically in Sect. 3.3.2, and by extension also to the flow rate. If possible, operation in the low U^* regime is recommended from a sensitivity point of view.

5 Conclusions

An electrochemical velocimetry technique suitable for microfluidic networks was realized by means of embedded microband electrodes and a redox couple in solution. A functional relationship between mean velocity and the reductive current drawn from the WE was identified for operation in the transport controlled mode. The measured amperometric signal is proportional to the bulk redox concentrations, indicating that high concentrations provide stronger signals. However, experimental results reveal that a few millimolar is sufficient for effective sensor operation. For practical applications, calibration curves may be obtained computationally from the electrochemical model, empirically from the mass transfer model or experimentally using a syringe pump with known flow rate. Scaling laws, capable of providing quick estimates, were developed based on a dimensionless velocity, U^*. Two velocity regimes were found with transition point at $U^* = 7.1$. In the high U^* regime, the amperometric signal scales as the cube root of mean velocity, cube root squared of WE width and inverse cube root of hydraulic diameter, whereas in the low U^* regime, the signal is independent of electrode width and directly proportional to the flow rate.

The proposed velocimetry technique is applicable to any cross-sectional channel geometry. The sensitivity of the amperometric response varies inversely with flow rate, which effectively normalizes the relative error of the measurements. High overall sensitivities were demonstrated, in particular in the low U^* regime. The flexibility of the sensor design introduces additional advantages: by tuning its channel and electrode geometry, the sensitivity can be optimized towards a specific application and its functionality can be expanded over a wide range of flow rates. In fact, this velocimetry technique can resolve all practicable Reynolds numbers experienced for laminar pressure-driven flow in microfluidic networks with known cross-sectional geometry.

Acknowledgments The funding for this research provided by a Natural Sciences and Engineering Research Council of Canada (NSERC) strategic grant is highly appreciated.

References

Amatore C, Belotti M, Chen Y, Roy E, Sella C, Thouin L (2004) Using electrochemical coupling between parallel microbands for in situ monitoring of flow rates in microfluidic channels. J Electroanal Chem 573:333–343

Auroux PA, Iossifidis D, Reyes DR, Manz A (2002) Micro total analysis systems. 2. Analytical standard operations and applications. Anal Chem 74:2637–2652

Ayliffe HE, Rabbitt RD (2003) An electric impedance based microelectromechanical system flow sensor for ionic solutions. Meas Sci Technol 14:1321–1327

Baldwin RP (2000) Recent advances in electrochemical detection in capillary electrophoresis. Electrophoresis 21:4017–4028

Bard AJ, Parsons R, Jordan J (eds) (1985) Standard potentials in aqueous solution. Marcel Dekker, New York

Booth J, Compton RG, Cooper JA, Dryfe RAW, Fisher AC, Davies CL, Walters MK (1995) Hydrodynamic voltammetry with channel electrodes: microdisc electrodes. J Phys Chem 99:10942–10947

Coleman JT, McKechnie J, Sinton D (2006) High-efficiency electrokinetic micromixing through symmetric sequential injection and expansion. Lab Chip 6(8):1033–1039

Duffy DC, McDonald JC, Schueller OJA, Whitesides GM (1998) Rapid prototyping of microfluidic systems in poly(dimethylsiloxane). Anal Chem 70(23):4974–4984

Erickson D (2005) Towards numerical prototyping of labs-on-chip: modeling for integrated microfluidic devices. Microfluid Nanofluid 1:301–318

Erickson D, Sinton D, Li D (2003) Joule heating and heat transfer in poly(dimethylsiloxane) microfluidic systems. Lab Chip 3(3):141–149

Fu R, Li D (2006) Flow velocity measurement in microchannels using temperature-dependent fluorescent dye. Microfluid Nanofluid (in press). DOI:10.1007/s10404–006–0102-y

Graetz L (1885) Über die Wärmeleitungsfähigkeit von Flüssigkeiten. Ann Physik 25:337–357

Incropera FP, De Witt DP (1990) Fundamentals of heat and mass transfer, 3rd edn. Wiley, New York

Kakac S, Shah RK, Aung W (1987) Handbook of single-phase convective heat transfer. Wiley, New York

Marken F, Eklund JC, Compton RG (1995) Voltammetry in the presence of ultrasound'' can ultrasound modify heterogeneous electron transfer kinetics? J Electroanal Chem 395:335–339

Meinhart CD, Wereley ST, Santiago JG (1999) PIV measurements of a microchannel flow. Exp Fluids 27:414–419

Muzikar M, Fawcett WR (2004) Use of ac admittance voltammetry to study very fast electron-transfer reactions. The $Ru(NH_3)_6^{3+/2+}$ system in water. Anal Chem 76:3607–3611

Newman J, Thomas-Alyea KE (2004) Electrochemical systems, 3rd Edn. Wiley, Hoboken

Nusselt W (1923) Der Warmeubergang in den Verbrennungskraftmaschinen. VDI Z 67:206–210

Nyholm L (2005) Electrochemical techniques for lab-on-a-chip applications. Analyst 130:599–605

Paeschke M, Dietrich F, Uhlig A, Hintsche R (1996) Voltammetric multichannel measurements using silicon fabricated microelectrode arrays. Electroanalysis 8(10):891–898

Probstein RF (2003) Physicochemical hydrodynamics—an introduction, 2nd edn. Wiley, Hoboken

Qiu H, Yin XB, Yan J, Zhao X, Yang X, Wang E (2005) Simultaneous electrochemical and electrochemiluminescence detection for microchip and conventional capillary electrophoresis. Electrophoresis 26:687–693

Ranz WE (1958) Electrolytic methods for measuring water velocities. AIChE J 4(3):338–342

Reyes DR, Iossifidis D, Auroux PA, Manz A (2002) Micro total analysis systems. 1. Introduction, theory, and technology. Anal Chem 74:2623–2636

Santiago JG, Wereley ST, Meinhart CD, Beebe DJ, Adrian RJ (1998) A particle image velocimetry system for microfluidics. Exp Fluids 25:316–319

Sinton D (2004) Microscale flow visualization. Microfluid Nanofluid 1:2–21

Squires TM, Quake SR (2005) Microfluidics: fluid physics at the nanoliter scale. Rev Mod Phys 77:977–1026

Wu J, Sansen W (2002) Electrochemical time of flight flow sensor. Sens Actuators A 97–98:68–74

Wu J, Ye J (2005) Micro flow sensor based on two closely spaced amperometric sensors. Lab Chip 5:1344–1347

Yang C, Kümmel M, Søeberg H (1991) Dynamic model for a thermal transit-time flow sensor. Chem Eng Sci 46(3):735–740

Zosel J, Guth U, Thies A, Reents B (2003) Flow measurements in micro holes with electrochemical and optical methods. Electrochim Acta 48:3299–3305

Appendix B

Hydrogen Peroxide as an Oxidant for Microfluidic Fuel Cells

Reproduced by permission of ECS – The Electrochemical Society

Journal of The Electrochemical Society, **154** (12) B1220-B1226 (2007)
0013-4651/2007/154(12)/B1220/7/$20.00 © The Electrochemical Society

Hydrogen Peroxide as an Oxidant for Microfluidic Fuel Cells

Erik Kjeang,[a,c,*] **Alexandre G. Brolo,**[b,c,**] **David A. Harrington,**[b,c,**]
Ned Djilali,[a,c] **and David Sinton**[a,c,z]

[a]Department of Mechanical Engineering, [b]Department of Chemistry, and [c]Institute for Integrated Energy Systems, University of Victoria, Victoria, British Columbia, Canada V8W 3P6

We demonstrate a microfluidic fuel cell incorporating hydrogen peroxide oxidant. Hydrogen peroxide (H_2O_2) is available at high concentrations, is highly soluble and exhibits a high standard reduction potential. It also enables fuel cell operation where natural convection of air is limited or anaerobic conditions prevail, as in submersible and space applications. As fuel cell performance critically depends on both electrode and channel architecture, several different prototype cells are developed and results are compared. High-surface area electrodeposited platinum and palladium electrodes are evaluated both ex situ and in situ for the combination of direct H_2O_2 reduction and oxygen reduction via the decomposition reaction. Oxygen gas bubbles produced at the fuel cell cathode introduce an unsteady two-phase flow component that, if not controlled, can perturb the co-laminar flow interface and reduce fuel cell performance. A grooved channel design is developed here that restricts gas bubble growth and transport to the vicinity of the cathodic active sites, enhancing the rate of oxygen reduction, and limiting crossover effects. The proof-of-concept microfluidic fuel cell produced power densities up to 30 mW cm^{-2} and a maximum current density of 150 mA cm^{-2}, when operated on 2 M H_2O_2 oxidant together with formic acid-based fuel at room temperature.

[DOI: 10.1149/1.2784185]

Manuscript submitted March 23, 2007; revised manuscript received August 13, 2007. Available electronically October 3, 2007.

Small fuel cells have received much interest in recent years as potential power supplies for the next generation of portable electronic devices.[1] Overall fuel cell performance based on two- or three-phase interface catalysis is enhanced with miniaturization, provided the active surface-to-volume ratio is inversely proportional to the characteristic length. One class of microstructured power supply is microfluidic fuel cells,[2-16] also called laminar flow-based fuel cells and membraneless fuel cells. A microfluidic fuel cell is defined here as a device that confines all fundamental components of a fuel cell to a single microstructured manifold. An image and schematic of a microfluidic fuel cell are shown in Fig. 1. In the case of nonspecific catalysts or active sites, these fuel cells exploit the characteristics of microfluidic co-laminar flow to separate anolyte and catholyte without the requirement of a physical barrier, i.e., membrane. Both streams contain supporting electrolyte that provides high conductivity for ionic transport. Interdiffusion between the two streams is restricted to an hourglass-shaped zone in the center of the channel, with maximum width at the channel walls scaling as the cube root of diffusion coefficient, channel height, downstream position, and inverse mean velocity.[17] Fuel and oxidant crossover is limited by positioning the anode and cathode on channel walls with adequate separation from the co-laminar interdiffusion zone. Given low rates of interdiffusion, the co-laminar configuration allows anolyte and catholyte compositions to be optimized independently[7] in order to improve kinetics and cell potential. Microfluidic fuel cells avoid some commonly encountered challenges in polymer electrolyte membrane-based fuel cells,[18] including membrane humidification control, membrane degradation, and liquid water management.

Proof-of-concept microfluidic fuel cells have been developed based on a variety of fuels: vanadium redox species,[2,3,11] formic acid,[6,10,14] methanol,[7,8,13] hydrogen,[9,15,16] and hydrogen peroxide.[12] The current density of these fuel cells was predominantly controlled by the rate of mass transport to the active sites,[5] typically in the cathodic half-cell.[8] Fuel cells based on dissolved oxygen were particularly limited by the low solubility of oxygen (2–4 mM).[6,7,9,10] Jayashree et al.[14] developed an integrated air-breathing cathode that allows gaseous oxygen transport from the ambient air, a source of oxygen that has significantly higher diffusivity and concentration than dissolved oxygen. The highest power density of air-breathing microfluidic fuel cells to date (26 mW cm^{-2})[14] was achieved using 1 M formic acid fuel and a graphite plate anode covered with Pd black nanoparticles. Air-breathing designs require a blank cathodic electrolyte stream that prevents fuel crossover and facilitates ionic transport between the electrodes. They are also dependent on free convection of oxygen from the ambient air which may reduce flexibility with respect to operating environments and scale-up opportunities.

The performance of microfluidic fuel cells can be improved by employing aqueous oxidants that are soluble at higher concentrations than dissolved oxygen. For example, power densities up to 38 mW cm^{-2} [11] and 70 mW cm^{-2} [2] have been obtained using vanadium redox couples as both fuel and oxidant. These redox fuel cells benefit from balanced anodic and cathodic streams. Similarly, Hasegawa et al.[12] demonstrated a microfluidic fuel cell employing hydrogen peroxide (H_2O_2) as both fuel and oxidant. The operation of that

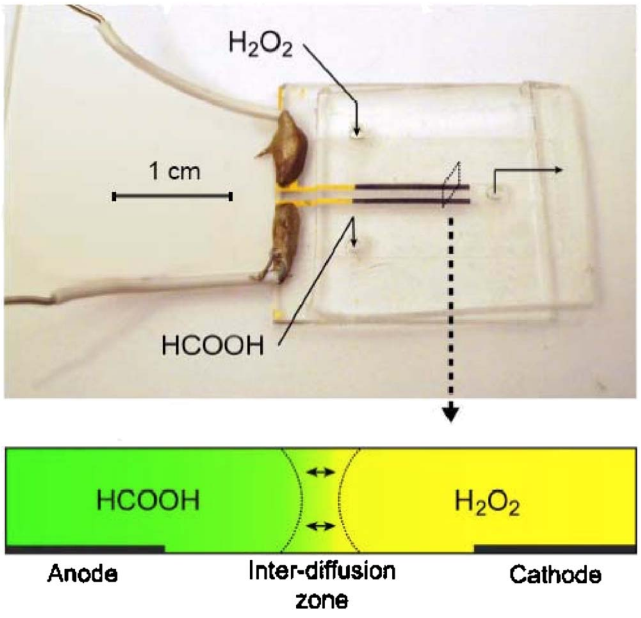

Figure 1. (Color online) Image of a microfluidic fuel cell with Pd electrodes using formic acid (HCOOH) fuel and hydrogen peroxide (H_2O_2) oxidant. The schematic cross-sectional view of the channel shows the interdiffusion of anolyte and catholyte that is characteristic of co-laminar flow. The channels employed here were 2 mm wide and 70–170 μm high, and the electrodes were 0.5 mm wide and 10 mm in active length.

---

[*] Electrochemical Society Student Member.
[**] Electrochemical Society Active Member.
[z] E-mail: dsinton@me.uvic.ca

cell, however, was dependent on net consumption of supporting electrolyte, with low overall energy density as a result.[7,12] Like common fuels methanol and formic acid, H_2O_2 is available at high concentrations and has high solubility in aqueous media, enabling balanced half-cell configurations. A microfluidic fuel cell design is developed here with the goal of harnessing these advantages. Established soft lithography techniques are employed for channel fabrication and electrode masking. H_2O_2 cathodes with different catalyst compositions and surface morphologies are produced via electrodeposition, and their electrochemical performance is evaluated both ex situ in a three-electrode electrochemical cell and in situ in a microfluidic fuel cell coupled with a generic formic acid-based anode.

Experimental

Electrochemistry.— Formic acid anolyte and hydrogen peroxide catholyte of different compositions were prepared using phosphate supporting electrolyte in Millipore Milli-Q water (Millipore, Billerica, MA). Specifically, the anolyte was prepared from potassium hydrogen phosphate (K_2HPO_4; ACP Chemicals Inc., Montreal, Canada) and concentrated formic acid (HCOOH; Sigma-Aldrich, Oakville, Canada) to the desired concentrations of 1 M HCOOH in 1–3 M phosphate (pH 6–8), and the catholyte was prepared from phosphoric acid (H_3PO_4; ACP) and 30% hydrogen peroxide (H_2O_2; EMD Chemicals Inc., Gibbstown, NJ) to 1–3 M H_2O_2 in 1–2 M phosphate (pH 0–1). All electrochemical experiments were driven by a PARSTAT 2263 potentiostat (Princeton Applied Research, Oak Ridge, TN) using a Ag|AgCl (sat. KCl) reference electrode (0.190 V vs SHE) and a platinum mesh counter electrode, where applicable. Individual electrode potentials in this article are given vs the Ag|AgCl reference electrode unless otherwise stated. Planar gold electrodes subject to catalyst electrodeposition were cleaned in piranha etch (3:1 w/w H_2SO_4:H_2O_2) for 2 min, followed by rinsing in Millipore water, and electrochemical cycling in 1 M hydrochloric acid (HCl; Anachemia, Montreal, Canada) between −0.5 and 0.6 V at 100 mV s^{-1} for 20 cycles. Platinum (Pt) was electrodeposited from a near-neutral plating bath containing 1.0% w/w chloroplatinic acid (H_2PtCl_6; Sigma-Aldrich) and 6.0% w/w ammonium phosphate (pH 8) prepared from ammonium hydroxide (NH_4OH; EMD) and H_3PO_4 in Millipore water. The plating solution was heated to 75°C and sonicated for 2 h until the bright yellow precipitate formed upon mixing of the constituents was fully dissolved and the solution turned into a uniform clear orange color. Palladium (Pd) was plated from an acidic plating bath consisting of 1.0% w/w palladium(II) chloride ($PdCl_2$; Sigma-Aldrich) and 1 M HCl in Millipore water, dissolved as a clear brown solution after 30 min sonication. The target Au electrode was immersed in the plating bath, and characterized by cyclic voltammetry at 50 mV s^{-1}. Electroplating was carried out under potentiostatic control until the desired loading was deposited, assuming 60% coulombic deposition efficiency.[19] The obtained electrodes were rinsed thoroughly with Millipore water before further use. Scanning electron micrographs were captured by a Hitachi S-3500N scanning electron microscope with a tungsten filament operated at 15 kV.

Fuel cell fabrication and testing.— Proof-of-concept microfluidic fuel cells were assembled using in-house microfabrication techniques. The fuel cell shown in Fig. 1 comprises two layers: a substrate upon which electrodes are formed, and a polymeric top layer housing the channel structure. The substrate was a 1 in. × 1 in. commercial 1000 Å gold slide (EMF Corp., Ithaca, NY) subject to gold etching combined with photolithography to attain the desired electrode structure. The electrode structures were patterned with negative photoresist (SU-8 25; Microchem, Newton, MA) over the gold, as previously reported,[20] and the uncovered parts were removed by immersion in gold etching solution (Type TFA; Transene Company Inc., Danvers, MA) for 20 min and chromium etching solution (0.8 M $K_3[Fe(CN)_6]$ in 3 M NaOH) for 1 min followed by thorough rinsing in Millipore water. The remainder of the photoresist was removed by sonication in acetone, until the desired gold electrodes were revealed. Wires were attached to the electrodes using conductive epoxy (Circuit Works CW2400; ITW Chemtronics, Kennesaw, GA) prior to catalyst electrodeposition. The T-channel structure required for the co-laminar flow was molded in poly(dimethylsiloxane) (PDMS; Dow Corning, Midland, MI), following established soft-lithographic protocols[21] and in-house developed procedures.[22] Ports for fluid handling were punched in the PDMS prior to assembly. The electrodeposited substrate and PDMS channel structure were plasma treated (PDC-32G; Harrick Sci., Pleasantville, NY) for 30 s to yield silanol surface groups that covalently bind glass to PDMS and render hydrophilic channel walls. When the two were aligned under a microscope and brought into contact, an irreversible seal was obtained.

Steady co-laminar flow of aqueous fuel and oxidant solutions required for fuel cell operation was driven by a syringe pump (PHD 2000; Harvard Apparatus, Holliston, MA) via Teflon tubing (Upchurch Sci., Oak Harbor, WA). Polarization data were obtained at room temperature by chronoamperometry under stepwise potentiostatic control from 0.0 V to the open-circuit voltage by 0.1 V increments. The cell current was monitored for 60 s at each potential to ensure steady state conditions. Current densities and power densities reported here were time averaged over the 60 s measurement interval and calculated based on the planar active area of the electrodes ($0.05\ cm^2$).

Results and Discussion

The half-cell reaction scheme for a cathode based on hydrogen peroxide in acidic media includes a combination of direct hydrogen peroxide reduction and indirect oxygen reduction following decomposition. The reactions and associated standard potentials at 298 K are[23]

$$H_2O_2 + 2H^+ + 2e^- \rightleftharpoons 2H_2O \quad E^\circ = 1.776 \text{ V vs SHE} \qquad [1]$$

$$H_2O_2 \rightleftharpoons O_2 + 2H^+ + 2e^- \quad E^\circ = 0.682 \text{ V vs SHE} \qquad [2]$$

$$O_2 + 4H^+ + 4e^- \rightleftharpoons 2H_2O \quad E^\circ = 1.229 \text{ V vs SHE} \qquad [3]$$

The standard potential for direct hydrogen peroxide reduction, Reaction 1, is more positive than most other oxidizers (e.g., oxygen or permanganate), therefore potentially establishing a higher electromotive force for fuel cell operation. However, the oxidation of peroxide to oxygen, Reaction 2, is facile on both Pt and Pd, and both Reactions 1 and 2 occur together. The effect of this is that the open circuit potential is a mixed potential, occurring at about 0.85 V on Pt in acid solution. Net reduction of hydrogen peroxide occurs only negative of this, so the actual overpotential for direct hydrogen peroxide reduction is relatively high. The combination of the two reactions is the catalyzed decomposition of hydrogen peroxide to oxygen and water, $2H_2O_2 \rightarrow 2H_2O + O_2$. (The uncatalyzed reaction, not requiring a Pt or Pd surface, is very slow on the time scale of these experiments.) Downstream recapture of O_2 and its reduction to water, Reaction 3, can reduce some of the losses from Reaction 2.

In order to evaluate the feasibility of hydrogen peroxide oxidant for microfluidic fuel cells, a suitable anodic half cell that does not constrain the overall fuel cell performance was required. Anodic systems based on formic acid have previously exhibited relatively high performance in terms of both current density and power density in microfluidic fuel cells[14] as well as polymer electrolyte membrane fuel cells based on liquid fuels, such as the direct formic acid fuel cell.[24] The half-cell reaction and standard potential at 298 K of a formic acid-based anode are[23]

$$CO_2 + 2H^+ + 2e^- \rightleftharpoons HCOOH \quad E^\circ = -0.199 \text{ V vs SHE} \qquad [4]$$

A fuel cell based on hydrogen peroxide reduction and formic acid oxidation thus has a standard cell potential of 1.975 V.

Electrocatalytic analysis.— Pure Pt and Pd electrodes were plated on gold and the electrochemical response of the deposits was

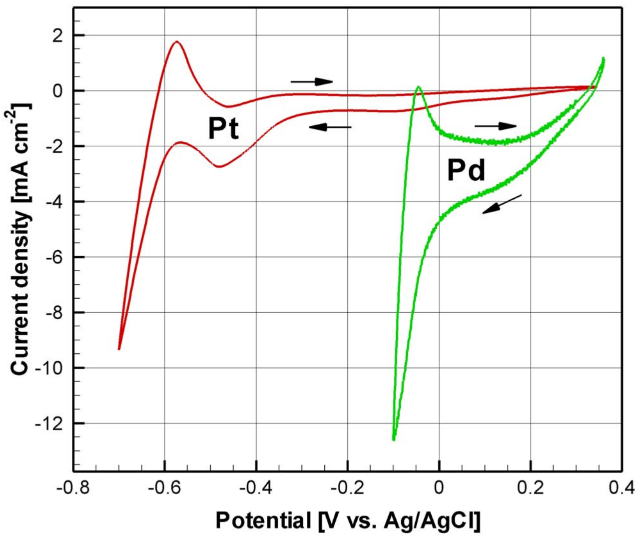

Figure 2. (Color online) Cyclic voltammograms for Pt and Pd electrodeposition on planar Au electrodes, measured at 50 mV s^{-1} scan rate (fourth cycle shown).

characterized ex situ in typical formic acid and hydrogen peroxide solutions. Bath electroplating generally progresses via a three-dimensional nucleation and growth model.[25] Nucleation can be either instantaneous or progressive: for instantaneous nucleation, all nuclei form at the same instant and grow with time; for progressive nucleation, on the other hand, new nuclei are formed as older nuclei grow and overlap. Since nucleation usually occurs at defects, dislocations, or edges, it is possible to control this behavior and synthesize specific morphologies by using substrates with known surface structure. The shape and size of the deposit also depends on kinetic parameters, e.g., whether the process is rate controlled or mass transport controlled. By careful tuning of the overpotential, one can obtain fractal growth leading to high surface area deposits.[19] The combination of the high catalytic surface area and the absence of adhesive agent (e.g., Nafion) makes this tuned electroplating methodology particularly suitable for microfluidic fuel cell applications.

Cyclic voltammograms shown in Fig. 2 were measured for Pt and Pd electrodeposition on planar Au electrodes from the open-circuit potential (OCP; 0.35 V) to −0.70 V (Pt), and from OCP (0.36 V) to −0.10 V (Pd). The large potential shift between the two curves was primarily caused by the pH difference of the plating baths. Deposition of Pt was expected to start around −0.3 V, with an increasing current toward the peak at −0.5 V. This is a well-known characteristic for nucleation and diffusion controlled growth.[19] At the peak, the active sites available on the WE surface limit the deposition current, forcing it back down toward a steady, diffusion-limited value. However, at −0.6 V there was a sharp increase in current due to the onset of hydrogen evolution, which concealed the deposition current. At these potentials, co-deposition of hydrogen took place, which can interfere with the quality and efficiency of the Pt deposition. As shown in Fig. 2, operation at near-neutral pH enabled the separation of Pt deposition and hydrogen evolution, a feature that was not possible in acidic solution due to the positive shift of the hydrogen standard potential. The plating bath employed for Pd was of a standard acidic type, in which it was not possible to completely separate Pd deposition and hydrogen evolution peaks (Fig. 2). An alkaline plating bath for Pd (not shown here) was also evaluated, however, the obtained catalyst structures had lower electrocatalytic activity than the ones from the more commonly used acidic bath.

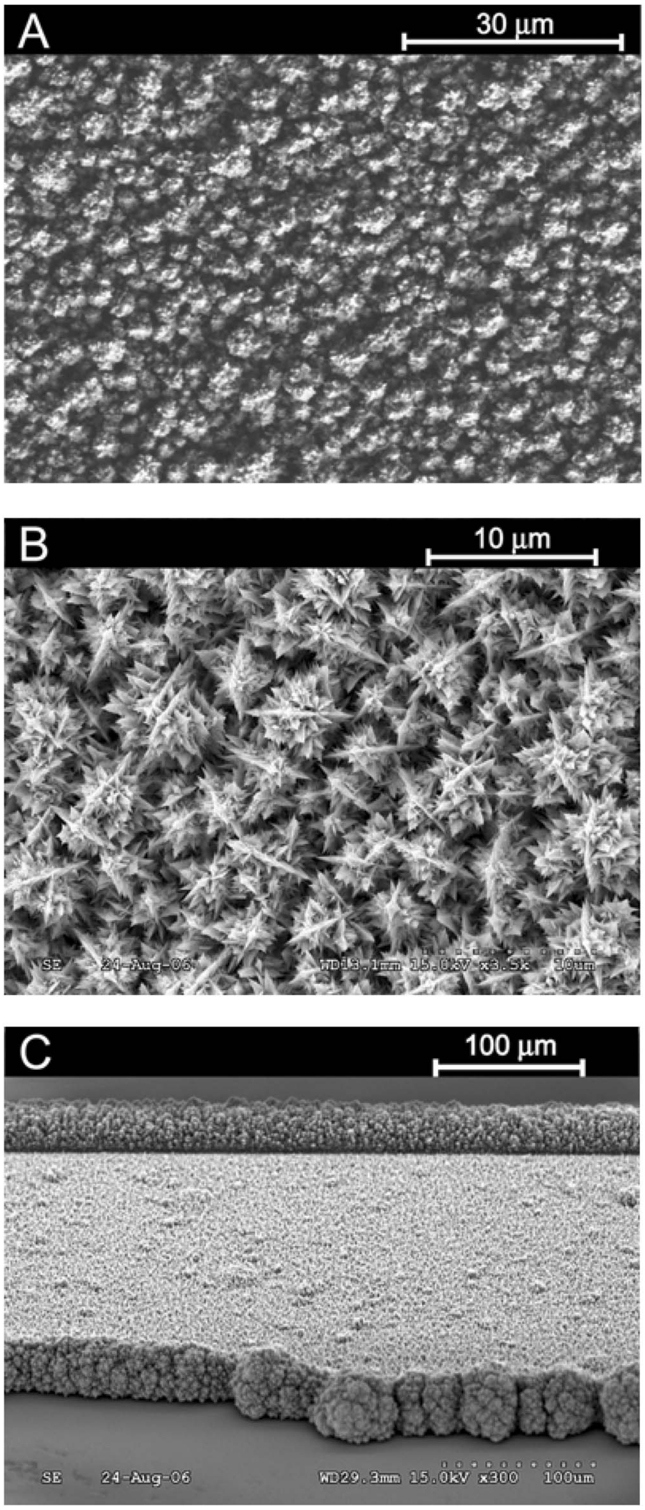

Figure 3. Scanning electron micrographs of the surface morphology of the electrodeposited Pt (A) and Pd (B) electrodes, and a side view (C) of the Pd electrode, captured at 1500×, 3500×, and 300× magnification, respectively.

The electrodeposition of Pt and Pd was carried out under potentiostatic control at −0.5 V and 0.0 V, respectively, where the deposition current was essentially transport limited in both cases and hydrogen co-deposition was negligible. The deposition charge was monitored until the desired catalyst loading was obtained (0.5–10 mg cm^{-2}). The current generally increased with time, which corresponded to the growth of the active surface area during the plating process. Figure 3 shows scanning electron micrographs of the obtained surface morphologies. The Pt morphology (Fig. 3a)

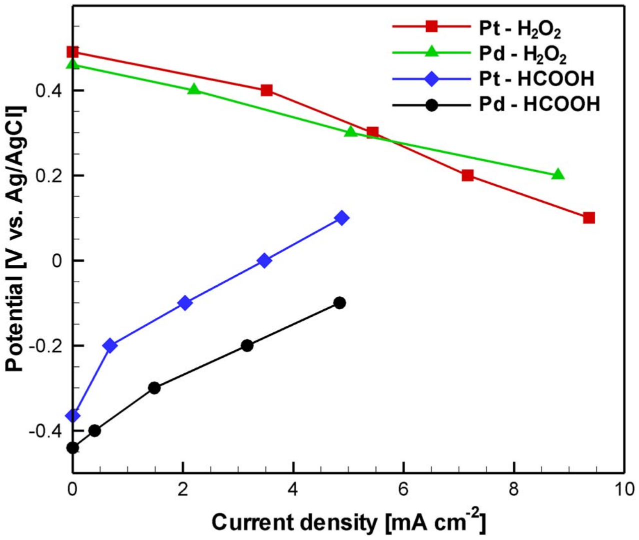

Figure 4. (Color online) Separate anode and cathode polarization data measured in a three-electrode electrochemical cell with electrodeposited Pt and Pd working electrodes. The anolyte was 0.2 M HCOOH in 0.2 M phosphate (pH 4) and the catholyte was 0.2 M H_2O_2 in 0.2 M phosphate (pH 1).

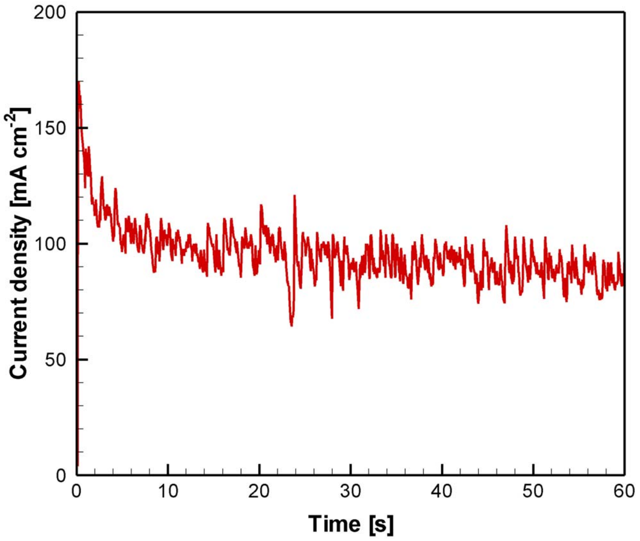

Figure 5. (Color online) Sample chronoamperometric curve for microfluidic fuel cell operation measured at 0.1 V cell voltage using 1 M HCOOH in 2 M phosphate (pH 7) anolyte and 3 M H_2O_2 in 2 M phosphate (pH 0) catholyte flowing at 300 μL min^{-1}.

was quite smooth with uniformly distributed grains and pores on the order of a few micrometers. The Pd surface structure (Fig. 3b) exhibited a more distinct fractal character with large features on the order of micrometers as well as features on the order of hundreds of nanometers and smaller. The active surface areas of the obtained Pd electrodes were therefore generally higher than for the Pt deposits. The expanded view of the Pd electrode (Fig. 3c) shows preferred growth at the edges of the gold and at some defects in the center, which reflects nucleation and diffusion-controlled fractal growth. Moreover, the edges of the electrode are exposed to a higher rate of diffusive transport that further promotes local growth under transport-limited plating conditions. The edge formations were ~40 μm high in the case of 5 mg cm^{-2} Pd loading.

The electrocatalytic activity of the Pt and Pd electrodes toward hydrogen peroxide reduction and formic acid oxidation was analyzed by cyclic voltammetry and chronoamperometry. Polarization data for individual electrode performance in a three-electrode electrochemical cell containing either H_2O_2 or HCOOH in phosphate electrolyte are shown in Fig. 4. The potential gap between the two sets of curves indicates that this fuel and oxidant combination is feasible for fuel cell operation. The Pt and Pd deposits were equally effective catalysts for H_2O_2 reduction. The OCP for this half cell was relatively low, owing to the parasitic nature of Reaction 2. The observed rate of gaseous oxygen evolution via Reactions 1 and 2 upon immersion of the electrodes in the H_2O_2 solution was higher for Pd than for Pt. The activation overpotential for HCOOH oxidation was essentially zero. Pd showed significantly higher activity than Pt in this case, in agreement with previous reports.[24,26]

Fuel cell testing.— Planar microfluidic fuel cells were fabricated according to the procedure outlined in the experimental section. The cell design is shown schematically in Fig. 1; fuel (HCOOH) and oxidant (H_2O_2) solutions enter the main channel via separate inlets and flow in a co-laminar configuration in parallel with the anode and cathode downstream toward the single outlet. The high-aspect ratio cross-sectional geometry of the channel (2 mm wide and 70–170 μm high) with electrodes placed perpendicularly to the co-laminar flow interface delays interdiffusion of the streams and enables high fuel utilization.[4] The supporting electrolyte provides high ionic conductivity within the streams, which facilitates rapid ionic charge transport between the electrodes. An array of different fuel cells was fabricated to study fuel cell performance as a function of the following parameters: cathode catalyst and loading, channel height and cross-sectional shape, and concentration and pH of fuel and oxidant solutions. A generic anode was employed in all cells, consisting of 5 mg cm^{-2} electrodeposited Pd, and the HCOOH concentration was fixed at 1 M. Polarization data were measured for all fuel cells under stepwise potentiostatic control. A selected current transient is presented in Fig. 5, showing an initial peak and then decay toward steady state over ~10 s. The time scale for stabilization is attributed to initial gas evolution partly blocking the active sites and the formation of concentration boundary layers for reactants as well as products, and is two orders of magnitude larger than the residence time in the channel at this flow rate. The unsteady oscillation pattern is attributed to the formation, growth, and expulsion of gas bubbles over the electrodes associated with O_2 evolution from peroxide oxidation at the cathode as well as product CO_2 evolution at the anode. The level of unsteadiness during the chronoamperometric measurements can be quantified by two methods: the variability, defined by the ratio between the maximum and average currents; and the standard deviation about the mean. In this case, the variability and standard deviation were 1.8 and 13%, respectively. The fuel cell design, incorporating a channel structure with three walls of optically transparent PDMS, enabled direct observation of these phenomena. Anodic CO_2 gas evolution started at low-to-moderate current densities (20 mA cm^{-2}), in contrast to previous microfluidic fuel cells using HCOOH fuel,[6,14] and was found to increase further with current density. The air-breathing HCOOH-based microfluidic fuel cell introduced by Jayashree et al.[14] operated under similar current densities, and exhibited peak power at 1 M HCOOH, however CO_2 evolution was not addressed in that study. The solubility of CO_2 in water is relatively high (0.15% w/w at 25°C and 1 atm partial CO_2 pressure,[23] neglecting the pH-dependent acid-base reactions) compared to the rate of product CO_2 formation experienced in the fuel cells, e.g., for the case shown in Fig. 5, the CO_2 turnover rate is approximately 0.05% w/w vs the flow rate of the anolyte, which is only one-third of the solubility limit. The flow cells under study, however, present different conditions than a generic solubility test and observations here indicate that the high local rates of CO_2 dissolution in microfluidic fuel cells can result in significant gas bubble formation below the solubility limit. Extensive O_2 evolution was also observed at the cathode, particularly at high current densities. The solubility of O_2 in water is

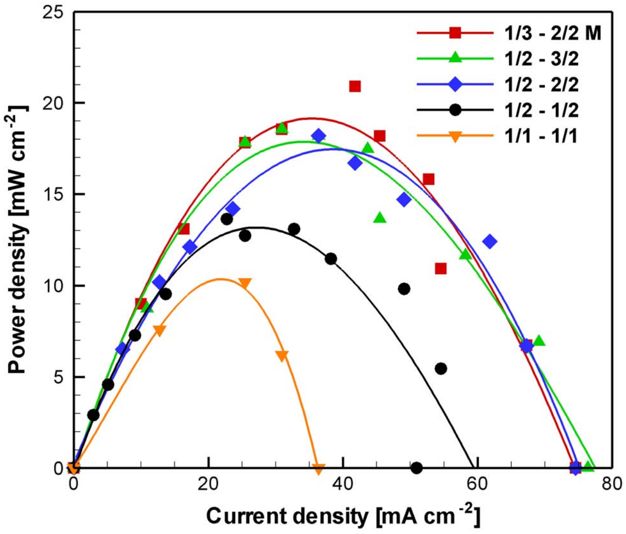

Figure 6. (Color online) Fuel cell power density curves measured experimentally using different combinations of anolyte and catholyte flowing at 300 μL min^{-1}. The numbers on the legend indicate HCOOH/phosphate and H_2O_2/phosphate molar concentrations of anolyte and catholyte, respectively. The lines are third-order polynomial curve fits to the experimental data (symbols). Both electrodes contained 5 mg cm^{-2} Pd and the channel was 170 μm high.

one order of magnitude less than for CO_2,[23] and thus the extensive O_2 bubble evolution is expected from H_2O_2 oxidation.

Figure 6 shows power density curves obtained using a proof-of-concept fuel cell design with 5 mg cm^{-2} Pd electrodes and a 170 μm high microchannel. Here, the effects of H_2O_2 concentration as well as anodic and cathodic supporting electrolyte concentrations were evaluated using a fixed HCOOH concentration (1 M) and flow rate (300 μL min^{-1}). The fuel cell produced 10 mW cm^{-2} when all concentrations were 1 M. The power density was improved by 33% by increasing both anodic and cathodic phosphate concentrations to 2 M, attributed to improved reaction kinetics and ionic conductivity as well as enhanced electromotive force and open-circuit voltage achieved by increasing the pH difference between the two streams.[7] Increasing the H_2O_2 concentration to 2 M provided an additional 33% increase in peak power density. Increasing the concentration further to 3 M did not, however, result in significant further improvement. We also investigated the use of a more alkaline anodic stream (3 M phosphate; pH 8), which improved performance by only 15% compared to the 2 M case, still without net consumption of supporting electrolyte.[7] In sum, a balanced pair of solutions that provided high power density at moderate concentration was 2 M H_2O_2 in 2 M phosphate (pH 0) together with 1 M HCOOH in 2 M phosphate (pH 7). This pair is denoted "standard solutions" in the following paragraphs.

The performance of various fuel cell designs was investigated using these standard solutions at fixed flow rates (60 and 300 μL min^{-1}). The parameters examined here were channel height, cathodic catalyst composition, the geometry of the electrode both at the fractal level and on the scale of the channel height (edge formations); and cross-sectional channel shape, as shown schematically for the six prototype cells in Fig. 7a. These parameters influence the boundary layer thickness, transport of reactants to the active sites, current collection, gaseous bubble formation, and rate of removal of bubbles through both advection and reaction. Bubble dynamics, in turn, influence local species transport as well as fuel and oxidant mixing and crossover. Figures 7b and c show the experimental power density data for each cell at the two different flow rates. Among the cells with Pd cathodes (cells I–III), the cell with 170 μm channel height (cell I) generally produced more power than the 70 μm cell (cell II). The relative size of the edge formations to the channel height, which is larger in the 70 μm cell, directed the majority of the flow to the interelectrode spacing. As observed visually, gas bubble stagnation over the electrodes limited the performance of the 70 μm cell, while the cell with a higher channel facilitated improved transport and bubble expulsion characteristics. The dynamic two-phase flow characteristics introduced by gas evolution can be beneficial for local transport rates and time-averaged current density,[27] but were found here to also perturb the co-laminar flow interface and cause unfavorable crossover effects if not controlled. Increasing the Pd loading from 5 (cell I) to 10 (cell III) mg cm^{-2} caused the performance to drop drastically at low flow rate (Fig. 7b) due to severe crossover effects attributed to expedited O_2 evolution. This crossover effect at high Pd loading was less severe at high flow rate (Fig. 7c), where bubble growth was restricted and expulsion was promoted by the increased flow rate. The average variability of the chronoamperometric data, given in Table I, provided a measure of the degree of crossover in each cell. Variability levels between 1.5 and 2 were observed routinely; these levels are related to the initial peak (Fig. 5) combined with convective transport and concentration boundary layer growth. Values above 2, however, are attributed to increased crossover effects. The electrode with high Pd loading (cell III) exhibited the largest variability at both flow rates.

The crossover problem was mitigated by depositing a thin adlayer of Pt over the Pd cathode (in cells IV and VI), thus reducing the rate of O_2 production. The cells with Pt on the cathode (cells IV–VI) showed reduced crossover at low flow rates (Fig. 7b) and also markedly improved performance at high flow rates (Fig. 7c). This effect is also evidenced in lower variability in Table I. The cell with a pure Pt cathode (cell V) generally performed better than the Pt/Pd cell with 70 μm channel (cell IV). This is attributed to a lack of Pd edge formations that negatively impacted species transport over the bulk of the electrode surface with the 70 μm channel height, consistent with the observations from Pd electrode cells (cells I–II). The best overall performance was achieved with the Pt/Pd cell with a grooved cross-sectional geometry (cell VI). Polarization and power density curves for this cell are studied separately in Fig. 8 using standard solutions at four different flow rates. Operation was demonstrated for flow rates spanning three orders of magnitude, with maintained open-circuit voltage near 1.1 V and current densities up to 150 mA cm^{-2}. Unlike the other fuel cell designs (cells I–V), this fuel cell is capable of steady operation without crossover issues at flow rates as low as 3 μL min^{-1}, equivalent to a residence time of $\sim$20 s. This capability is attributed to the cross-sectional shape of the channel: the channel sections directly above the electrodes are higher (140 μm) than the center part of the channel over the interelectrode spacing (70 μm). Gas evolved from each electrode is trapped in the high channel sections directly above the respective electrode. The result is a source of O_2 to the cathode, and a containment of CO_2 over the anode. In addition, the grooved channel design enables preferential flow (higher velocity and transport rate) over the electrodes, in contrast to the other cells (I–V) with uniform channel height. Employing this cell design, detrimental crossover effects are minimized and the mixing interface is confined and stabilized in the center of the channel sufficiently far away from the edges of the electrodes; the produced O_2 is captured and constrained within the direct vicinity of the cathodic active sites. The maximum power density measured here was 30 mW cm^{-2} at 300 μL min^{-1}, which is comparable to air-breathing cells (26 mW cm^{-2})[14] and higher than cells based on dissolved oxygen ($\sim$0.2 mW cm^{-2});[6,10] all of which were also utilizing HCOOH as fuel.

Conclusion

Microfluidic fuel cell operation based on hydrogen peroxide (H_2O_2) oxidant was demonstrated employing electrodeposited platinum and palladium electrodes with high surface area. The cathode design of these fuel cells allows some recapture of O_2 that is pro-

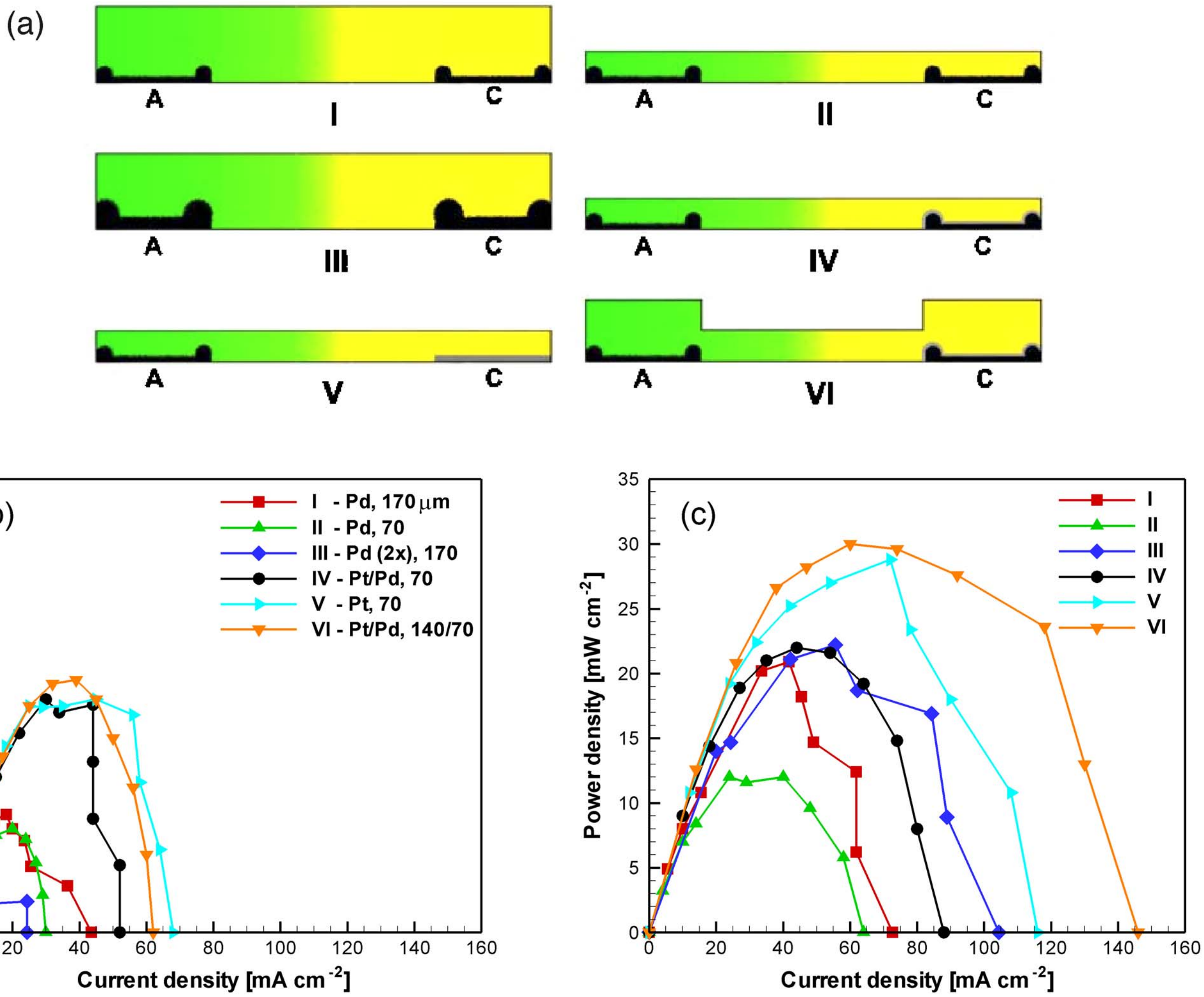

Figure 7. (Color online) Schematic (A) of the six different fuel cell designs (I–VI) studied here, and associated power density curves obtained experimentally at 60 (B) and 300 (C) μL min^{-1} flow rates. The legend indicates cathode catalyst material and channel height in μm. Standard solutions were used (1 M HCOOH in 2 M phosphate and 2 M H_2O_2 in 2 M phosphate).

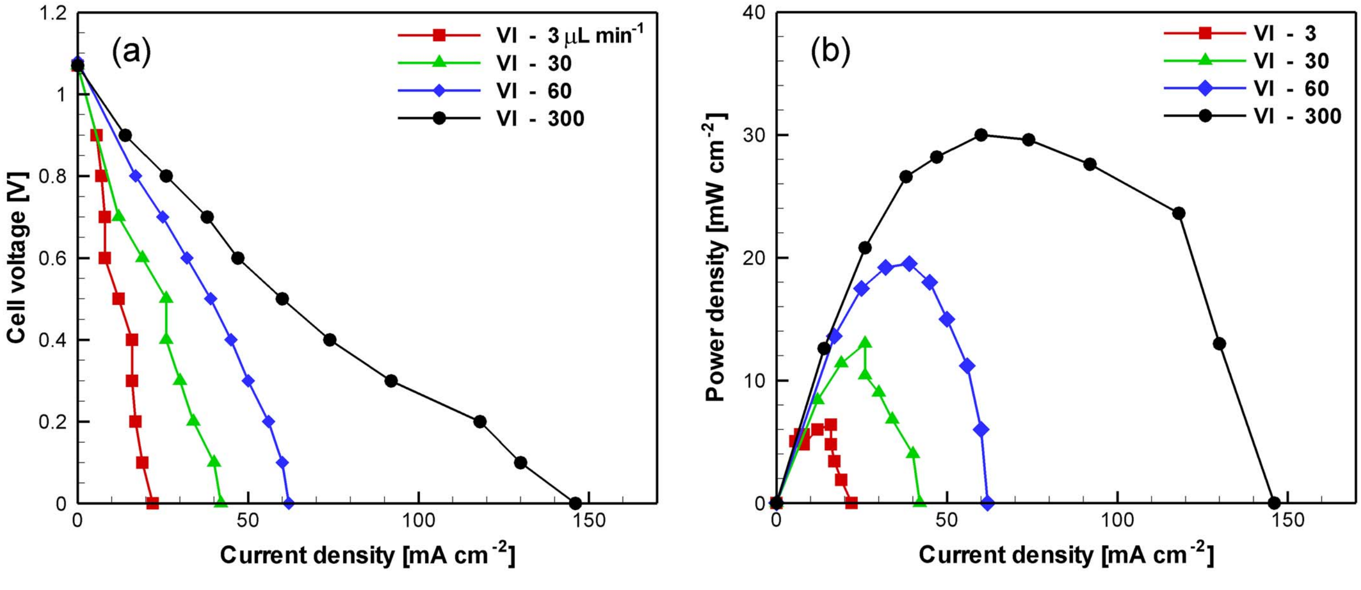

Figure 8. (Color online) Polarization (A) and power density (B) curves obtained experimentally at flow rates ranging from 3 to 300 μL min^{-1}. Fuel cell (VI) (Pt/Pd cathode and 140/70 μm channel) was employed using standard solutions (1 M HCOOH in 2 M phosphate and 2 M H_2O_2 in 2 M phosphate).

Table I. Average variability measured for fuel cells (I–VI) using standard solutions at 60 and 300 μL min^{-1}.

Flow rate (μL/min)	Variability					
	I	II	III	IV	V	VI
60	3.1	2.1	6.5	1.8	1.6	2.0
300	1.8	1.7	2.5	1.7	1.5	1.6

duced by parasitic oxidations of H_2O_2. We developed a membraneless microfluidic fuel cell design with a grooved channel geometry that (*i*) utilizes gas evolution and unsteady two-phase flow characteristics to enhance local transport rates and time-averaged current density, and (*ii*) restricts oxygen bubble growth and expulsion to the channel section directly above the cathode in order to enhance the rate of oxygen reduction and prevent detrimental fuel and oxidant crossover effects. Our proof-of-concept H_2O_2-based microfluidic fuel cell demonstrated competitive power density and current density levels that were comparable to air-breathing designs and significantly higher than cells based on dissolved oxygen. In addition, H_2O_2-based cells are acquiescent to operation where natural convection of air is limited and anaerobic conditions prevail, for example, in submersible and space applications. The performance of H_2O_2-based cathodes, as well as overall fuel cell performance, would further benefit from a catalyst optimization study within the framework of a microfluidic fuel cell, including Pt and Pd nanoparticles and various high-surface area Au electrodes.

Acknowledgments

Funding for this research provided by the Canadian Natural Sciences and Engineering Research Council (NSERC) and Angstrom Power, Inc., is highly appreciated.

University of Victoria assisted in meeting the publication costs of this article.

References

1. C. K. Dyer, *J. Power Sources*, **106**, 31 (2002).
2. E. Kjeang, B. T. Proctor, A. G. Brolo, D. A. Harrington, N. Djilali, and D. Sinton, *Electrochim. Acta*, **52**, 4942 (2007).
3. E. Kjeang, J. McKechnie, D. Sinton, and N. Djilali, *J. Power Sources*, **168**, 379 (2007).
4. A. Bazylak, D. Sinton, and N. Djilali, *J. Power Sources*, **143**, 57 (2005).
5. M. H. Chang, F. Chen, and N. S. Fang, *J. Power Sources*, **159**, 810 (2006).
6. E. R. Choban, L. J. Markoski, A. Wieckowski, and P. J. A. Kenis, *J. Power Sources*, **128**, 54 (2004).
7. E. R. Choban, J. S. Spendelow, L. Gancs, A. Wieckowski, and P. J. A. Kenis, *Electrochim. Acta*, **50**, 5390 (2005).
8. E. R. Choban, P. Waszczuk, and P. J. A. Kenis, *Electrochem. Solid-State Lett.*, **8**, A348 (2005).
9. J. L. Cohen, D. J. Volpe, D. A. Westly, A. Pechenik, and H. D. Abruna, *Langmuir*, **21**, 3544 (2005).
10. J. L. Cohen, D. A. Westly, A. Pechenik, and H. D. Abruna, *J. Power Sources*, **139**, 96 (2005).
11. R. Ferrigno, A. D. Stroock, T. D. Clark, M. Mayer, and G. M. Whitesides, *J. Am. Chem. Soc.*, **124**, 12930 (2002).
12. S. Hasegawa, K. Shimotani, K. Kishi, and H. Watanabe, *Electrochem. Solid-State Lett.*, **8**, A119 (2005).
13. R. S. Jayashree, D. Egas, J. S. Spendelow, D. Natarajan, L. J. Markoski, and P. J. A. Kenis, *Electrochem. Solid-State Lett.*, **9**, A252 (2006).
14. R. S. Jayashree, L. Gancs, E. R. Choban, A. Primak, D. Natarajan, L. J. Markoski, and P. J. A. Kenis, *J. Am. Chem. Soc.*, **127**, 16758 (2005).
15. S. M. Mitrovski, L. C. C. Elliott, and R. G. Nuzzo, *Langmuir*, **20**, 6974 (2004).
16. S. M. Mitrovski, and R. G. Nuzzo, *Lab Chip*, **6**, 353 (2006).
17. R. F. Ismagilov, A. D. Stroock, P. J. A. Kenis, G. Whitesides, and H. A. Stone, *Appl. Phys. Lett.*, **76**, 2376 (2000).
18. E. Kjeang, N. Djilali, and D. Sinton, *Microfluidic Fuel Cells*, in the *Encyclopedia of Micro- and Nanofluidics*, D. Li, Editor, Springer, Berlin.
19. J. J. Whalen, J. D. Weiland, and P. C. Searson, *J. Electrochem. Soc.*, **152**, C738 (2005).
20. E. Kjeang, B. Roesch, J. McKechnie, D. A. Harrington, N. Djilali, and D. Sinton, *Microfluid. Nanofluid.*, **3**, 403 (2007).
21. D. C. Duffy, J. C. McDonald, O. J. A. Schueller, and G. M. Whitesides, *Anal. Chem.*, **70**, 4974 (1998).
22. J. T. Coleman, J. McKechnie, and D. Sinton, *Lab Chip*, **6**, 1033 (2006).
23. *CRC Handbook of Chemistry and Physics*, CRC Press, Boca Raton, FL (2002).
24. Y. M. Zhu, Z. Khan, and R. I. Masel, *J. Power Sources*, **139**, 15 (2005).
25. A. Milchev, *Electrocrystallization Fundamentals of Nucleation and Growth*, Kluwer, Boston (2002).
26. R. S. Jayashree, J. S. Spendelow, J. Yeom, C. Rastogi, M. A. Shannon, and P. J. A. Kenis, *Electrochim. Acta*, **50**, 4674 (2005).
27. A. Gunther and K. F. Jensen, *Lab Chip*, **6**, 1487 (2006).

Appendix C

Planar and Three-Dimensional Microfluidic Fuel Cell Architectures Based on Graphite Rod Electrodes

Reproduced by permission of Elsevier

Available online at www.sciencedirect.com

ScienceDirect

Journal of Power Sources 168 (2007) 379–390

JOURNAL OF POWER SOURCES

www.elsevier.com/locate/jpowsour

Planar and three-dimensional microfluidic fuel cell architectures based on graphite rod electrodes

Erik Kjeang, Jonathan McKechnie, David Sinton*, Ned Djilali

Department of Mechanical Engineering, and Institute for Integrated Energy Systems (IESVic),
University of Victoria, P.O. Box 3055 STN CSC, Victoria, BC V8W 3P6, Canada

Received 12 December 2006; received in revised form 1 February 2007; accepted 2 February 2007
Available online 12 March 2007

Abstract

We propose new membraneless microfluidic fuel cell architectures employing graphite rod electrodes. Commonly employed as mechanical pencil refills, graphite rods are inexpensive and serve effectively as both electrode and current collector for combined all-vanadium fuel/oxidant systems. In contrast to film-deposited electrodes, the geometry and mechanical properties of graphite rods enable unique three-dimensional microfluidic fuel cell architectures. Planar microfluidic fuel cells employing graphite rod electrodes are presented here first. The planar geometry is typical of microfluidic fuel cells presented to date, and permits fuel cell performance comparisons and the evaluation of graphite rods as electrodes. The planar cells produce a peak power density of 35 mW cm^{-2} at 0.8 V using 2 M vanadium solutions, and provide steady operation at flow rates spanning four orders of magnitude. Numerical simulations and empirical scaling laws are developed to provide insight into the measured performance and graphite rods as fuel cell electrodes.

We also present the first three-dimensional microfluidic fuel cell architecture with multiple electrodes. The proposed fuel cell architecture, consisting of a hexagonal array of graphite rods, enables scale-up/integration of microfluidic fuel cell technology as well as power conditioning flexibility beyond that of the traditional fuel cell stack. When provided the same flow rate as the planar cell, the array cell generated an order of magnitude higher power output. The array architecture also enabled unprecedented levels of single pass fuel utilization, up to 78%.

Keywords: Microfluidic fuel cell; Membraneless fuel cell; Laminar flow-based fuel cell; Vanadium redox couple; Graphite rod; Array architecture fuel cell

1. Introduction

Technical development and miniaturization efforts in the area of portable electronics have generated unprecedented demand for small and efficient power supplies. The cost tolerance associated with the development of new solutions for small-scale power generation is therefore relatively high [1]. Microstructured fuel cells are considered a technology with the potential to facilitate these accelerating power requirements [2]. Proton exchange membrane (PEM) fuel cells based on hydrogen provide competitive power densities, but the energy density of such fuel cell systems is limited by on-board fuel storage. In general, liquid fuels enable higher energy density than gaseous fuels. Direct methanol fuel cells, for example, are capable of combining relatively high power densities and energy densities [3–5]. There are, however, several challenges associated with these, for instance, methanol crossover through the membrane and slow anode kinetics, which reduce efficiency and open-circuit voltage [6].

Microfluidic fuel cells, also called laminar flow-based fuel cells or membraneless fuel cells, provide an alternative avenue towards miniaturized power supplies. A microfluidic fuel cell is defined here as a device that confines all fundamental components of a fuel cell to a single microstructured manifold. In the case of non-specific catalysts or active sites, such fuel cells exploit the relatively low rates of diffusive mixing inherent to co-laminar microfluidic flow to maintain the separation of anolyte and catholyte streams flowing side-by-side, thereby eliminating the need for a physical barrier such as a membrane [7]. Ionic conduction is facilitated by a supporting electrolyte contained within the reactant streams. Mixing of the two streams occurs by transverse diffusion only, and is restricted to an interfacial width

---

* Corresponding author. Tel.: +1 250 721 8623; fax: +1 250 721 6051.
E-mail address: dsinton@me.uvic.ca (D. Sinton).

0378-7753/$ – see front matter © 2007 Elsevier B.V. All rights reserved.
doi:10.1016/j.jpowsour.2007.02.087

Nomenclature

a	chemical activity
c	concentration ($\mathrm{mol\,m^{-3}}$)
d	rod diameter (m)
D	solute diffusivity ($\mathrm{m^2\,s^{-1}}$)
D_h	hydraulic diameter (m)
E	electrochemical potential (V)
E°	standard redox potential (V)
F	Faraday's constant ($\mathrm{C\,mol^{-1}}$)
h	channel height (m)
I	current (A)
J	current density ($\mathrm{A\,m^{-2}}$)
l	active length of rod (m)
n	number of electrons
p	pressure (Pa)
Q	flow rate ($\mathrm{m^3\,s^{-1}}$)
Q_J	current source ($\mathrm{A\,m^{-3}}$)
R	universal gas constant ($\mathrm{J\,mol^{-1}\,K^{-1}}$)
R_s	ohmic resistance (Ω)
s	inter-electrode spacing (m)
T	temperature (K)
U	mean velocity ($\mathrm{m\,s^{-1}}$)
V	electric potential (V)
w	Channel width (m)
W	pumping power (W)

Greek letters

η	fuel utilization
μ	dynamic viscosity ($\mathrm{kg\,m^{-1}\,s^{-1}}$)
σ	electrical conductivity ($\mathrm{S\,m^{-1}}$)

Subscripts

e	electrode
ox	oxidized species
red	reduced species
0	initial value

at the center of the channel. This inter-diffusion zone [8] has an hourglass shape with a maximum width at the channel walls [7]. Anode and cathode are integrated on the walls of the manifold sufficiently far away from the co-laminar inter-diffusion zone in order to prevent fuel crossover. The microfluidic fuel cell design avoids many of the issues encountered in polymer electrolyte membrane-based fuel cells [9], including membrane humidification, membrane degradation, and liquid water management. In addition, the co-laminar configuration allows the composition of the anolyte and catholyte streams to be chosen independently [10], thus providing an opportunity to improve reaction rates and cell voltage. Another significant benefit associated with microfluidic fuel cells is cost. Single microfluidic fuel cells can be manufactured by inexpensive, well-established micromachining and microfabrication methods and the cost associated with membrane and auxiliary systems, which is significant for most other fuel cells, is eliminated. Incorporation of this technology in applications will require scale-up, that is, the integration of multiple microfluidic fuel cells, and this has yet to be addressed.

Proof-of-concept microfluidic fuel cells based on vanadium redox species [11], formic acid [12–14], methanol [10,15,16], hydrogen [17–19], and hydrogen peroxide [20] have recently been developed. The majority of these devices employed a single Y- or T-shaped co-laminar microfluidic network featuring fuel and oxidant dissolved in aqueous streams of supporting electrolyte and electrodes placed on opposite channel walls parallel to the inter-diffusion zone. The current density of these fuel cells was primarily restricted by the rate of mass transport to the active sites [21], typically in the cathodic half-cell [15]. For cells using dissolved oxygen in the cathodic stream, the maximum power density reported to date, $5\,\mathrm{mW\,cm^{-2}}$ [10], was predominantly limited by the low solubility of oxygen (2–4 mM). The integration of an air-breathing porous cathode structure allows gaseous oxygen transport from the ambient air, a source of oxygen that has significantly higher diffusivity and concentration than dissolved oxygen. Jayashree et al. [14] developed the first microfluidic fuel cell with integrated air-breathing cathode, using a graphite plate anode covered with Pd black nanoparticles and a porous carbon paper cathode covered with Pt black nanoparticles. Peak power density, $26\,\mathrm{mW\,cm^{-2}}$, was achieved with 1 M formic acid in 0.5 M sulfuric acid. Air-breathing designs yet require a blank cathodic electrolyte stream with flow rate similar to the anodic stream in order to prevent fuel crossover and facilitate ionic transport between the electrodes. The air-breathing feature also reduces the feasibility of scale-up by three-dimensional stacking of individual cells.

The use of alternative oxidants, soluble at higher concentrations than dissolved oxygen, provides another avenue towards improved performance of mass-transfer limited microfluidic fuel cells. Vanadium redox batteries [22,23] utilize two different aqueous vanadium redox couples, $\mathrm{V^{2+}/V^{3+}}$ and $\mathrm{VO^{2+}/VO_2{}^{+}}$, as fuel and oxidant, respectively, dissolved in dilute sulfuric acid. This combination of vanadium redox pairs is also suitable for microfluidic fuel cell operation for several reasons: they have high solubility and enable relatively high redox concentrations up to 5.4 M [24]; they provide well-balanced electrochemical half-cells in terms of reaction rates and transport characteristics; they have a large difference in formal redox potentials resulting in a high open-circuit voltage (up to ∼1.7 V at uniform pH) [11]; the reactions are facilitated by plain carbon electrodes that do not require any precious metal catalysts such as Pt or Pd; and the all-vanadium system enables electrolytic regeneration of fuel and oxidant from the used solutions without complex separation schemes. The highest power density of all microfluidic fuel cells published to date, $38\,\mathrm{mW\,cm^{-2}}$, was achieved using vanadium redox couples [11]. As in other microfluidic fuel cell technologies, however, system integration is challenging, and the energy density is limited by the solubility of the fuel and oxidant.

The power output of a single planar microfluidic fuel cell is inadequate for most practical applications. The feasibility of enlarging a single planar cell, i.e. increasing the geometrical area of electrodes and microchannel, is limited by structural constraints, increased fuel/oxidant inter-diffusion, and increased ohmic losses if the average distance between anodic and cathodic active sites becomes large. In order to produce adequate power, multiple independent planar cells could be accommodated on a single plane, and then these planes could be stacked as in typical PEM fuel cells. The volumetric power density of such devices would however be limited by the volume of the sealing and structural elements separating the cells. In traditional PEM fuel cell stacks, which are limited by similar issues [25], the bipolar plates serve as structural and electrical components. The inherent advantage of non-planar electrode–electrolyte interfaces has been recognized and demonstrated for such cells using, e.g. waved membrane-electrode assemblies [25]. In contrast, the microfluidic fuel cells presented to date contain mostly non-participating structural material such as glass or poly(dimethylsiloxane) (PDMS). The scale-up of microfluidic fuel cell technology in a volumetrically efficient manner remains a challenge.

The objective of this study is to develop membraneless microfluidic fuel cell architectures employing low-cost graphite rod electrodes. Graphite rod electrodes provide reaction sites and current collection within a single stand-alone structure that requires no additional catalyst or electrode support materials. Experimental as well as numerical and analytical methods are applied to a planar microfluidic fuel cell architecture employing graphite rod electrodes. A three-dimensional microfluidic fuel cell architecture consisting of a hexagonal array of graphite rods is presented. Significant performance gains in terms of both peak power output and fuel utilization are demonstrated with prototypes of both planar and three-dimensional architectures.

2. Experimental

2.1. Microfabrication

2.1.1. Planar cell

A schematic of the planar cell configuration is given in Fig. 1. The cells were manufactured in house, and consist of two layers: a substrate that contains the graphite rod electrodes, and a polymeric top layer that contains the channel structure. Graphite rods were embossed in the base substrate according to the following procedure: a 2 in. × 3 in. microscope glass slide was coated with a 1 mm layer of polyurethane (PMC-790; Smooth-On Inc., Easton, PA) and cured for 2 h on a hot plate at 65 °C. Upon solidification, the polyurethane substrate was placed in an aluminum substrate holder. Two 0.5 mm-diameter graphite rods (Mars micro carbon, type HB; Staedtler, Germany) were fitted in a different custom-made aluminum holder with two parallel grooves that uniformly separated the rods by 1.0 mm and held them in place. The holder was sprayed with universal mold release (Smooth-On Inc.) before use. Both parts were heated on a hot plate to 160 °C and mechanically pressed together to fuse the graphite rods into the softened polyurethane layer. The assembly was removed from the hot plate with the pressure still applied, and allowed to cool down. The aluminum plates were then removed, leaving the graphite rods embossed in the hardened polyurethane layer. The substrate was finished by grinding down the rods to achieve a flush, flat electrode surface. Wires were attached to one end of the rods using conductive epoxy (Circuit Works CW2400; ITW Chemtronics, Kennesaw, GA).

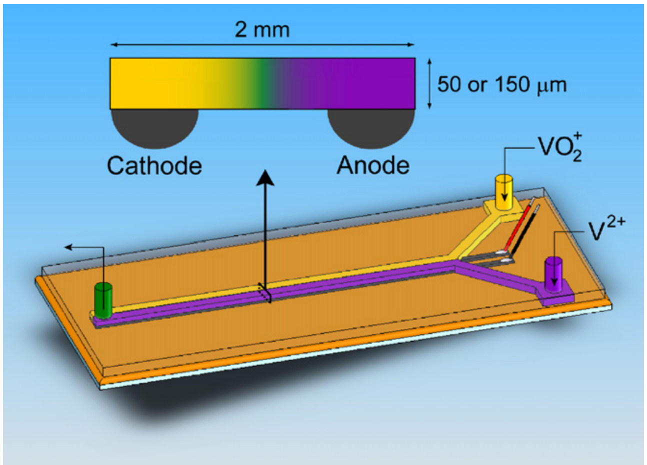

Fig. 1. Schematic of a graphite rod-based microfluidic fuel cell of the planar cell type. The cell employs vanadium redox couples as fuel (V^{2+}, violet) and oxidant ($VO_2{}^+$, yellow), shown in representative colors (For interpretation of the references to color in this figure legend, the reader is referred to the web version of the article.).

The top layer of the planar cell, containing the Y-shaped microchannel, was fabricated by replica molding in poly(dimethylsiloxane) (PDMS; Dow Corning, Midland, MI) following established soft-lithographic protocols [26], and process specifics described elsewhere [27]. The channels were 2 mm wide and either 50 or 150 μm high. A master that defines the channel pattern was created by photolithography in negative photoresist (SU-8 50; Microchem, Newton, MA). This structure was cast into a slab of PDMS, which was peeled off the master after curing. Inlet/outlet holes were punched in the PDMS before assembly. The PDMS slab was placed over the polyurethane substrate and the two were aligned precisely under a microscope. While operating the cell, a reversible seal was accomplished by pressing the two parts together with an aluminum clamp. This type of bond allows cleaning of the cell and substitution of the channel structure, such that the substrate may be re-used after each trial. Alternatively, an irreversible seal that does not require clamping can be obtained by plasma-treating the PDMS, which renders hydrophilic channel walls and facilitates covalent binding to the substrate. The electrodes of the assembled fuel cell had a planar active area of 0.165 cm^2 (0.5 mm wide and 33 mm active length). Overall, the above described fabrication procedure is rapid and economical. A set of planar cell units can be fabricated in less than 4 h with a total material cost of US$ 2 per cell.

2.1.2. Three-dimensional array cell

The inherent advantage of non-planar electrode–electrolyte interfaces has, as noted earlier, been recognized before in the context of PEM fuel cell. The array architecture fuel cell proposed here and shown in Fig. 2 uses cylindrical graphite rods as electrodes. This cell comprises of 29 graphite rods mounted inside a 2 mm × 7 mm × 39 mm cavity that was CNC-machined

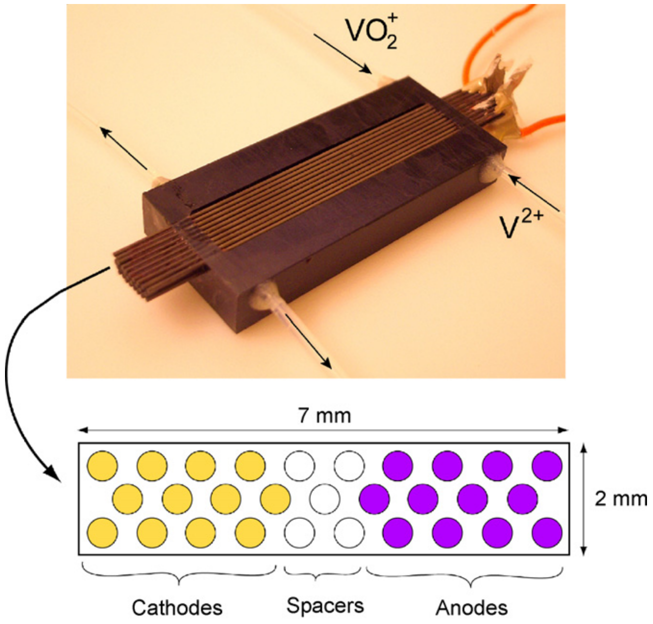

Fig. 2. Three-dimensional vanadium-based microfluidic fuel cell with the array architecture. Graphite rods are mounted in a single CNC-machined cavity. The cell comprises 12 anodes and 12 cathodes that are essentially independent. The five rods in the center of the device are exposed to co-laminar inter-diffusion of anolyte and catholyte and are not electrically connected.

in a 6 mm × 19 mm × 44 mm block of Delrin. Delrin was chosen as it is a heat resistant, inflexible and chemically resilient acetal polymer. To hold and separate the graphite rods, an array of holes in a hexagonal pattern were drilled in the end plates of the cavity. The 0.5 mm diameter graphite rods were fitted in the cavity through the holes and sealed using positive photoresist (SPR 220-7.0; Rohm and Haas, Marlborough, WA). Separate wires were attached to the anodes and cathodes at the end of the rods using conductive epoxy. Inlet and outlet holes were drilled in the sides of the Delrin block and Teflon tubes (Upchurch Scientific, Oak Harbor, WA) were inserted for fluid handling. A thin slab of PDMS formed the top wall of the cavity, and during operation the seal was ensured by an aluminum clamp. The total active area exposed to the fluid was 7.3 cm^2 per electrode.

2.2. *Preparation of vanadium solutions*

Vanadium-based fuel (V^{2+}) and oxidant (VO_2^+) solutions were prepared according to the following procedure: fresh sulfuric acid supporting electrolyte solution was prepared from Millipore Milli-Q water (Millipore, Billerica, MA) and concentrated sulfuric acid (EMD Chemicals Inc., Gibbstown, NJ). Vanadium sulfate oxide hydrate ($VOSO_4 \cdot XH_2O$; Alfa Aesar, Ward Hill, MA) was dissolved in the supporting electrolyte by sonication at 50 °C until a clear blue VO^{2+}-solution was obtained. Two different solutions were prepared: 1 M VO^{2+} in 1 M H_2SO_4, and 2 M VO^{2+} in 2 M H_2SO_4.

The required V^{2+} and VO_2^+ solutions were generated from VO^{2+}-solution in an electrolytic flow cell with carbon felt electrodes divided by a Nafion membrane. The VO^{2+}-solution was divided into three equal parts by volume: one part (200 mL) was added to the positive half-cell and the remaining two parts (400 mL) were added to the negative half-cell. Given the instability of the V^{2+} solution in contact with air, it was necessary to continuously purge the negative half-cell with N_2. The solutions were pumped through the cell while applying a fixed electrolytic current of 10 A. The cell voltage was 1.5–1.7 V while charging. Charging was complete after 50 min when the cell voltage quickly rose above 2.0 V, which was also confirmed by the sudden color change in the two compartments. The fully charged purple V^{2+} solution and yellow VO_2^+ solution were removed and stored under an N_2 blanket in air-tight bottles. The current efficiency during charging was calculated to be 99.7%. The use of carbon electrodes ensured that no H_2 or O_2 bubbles were produced during the experiment. The solutions demonstrated high stability under storage for several months with only minor degradation.

The anolyte and catholyte can be regenerated from the mixed (used) solution collected from the outlet(s) of the fuel cells (normally a 50/50 mixture of V^{3+} and VO^{2+} when stabilized) by pouring equal parts into the positive and negative half-cells and repeating the charging procedure.

2.3. *Fuel cell diagnostics*

The steady co-laminar flow of vanadium solutions required for fuel cell operation was driven by a syringe pump (PHD 2000; Harvard Apparatus, Holliston, MA) via flexible Tygon tubing (planar cell) or Teflon tubing (array cell). Polarization data were obtained at room temperature by chronoamperometry under stepwise potentiostatic control from 0.0 V to open-circuit voltage in 0.1 V increments, using a PARSTAT 2263 potentiostat (Princeton Applied Research, Oak Ridge, TN). The cell current was monitored until steady state was reached, which usually occurred within 120 s. Current densities and power densities for the planar cells reported here are based on the planar active area of the electrodes (0.165 cm^2).

The combined ohmic resistance of the planar cells was evaluated by electrochemical impedance spectroscopy (EIS) using the same potentiostat. An ac amplitude of 5 mV rms was applied over the frequency range from 50 kHz to 0.5 Hz. The ohmic cell resistance was recorded as the high-frequency real axis intercept of the Nyquist plot of impedance. The EIS data were averaged from measurements at four different flow rates (2.5, 10, 60 and 120 $\mu L\,min^{-1}$) using 1 M solutions at 0.5 V cell voltage.

3. Theory

3.1. *Numerical current distribution analysis*

A primary current distribution model of a 2D cross-sectional plane (Fig. 1) of the co-laminar flow channel was developed for the planar cells in order to quantify in-channel ionic resistance between anode and cathode. The current density ($\vec{J}$) and potential (V) distribution in the channel are coupled and can be solved for simultaneously by considering the electrolyte as a dc conductive medium with electrical conductivity σ governed by

Ohm's law:

$$\vec{J} = -\sigma \nabla V \tag{1}$$

The potential distribution is described by Poisson's equation;

$$-\nabla(\sigma \nabla V) = Q_j \tag{2}$$

where Q_j represents internal current sources. By assuming isotropic conditions, negligible Joule heating (strong convective heat transfer), and no homogeneous reactions ($Q_j = 0$), Eq. (2) turns into the Laplace equation:

$$\nabla^2 V = 0 \tag{3}$$

This governing equation is subject to Neumann boundary conditions (uniform current density normal to the surface) at the anode and cathode surface, and electric insulation at the remaining boundaries (see Fig. 1). The domain was discretized by adaptive meshing and the equations solved for the 2D potential distribution using a direct stationary linear solver available within the commercial software package COMSOL Multiphysics 3.2 (COMSOL Inc., Stockholm, Sweden) under mesh independence control. The total in-channel ohmic resistance was finally obtained by integrating the normalized local current density over the entire domain, i.e.:

$$R_s = \frac{1}{\sigma d^2 l} \int_{A_c} J^{*2} \, dA \tag{4}$$

Here, d and l are the diameter and active length of the graphite rod electrodes, respectively, and the current density (J) is normalized with respect to the current density at the electrodes, J_e, as $J^* = J/J_e$.

3.2. Transport limitation analysis

The theoretical maximum current density of a microfluidic fuel cell, assuming rapid electrochemical reactions, is controlled by the rate of convective/diffusive transport of reactants to the surface of the electrodes. In the transport controlled regime, the boundary condition on the surface of the electrode is defined by zero concentration [28]:

$$c_e = 0 \tag{5}$$

A concentration boundary layer that depends on the flow characteristics will thus develop in the channel, starting at the leading edge of the electrode. To approximate the total flux of reactant to the electrode and sequentially the current, one can consider the limiting case of internal, fully developed laminar flow between two flat plates with one reacting wall, which is a pseudo-3D case that neglects the effects of the side walls of the channel. There is no analytical solution to the described convective/diffusive mass transport problem available in the literature; however, the extensive body of empirical heat transfer correlations may be used together with the heat and mass-transfer analogy to derive approximate scaling laws. The scaling laws employed here were adapted from the analysis provided by Kjeang et al. [29], which focused on the generation of a redox couple at an embedded electrode in a microfluidic channel flow. Only the most relevant details are provided here, and the reader is referred elsewhere [29] for the derivations. The analysis is based on dimensionless scaling of the mean velocity;

$$U^* = \frac{U D_h^2}{l D} \tag{6}$$

where U is the mean velocity, D_h the hydraulic diameter, and D is the diffusion coefficient ($D \approx 10^{-10}\,\mathrm{m^2\,s^{-1}}$). There are two distinct regimes: (i) the high U^* regime, which covers most practical flow rates experienced in microfluidic fuel cells; and (ii) the low U^* regime for low flow rates in channels with small hydraulic diameter. In the high U^* regime, the transport-limited current is proportional to the cubic root of the mean velocity [29]:

$$I = -1.849 F d c_0 \left(\frac{l^2 D^2 U}{D_h} \right)^{1/3} \tag{7}$$

Moreover, the current is proportional to the electrode diameter and the initial vanadium concentration (c_0), and scales as the square of the cubic root of the active length and the inverse cubic root of the hydraulic diameter. This analysis is based on the following assumptions: pseudo-3D momentum and species transport neglecting transverse components, and constant bulk concentration equal to the initial concentration. Alternatively, Eq. (7) can be written in terms of flow rate (Q):

$$I = -1.849 F d c_0 \left(\frac{l^2 D^2 Q}{D_h h w} \right)^{1/3} \tag{8}$$

For high-aspect ratio channels, $D_h \approx 2h$, and the current scales as $h^{-2/3}$ and $w^{-1/3}$ versus the channel height and width, respectively, at constant flow rate. In addition, if we introduce the dimensionless current;

$$I^* = \frac{I}{F d l c_0 D / D_h} \tag{9}$$

we obtain a linear correlation between I^* and $U^{*1/3}$:

$$I^* = -1.849 U^{*1/3} \tag{10}$$

This equation is capable of predicting the transport-limited current independently of initial concentrations and channel geometry within the high U^* regime.

In the low U^* regime, the flux of reactant entering the channel is equal to the rate of the electrochemical reactions, such that all reactant molecules are converted into product species and useful current. We assume that diffusion is strictly two-dimensional and neglect transverse diffusion in the cross-stream direction. In this case, the maximum current is directly proportional to inlet concentration and flow rate [29]:

$$I = -F c_0 Q \tag{11}$$

Again, we can use the dimensionless quantities I^* and U^* to derive a relationship that is valid for high-aspect ratio channels under any conditions within the low U^* regime:

$$I^* = -\tfrac{1}{2} U^* \tag{12}$$

The transition point between the high U^* regime and the low U^* regime occurs at $U^{*1/3} = 1.9$ [29].

4. Results and discussion

4.1. Planar cell operation

A set of planar microfluidic fuel cells, as shown schematically in Fig. 1, were fabricated and vanadium solutions of concentrations 1 and 2 M were freshly prepared using the procedures described in Section 2. Graphite rods, i.e. common mechanical pencil refills that are available off-the-shelf, were used as electrodes without additional catalyst or electrode support materials. Note that small amounts of clays are typically used to bind the graphite in pencil leads; the exact composition depends on hardness and is not supplied by manufacturers.

4.1.1. Open-circuit voltage and redox concentrations

The appropriate anodic and cathodic vanadium redox reactions and standard redox potentials are [30]:

$$V^{3+} + e^- \leftrightarrow V^{2+} \qquad E^\circ = -0.255\ \text{V versus SHE} \tag{13}$$

$$VO_2{}^+ + 2H^+ + e^- \leftrightarrow VO^{2+} + H_2O \qquad E^\circ = 0.991\ \text{V versus SHE} \tag{14}$$

A fuel cell based on these two half-cell reactions thus has a theoretical reversible cell potential of 1.246 V. Portions of the V^{2+} and $VO_2{}^+$ solutions were characterized separately in a three-electrode electrochemical cell with a graphite rod working electrode. The measured open-circuit potentials (OCPs) were −0.317 and 1.116 V (1 M), and −0.309 and 1.192 V (2 M) (versus SHE), respectively. The maximum cell potentials for fuel cell operation based on these solutions are 1.43 V (1 M) and 1.50 V (2 M). By assuming that the open-circuit potentials are reversible potentials, their departure from the standard potentials is related to the solution concentrations by the Nernst equation [31]:

$$E = E^\circ - \frac{RT}{nF} \ln\left(\frac{a_{\text{red}}}{a_{\text{ox}}}\right) \tag{15}$$

In our case, $T = 298$ K, $n = 1$ for both redox pairs, and a is the activity. If we assume equal activity coefficients, the activity ratio can be approximated by the redox concentration ratio. Using this analysis, the following redox concentration ratios were obtained: 92% V^{2+}/8% V^{3+} and 99.2% $VO_2{}^+$/0.8% VO^{2+} (1 M); 89% V^{2+}/11% V^{3+} and 99.8% $VO_2{}^+$/0.2% VO^{2+} (2 M). These highly biased concentration ratios explain the enhanced cell potentials measured here. The cell potential can be increased beyond 1.50 V by the use of high-purity vanadium solutions, e.g. Ferrigno et al. [11] achieved 1.67 V with approximately 99.9% $VO_2{}^+$/0.1% VO^{2+} and 99.9% V^{2+}/0.1% V^{3+} concentration ratios at 1 M.

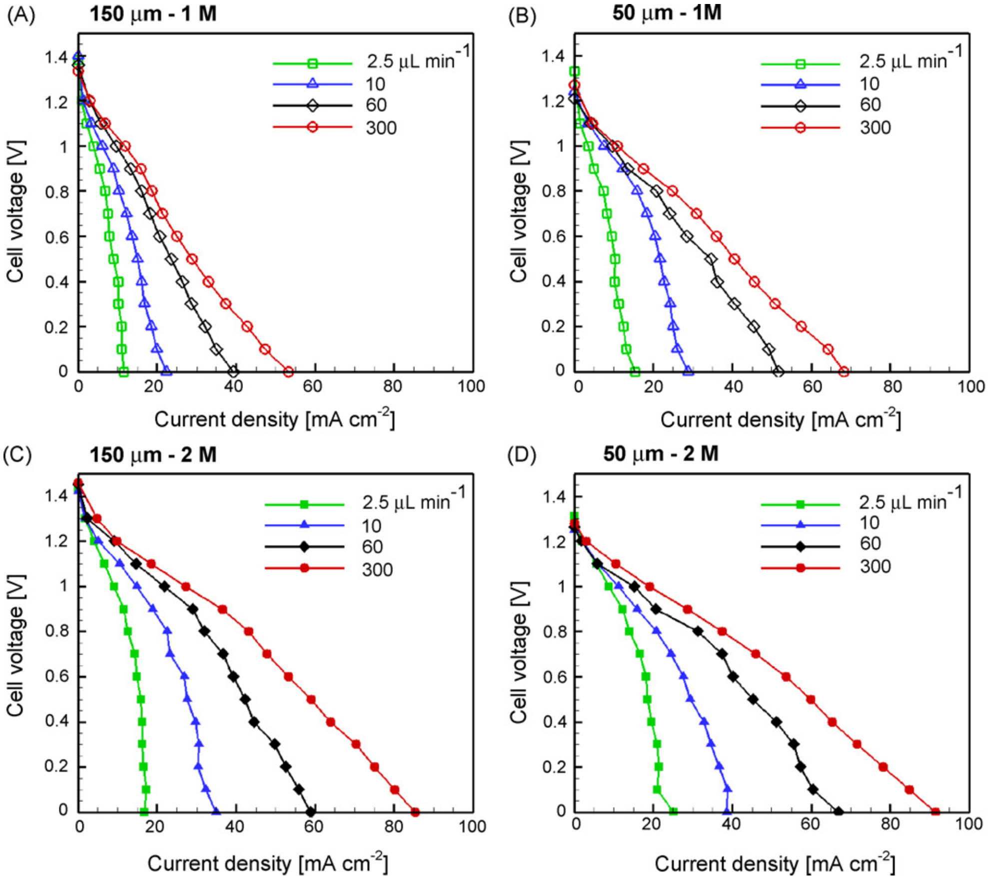

Fig. 3. Experimentally determined polarization curves for the planar cells using 1 M (A and B) and 2 M (C and D) vanadium solutions in 150 μm (A and C) and 50 μm (B and D) high microfluidic channels. The legend indicates flow rate per stream.

4.1.2. Polarization

The performance of the planar cell architecture was evaluated for four different combinations of channel height and vanadium concentration: (i) 150 μm and 1 M; (ii) 150 μm and 2 M; (iii) 50 μm and 1M; (iv) 50 μm and 2 M. Polarization data were measured by chronoamperometry under potentiostatic control at steady state conditions. The amperometric measurements were remarkably steady and predictable with an initial current peak as the cell potential was applied that decreased continuously over time towards the steady state current. Furthermore, repeated trials showed highly reproducible trends with an average standard deviation of less than 2%. The polarization data were reproducible under galvanostatic control, indicating that the same internal conditions are established independently of the control method. The planar cells were successfully operated at flow rates spanning four orders of magnitude. Fig. 3 shows polarization data at flow rates between 2.5 and 300 μL min^{-1} per stream. The open-circuit voltages measured in the fuel cells were 1.19–1.41 and 1.24–1.46 V for 1 and 2 M solutions, respectively. Although 1–17% less than the values measured in the electrochemical cell, these open-circuit voltages are significantly higher than those possible in methanol/oxygen or hydrogen/oxygen fuel cells [30]. The obtained values were generally higher for the 150 μm channel height than for the thinner 50 μm channel. The polarization trends at low flow rates show typical signs of mass-transfer limitations as the cell voltage drops quickly at a limiting current. The impact of mass-transfer limitations from the bulk solution is reduced by enhanced convective transport at high flow rates, as indicated by the increasing current densities at higher flow rates. At 300 μL min^{-1}, for example, there was no indication of bulk transport limitations. The slope of the polarization curves is steadier at high flow rates, which indicates that the produced current was limited by a combination of ohmic resistance, faradaic electrochemical impedance, and species transport to and from the active sites. Given the same flow rate, the convective velocity in the 50 μm channel was triple that in the 150 μm channel. The result of the increased velocity was a thinner diffusion layer and higher maximum current density, particularly in the case of 1 M solutions. A more quantitative analysis of these transport effects is provided through the transport limitation analysis in Section 4.1.6. The highest current density produced was 92 mA cm^{-2} at 300 μL min^{-1} and 2 M vanadium solutions.

4.1.3. Power density

The corresponding power density data shown in Fig. 4 were obtained by multiplying the current density by the cell voltage. The most prominent effect identified here is the strong dependence of power density on both flow rate and vanadium concentrations. These results indicate that the power output of these devices is primarily controlled by transport characteristics and that the electrochemical reactions are relatively

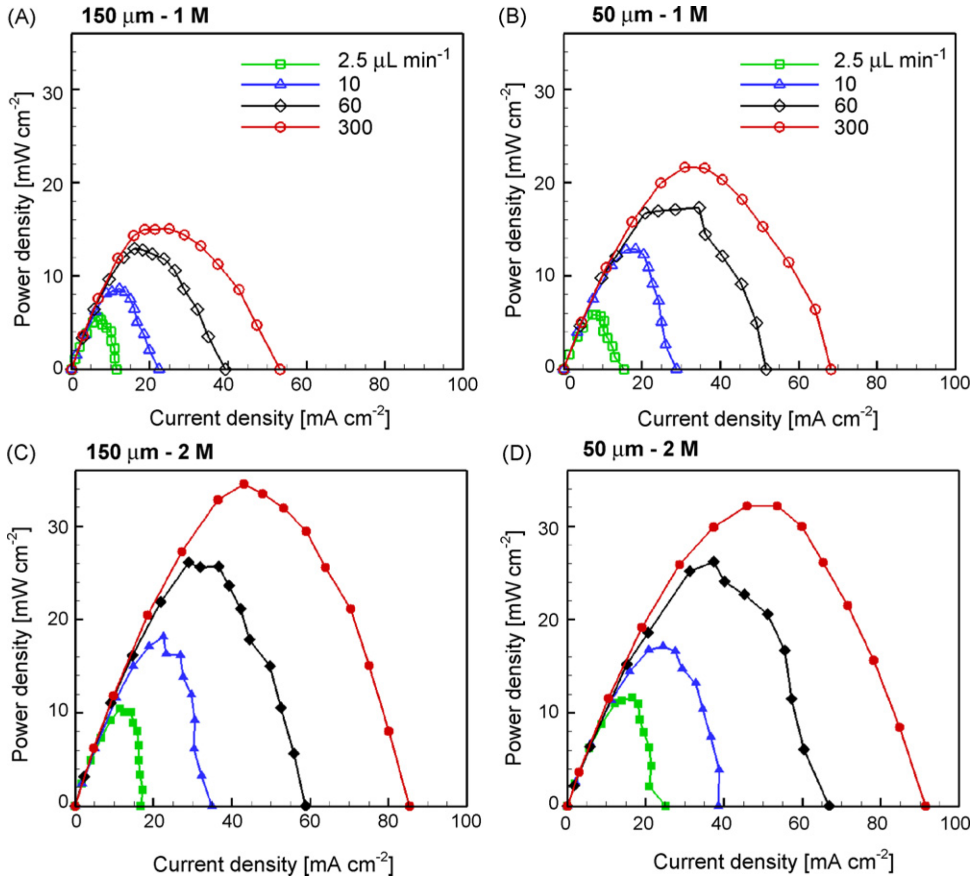

Fig. 4. Power density curves for planar cell operation using 1 M (A and B) and 2 M (C and D) vanadium solutions in 150 μm (A and C) and 50 μm (B and D) high microfluidic channels, based on the polarization data in Fig. 3. The legend in A and B indicates flow rate per stream, also representative for C and D.

fast. In the context of the evaluation of graphite rods as carbon microfluidic fuel cell electrodes, this is an encouraging result.

Peak power was generally achieved within a cell voltage range of 0.6–0.9 V, which can be considered a competitive range compared to most other types of fuel cells. The highest peak power density in this study, 35 mW cm^{-2} at 0.8 V, was obtained for the 150 μm cell at the highest flow rate (300 μL min^{-1}) and 2 M vanadium concentrations. This level of power density is similar to that of previous vanadium-based microfluidic fuel cells [11] although the flow rate used here was only 1/5 as high. Moreover, this power density is 35–100% higher than air-breathing cells [14,16] and seven times higher than the best cells based on dissolved oxygen [10].

Points of peak power density for each curve are plotted for comparison in Fig. 5A versus the logarithm of the flow rate. It is noteworthy that the 150 μm cell was capable of reaching higher peak power densities than the 50 μm cell at high flow rates of 2 M vanadium, despite lower maximum current densities. This feature is attributed to the higher open-circuit voltage measured for the larger channel, which indicates superior electrochemical characteristics and larger electromotive force. The effect of channel height is nevertheless more dominant at 1 M concentrations, where the 50 μm cell performs significantly better than the 150 μm cell. In addition, the improvements in power density upon switching from 1 to 2 M vanadium are much larger for the 150 μm cell than the 50 μm cell; at 300 μL min^{-1}, for example, the peak power of the 150 μm cell was enhanced by 230% compared to a mere 49% for the 50 μm cell. The difference between the two cells is related to the stronger convective transport experienced by the 50 μm cell, as will be discussed further in Section 4.1.6. The continuous slope of peak power density versus flow rate shown for all cases in Fig. 5A demonstrates the ability to tune the flow rate to satisfy unsteady power requirements of applications. The response time of the fuel cell to a transient duty cycle is expected to be on the order of 1–10 s, depending on the flow rate regime.

The pumping power required to sustain steady co-laminar flow in high-aspect ratio channels can be estimated based on laminar flow theory as the pressure drop multiplied by the flow rate according to Ref. [32]:

$$W = \Delta p Q = \frac{32\mu l Q^2}{wh D_\mathrm{h}^2} = \frac{8\mu l Q^2}{wh^3} \qquad (16)$$

By neglecting the pressure drop associated with inlet channels and off-chip tubing as well as other losses, and using the dynamic viscosity (μ) for water, the pumping power required for the highest flow rate and smallest channel under study becomes $W \approx 20$ μW. This power requirement is less than 1% of the power output of the fuel cell, and can therefore be neglected.

4.1.4. Fuel utilization

The coulombic single pass fuel utilization is defined as the current output divided by the flux of reactant entering the channel:

$$\eta = \frac{I}{nFc_0 Q} \qquad (17)$$

The geometry of the planar cells is well suited to achieve high fuel utilization at low flow rates. Specifically, the mixing interface between the streams is perpendicular to the electrode surfaces, and the high-aspect ratio ensures that the electrode area is large compared to that of the mixing interface [7]. This configuration limits inter-diffusive fuel/oxidant crossover, thereby enabling operation at low-range flow rates and high fuel utilization. The maximum single pass fuel utilization obtained for the planar cells is presented in Fig. 5B as a function of flow rate for all cases under study. As expected, the fuel utilization was maximized for the lowest flow rates, and decreased with flow rate. The moderate penalty in power density associated with the transition to low flow rates (Fig. 5A), from ~30 down to ~10 mW cm^{-2}, is offset by a large boost in fuel utilization from ~1 to ~40%. The highest fuel utilization obtained here was 63% (1 M, 2.5 μL min^{-1}, 50 μm). This level is remarkably high: the highest fuel utilization presented to date for other microfluidic fuel cells was 33% [14], although the fuel utilization levels at practical flow rates and cell voltages were typically less than 1%. Highly practical operational characteristics in terms of both power density and fuel utilization were achieved here, in particular with the 50 μm cell operating at 2.5 μL min^{-1} with

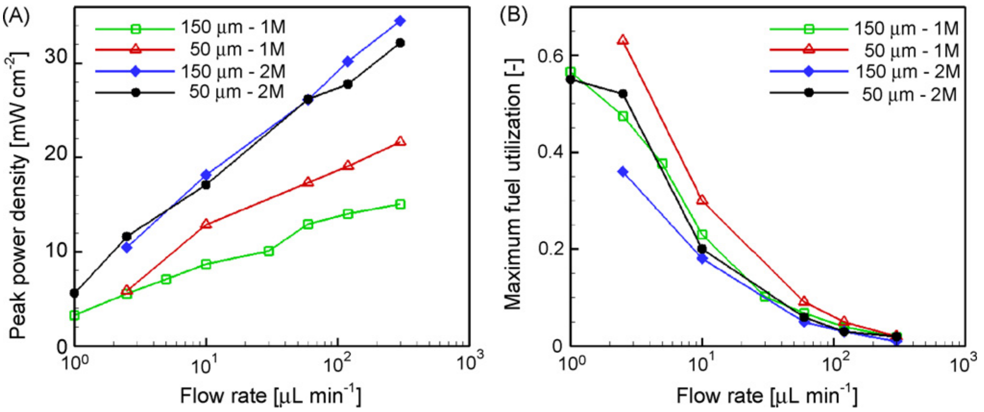

Fig. 5. Experimental results of peak power density (A) and maximum fuel utilization (B) for planar cells with different channel heights and vanadium concentrations (indicated in the legend), plotted vs. the logarithm of the flow rate per stream.

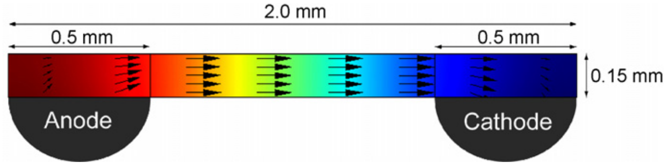

Fig. 6. Numerically determined electrical potential distribution inside the microfluidic channel of a single cell (obtained from the primary current distribution model). Red and blue colors represent high and low electrical potentials, respectively, and the arrows show the current distribution facilitated by ionic transport (For interpretation of the references to color in this figure legend, the reader is referred to the web version of the article.).

2 M vanadium. This configuration enabled a power density of 11 mW cm^{-2} at 0.6 V combined with a single pass fuel utilization of 38%.

4.1.5. Ohmic resistance

The ohmic resistance in the channel is proportional to the average charge transfer distance between anode and cathode, which can be approximated by the following scaling law:

$$R_s = \frac{s}{\sigma h l} \tag{18}$$

Since the inter-electrode spacing (s) is relatively large (1 mm), ohmic resistance in microfluidic fuel cells is generally higher than in membrane-based fuel cells. One way to reduce ohmic resistance is to increase the concentration of the supporting electrolyte. For example, the conductivity of dilute sulfuric acid increases from 35 S m^{-1} for 1 M to 58 S m^{-1} for 2 M concentration at 25 °C [30]. A primary current distribution model that essentially considers the channel a 2D electrostatic conductor was developed (Section 3.1) in order to obtain a prediction of the total ohmic resistance in the flow channel of the planar cells with geometry shown in Fig. 1. The results obtained for the 150 μm cell are given in Fig. 6: the normalized ionic current distribution between anode and cathode is shown by the arrows; and the normalized electrical potential distribution is shown in the background, with red and blue colors representing high and low electrical potential, respectively. The electrical potential distribution modeled here is induced by ohmic resistance, and is partly contributing to the losses in electrochemical cell potential. The total in-channel ohmic resistance was integrated using Eq. (4) for the two planar cell geometries studied here. Electrochemical impedance spectroscopy was performed experimentally to estimate the overall ohmic resistance of the cell. This measurement includes contributions from in-channel ionic resistance as well as electrical series resistance introduced by electrodes, contacts and wires. The results from the scaling analysis, the current distribution model and the EIS investigation are compared in Table 1. As expected, the scaling law underestimates the in-channel resistance compared to the results obtained by the current distribution model, which includes the effects of electrode and cell geometry. The difference between the results from the model and the EIS study indicate the magnitude of the additional electrical series resistance component included in the EIS results. The ohmic resistance of the graphite rods was ~3 Ω per electrode, as measured with a multimeter across a 60 mm long individual rod, which only constitutes a fraction of the overall resistance measured by EIS. The majority of the ohmic resistance is therefore associated with ionic charge transport in the channel and external electrical contacts. Interestingly, the EIS results were very similar for both channel heights, unlike those obtained by the current distribution model. Given the large difference between EIS and model results for 150 μm, we believe that the resistances measured by EIS are dominated by the electrical contact resistance component, and that the agreement between EIS and model results for 50 μm is serendipitous. The in-channel resistance should therefore be much smaller than predicted by the other methods. This inevitably raises the question whether or not the charge transfer mechanism proposed here is entirely valid for this type of microfluidic fuel cells. It is possible, for instance, that some local depletion or accumulation of ions masks the in-channel ohmic resistance. A thorough EIS investigation of these phenomena is currently under development by our group.

Table 1
Ohmic resistance of planar cells with channel height h and 1 M vanadium solutions, obtained by the scaling law (Eq. (18)), the primary current distribution model (Eq. (4)), and electrochemical impedance spectroscopy (EIS)

h (μm)	Scaling (Ω)	Model (Ω)	EIS (Ω)
150	6	8	22
50	17	23	24

4.1.6. Transport limitation analysis

Scaling laws for the convective/diffusive transport-limited current density were presented in Section 3.2. Two transport regimes were identified: the low U^* regime and the high U^* regime, based on the dimensionless mean velocity given in Eq. (6). The transport-limited current is proportional to the flow rate in the low U^* regime and scales as the cube root of the flow rate in the high U^* regime. The maximum current densities measured experimentally for the 150 μm planar cell with 1 M solutions are compared to the scaling laws in Fig. 7A. In this case, the maximum current density follows the scaling laws very closely in both flow regimes, except at the highest flow rate (300 μL min^{-1}). This operating case is therefore predominantly limited by convective transport from the bulk fluid, rather than any reaction kinetics associated with graphite rod based electrodes. Fig. 7B shows experimental data for all four cases studied here, plotted together using the dimensionless quantities I^* and $U^{*1/3}$ to represent maximum current density and mean velocity, respectively. Using these variables, the scaling curves in both U^* regimes collapse into a single function, which is linear above the transition point to the high U^* regime at $U^{*1/3} = 1.9$. The experimental currents are entirely transport-limited at low flow rates for all cases. At high flow rates, however, the transport-limitation is generally not reached. This effect may be explained as follows: the rate of convective transport increases with flow rate, vanadium concentration and inverse channel height. As convective transport becomes stronger (see Fig. 7B), demand on the electrochemical and electrical aspects of the cell increases, and thus effects of non-ideal reaction kinetics and ohmic resistance become sig-

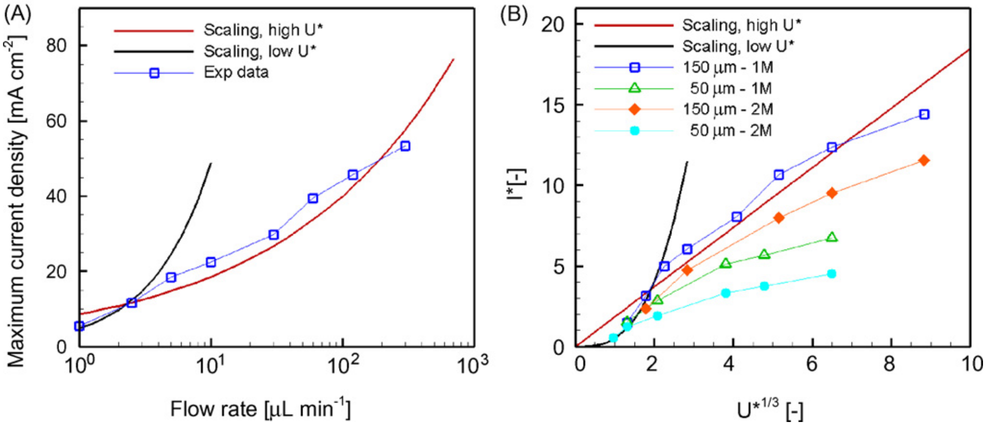

Fig. 7. Transport limitation analysis: (A) maximum current density measured experimentally for a planar cell with 1 M vanadium concentrations and 150 µm channel height, and (B) for different vanadium concentrations and channel heights based on dimensionless variables for maximum current density (I^*) and flow rate ($U^{*1/3}$). Also plotted are the empirical scaling laws for the transport-limited cases at high and low U^*.

nificant. This is especially noticeable in the 50 µm cell which experiences the highest velocities for a given flow rate. In these cases, the current is not strictly transport limited, but is controlled by a combination of factors related to transport, electrochemistry and ohmic resistance. In sum, the current density was predominantly limited by convective/diffusive transport as opposed to reaction kinetics. The ability to reach transport-limited operation over a wide range of flow rates demonstrates the viability of graphite rod electrodes as core fuel cell components.

4.2. Array cell operation

Three-dimensional array architecture fuel cells with design shown in Fig. 2 were fabricated according to the procedure described in Section 2.1.2. The array cell design is based on 29 graphite rods of 0.5 mm diameter assembled inside a single cavity. The average spacing between the rods was 200 µm, and thus the flow characteristics within the available space are microfluidic in nature and similar to those of the planar cells. Although the inter-diffusion zones located in between the central rods in the array cell are non-planar, the width of these inter-diffusion zones is expected to grow at a similar rate as for the planar cells. To compensate for the inter-diffusion zone, the five central rods are electrically insulated (see Fig. 2). This inter-diffusion zone is flanked by 12 individual anodes and 12 individual cathodes. For the purposes of this study, all 12 electrodes of each type were connected in parallel. This simple configuration enabled performance comparison with the planar cells; however, alternative electrode connection combinations are numerous. The array architecture inherently provides many more options with respect to power conditioning than a conventional stack. Conceivably electrode connections could be made dynamically via control electronics in response to load, and thus enable dynamic power conditioning at the fuel cell level. With respect to scalability, the array cell configuration may be readily expanded in both vertical (preferable) and horizontal directions to increase capacity. Scale-up of these cells requires only an enlarged cavity, in contrast to the volumetric costs of additional substrates and fluid delivery networks associated with stacking planar cells.

4.2.1. Open-circuit voltage and redox concentrations

The V^{2+} and $VO_2{}^+$ solutions utilized for the array cell were similar to the 1 M solutions used in the planar cell study except for the redox concentration ratios. The open-circuit potentials, measured in a three-electrode electrochemical cell, were −0.272 and 1.061 V (versus SHE). The maximum cell potential for fuel cell operation based on these solutions is 1.33 V. Using the Nernst equation, Eq. (15), the following redox concentration ratios were obtained: 64% V^{2+}/36% V^{3+} and 94% $VO_2{}^+$/6% VO^{2+}. The feed concentration was therefore limited to 0.64 M.

4.2.2. Polarization

Polarization data were measured for the array cell according to the procedure previously described for planar cell operation. Fig. 8A shows polarization data at flow rates between 10 and 2000 µL min^{-1} per stream, plotted as cell voltage versus current. Also plotted for comparison are the results of planar cell operation at 300 µL min^{-1} (150 µm channel and 1 M vanadium). The open-circuit voltages measured in the array cell ranged from 0.84 V at 10 µL min^{-1} to 1.36 V at 2000 µL min^{-1}. This increasing trend is attributed to the more uniform solution distribution encountered at high flow rates. Operation at flow rates less than 10 µL min^{-1} was found to be impractical due to the sharp drop in cell voltage induced by increased inter-diffusion and non-uniform flow. The cross-sectional flow area in the bundle is about 30 times larger than the 150 µm planar cell, and the mean convective velocity is therefore 30 times less at a fixed flow rate. The overall shape of the polarization curves are similar to the ones measured for the planar cells, and as before, some transport limitation behavior is apparent at lower flow rates. However, the currents obtained with the array cell are notably higher than for planar cell operation at the same flow rate. The maximum current measured here was 86 mA at 2000 µL min^{-1}.

4.2.3. Power output

The power curves obtained experimentally for array cell operation are shown in Fig. 8B together with the power curve generated by the 150 µm planar cell (at 300 µL min^{-1} and 1 M). The array cell produced more power than the planar cell at all

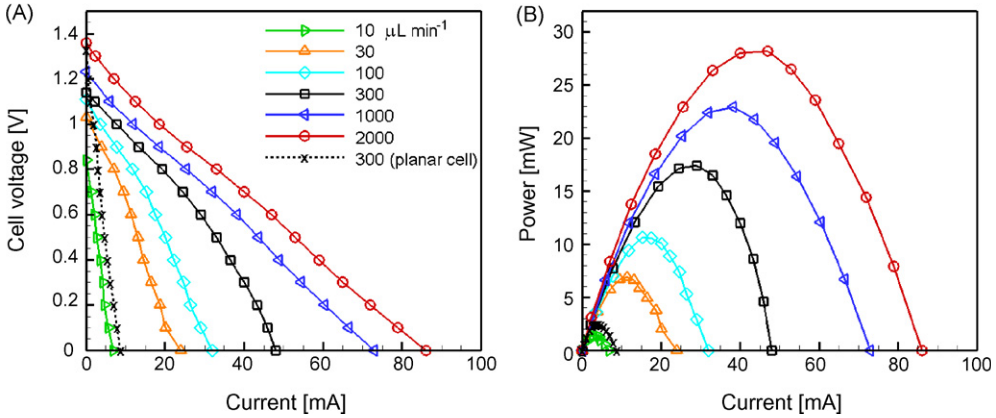

Fig. 8. Polarization (A) and power (B) curves obtained experimentally for array cell operation at flow rates per stream as indicated, using 0.64 M vanadium solutions. The data are compared to planar cell operation using 1 M solutions at 300 μL min^{-1} flow rates in a 150 μm high channel.

flow rates above 10 μL min^{-1}, and its power output increased substantially with flow rate. Fig. 9A presents peak power as a function of logarithmic flow rate for the array cell and planar cell. At a fixed flow rate of 300 μL min^{-1}, the array cell produced seven times more power (17.4 mW) than the planar cell (2.5 mW). This is considered an appropriate performance comparison, given that the 'cost' in terms of fuel and oxidant supply is identical. The array cell also operated effectively at low flow rates; for example, the array cell produced 6.9 mW at 30 μL min^{-1}, which is nearly three times more than the planar cell could produce at 300 μL min^{-1}, a 10 times higher flow rate.

The highest power output measured for the array cell was 28 mW at 0.6 V and 2000 μL min^{-1}. Based on the total active area of the array cell, this power level is equivalent to a moderate power density of 3.8 mW cm^{-2}. This relatively low power density compared to those of the planar cells is attributed to several factors: the significantly lower V^{2+} concentration (0.64 M); the higher in-channel ohmic resistance; the non-uniform flow distribution; and most importantly, the lower convective velocity at fixed flow rate.

In the context of a fuel cell stack, volumetric power density is a more relevant metric. For the array cell, the volumetric power density based on the entire volume of the cavity was 52 mW cm^{-3}. Though this volumetric power density is nominally higher than for the planar cells at 1 M, a direct comparison is ambiguous at this stage since no attempt has been made to quantify and minimize the "overhead" volumes of supporting infrastructure (i.e. walls, substrates and fluid manifolds). Suffice it to state that the proof-of-concept three-dimensional cell with its uniquely scalable array architecture demonstrated an order of magnitude higher power output than the planar design.

4.2.4. Fuel utilization

The maximum coulombic single pass fuel utilization of the array cell is shown in Fig. 9B as a function of the logarithmic flow rate, and compared to planar cell operation (150 μm and 1 M). The array cell is capable of reaching higher fuel utilization levels than the planar cells due to its reduced relative inter-electrode spacing. The highest fuel utilization obtained by the array cell was 78%, which is remarkably high. In addition, at any given flow rate above 30 μL min^{-1}, the fuel utilization capability of the array cell was approximately one order of magnitude higher than for the planar cell. Practical operational characteristics were identified at 30 μL min^{-1}; at this flow rate, the array cell produced 6.6 mW at 0.5 V combined with 43% single pass fuel utilization. Fuel-efficient array cell operation at low-

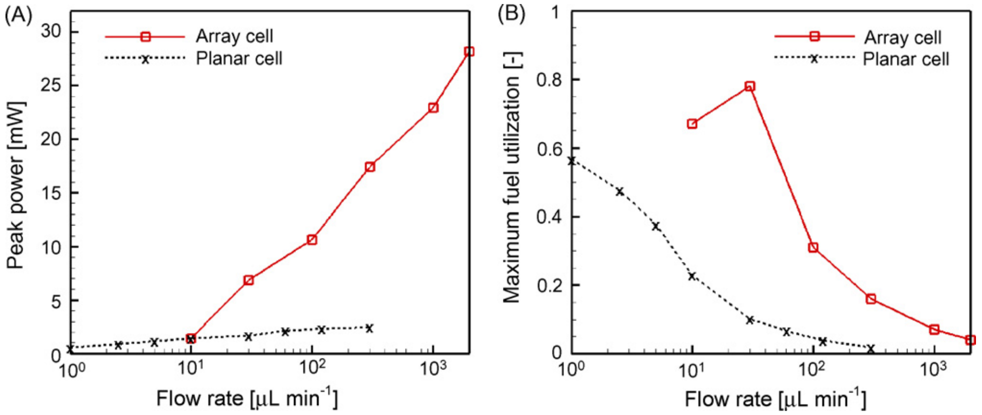

Fig. 9. Peak power (A) and maximum fuel utilization (B) determined experimentally for array cell operation using 0.64 M vanadium concentrations, compared to that of the planar cell with 1 M vanadium concentrations and 150 μm channel height. The data are plotted vs. the logarithm of the flow rate per stream.

range flow rates is a key finding for future research in this field: as microfluidic fuel cell technology transitions from proof-of-concept planar cell structures to integrated three-dimensional architectures with multiple cells, fuel utilization becomes an increasingly important parameter.

5. Conclusions

New membraneless microfluidic fuel cell designs were demonstrated based on graphite rod electrodes. Low-cost graphite rods, available as mechanical pencil refills, provided both reaction sites and current collectors for the combined all-vanadium fuel and oxidant system without additional catalyst requirements. Planar single cells, comparable to existing fuel cell designs, were manufactured and evaluated experimentally to confirm the viability of the proposed graphite rod electrodes. Planar cell operation was demonstrated for flow rates spanning four orders of magnitude with a maximum power density of $35\,\mathrm{mW\,cm^{-2}}$. Empirical transport analysis verified that the performance was primarily restricted by convective/diffusive transport from the bulk. Particularly effective planar cell operation was shown at low flow rates, achieving unprecedented levels of fuel utilization up to 63% per single pass.

Unlike film-deposited electrodes, graphite rod electrodes enable unique three-dimensional array cell integration. Our proof-of-concept three-dimensional microfluidic fuel cell architecture, based on a hexagonal array of graphite rods, produced an order of magnitude more power than the planar cell at similar flow rates. Furthermore, highly efficient array cell operation was demonstrated at low to moderate flow rates, achieving even higher fuel utilization than the planar cell. The array cell, with multiple anodes and cathodes, provides great power conditioning flexibility in series and/or parallel configurations, as well as unique scalability by vertical expansion without additional fluid manifold requirements or performance loss. We expect that fuel cell performance would further benefit from increasing the concentration and purity level of both supporting electrolyte and vanadium redox species, and by optimizing the rod diameter and characteristic spacing of the array cell.

Acknowledgments

The funding for this research provided by a Natural Sciences and Engineering Research Council (NSERC) strategic grant and by Angstrom Power Inc. is highly appreciated. The authors would also like to thank Dr. Clive Brereton and Evan Hobenshield at NORAM Engineering and Constructors Ltd. for experimental support.

References

[1] C.K. Dyer, J. Power Sources 106 (2002) 31–34.

[2] G. McLean, N. Djilali, M. Whale, T. Niet, 10th Canadian Hydrogen Conference, Quebec City, QC, Canada, 2000.

[3] N.T. Nguyen, S.H. Chan, J. Micromech. Microeng. 16 (2006) R1–R12.

[4] E. Kjeang, J. Goldak, M.R. Golriz, J. Gu, D. James, K. Kordesch, Fuel Cells 5 (2005) 486–498.

[5] G.Q. Lu, C.Y. Wang, T.J. Yen, X. Zhang, Electrochim. Acta 49 (2004) 821–828.

[6] S. Wasmus, A. Kuver, J. Electroanal. Chem. 461 (1999) 14–31.

[7] A. Bazylak, D. Sinton, N. Djilali, J. Power Sources 143 (2005) 57–66.

[8] R.F. Ismagilov, A.D. Stroock, P.J.A. Kenis, G. Whitesides, H.A. Stone, Appl. Phys. Lett. 76 (2000) 2376–2378.

[9] S. Litster, D. Sinton, N. Djilali, J. Power Sources 154 (2006) 95–105.

[10] E.R. Choban, J.S. Spendelow, L. Gancs, A. Wieckowski, P.J.A. Kenis, Electrochim. Acta 50 (2005) 5390–5398.

[11] R. Ferrigno, A.D. Stroock, T.D. Clark, M. Mayer, G.M. Whitesides, J. Am. Chem. Soc. 124 (2002) 12930–12931.

[12] E.R. Choban, L.J. Markoski, A. Wieckowski, P.J.A. Kenis, J. Power Sources 128 (2004) 54–60.

[13] J.L. Cohen, D.A. Westly, A. Pechenik, H.D. Abruna, J. Power Sources 139 (2005) 96–105.

[14] R.S. Jayashree, L. Gancs, E.R. Choban, A. Primak, D. Natarajan, L.J. Markoski, P.J.A. Kenis, J. Am. Chem. Soc. 127 (2005) 16758–16759.

[15] E.R. Choban, P. Waszczuk, P.J.A. Kenis, Electrochem. Solid State Lett. 8 (2005) A348–A352.

[16] R.S. Jayashree, D. Egas, J.S. Spendelow, D. Natarajan, L.J. Markoski, P.J.A. Kenis, Electrochem. Solid State Lett. 9 (2006) A252–A256.

[17] J.L. Cohen, D.J. Volpe, D.A. Westly, A. Pechenik, H.D. Abruna, Langmuir 21 (2005) 3544–3550.

[18] S.M. Mitrovski, L.C.C. Elliott, R.G. Nuzzo, Langmuir 20 (2004) 6974–6976.

[19] S.M. Mitrovski, R.G. Nuzzo, Lab Chip 6 (2006) 353–361.

[20] S. Hasegawa, K. Shimotani, K. Kishi, H. Watanabe, Electrochem. Solid State Lett. 8 (2005) A119–A121.

[21] M.H. Chang, F. Chen, N.S. Fang, J. Power Sources 159 (2006) 810–816.

[22] M. Rychcik, M. Skyllaskazacos, J. Power Sources 22 (1988) 59–67.

[23] M. Skyllaskazacos, F. Grossmith, J. Electrochem. Soc. 134 (1987) 2950–2953.

[24] W. SkyllasKazacos, C. Menictas, M. Kazacos, J. Electrochem. Soc. 143 (1996) L86–L88.

[25] W.R. Merida, G. McLean, N. Djilali, J. Power Sources 102 (2001) 178–185.

[26] D.C. Duffy, J.C. McDonald, O.J.A. Schueller, G.M. Whitesides, Anal. Chem. 70 (1998) 4974–4984.

[27] J.T. Coleman, J. McKechnie, D. Sinton, Lab Chip 6 (2006) 1033–1039.

[28] R.F. Probstein, Physicochemical Hydrodynamics—An Introduction, John Wiley and Sons, Inc., Hoboken, NJ, 2003.

[29] E. Kjeang, B. Roesch, J. McKechnie, D.A. Harrington, N. Djilali, D. Sinton, Microfluid. Nanofluid., doi:10.1007/s10404-006-0128-1.

[30] D.R. Lide (Ed.), CRC Handbook of Chemistry and Physics, 83rd ed., CRC Press, Boca Raton, FL, 2002.

[31] J. Newman, K.E. Thomas-Alyea, Electrochemical Systems, third ed., John Wiley & Sons, Inc., Hoboken, NJ, 2004.

[32] E. Kjeang, D. Sinton, D.A. Harrington, J. Power Sources 158 (2006) 1–12.

Appendix D

High-Performance Microfluidic Vanadium Redox Fuel Cell

Reproduced by permission of Elsevier

Available online at www.sciencedirect.com
ScienceDirect
ELSEVIER
Electrochimica Acta 52 (2007) 4942–4946
ELECTROCHIMICA Acta
www.elsevier.com/locate/electacta

High-performance microfluidic vanadium redox fuel cell

Erik Kjeang [a,c], Brenton T. Proctor [a,c], Alexandre G. Brolo [b,c],
David A. Harrington [b,c], Ned Djilali [a,c], David Sinton [a,c,*]

[a] Department of Mechanical Engineering, University of Victoria, 3800 Finnerty Road, Victoria, BC V8W2Y2, Canada
[b] Department of Chemistry, University of Victoria, 3800 Finnerty Road, Victoria, BC V8W2Y2, Canada
[c] Institute for Integrated Energy Systems (IESVic), University of Victoria, 3800 Finnerty Road, Victoria, BC V8W2Y2, Canada

Received 13 October 2006; received in revised form 23 January 2007; accepted 24 January 2007

Abstract

We demonstrate a new microfluidic fuel cell design with high-surface area porous carbon electrodes and high aspect ratio channel, using soluble vanadium redox species as fuel and oxidant. The device exhibits a peak power density of 70 mW cm^{-2} at room temperature. In addition, low flow rate operation is demonstrated and single pass fuel utilization levels up to 55% are achieved. The proposed design facilitates cost-effective and rapid fabrication, and would be applicable to most microfluidic fuel cell architectures.

Keywords: Microfluidic fuel cell; Membraneless fuel cell; Laminar flow-based fuel cell; Vanadium redox couple; Microstructured electrodes

1. Introduction

Microstructured fuel cells [1] are considered the most promising technology capable of facilitating the next generation of portable power supplies. These devices benefit from the increased surface-to-volume ratio accompanying miniaturization. Recently developed microfluidic fuel cells, or laminar flow-based fuel cells, exploit the laminar nature of microscale flows to maintain the separation of fuel and oxidant streams flowing side-by-side (Fig. 1). The anolyte and catholyte are also good ionic conductors, thereby eliminating the need for a separate electrolyte. Mixing of the two streams occurs by transverse diffusion only, and is restricted to an interfacial width at the center of the channel. The inter-diffusion zone at a co-laminar flow interface has an hourglass shape, with maximum width (δ_x) at the channel walls, scaling as the cube root of diffusion coefficient (D), channel height (H), downstream position (z) and inverse mean velocity (U) [2]:

$$\delta_x \propto \left(\frac{DHz}{U}\right)^{1/3} \quad (1)$$

The co-laminar configuration offers a wide range of benefits: fuel and oxidant streams may be combined in a single manifold; no ion exchange membrane is needed; sealing and manifolding as well as fluid delivery requirements are reduced; and issues related to fuel crossover and water management are eliminated.

The first microfluidic fuel cell was presented by Choban et al. [3], followed by proof-of-concept devices based on vanadium redox couples [4], formic acid [5–7], methanol [8–10], hydrogen peroxide [11], and hydrogen [12–14]. The power density of these cells was predominantly limited by the rate of mass transport to the active sites [15]. For cells using formic acid and methanol, peak power (5 mW cm^{-2}) [9] was primarily restricted by low solubility of oxygen in the cathode stream. Jayashree et al. [7] addressed this limitation by incorporating an air-breathing cathode that allowed gaseous oxygen transport from the ambient air, thus achieving considerably higher power output (26 mW cm^{-2}). Vanadium redox couples are a promising alternative that enable improved power density as well as regeneration of fuel and oxidant [4]. Vanadium redox fuel cells utilize two soluble vanadium redox couples, V^{2+}/V^{3+} and VO^{2+}/VO_2^+, as anolyte and catholyte, respectively, providing a balanced electrochemical system in terms of species transport characteristics and reaction rates. Benefits include: the aqueous fuel and oxidant combination is soluble at relatively high concentrations up to 5.4 M [16]; precious-metal electrocatalysts (such as Pt and Pd) are not required; the reactions do not evolve gaseous

---

* Corresponding author. Tel.: +1 250 721 8623; fax: +1 250 721 6051.
E-mail address: dsinton@me.uvic.ca (D. Sinton).

0013-4686/$ – see front matter © 2007 Elsevier Ltd. All rights reserved.
doi:10.1016/j.electacta.2007.01.062

products; and a relatively high open-circuit voltage (∼1.5 V) can be obtained at uniform pH. Ferrigno et al. [4] reported a maximum power density of 38 mW cm^{-2} with 1 M vanadium solutions in 25% sulfuric acid flowing at 1.5 mL min^{-1} per stream over Au-supported carbon electrodes. This is the highest power density of a microfluidic fuel cell previously reported.

Fuel utilization, a critical measure of overall fuel cell performance, has been low for most microfluidic fuel cells (frequently less than 1%) [5,6,12], usually restricted by geometrical constraints and the use of high flow rates. In this paper, we present a new microfluidic fuel cell design employing porous carbon electrodes with high-surface area, high aspect ratio (width/height) channel geometry, and vanadium redox couples with relatively high concentration as fuel and oxidant. We demonstrate how the porous electrode material improves mass transport to the active sites and therefore generates higher current density than planar electrodes at high flow rates. We also investigate the feasibility of operation in the low flow rate regime, where the high aspect ratio comes into play, in order to improve fuel utilization.

2. Methods

2.1. Microfabrication

The microfluidic vanadium redox fuel cell, shown schematically in Fig. 1, was assembled using in-house microfabrication techniques. The base substrate was patterned with carbon strip electrodes according to the following procedure: a 2 in. × 3 in. microscope glass slide was coated with 1 mm polyurethane (PMC-790; Smooth-On Inc., Easton, PA) and cured for a few hours on a hot plate at 65 °C to solidify. High-surface area porous carbon electrodes were cut to size (40 mm long and 400 μm wide) from sheets of Toray carbon paper (B-2 Designation TGPH-090; E-TEK, Somerset, NJ) with typical thickness 260 μm, typical density 0.49 g cm^{-3} and 78% porosity. The carbon strips were fitted in a custom-made aluminum holder with grooves that uniformly separate the bands by 1.2 mm and hold them in place. The holder was sprayed with universal mold release (Smooth-On Inc., Easton, PA) before use. The polyurethane substrate was placed in a different aluminum holder and heated to 160 °C on a hot plate. When fully heated, the two aluminum plates were mechanically pressed together to fuse the carbon strips into the softened polyurethane layer. The assembly was removed from the hot plate with the pressure still applied, and allowed to cool down. The aluminum plates were then removed, leaving the carbon electrodes embossed in the hardened polyurethane layer. Wires were attached to the end of the carbon electrodes using conductive epoxy (Circuit Works CW2400; ITW Chemtronics, Kennesaw, GA).

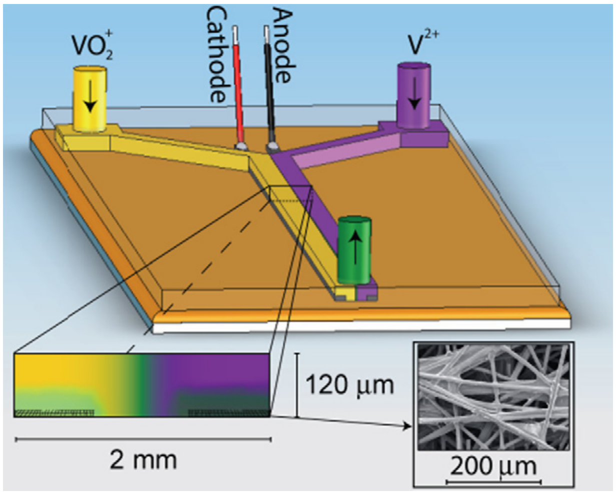

Fig. 1. Schematic of the microfluidic vanadium redox fuel cell with high-surface area porous carbon electrodes. Aqueous vanadium redox species are employed as fuel (V^{2+}: purple) and oxidant (VO_2^+: yellow). The solution colours shown are representative of the employed solutions.

The top part of the fuel cell, containing the Y-shaped 120 μm high and 2 mm wide microchannel, was fabricated by replica molding in poly(dimethylsiloxane) (PDMS; Dow Corning, Midland, MI) following established soft-lithographic protocols [17], and specifics described elsewhere [18]. In short, a 120 μm high master that defines the channel pattern was created by photolithography in negative photoresist (SU-8 50; Microchem, Newton, MA). This structure was cast into a slab of PDMS, which was peeled off the master after curing. Inlet/outlet holes were punched in the PDMS before assembly. The PDMS slab was placed over the polyurethane substrate and the two were aligned precisely under a microscope. While operating the cell, a reversible seal was accomplished by pressing the two parts together with an aluminum clamp. This type of bond allows cleaning of the cell and substitution of the channel structure, such that the substrate may be re-used after each trial. Alternatively, an irreversible seal that does not require clamping can be obtained by plasma-treating the PDMS, which renders hydrophilic channel walls and facilitates covalent binding to the substrate. The electrodes of the assembled fuel cell had a geometrical active area of 0.108 cm^2 (400 μm width and 27 mm active length).

Overall, the described fabrication procedure is rapid and economical. An array of fuel cells can be fabricated in less than 4 h with a total material cost of US$ 3 per cell.

2.2. Preparation of vanadium solutions

Fresh 2 M sulfuric acid supporting electrolyte solution was prepared from Millipore Milli-Q water (Millipore, Billerica, MA) and concentrated sulfuric acid (EMD Chemicals Inc., Gibbstown, NJ). Vanadium sulfate oxide hydrate ($VOSO_4 \cdot XH_2O$; Alfa Aesar, Ward Hill, MA) was dissolved in the supporting electroyte by sonication at 50 °C until a clear blue VO^{2+}-solution of concentration 2 M was obtained.

A large-scale electrolytic flow cell with 4 in. × 6 in. carbon felt electrodes separated by a Nafion membrane was used to generate the required V^{2+} and VO_2^+ solutions. The VO^{2+}-solution was divided into three equal parts by volume: one part (200 mL) was transferred to the positive half-cell and two parts (400 mL) were poured into the negative half-cell. The negative half-cell was continuously purged with nitrogen, given the instability of the V^{2+} solution in contact with air. The solutions were pumped through the cell while applying a fixed current density of 65 mA cm^{-2} (10 A). The cell voltage was 1.5–1.7 V while charging. Charging of the solutions was complete after 50 min when the cell voltage quickly rose above 2.0 V, which was also confirmed by the sudden color change in the two compartments. The fully charged purple V^{2+} solution and yellow VO_2^+ solution were removed and stored under a nitrogen blanket in air-tight bottles. The current efficiency during charging was calculated to be 99.7%. No hydrogen or oxygen bubbles were produced during the experiment, attributed to the use of carbon electrodes.

The vanadium solutions can be regenerated from the solution collected at the outlet reservoir of the fuel cell (normally a 50/50 mixture of V^{3+} and VO^{2+} when stabilized) by pouring equal parts into the positive and negative half cells and repeating the charging procedure.

2.3. Fuel cell diagnostics

Steady pressure-driven co-laminar flow of vanadium solutions through the fuel cell was driven by a syringe pump (PHD 2000; Harvard Apparatus, Holliston, MA) via Tygon flexible tubing. Polarization data were obtained by stepwise potentiostatic chronoamperometry from 0.0 V to the open circuit voltage by 0.1 V increments, using a PARSTAT 2263 potentiostat (Princeton Applied Research, Oak Ridge, TN). The cell current was monitored until steady state was reached, which usually occurred within 180 s. Current densities are based on the geometrical active area of the electrodes ($0.108\,\mathrm{cm}^2$).

The combined ohmic resistance of the fuel cell and the overall active surface area of the electrodes were evaluated by electrochemical impedance spectroscopy (EIS) using the same potentiostat. An ac amplitude of 5 mV rms was applied over the frequency range from 50 kHz to 0.1 Hz. Impedance spectra were recorded at three different flow rates (10, 60 and 300 $\mu\mathrm{L\,min}^{-1}$; Re = 0.4, 2 and 10), each one at three different cell voltages (0.0, 0.5 and 1.2 V). The ohmic cell resistance was measured as the high-frequency real axis intercept of the Nyquist plot of impedance. Each impedance spectrum was fitted to the conventional equivalent circuit with a solution resistance in series with a parallel combination of a CPE-element and a charge-transfer resistor. The double-layer capacitance was extracted from the CPE parameters and the resistances using the procedure developed by Brug et al. [19]. The overall active surface area of the electrodes was calculated assuming a capacitance of $7\,\mu\mathrm{F\,cm}^{-2}$ for a flat surface, which is typical for activated carbon fibers in sulfuric acid electrolyte [20]. All measurements were averaged from the nine impedance spectra.

3. Results and discussion

3.1. Theoretical open-circuit voltage

The vanadium redox reactions for the anodic and cathodic half-cells are [21]:

$$V^{2+} \rightleftharpoons V^{3+} + e^-, \quad E^\circ = -0.255\,\mathrm{V\ versus\ SHE}$$

$$VO_2^+ + 2H^+ + e^- \rightleftharpoons VO^{2+} + H_2O,$$
$$E^\circ = 0.991\,\mathrm{V\ versus\ SHE}$$

The overall cell reaction has a theoretical standard cell potential of 1.246 V at 298 K. Samples of the V^{2+} and VO_2^+ solutions were characterized individually in a three-electrode electrochemical cell with a graphite rod working electrode. The measured open-circuit potentials were 1.192 and −0.309 V (versus SHE), respectively. Assuming that the open-circuit potentials are reversible potentials, their departure from the standard potentials is related to the solution concentrations by the Nernst equation:

$$E = E^\circ - \frac{RT}{nF} \ln\left(\frac{a_{\mathrm{red}}}{a_{\mathrm{ox}}}\right) \tag{2}$$

Here, $T = 298\,\mathrm{K}$, $n = 1$ for both redox pairs, and a is the activity. We assume equal activity coefficients for the redox species and $a_{H+} = 2$ equal activity coefficients, the activity ratio can be approximated by the redox concentration ratio. In our case, the redox concentrations are highly biased (99.8% VO_2^+/0.2% VO^{2+} and 89% V^{2+}/11% V^{3+}), thereby increasing the theoretical cell potential to 1.50 V. The cell potential can be increased beyond 1.50 V by the use of high-purity vanadium solutions, e.g., Ferrigno et al. [4] achieved 1.67 V with approximately 99.9% VO_2^+/0.1% VO^{2+} and 99.9% V^{2+}/0.1% V^{3+} solutions at 1 M.

3.2. Polarization

Fuel cell performance was evaluated using 2 M vanadium in 2 M H_2SO_4. Polarization data were obtained at steady-state under potentiostatic control. Repetitive trials were performed with an average standard deviation of 2%. We were also able to reproduce the polarization data using galvanostatic control, indicating that the same internal conditions are established independently of the control method. Moreover, the results presented here were reproducible within 20%, on different days with different cells and solutions. The polarization curves in Fig. 2a show operation of the fuel cell at flow rates spanning four orders of magnitude. The fuel cell had an open-circuit voltage (OCV) ranging from 1.25 to 1.38 V, obtained at 1 and 60 $\mu\mathrm{L\,min}^{-1}$, respectively. These OCVs are 83% and 92% of the theoretical OCV of 1.50 V, determined by separate characterization of anolyte and catholyte in a three-electrode electrochemical cell. The polarization data show that current density increases with flow rate, which indicates that mass transport limitations are significant and that the electrochemical redox reactions are relatively fast. On the other hand, the change to more negative slopes at higher current densities typically associated with diffusion control was not observed, which indicates kinetic or mixed control. Current densities up to $243\,\mathrm{mA\,cm}^{-2}$ were generated at the highest flow rate.

A combined ohmic resistance of 9 Ω on average was determined by electrochemical impedance spectroscopy, including the effects of in-channel ionic resistance plus electrical resistance in electrodes, contacts and wires. Ferrigno et al. [4] reported an internal resistance of only 3 Ω under similar geometrical conditions. This low ohmic resistance, compared to our case, is attributed to the use of stronger supporting electrolyte (25% H_2SO_4) and the integration of highly conductive current collectors (Au). The performance of our fuel cell design

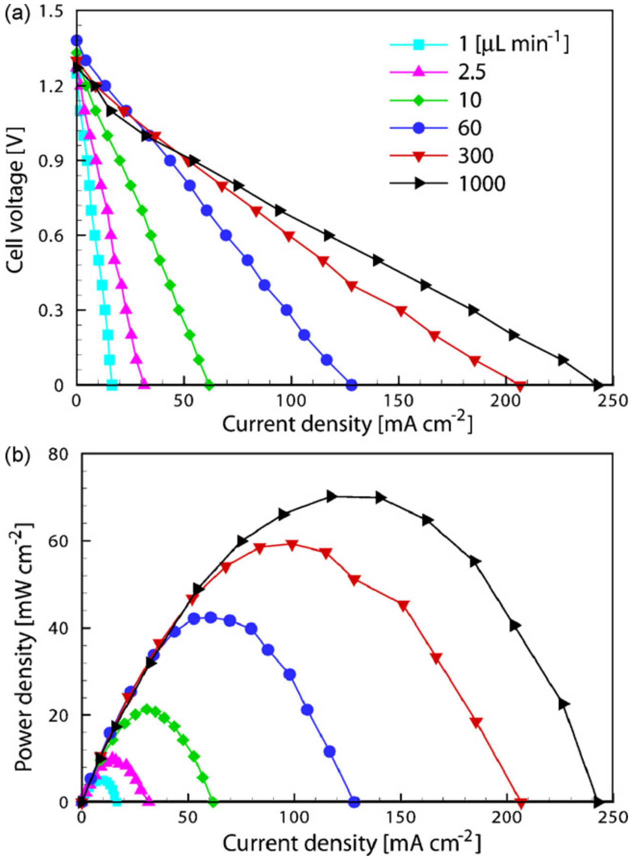

Fig. 2. Measured polarizarion (a) and power density (b) curves for the microfluidic fuel cell employing 2 M vanadium solutions at room temperature and flow rates as indicated.

becomes partially hindered by its relatively high ohmic resistance, in particular at high current densities, where the IR-drop is large (e.g. ∼200 mV at 200 mA cm^{-2}). It is noteworthy, however, that the slopes of the polarization curves are still a factor of 5 or more away from pure ohmic control.

3.3. Power density

Fig. 2b presents power density curves based on the polarization data. The maximum power density increases substantially with flow rate, confirming that the performance is partially controlled by the rate of convective transport. The highest power density observed was 70 mW cm^{-2}, at 0.6 V and 1000 µL min^{-1} flow rate. This level of peak power density is higher than previous vanadium redox fuel cells [4] and air-breathing fuel cells [7,10], and an order of magnitude higher than dissolved oxygen-based fuel cells [3,5,6,8,9,12]. Operation of the fuel cell at flow rates above 1000 µL min^{-1} is impractical, as the limited gain in power density cannot justify the declining fuel utilization. In order to evaluate the benefit associated with the high-surface area porous carbon electrodes, we fabricated an otherwise similar fuel cell with planar graphite electrodes. A comparison at 300 µL min^{-1} revealed that the porous electrodes generated a 72% higher peak power density (59 mW cm^{-2}) than the planar electrodes (35 mW cm^{-2}) under similar conditions. On the other hand, the peak power densities generated by the porous and planar electrode configurations are *approximately equal* at low flow rates: at 2.5 µL min^{-1}, both configurations produced 10 mW cm^{-2}. In the low flow rate regime, the power generated by the fuel cell is primarily controlled by transport from the bulk fluid. Complete depletion occurs at the electrodes and the concentration boundary layer thickness is on the order of the channel height, independent of electrode structure and porosity. At medium to high flow rates, however, fuel cell performance is controlled by a combination of factors including convective/diffusive transport, electrochemical kinetics, ohmic resistance, and active area. A theoretical estimate of the total active area of the porous electrodes was obtained through idealization of the structure as a repeatable 3D network of fibers. For 10 µm diameter fibers, 78% porosity and 260 µm thickness, the average fiber spacing becomes 36 µm, leading to an overall surface area 23 times larger than the planar area. The active surface area was also calculated from impedance data according to the method described in Section 2.3, and found to be 27 times the planar area, in good agreement with the theoretical estimate. Moreover, for fluid flow over fibrous media with comparatively large hollow spaces and large average fiber spacing (Fig. 1), the no-slip condition at the fluid/structure interface does generally not apply, as shown both analytically [22,23] and experimentally [24]. An effective slip velocity exists at the interface, accompanied by a small parallel drift velocity profile inside the top portion of the porous medium. The magnitude of the drift velocity and its penetration depth both depend on the permeability of the material and the mean velocity in the channel. For fuel cell operation, this effect contributes favorably to the replenishment of the concentration boundary layer and overall rates of convective/diffusive transport to the active sites. In summary, the improved performance of the porous carbon electrodes over the planar electrode design here and other microfluidic fuel cell designs [3–14] is dominated by an order of magnitude higher active surface area combined with enhanced transport characteristics. The rate at which the power density increases with flow rate for the porous electrode design compared to the planar design illustrates that the combination of strong convective transport and high-porosity electrodes is particularly attractive for microfluidic fuel cells.

3.4. Fuel utilization

The geometry of the cell is well suited to achieve high fuel utilization at low flow rates. Specifically, the mixing interface is perpendicular to the electrode surfaces, and the high aspect ratio ensures the electrode area is large compared to that of the mixing interface [25]. The maximum Coulombic fuel utilization per single pass and peak power densities obtained experimentally are plotted together in Fig. 3 as a function of flow rate. As the flow rate is reduced, fuel utilization increases with a corresponding decrease in peak power density. Balanced performance, in terms of both power density and fuel utilization, is achieved at low to moderate flow rates. The highest fuel utilization measured here was 55% (at 1 µL min^{-1}), which compares favorably to previous vanadium cells (≤10%) [4], air-breathing cells (≤33%) [7], and dissolved oxygen-based cells (≤15%) [8]. At this low

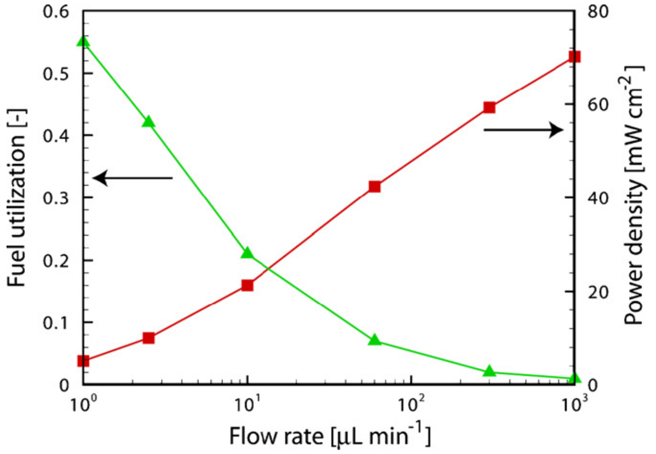

Fig. 3. Maximum fuel utilization per single pass (green line) and peak power density (red line) obtained experimentally at room temperature as a function of (logarithmic) flow rate per stream.

flow rate, broadening of the mixed region over the electrodes resulted in a reduced OCV (1.25 V), and operation at flow rates below 1 μL min^{-1} proved impractical due to this effect. The drop in OCV experienced experimentally at the limiting flow rate indicates that the inter-diffusion width was on the order of the inter-electrode spacing (1.2 mm). The ability to reach fuel utilization up to 55%, although the electrodes only cover 40% of the substrate surface under the channel (Fig. 1), indicates that favorable transverse diffusion of reactants takes place within the channel. Operation of the fuel cell at low flow rates thus involves two types of transverse diffusion effects: (i) useful transport of reactant from the center of the channel to the electrodes and (ii) unfavorable broadening of the inter-diffusion zone.

4. Conclusions

This work demonstrated a microfluidic vanadium redox fuel cell employing porous electrodes with high active surface area. Operation at high flow rate resulted in a peak power density of 70 mW cm^{-2} and operation at low flow rate resulted in a maximum fuel utilization of 55%. The described microfluidic fuel cells are fabricated by rapid and inexpensive microfabrication methods, and do not require expensive materials such as platinum and gold. We expect performance would further benefit from increasing the concentration and purity level of both supporting electrolyte and vanadium redox species, incorporating highly conductive current collectors, and optimizing the porosity of the carbon electrodes. We project that the integration of similar high-surface area electrodes or catalyst supports would boost the performance of most other microfluidic fuel cell architectures as well. In particular, the integration of electrode features of characteristic scale 10–100 μm, about one order of magnitude smaller than the channel dimensions, enables substantially increased active area combined with enhanced transport characteristics, which delays otherwise commonly encountered transport limitations.

Acknowledgments

Funding for this research was provided by the Natural Sciences and Engineering Research Council of Canada (NSERC) and Angstrom Power Inc. The authors thank Dr. Clive Brereton and Evan Hobenshield at NORAM Engineering and Constructors Ltd. for experimental assistance.

References

[1] G. McLean, N. Djilali, M. Whale, T. Niet, Proceedings of the 10th Canadian Hydrogen Conference, Quebec City, 2000.
[2] R.F. Ismagilov, A.D. Stroock, P.J.A. Kenis, G. Whitesides, Appl. Phys. Lett. 76 (2000) 2376.
[3] E.R. Choban, L.J. Markoski, J. Stoltzfus, J.S. Moore, P.A. Kenis, Power Sources Process. 40 (2002) 317.
[4] R. Ferrigno, A.D. Stroock, T.D. Clark, M. Mayer, G.M. Whitesides, J. Am. Chem. Soc. 124 (2002) 12930.
[5] E.R. Choban, L.J. Markoski, A. Wieckowski, P.J.A. Kenis, J. Power Sources 128 (2004) 54.
[6] J.L. Cohen, D.A. Westly, A. Pechenik, H.D. Abruna, J. Power Sources 139 (2005) 96.
[7] R.S. Jayashree, L. Gancs, E.R. Choban, A. Primak, D. Natarajan, L.J. Markoski, P.J.A. Kenis, J. Am. Chem. Soc. 127 (2005) 16758.
[8] E.R. Choban, P. Waszczuk, P.J.A. Kenis, Electrochem. Solid-State Lett. 8 (2005) A348.
[9] E.R. Choban, J.S. Spendelow, L. Gancs, A. Wieckowski, P.J.A. Kenis, Electrochim. Acta 50 (2005) 5390.
[10] R.S. Jayashree, D. Egas, J.S. Spendelow, D. Natarajan, L.J. Markoski, P.J.A. Kenis, Electrochem. Solid-State Lett. 9 (2006) A252.
[11] S. Hasegawa, K. Shimotani, K. Kishi, H. Watanabe, Electrochem. Solid-State Lett. 8 (2005) A119.
[12] J.L. Cohen, D.J. Volpe, D.A. Westly, A. Pechenik, H.D. Abruna, Langmuir 21 (2005) 3544.
[13] S.M. Mitrovski, L.C.C. Elliott, R.G. Nuzzo, Langmuir 20 (2004) 6974.
[14] S.M. Mitrovski, R.G. Nuzzo, Lab Chip 6 (2006) 353.
[15] M.-H. Chang, F. Chen, N.-S. Fang, J. Power Sources 159 (2006) 810.
[16] M. Skyllas-Kazacos, C. Menictas, M.J. Kazacos, J. Electrochem. Soc. 143 (1996) L86.
[17] D.C. Duffy, J.C. McDonald, O.J.A. Schueller, G.M. Whitesides, Anal. Chem. 70 (1998) 4974.
[18] J.T. Coleman, J. McKechnie, D. Sinton, Lab Chip 6 (2006) 1033.
[19] G.J. Brug, A.L.G. Van den Eeden, M. Sluyters-Rehbach, J.H. Sluyters, J. Electroanal. Chem. 176 (1984) 275.
[20] Y. Soneda, M. Toyoda, K. Hashiya, J. Yamashita, M. Kodama, H. Hatori, M. Inagaki, Carbon 41 (2003) 2653.
[21] D.R. Lide (Ed.), CRC Handbook of Chemistry and Physics, 83rd ed., CRC Press, Boca Raton, FL, 2002.
[22] D.F. James, A.M.J. Davis, J. Fluid Mech. 426 (2001) 47.
[23] A.V. Kuznetsov, Appl. Sci. Res. 56 (1996) 53.
[24] M.F. Tachie, D.F. James, I.G. Currie, J. Fluid Mech. 493 (2003) 319.
[25] A. Bazylak, D. Sinton, N. Djilali, J. Power Sources 143 (2005) 57.

Appendix E

A Microfluidic Fuel Cell with Flow-Through Porous Electrodes

A Microfluidic Fuel Cell with Flow-Through Porous Electrodes

Erik Kjeang,[a] *Raphaelle Michel,*[a] *David Harrington,*[b] *Ned Djilali,*[a] *and David Sinton,*[a,]*.

[a] Department of Mechanical Engineering, [b]Department of Chemistry, and Institute for Integrated Energy Systems (IESVic), University of Victoria, 3800 Finnerty Road, Victoria, BC, V8W2Y2, Canada
* dsinton@me.uvic.ca

RECEIVED DATE (to be automatically inserted after your manuscript is accepted if required according to the journal that you are submitting your paper to)

Abstract: A microfluidic fuel cell architecture incorporating flow-through porous electrodes is demonstrated. The design is based on cross-flow of aqueous vanadium redox species through the electrodes into an orthogonally arranged co-laminar exit channel, where the waste solutions provide ionic charge transfer in a membraneless configuration. This flow-through architecture enables utilization of the three-dimensional active area inside the porous electrodes and provides enhanced rates of convective/diffusive transport without increasing the parasitic loss required to drive the flow. Prototype fuel cells are fabricated by rapid prototyping with total material cost estimated at 2 USD/unit. Improved performance as compared to previous microfluidic fuel cells is demonstrated, including power densities at room temperature up to 131 mW cm^{-2}. In addition, high overall energy conversion efficiency is obtained as relatively high levels of fuel utilization and cell voltage are achieved concurrently. When operated at 1 μL min^{-1} flow rate, the fuel cell produced 20 mW cm^{-2} at 0.8 V combined with an active fuel utilization of 94%. Finally, we demonstrate in situ fuel and oxidant regeneration by running the flow-through architecture fuel cell in reverse.

Keywords: Microfluidic fuel cell; membraneless fuel cell; laminar flow-based fuel cell; vanadium redox couple; flow-through electrode; porous electrode

1. Introduction

The high energy density demand in portable applications is making microstructured fuel cells an increasingly attractive technology.[1] Microfluidic fuel cells,[2-17] or laminar flow-based fuel cells, represent a relatively new type of small scale fuel cell technology based on inexpensive microfabrication methods and low-cost materials. A microfluidic fuel cell is defined as a device that incorporates all fundamental components of a fuel cell to a single microfluidic channel and its walls. These fuel cells operate without a membrane, and the most common configurations rely on the laminar nature of microscale flows to maintain sufficient separation of fuel and oxidant streams. Ionic charge transfer is facilitated by a supporting electrolyte contained in the co-laminar streams. Inter-diffusion is restricted to an interfacial width at the center of the channel, and the electrodes are positioned sufficiently far away from this inter-diffusion zone to prevent crossover effects. Microfluidic fuel cells provide a number of unique advantages: fuel and oxidant streams may be combined in a single microchannel; no ion exchange membrane is needed; sealing, manifolding, and fluid delivery requirements are reduced; and issues related to membrane hydration and water management are eliminated.

Microfluidic fuel cell devices have been demonstrated based on a number of fuels, including vanadium ions,[9,14,15] formic acid,[4,8,12,13] methanol,[5,6,11] hydrogen, [7,16,17] and hydrogen peroxide,[10] combined with oxidants such as vanadium ions,[9,14,15] oxygen,[4-8,11,12,16,17] or hydrogen peroxide.[10,13] The power densities of these cells were mainly restricted by the solubility of the reactants and the associated rate of convective/diffusive mass transport to the active sites.[3] Cell designs using oxygen have the benefit of ‘free’ oxidant available in the ambient air. Such air-breathing designs require a blank cathodic electrolyte stream and have shown moderate power densities. The highest power density levels of the microfluidic fuel cells reported to date were achieved using vanadium redox couples in both half-cells; V^{2+}/V^{3+} as anolyte and VO^{2+}/VO_2^+ as catholyte.[9,14,15] These vanadium redox fuel cells benefit from a rapid and balanced electrochemical system in terms of species transport characteristics and reaction rates, as well as a relatively high open-circuit voltage (~1.5 V). In addition, the vanadium redox reactions take place on carbon electrodes without any additional electrocatalyst and associated cost.

The capability of reaching high levels of fuel utilization per single pass has been a major challenge associated with microfluidic fuel cell technology to date.[2] In previous work,[14,15] we demonstrated that a high aspect ratio (width/height) cross-sectional channel geometry in combination with the all-liquid vanadium redox system enabled fuel utilization levels around 50% per single pass at low flow rates. Although an improvement over previous designs, fuel utilization was still limited by geometrical constraints, and high fuel utilization could only be achieved at low cell voltages. It was also demonstrated that incorporating porous electrodes[15] provided up to 72% higher power density than planar electrodes; an improvement attributed to the increased active area and the enhanced species transport characteristics resulting from some flow penetration within the porous medium. In order to reach practical energy conversion efficiency, however, it is necessary to sustain high levels of fuel utilization at high power densities, and perhaps more importantly, at high operational cell voltages.

Microfluidic fuel cells have additional characteristics that have yet to be exploited through fuel cell design. Specifically, the reactants, products and electrolyte are all in the same liquid phase, and the reaction zones are solid-liquid interfaces. These characteristics provide potential for a variety of three-dimensional fuel cell architectures. In this work, we present a microfluidic fuel cell incorporating flow-through porous electrodes that effect three-dimensional reaction zones. The proposed microfluidic fuel cell has two unique features: (i) hydrophilic electrode treatment that promotes saturation of the porous electrode, and thus increases the effective active area; and (ii) a three-dimensional flow-through architecture that improves utilization of the active area through enhanced transport.

2. Methods

2.1. Microfabrication

Microfluidic fuel cell prototypes of the flow-through electrode architecture as well as the established architecture[15] with electrodes mounted on the bottom of a co-laminar flow channel were assembled using in-house developed microfabrication techniques. The previously established architecture will be termed ‘flow-over’, to differentiate it from the ‘flow-through’ architecture developed through this work. The fabrication procedures for the two designs differ somewhat and are presented separately in the following subsections.

2.1.1. Flow-through architecture fuel cell

Porous carbon strip electrodes were cut to size (20 mm long and 1 mm wide) from sheets of Toray carbon paper (B-2 Designation TGPH-090; E-TEK, Somerset, NJ) with typical thickness 300 μm (measured), typical density 0.49 g cm^{-3} and 78% porosity. The carbon strips were rendered hydrophilic by annealing (~1 s) in a propane flame. The heat treated carbon strips were fitted in custom-sized grooves (20 mm x 1 mm x 300 μm, separated by 1 mm), fabricated by replica molding in poly(dimethylsiloxane) (PDMS; Dow Corning, Midland, MI) according to established soft-lithographic protocols.[18] A 300 μm high master that defines the two grooves plus the channel structure was created by photolithography in negative photoresist (SU-8 50; Microchem, Newton, MA). The master had a dual-layer structure. The first layer was 150 μm thick and encompassed all flow channels and electrode grooves. The second layer, which was also 150 μm thick and patterned on top of the first layer, included electrode grooves and the channel pattern from the inlets to the electrodes. Upon casting of this dual-layered master into PDMS, a negative imprint was obtained that accommodated both electrode grooves and complete fluid manifolding. As shown schematically in Figure 1a, the obtained PDMS part was placed face up on a 1” x 3” microscope glass slide for structural support, and the heat treated carbon strip electrodes were fitted in its grooves, thereby finalizing the bottom part of the fuel cell. The top of the cell was sealed with a flat layer of PDMS, with previously punched holes for the inlets, outlet, and electrical contacts. An irreversible seal was created by plasma-treating both PDMS parts, which renders hydrophilic channel walls and facilitates covalent binding upon assembly. The holes in the top PDMS part were aligned with the grooves of the bottom part during assembly of the final device (Figure 1a). The electrodes of the assembled fuel cell had an active volume of 0.3 mm x 1 mm x 12 mm (3.6 μL). Wires were attached to the exposed ends of the carbon electrodes using PELCO® conductive silver 187 (Ted Pella Inc., Redding, CA). The co-laminar flow of vanadium solutions through the fuel cell was driven by a syringe pump (PHD 2000; Harvard Apparatus, Holliston, MA) via Teflon® tubing (1/16” diameter; S.P.E. Limited, North York, ON, Canada) to the inlets and a larger Tygon® tube (3 mm diameter; Fisher Sci., Pittsburgh, PA) from the outlet to the outlet reservoir. The described fabrication procedure is relatively quick and economical. Excluding external wires and tubes, the fuel cell contained only PDMS and carbon paper, and the total estimated material cost is 2 USD per cell.

2.1.2. Flow-over architecture fuel cell

Fuel cells with the established flow-over architecture[15] were fabricated according to the procedure outlined in section 2.1.1, with the following modifications: The flow-over unit consisted of two parts. A bottom PDMS part contained the electrodes and a top PDMS part accommodated the microfluidic channel network. The bottom part was a PDMS slab with two custom-shaped grooves (20 mm x 1 mm x 300 μm) separated by 1 mm. The carbon strip electrodes were fitted into these grooves. The top part contained a T-shaped 150 μm high and 3 mm wide microchannel that was aligned with the carbon electrodes during assembly.

2.2. Preparation of vanadium solutions

Vanadium stock electrolyte was purchased from Highveld, South Africa, and received as 2 M vanadium redox species (50/50 V^{3+}/VO^{2+}) in 4 M sulfuric acid with proprietary stabilizing agents. The V^{2+} and VO_2^+ solutions used as anolyte and catholyte, respectively, were generated from the stock electrolyte in a large-scale electrolytic flow cell with carbon felt electrodes divided by a Nafion membrane, as previously described.[15]

2.3. Fuel cell diagnostics

Polarization data were measured after flow stabilization at a given flow rate by chronoamperometry under stepwise potentiostatic control from 0.0 V to the open circuit voltage by 0.2 V increments, using a PARSTAT 2263 potentiostat (Princeton Applied Research, Oak Ridge, TN). The current generated by the cell was monitored until steady state was reached (30-300 s, depending on the flow rate). Anodic and cathodic polarization were measured using the opposite in-channel carbon electrode as counter electrode and an external saturated calomel reference electrode (SCE) placed in the outlet reservoir. Due to the three-dimensional architecture, it is somewhat awkward to define an area with which to characterize the performance of the flow-through cell in terms of current density. Specifically, the flow-normal area of each electrode is 300 μm x 12mm (0.036 cm^2), while the vertically-projected area of each electrode is significantly larger (1 mm x 12 mm = 0.12 cm^2). Current densities and power densities reported here were calculated based on the larger, vertically-projected area of the electrodes.

The ohmic resistance of the fuel cell was measured by electrochemical impedance spectroscopy (EIS), using the same potentiostat. Impedance spectra were recorded for each flow rate at the open-circuit cell voltage, by applying an ac amplitude of 5 mV rms over the frequency range from 50 kHz to 0.1 Hz. The combined ohmic cell resistance was obtained from the high-frequency real axis intercept of the Nyquist plot of impedance.

3. Results and discussion

Microfluidic vanadium redox fuel cell operation is based on the following anodic and cathodic redox reactions and associated standard redox potentials at 298 K:[19]

$V^{3+} + e^- \leftrightarrow V^{2+}$ $E^\circ = -0.496$ V vs. SCE (1)

$VO_2^+ + 2H^+ + e^- \leftrightarrow VO^{2+} + H_2O$ $E^\circ = 0.750$ V vs. SCE (2)

The overall cell reaction has a theoretical standard cell potential of 1.246 V. The cell potential can however be increased beyond 1.50 V by the use of high-purity vanadium solutions.[9,15] The theoretical maximum current density of a microfluidic fuel cell is controlled by the rate of convective/diffusive transport of reactants and products in the liquid phase to and from the surface of the electrodes. In the limiting case, the concentration of reactant is zero at the surface, and a concentration boundary layer is formed in the channel that limits the flux of reactant to the surface depending on the flow characteristics. Overall fuel cell performance, usually measured by power density, is however influenced by other factors as well. In our previous study of microfluidic vanadium redox fuel cells with planar electrodes based on graphite rods,[14] it was found that the performance of the cell was controlled by a combination of species transport, electrochemical kinetics and ohmic resistance. Improved performance was enabled by the implementation of porous electrodes;[15] the overall electrochemical kinetics were improved by the increased active surface area, and the rate of species transport to the active sites was enhanced by a partial flow velocity inside the top portion of the porous medium, although the penetration depth was limited.

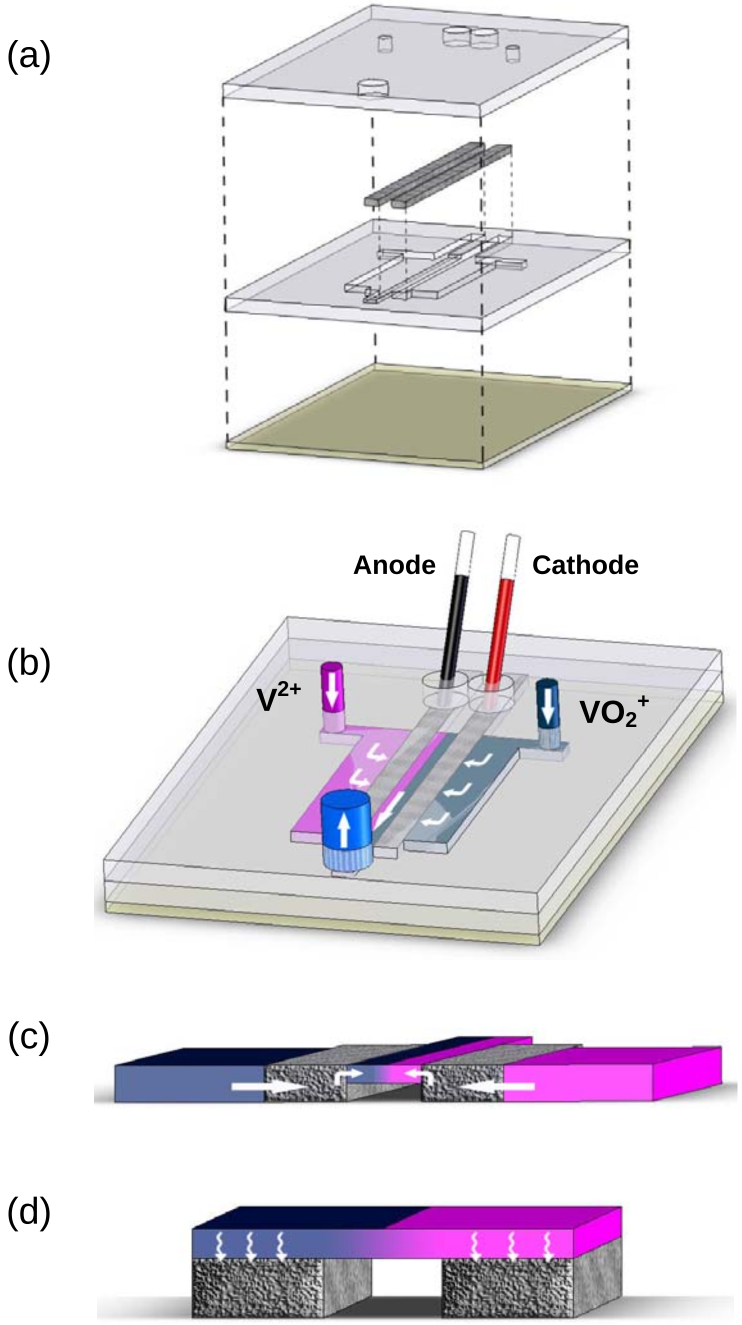

Figure 1. Schematics of: (a) fabrication and (b) operation of the microfluidic fuel cell architecture with flow-through electrodes; and cross-sectional geometry of (c) the flow-through architecture and (d) the established flow-over architecture fuel cell, employing aqueous vanadium redox species as fuel (V^{2+} - purple) and oxidant (VO_2^+ - black). The solution colors shown are characteristic of the employed solutions.

The microfluidic vanadium redox fuel cells employed here are shown schematically in Figure 1. Figures 1c-1d provide a schematic comparison of the new flow-through architecture (c) to the established flow-over architecture (d). In contrast to the flow-over cell, the flow-through cell is designed to direct the flow of vanadium fuel and oxidant solutions uniformly through the porous electrode structures. This strategy achieves utilization of the full depth of the electrode and associated active area, and provides enhanced species transport from the bulk to the active sites. The electrolyte streams enter the fuel cell on each side via a deep (300 μm) feed section that distributes the flow towards the side of the porous strip electrode (Figure 1b). The flow is guided at a low mean velocity from the feed section orthogonally through the 300 μm deep and 1 mm wide porous electrode into the less deep (150 μm) co-laminar exit section, where it is brought downstream to the outlet at a significantly higher mean velocity. The co-laminar exit section, which effectively employs the waste solutions as an ionic charge transfer medium, was given a high aspect ratio (width/depth) cross-sectional profile to confine the inter-diffusion/crossover zone to the center of the channel. In the flow-over cell (Figure 1d), diffusive mixing in the co-laminar channel represents loss of reactant, or fuel/oxidant cross-over. In contrast, in the flow-through cell (Figure 1c), the reactants are consumed prior to reaching the central channel, and the co-laminar streaming merely separates the waste products of the electrodes while providing proton transport. With respect to flow distribution in the flow-through cell, the pressure drop over the porous electrode is an estimated two orders of magnitude higher than the serially connected distribution channel. Thus assuming an effectively uniform pore distribution, a spatially uniform flow rate of reactant through the porous electrode is expected.

The microfluidic fuel cell prototype with flow-through porous electrodes was operated at flow rates spanning three orders of magnitude, from 1 to 300 μL min^{-1} per stream, using 2 M vanadium ions in 4 M sulfuric acid electrolyte. An advantage inherent to the use of the optically transparent PDMS material in combination with the distinctive colors of the vanadium species is that fuel cell operation under co-laminar flow can be observed visually. Figure 2a shows an image of the fuel cell operating at open-circuit, i.e. no current was drawn from the cell. The anolyte (V^{2+} - violet) and catholyte (VO_2^+ - black) streams passed through the electrodes orthogonally and filled the co-laminar exit section between the electrodes from both sides. The microfluidic co-laminar flow characteristics were maintained towards the outlet and diffusive mixing was restricted to the center of the channel. The absence of electrochemical reactions at the open-circuit voltage was confirmed by the uniform colors. The image in Figure 2b corresponds to steady state operation at 0.8 V cell voltage. As current was drawn from the cell, the violet color of the anolyte changed to light green (V^{3+}) and the black color of the catholyte changed to turquoise (VO^{2+}), as the solutions passed through the electrodes. The distinct color change provided an optical indication that much of the initial vanadium species had undergone electrochemical reaction, and that mixing of the streams was still restricted to the center of the channel.

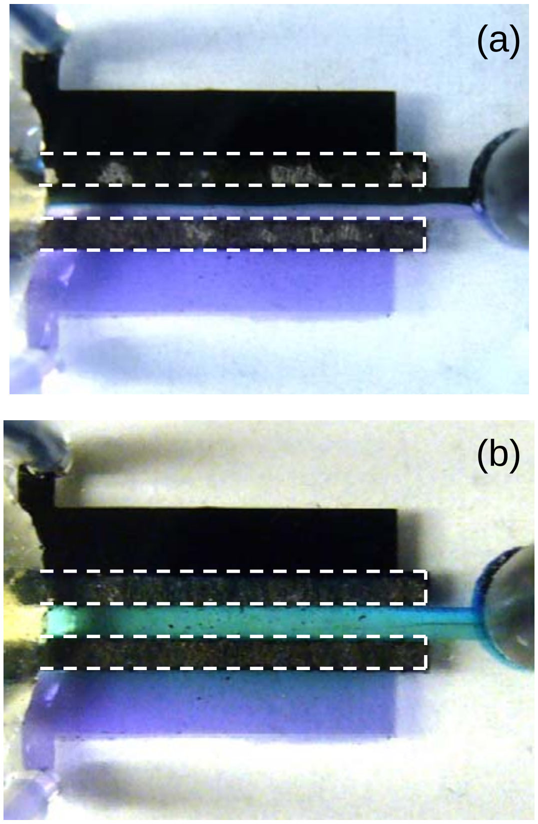

Figure 2. Images obtained during steady state operation of the microfluidic fuel cell with flow-through porous electrodes at (a) open-circuit and (b) 0.8 V cell voltage. The vanadium electrolytes contain V^{2+} (purple) and V^{3+} (light green) at the anode, and VO_2^+ (black) and VO^{2+} (turquoise) at the cathode. The flow rate was 1 µL min^{-1} per stream. Dashed lines indicate the extent of the porous electrodes.

3.1. Polarization

Steady state polarization data were obtained at room temperature under potentiostatic control. The results were also reproducible under galvanostatic control, and the average standard deviation of repeated experimental trials was less than 1% with the same cell and within 7% using different cells. The stability of the current generated by the fuel cell was evaluated by an extended potentiostatic experiment performed at a practical cell voltage (0.8 V) in the low flow rate regime (1 μL min^{-1}), the result of which is shown in Figure 3. After a brief transient period, the current density was quite steady throughout the entire 10 h time period, showing typical variations of ± 2%. No performance degradation was detected during this test; in fact, the highest hourly-averaged current density in the steady phase was recorded during the 8th hour. Deviations about the average current density are attributed to the low flow rate and the associated unsteady reactant feed; at higher flow rates, the current density is expected to have less noise.

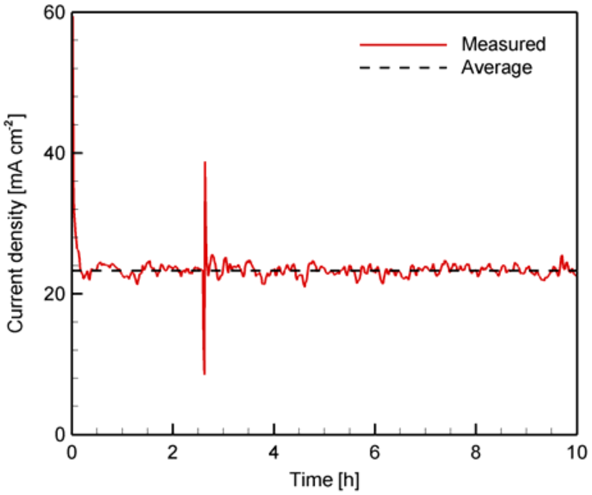

Figure 3. Flow-through fuel cell steady state chronoamperometric data measured at 0.8 V cell voltage and 1 μL min^{-1} flow rate.

The polarization curves in Figure 4 show steady state operation of the new fuel cell prototype at four different flow rates from 1 to 300 μL min^{-1}. The highest flow rate used here corresponds to Reynolds numbers from Re ~ 10^{-2} in the porous medium up to Re ~ 20 at the outlet of the co-laminar exit channel. The open-circuit voltage of the fuel cell was 1.53-1.55 V, and current densities up to 326 mA cm^{-2} were generated. Several trends can be identified based on these data: As expected, the current density increased with flow rate, which is a consequence of mass transport combined with relatively fast electrochemical redox reactions. However, the steep negative slope observed at the lowest flow rate, associated with predominant mass transport control, becomes less significant as the flow rate is increased. Above 60 μL min^{-1} the polarization curves become more linear and further increasing the flow rate results in only marginally increased performance. This effect is attributed to the parasitic ohmic voltage loss caused by series resistance in the cell, which is proportional to the current density. The combined ohmic resistance, including both in-channel ionic resistance and electrical resistance in electrodes, contacts and wires, was measured by electrochemical impedance spectroscopy (EIS) to be 27.6 Ω at 300 μL min^{-1}. This value is higher than for previous cells[9,15] and constitutes 70% of the average slope of the corresponding polarization curve (39.6 Ω).

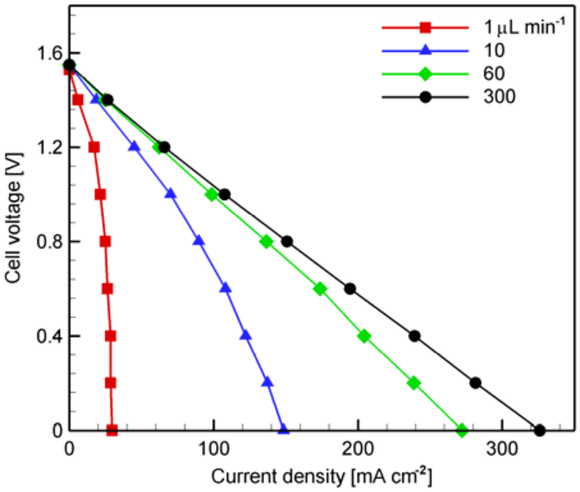

Figure 4. Flow-through fuel cell polarization data obtained under potentiostatic control at steady state and room temperature, using four different flow rates (as indicated).

Individual anodic and cathodic polarization curves are presented in Figure 5 versus an external SCE reference electrode at two different flow rates. This type of plot is normally used in fuel cell analysis to assess which one of the electrodes is limiting the overall fuel cell performance. In this case, a highly symmetric polarization pattern was observed, indicating that neither of the electrodes imposed an overall restriction on the cell, and that the electrochemical system was well-balanced with respect to both electrochemical kinetics and mass transport. This desired characteristic confirms the viability of the proposed flow-through porous electrode architecture for microfluidic fuel cells.

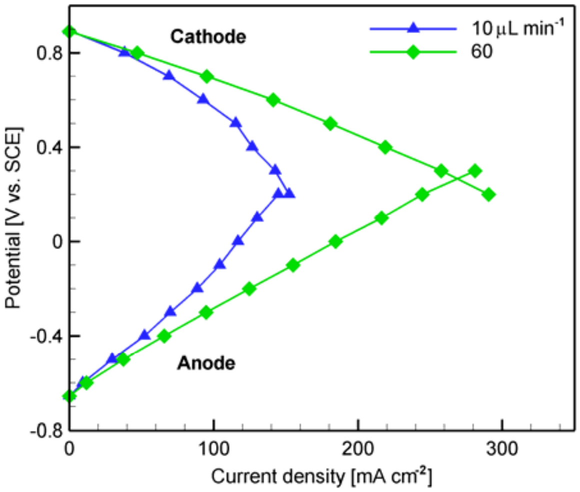

Figure 5. Steady state anodic and cathodic polarization data for the flow-through fuel cell measured *in situ* at room temperature under potentiostatic control, at two different flow rates (10 and 60 μL min^{-1}), using the opposite fuel cell electrode as counter electrode and an external SCE reference electrode.

3.2. Power density

Power density curves, calculated from the polarization data given in the previous section, are shown in Figure 6. These results demonstrate high levels of power density, which will be compared with other designs in Section 3.3. The overall power density increases considerably with flow rate, which again confirms the partial mass transport control. The highest power density obtained here was 121 mW cm^{-2} at 0.8 V and 300 μL min^{-1}. Operation at higher flow rates would be possible, but with limited gain due to the high ohmic resistance. The parasitic power loss associated with pumping the solutions through the porous electrodes was estimated from the pressure drop for flow within porous media. Due to the low Reynolds number of the cross-flow (Re ~ 10^{-2}), this pressure drop is quite small. The total pumping power required to sustain the flow through the porous electrodes and the surrounding channel structure[14] is therefore estimated to be less than 1% of the fuel cell output power under typical conditions.

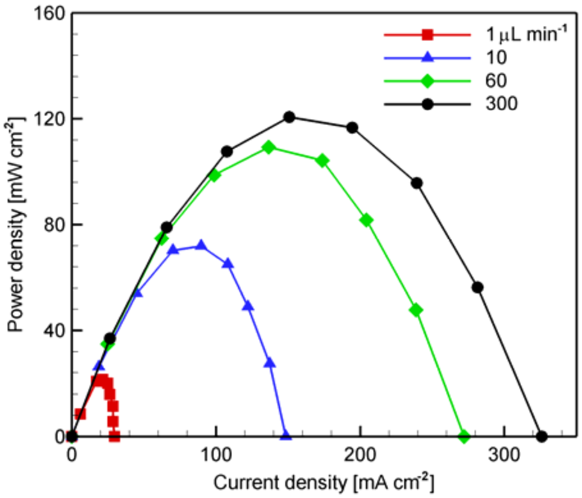

Figure 6. Flow-through fuel cell power density curves obtained from room temperature fuel cell polarization data at four different flow rates (as indicated).

3.3. Performance comparison

The performance of the microfluidic fuel cell with flow-through porous electrodes is compared to previous results obtained using flow-over architecture cells with planar[14] and untreated porous[15] electrodes mounted on the bottom of the co-laminar flow channel. Also, in order to evaluate the performance benefits associated with hydrophilic heat treated porous electrodes, a flow-over cell incorporating hydrophilic porous electrodes was fabricated. In Figure 7, a performance comparison based on (a) peak power density and (b) active fuel utilization at 0.8 V is provided. All plots are given as a function of flow rate per stream, which can be considered a measure of operational cost in terms of reactant supply. Compared to the previously reported flow-over cells using untreated porous electrodes, the flow-through architecture produced notably high power densities across all flow rates tested: the level of improvement ranges from two times at high flow rates to four times at low flow rates. These power density levels confirm that a larger portion of the total active area was being utilized and that the convective/diffusive species transport to the active sites has been improved considerably. The flow-over fuel cell with hydrophilic porous electrodes also generated higher power density than the previous fuel cell with untreated porous electrodes, but generally less than the flow-through architecture. At the highest flow rate, however, the flow-over cell produced the highest peak power density, 131 mW cm^{-2}, as compared to 120 mW cm^{-2} provided by the flow-through cell. The slope of the peak power density curve for the flow-through cell shows diminishing returns at high flow rates. This limitation of the flow-through cell is attributed to the ohmic resistance (27.7 Ω) that is significantly higher than the flow-over cell (19.9 Ω), as measured by EIS at 120 μL min^{-1}. Overall, these results highlight the importance of the hydrophilic porous electrode treatment, the effectiveness of the flow-through architecture, and the potential for significantly increased performance by reducing the ohmic resistance in the flow-through cell.

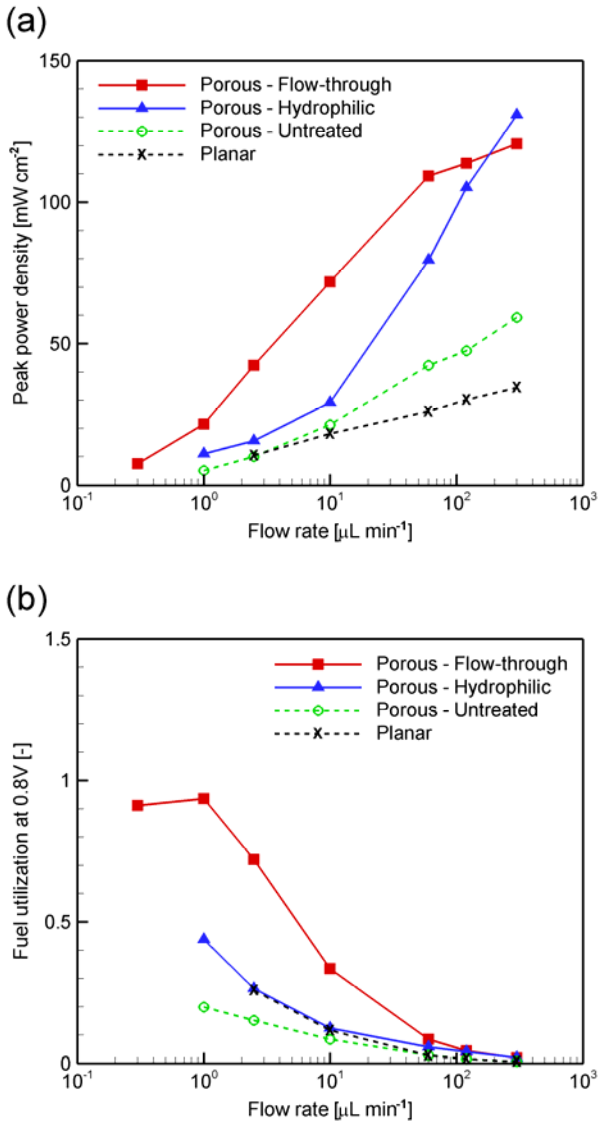

Figure 7. Performance comparison between the flow-through fuel cell and flow-over fuel cells (with electrodes mounted on the bottom of the co-laminar flow channel), in terms of (a) peak power density and (b) active fuel utilization at 0.8 V cell voltage, as a function of the flow rate (logarithmic). The vanadium redox concentrations were 2 M in all cases.

In addition to high power density levels, high Coulombic fuel utilization per single pass is desirable. Figure 7b presents active fuel utilization measured at a practical cell voltage of 0.8 V as a function of flow rate for the four fuel cell designs under study. The flow-through architecture provided higher fuel utilization than all the other designs. The highest fuel utilization measured at this cell voltage was 94%, obtained with the flow-through architecture at 1 μL min^{-1}. At such high levels of fuel utilization, fuel and oxidant crossover is irrelevant, given that essentially all the reactants have been consumed while passing through the electrodes. The ability to combine high fuel utilization with high power density at high operational cell voltage is unique to the flow-through microfluidic fuel cell architecture presented here. At 0.8 V, for example, the fuel cell produced 20 mW cm^{-2} combined with 94% active fuel utilization under steady state operation. Based on the theoretical standard cell potential (1.246 V), this is equal to an overall single pass energy conversion efficiency of 60%.

If the reactions described in Eq. (1) and (2) are completed for all respective species, the fuel utilization is considered 100%. It is noteworthy, however, that the produced species still constitute a redox pair (i.e. V^{3+}/VO^{2+}), and thus there is potential to gain further electrons from their reaction at the respective electrodes. Through this effect nominal fuel utilization over 100% was in fact observed at low flow rates and low operational cell voltages ($\leq$0.4 V). The data presented in Figure 7b were measured at a more practical cell voltage of 0.8V, where the current contribution from the secondary redox reaction is negligible.

3.4. *In situ* regeneration

With the flow-through microfluidic fuel cell architecture demonstrated here, there is the additional opportunity for *in situ* regeneration. The initial fuel and oxidant species can be regenerated by running the cell in an electrolytic format, i.e. pumping waste solution back into the cell and applying an electrolytic cell voltage. Figure 8 shows images obtained during reverse operation. Although an air bubble was present in the central channel, it was possible to establish proof-of-concept regeneration with this cell. While holding the cell potential at 0.0 V (i.e. open-circuit) and running the reverse flow at 1 μL min^{-1}, the cell current was zero and the solutions were green in both half-cells (Figure 8a).

Thereafter, the applied cell potential was held constant at 1.5 V while running the cell in reverse for 30 min (Figure 8b). In this case, purple V^{2+} and black VO_2^+ were identified in the anodic and cathodic half cells, respectively, and a steady regeneration current with a time-averaged current density of 45 mA cm^{-2} was measured. Our current focus is to study the operation in the regenerative mode and investigate the feasibility and roundtrip efficiency of a regenerative microfluidic fuel cell, i.e. a microfluidic battery, based on the fuel cell architecture demonstrated here.

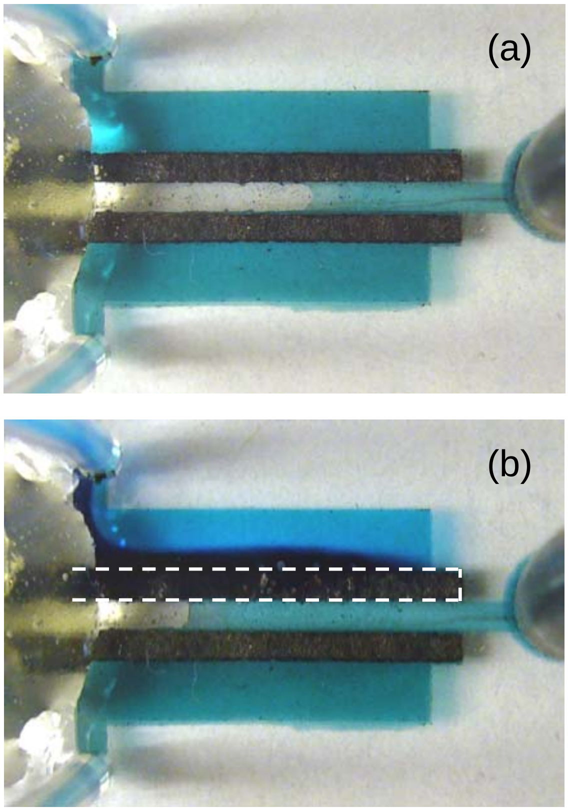

Figure 8. Images demonstrating the *in situ* regeneration capability of the new microfluidic fuel cell architecture when operated on the all-vanadium redox system. Fully mixed waste solution (~50/50 V^{3+}/VO^{2+}) is flowing in the reverse direction from right to left at 1 μL min^{-1} per stream, and a cell voltage of (a) 0.0 V (open-circuit) and (b) 1.5 V is applied to the cell. Dashed lines indicate the extent of the porous electrodes.

4. Conclusions

In this work, a microfluidic fuel cell architecture incorporating flow-through porous electrodes and employing the all-vanadium redox system was presented. In contrast to previous work, the flow-through architecture is designed to direct the flow of fuel and oxidant solutions uniformly through the porous electrode structures prior to combination of the waste streams in a co-laminar format. This strategy achieves utilization of the full depth of the porous electrode and associated active area, and provides enhanced species transport from the bulk to the active sites. Performance levels were demonstrated that for microfluidic fuel cells are unprecedented to date: power densities up to 131 mW cm^{-2}, near complete fuel utilization, and high operational cell voltages. The fuel cell also had the capability to combine these three characteristics during steady state operation, resulting in high overall energy conversion efficiency. We expect performance would further benefit from increasing the concentration of the vanadium redox species, optimizing the microstructure and porosity of the flow-through carbon electrodes, and most importantly, reducing the combined ohmic resistance of the cell. In addition, proof-of-concept *in situ* regeneration of the initial fuel and oxidant species was established by running the fuel cell in reverse.

Acknowledgment: This research was funded by the Natural Sciences and Engineering Research Council of Canada (NSERC) and Angstrom Power Inc. Experimental assistance provided by Dr. Clive Brereton and Evan Hobenshield at NORAM Engineering and Constructors Ltd. and infrastructure funding from Canada Foundation for Innovation (CFI) were highly appreciated.

References

(1) Dyer, C. K. *Journal of Power Sources* **2002**, *106*, 31-34.

(2) Bazylak, A.; Sinton, D.; Djilali, N. *Journal of Power Sources* **2005**, *143*, 57-66.

(3) Chang, M. H.; Chen, F.; Fang, N. S. *Journal of Power Sources* **2006**, *159*, 810-816.

(4) Choban, E. R.; Markoski, L. J.; Wieckowski, A.; Kenis, P. J. A. *Journal of Power Sources* **2004**, *128*, 54-60.

(5) Choban, E. R.; Spendelow, J. S.; Gancs, L.; Wieckowski, A.; Kenis, P. J. A. *Electrochimica Acta* **2005**, *50*, 5390-5398.

(6) Choban, E. R.; Waszczuk, P.; Kenis, P. J. A. *Electrochemical and Solid State Letters* **2005**, *8*, A348-A352.

(7) Cohen, J. L.; Volpe, D. J.; Westly, D. A.; Pechenik, A.; Abruna, H. D. *Langmuir* **2005**, *21*, 3544-3550.

(8) Cohen, J. L.; Westly, D. A.; Pechenik, A.; Abruna, H. D. *Journal of Power Sources* **2005**, *139*, 96-105.

(9) Ferrigno, R.; Stroock, A. D.; Clark, T. D.; Mayer, M.; Whitesides, G. M. *Journal of the American Chemical Society* **2002**, *124*, 12930-12931.

(10) Hasegawa, S.; Shimotani, K.; Kishi, K.; Watanabe, H. *Electrochemical and Solid State Letters* **2005**, *8*, A119-A121.

(11) Jayashree, R. S.; Egas, D.; Spendelow, J. S.; Natarajan, D.; Markoski, L. J.; Kenis, P. J. A. *Electrochemical and Solid State Letters* **2006**, *9*, A252-A256.

(12) Jayashree, R. S.; Gancs, L.; Choban, E. R.; Primak, A.; Natarajan, D.; Markoski, L. J.; Kenis, P. J. A. *Journal of the American Chemical Society* **2005**, *127*, 16758-16759.

(13) Kjeang, E.; Brolo, A. G.; Harrington, D. A.; Djilali, N.; Sinton, D. *Journal of the Electrochemical Society* 2007, 154, B1220-B1226.

(14) Kjeang, E.; McKechnie, J.; Sinton, D.; Djilali, N. *Journal of Power Sources* **2007**, *168*, 379-390.

(15) Kjeang, E.; Proctor, B. T.; Brolo, A. G.; Harrington, D. A.; Djilali, N.; Sinton, D. *Electrochimica Acta* **2007**, *52*, 4942-4946.

(16) Mitrovski, S. M.; Elliott, L. C. C.; Nuzzo, R. G. *Langmuir* **2004**, *20*, 6974-6976.

(17) Mitrovski, S. M.; Nuzzo, R. G. *Lab on a Chip* **2006**, *6*, 353-361.

(18) Duffy, D. C.; McDonald, J. C.; Schueller, O. J. A.; Whitesides, G. M. *Analytical Chemistry* **1998**, *70*, 4974-4984.

(19) *CRC Handbook of Chemistry and Physics*; 83rd ed.; CRC Press: Boca Raton, FL, 2002.

TOC Graphic

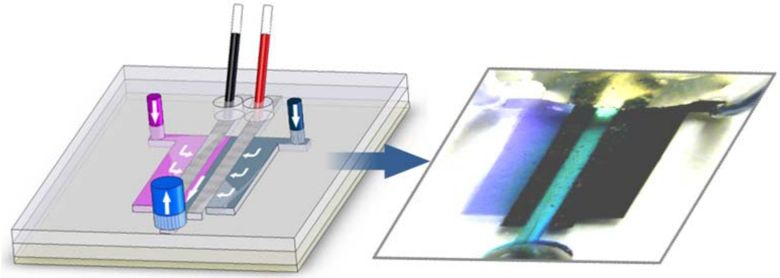

Appendix F

An Alkaline Microfluidic Fuel Cell Based on Formic Acid and Hypochlorite Bleach

An Alkaline Microfluidic Fuel Cell based on Formic Acid and Hypochlorite Bleach

Erik Kjeang,[a,c] Raphaelle Michel,[a,c] David A. Harrington,[b,c] Ned Djilali,[a,c] and David Sinton[a,c*]

[a]*Department of Mechanical Engineering,* [b]*Department of Chemistry, and* [c]*Institute for Integrated Energy Systems (IESVic), University of Victoria, 3800 Finnerty Road, Victoria, BC, V8W2Y2, Canada*

[*]*dsinton@me.uvic.ca*

Abstract

An alkaline microfluidic fuel cell is demonstrated employing formic acid-based fuel and sodium hypochlorite oxidant, also known as hypochlorite bleach. Both formic acid and sodium hypochlorite are available and stable as highly concentrated liquids, thereby facilitating fuel cell systems with high overall energy density. The alkaline anodic half-cell prevents gaseous CO_2 formation via carbonate absorption, while sustaining the rapid kinetics associated with formic acid oxidation in acidic media. Both half-cells provide high current densities at relatively low overpotentials and are free of gaseous products that may otherwise limit microfluidic fuel cell performance. The microfluidic fuel cell takes advantage of a membraneless architecture with flow-through porous electrodes. Power densities up to 52 mW cm^{-2} and overall energy conversion efficiencies up to 30% per single pass are demonstrated at room temperature using 1.2 M formate fuel and 0.67 M hypochlorite oxidant. The alkaline formate/hypochlorite fuel and oxidant combination demonstrated here, or either one of its individual half-cells, may also be useful in conventional membrane-based fuel cell designs.

Keywords

Microfluidic fuel cell; membraneless fuel cell; laminar flow-based fuel cell; formic acid; formate; carbonate; hypochlorite; bleach; flow-through porous electrode

1. Introduction

A microfluidic fuel cell is defined as a device that incorporates all fundamental components of a fuel cell within a single microfluidic channel and its walls. Since its invention in 2002, microfluidic fuel cell technology has developed rapidly [1-22] and is now considered a candidate for commercial small-scale portable power generation. Microfluidic fuel cells operate without a membrane, and the most common configurations rely on the laminar nature of flow in microstructures to maintain sufficient separation of fuel and oxidant streams, flowing side-by-side in a co-laminar format. Supporting electrolyte contained in both co-laminar streams facilitate ionic conduction between the electrodes. Mixing by diffusion is restricted to an interfacial width at the center of the channel, depending on mean velocity and channel geometry. The electrode spacing is typically an order of magnitude larger than the inter-diffusion width. Microfluidic fuel cells have several advantages as compared to traditional proton exchange membrane (PEM)-based fuel cells: fuel and oxidant streams may be combined in a single microchannel; fuel and/or oxidant crossover can be mitigated by adjusting the flow rate of the co-laminar streams; no ion exchange membrane is required; sealing, manifolding, and fluid delivery infrastructure requirements are reduced; and issues related to membrane hydration and water management are eliminated. In addition, microfluidic fuel cells may be manufactured using inexpensive microfabrication methods and low-cost materials.

Microfluidic fuel cells with room-temperature power densities on the order of 100 mW cm^{-2} have been demonstrated [15, 16]. Operation at high power densities has, however, resulted in low overall energy conversion efficiency due to low single-pass fuel utilization. To mitigate this problem, a new microfluidic fuel cell architecture with flow-through porous electrodes was recently developed by our group [15]. The flow-through design is based on cross-flow of reactant through the porous electrodes into a co-laminar center channel with orthogonally directed flow in which the waste solutions facilitate ionic charge transfer in a membraneless configuration. This cell architecture enables improved utilization of the three-dimensional active area inside the porous electrodes and provides enhanced rates of convective/diffusive transport to the active sites without increasing the parasitic loss required to drive the flow. When operated on 2 M vanadium solutions, the flow-through design demonstrated a high level of overall energy conversion efficiency, as a relatively high level of fuel utilization and cell voltage were achieved concurrently. The overall energy density of a microfluidic fuel cell system based on vanadium redox species is however limited by the solubility and concentration of these ions, and the associated redox reactions can only provide one electron per ion.

In the context of fuel and oxidant combinations for microfluidic fuel cell systems with practical energy density, the following attributes are desirable: both reactants and products are available and stable at high concentration in the liquid phase; the reactants provide at least two electrons per molecule; spontaneous and/or electrochemically activated decomposition into gaseous products are prevented; the fuel and oxidant do not react upon mixing; and if the anodic and cathodic supporting electrolytes are different, both fuel and oxidant species are stable in both electrolytes.

Several different fuels have been employed in microfluidic fuel cells presented to date. These include hydrogen [7, 18, 19], methanol [5, 6, 11], formic acid [4, 8, 12, 13], vanadium redox species [9, 14-16], and hydrogen peroxide [10]. Most liquid hydrocarbon fuels produce carbon dioxide (CO_2) as the end product after complete electrochemical conversion. Typically, CO_2 evolves as a gaseous product in acidic or neutral media [13] unless the current densities are low enough to fully dissolve it in the fuel or electrolyte stream [4]. Formic acid is an established fuel with high energy density that has previously been used in both PEM-based direct formic acid fuel cells [23, 24] and microfluidic fuel cells [4, 8, 12, 13], and its electrochemical kinetics on palladium catalyst are fast, thereby allowing much higher power densities than other hydrocarbon fuels such as methanol [25]. In contrast to acidic and neutral media, alkaline media have the capability of absorbing large amounts of CO_2 as carbonates with the additional benefit of automated carbon sequestration. An alkaline formate fuel from concentrated formic acid therefore accomplishes all the criteria for an all-liquid microfluidic fuel cell system with high energy density.

The oxidants employed in microfluidic fuel cells to date have been oxygen [4-8, 18, 19], air [11, 12], vanadium redox species [9, 14-16], and hydrogen peroxide [10, 13]. Among these, only hydrogen peroxide is available as a highly concentrated liquid. Direct hydrogen peroxide reduction on common catalysts such as platinum and palladium is however accompanied by vigorous oxygen gas evolution from its decomposition [13]. Alternative liquid oxidants that have been employed in fuel cells or flow batteries include permanganate [4, 26] and hypochlorite [27, 28]. Permanganate is a strong oxidant that enables high current densities and highly positive reduction potentials in acidic media [29]. Reports have shown, however, that product manganese dioxide precipitate can clog the pores of a microporous electrode in the absence of stirring [26]. The use of permanganate oxidant in microfluidic fuel cells that incorporate both microporous electrodes and microscale channels should therefore be avoided. Hypochlorite, in contrast, does not produce any precipitate, and has shown benign electrochemical characteristics as an oxidant in magnesium, zinc and aluminum semi-fuel cells [27, 28] using palladium/iridium and platinum catalysts. Hypochlorite oxidant has many useful characteristics for microfluidic fuel cell implementation: relatively high standard reduction potential and rapid kinetics; high solubility in aqueous media; highly soluble reduction product (chloride); and finally, no gaseous decomposition reactions take place when the hypochlorite is stabilized in alkaline electrolyte [27]. Furthermore, hypochlorite solution is produced in large quantities as domestic bleach. Sodium hypochlorite bleach is considered relatively safe and is available at very low cost. Hypochlorite therefore meets all the criteria of an all-liquid microfluidic fuel cell with high energy density. Additionally, the product sodium chloride is common and non-toxic.

In this work, a microfluidic fuel cell based on alkaline formate and hypochlorite bleach is presented. Both palladium and gold porous electrodes are formed via electrodeposition on a porous carbon substrate. The electrochemical responses of the porous electrodes are characterized in a stationary three-electrode cell prior to *in situ* tests and fuel cell implementation.

2. Experimental

2.1. Preparation of solutions

Alkaline formate fuel solution was obtained by adding 5wt% concentrated formic acid ($HCOOH$; Fisher Sci., Fair Lawn, NJ) to a 10wt% (2.8 M) sodium hydroxide ($NaOH$) electrolyte prepared by dissolving NaOH pellets (EMD Chemicals, San Diego, CA) in Millipore Milli-Q water (Millipore, Billerica, MA). After stabilization the obtained solution contained 1.2 M formate and 1.6 M OH^-. Alkaline hypochlorite (ClO^-) oxidant solution (0.67 M) was prepared by dissolving 10wt% (2.8 M) NaOH pellets directly in a 5% sodium hypochlorite solution ($NaOCl$; Caledon, Georgetown, Canada) or 5.25% hypochlorite bleach (Javex-5; Colgate-Palmolive, Toronto, Canada). The gold (Au) plating solution consisted of 17 mM potassium gold cyanide ($KAu(CN)_2$; Degussa, Frankfurt, Germany) dissolved in Millipore Milli-Q water, followed by the successive addition of 0.4 M citric acid ($C_6H_8O_7$; Matheson Coleman & Bell, Montreal, Canada) and 0.4 M sodium citrate ($Na_3C_6H_5O_7$; Merck, Montreal, Canada) to a final pH of 3-5. The palladium (Pd) plating solution consisted of 1.0wt% palladium(II) chloride ($PdCl_2$; SigmaAldrich) in 1 M hydrochloric acid (HCl; Anachemia, Montreal, Canada) in Millipore Milli-Q water. All chemicals used were ACS grade except the hypochlorite bleach.

2.2. Electrodeposition

Porous carbon electrodes subject to catalyst deposition were cut to 25 mm x 1 mm strips from sheets of Toray carbon paper (B-2 Designation TGPH-090; E-TEK, Somerset, NJ) with typical thickness 300 μm (measured), typical density 0.49 g cm^{-3} and 78% porosity. A 20 mm long section of the carbon strips were rendered hydrophilic by annealing (~1 s) in a propane flame, and the hydrophilic electrodes were supported on glass slides with wires attached using PELCO® conductive silver 187 (Ted Pella Inc., Redding, CA) covered by regular epoxy. The strip electrodes were rinsed thoroughly in Millipore Milli-Q water before and after each plating sequence. Electrodeposition of Au and Pd on the porous carbon electrodes was performed by immersing the hydrophilic electrode parts in a bath containing either Au or Pd plating solution, together with a Pt mesh counter electrode and a saturated calomel reference electrode (SCE). The carbon working electrode was aligned with the counter electrode to obtain a uniform current distribution during plating. All electrochemical experiments in this study were driven by a PARSTAT 2263 potentiostat (Princeton Applied Research, Oak Ridge, TN), and all individual electrode potentials are given versus the SCE (sat. KCl) reference electrode (0.241 V vs. SHE). Each electrodeposition experiment started with a cyclic voltammogram (3 cycles) of a bare porous carbon electrode in the Au plating solution from the open circuit potential (OCP) to -1.1 V, followed by electroplating under potentiostatic control at -1.1 V for 60 min. The Au loading of the obtained porous gold electrodes was not assessed. Porous Pd electrodes were obtained by electrodeposition of Pd on the fresh Au layer by a similar procedure [13]: a cyclic voltammogram (3 cycles) was measured with the porous Au electrode in the Pd plating solution from the OCP to -0.1 V, followed by electroplating under potentiostatic control at 0.0 V until a desired loading of 5 mg cm^{-2} had been deposited, typically after 20-30 min, calculated in real time by integrating the current profile and assuming a 60% coulombic plating efficiency [30]. Scanning electron micrographs were captured by a Hitachi S-3500N scanning electron microscope with a tungsten filament operated at 15 kV.

2.3. Fuel cell fabrication

An array of microfluidic fuel cells with flow-through porous electrodes was assembled using in-house developed microfabrication techniques detailed in a previous study [15]. In short, one 20 mm long porous Pd anode and one 20 mm long porous Au cathode were cut from the electrodeposited strip electrodes and fitted in custom-sized grooves (20 mm x 1 mm x 300 µm, separated by 1 mm), fabricated in a poly(dimethylsiloxane) (PDMS; Dow Corning, Midland, MI) part. The PDMS part had a dual layer structure: a 300 µm deep section that defined the two electrode grooves plus the two inlet channel structures, and a 150 µm deep layer accommodating the co-laminar flow channel between the electrodes, leading towards the outlet. The fourth wall of the microfluidic device was provided by a flat layer of PDMS, with previously punched holes for the inlets, outlet, and electrical contacts, which was sealed irreversibly on top of the other PDMS part after plasma-treating. External wiring was contacted to the exposed ends of the carbon strip electrodes using PELCO® conductive silver 187 covered with regular epoxy.

2.4. Fuel cell testing

The co-laminar flow of formate and hypochlorite solutions through the fuel cell was driven by a syringe pump (PHD 2000; Harvard Apparatus, Holliston, MA) via Teflon® tubing (1/16” diameter; S.P.E. Limited, North York, ON, Canada) to the inlets and through a larger Tygon® tube (3 mm diameter; Fisher Sci., Pittsburgh, PA) from the outlet to the outlet reservoir. The desired flow rate was adjusted and the co-laminar flow was stabilized before initiation of the electrochemical measurements. Cell polarization data were measured by chronoamperometry under stepwise potentiostatic control from the open circuit cell voltage down to 0.0 V by -0.2 V increments, using the PARSTAT potentiostat. The current transient generated by the cell was monitored until steady state was reached, which typically occurred within 180s. Polarization of individual electrodes was measured versus an external SCE reference electrode placed in the outlet reservoir, using the opposite fuel cell electrode as counter electrode. Current densities and power densities reported here were calculated based on the geometric active area of the electrodes (0.12 cm^2), in keeping with previous studies [15]. The ohmic resistance of the fuel cell and its individual electrodes was measured by electrochemical impedance spectroscopy (EIS), using the PARSTAT 2263 potentiostat. Impedance spectra were recorded at the open-circuit cell voltage, by applying an ac amplitude of 5 mV rms over the frequency range from 50 kHz to 0.5 Hz with 30 log spaced data points. The ohmic resistance was detected as the high-frequency real axis intercept of the Nyquist plot of impedance. For *in situ* EIS measurements, the flow rate was fixed at 60 $\mu L\ min^{-1}$.

3. Results and discussion

3.1. Reaction scheme

At the pH used here, the fuel exists predominantly as formate ($HCOO^-$), the oxidant as hypochlorite (ClO^-) and the CO_2 as carbonate. The reactions, written in terms of these species, lead to the following standard electrode potentials (vs. SCE) at 298 K ((1) calculated from Gibbs' energies of formation in [31] and (2) taken from [32]):

Anode:

$$HCOO^- + 3OH^- \leftrightarrow CO_3^{2-} + 2H_2O + 2e^- \qquad E^0 = -1.17\ \text{V} \tag{1}$$

Cathode:

$$ClO^- + H_2O + 2e^- \leftrightarrow Cl^- + 2OH^- \qquad E^0 = 0.57\ \text{V} \tag{2}$$

Overall cell reaction:

$$HCOO^- + ClO^- + OH^- \leftrightarrow CO_3^{2-} + Cl^- + H_2O \qquad E^0_{cell} = 1.74\ \text{V} \tag{3}$$

Note that the actual electrode and cell potentials also depend on pH and concentration of the aqueous species according to the Nernst equation. The formation of carbonates involves some net consumption of OH^-, which is available at high concentration in the alkaline electrolyte.

3.2. Electrodeposition of porous electrodes

To reduce the activation overpotentials of the proposed electrochemical reaction scheme, suitable catalysts need to be added to the electrodes. In this study, palladium (Pd) and gold (Au) were selected as the catalysts for anodic formate oxidation and cathodic hypochlorite reduction, respectively. Pd and Au were electrodeposited on porous carbon paper substrates in order to develop porous Pd and Au electrodes compatible with the unique co-laminar flow mechanism of the microfluidic fuel cell with flow-through porous electrodes [15]. Coating of the carbon fibers with Au may also be advantageous towards reducing the overall ohmic resistance of the electrodes, which was relatively high for the bare porous carbon electrodes used previously with this cell architecture [15]. Figure 1a shows a typical cyclic voltammogram of a bare porous carbon electrode in the gold cyanide plating bath. The overpotential for Au plating is relatively high; plating effectively started at -0.6 V, which was about 800 mV negative of the open circuit potential (OCP). Hydrogen evolution started at about -1.0 V on the first scan and at -0.8 V on consecutive scans. The difference between the three cycles is associated with the fresh Au deposit on the carbon electrode that reduced the overpotential for hydrogen evolution, which is relatively high on bare carbon. Au plating below -0.8 V was therefore accompanied by hydrogen evolution. The viability of potentiostatic Au plating on porous electrodes was evaluated at three different potentials: -0.7 V, -0.9 V and -1.1 V, with results shown in Figure 1b. The plating current at -0.7 V was essentially free from hydrogen evolution and therefore quite low, although it showed a linear increase over time attributed to the nucleation and growth of Au grains. The plating currents measured at -0.9 V and -1.1 V were dominated by hydrogen evolution, which also increased over time as the surface area of the Au deposit was enlarged. Images of the final Au deposits captured by scanning electron microscopy (SEM) are presented in Figure 2. These images provide a useful illustration of the microstructure and degree of coverage achieved in the deposition of Au on the porous carbon electrodes. With respect to the electrochemical performance of a porous electrode, both high coverage and high specific surface area are desirable characteristics. Figure 2a shows the granular Au structure obtained at -0.7 V. At -0.9 V (Figure 2b), a similar granular structure was observed with significantly higher loading. The image of the deposit obtained at -1.1 V (Figure 2c) indicates a high degree of coverage with different surface morphology. Most importantly, the Au deposit appeared much more uniform over the observable depth of the porous electrode at -1.1 V compared to the other potentials.

The porous Au electrode deposited at -1.1 V was further analyzed with images obtained at three different magnifications, shown in Figure 3. These images demonstrate the quality of the obtained Au deposit in the context of fuel cell implementation: the outer surfaces of the electrode were uniformly coated (Figure 3a); all observable fibers throughout the 3-D porous matrix showed effectively complete coverage (Figure 3b); and the surface morphology had dendritic features with size < 1 μm indicating a high specific surface area (Figure 3c). The improved 3-D coverage at high overpotentials is attributed to the continuous hydrogen gas evolution introducing a local two-phase flow component. Specifically, as hydrogen bubbles were released from the porous matrix, fresh plating solution was introduced into the matrix. In sum, electrodeposition of Au on porous carbon electrodes was shown to be very effective at -1.1 V. Similarly fabricated porous Au electrodes were also used to make porous Pd electrodes, by coating an additional Pd layer (5 mg cm^{-2}) following our previously described Pd electrodeposition methodology [13], with details outlined in Section 3.2.

3.3. *Ex situ* half-cell characterizations

The porous Pd anodes and Au cathodes were characterized electrochemically in a stationary three-electrode electrochemical cell in the alkaline formate or hypochlorite solutions, respectively, to analyze their performance and suitability for microfluidic fuel cell implementation. Cyclic voltammograms measured *ex situ* for a porous Pd anode, a porous Au cathode, and a porous Pd cathode are shown in Figure 4. The Pd anode produced high current densities up to 340 mA cm^{-2} at quite low overpotentials, in the absence of convective motion. As expected, no gas evolution was observed in this anodic half-cell, indicating that the product is carbonate, without any CO_2. The OCP of this half-cell was measured to -0.99 V, within 0.2 V of the standard potential of reaction (1). The ohmic resistance of the Pd anode was measured as 3.6 Ω by electrochemical impedance spectroscopy (EIS), as described in Section 3.4.

The Au and Pd cathodes also delivered notably high current densities up to 230 and 330 mA cm^{-2}, respectively, despite the lack of convective transport. The Au cathode, however, exhibited a 250 mV higher overpotential than the Pd cathode for the hypochlorite reduction reaction (2). As shown, Au is not an ideal catalyst for hypochlorite reduction, but it does have a significant advantage with respect to integration in microfluidic fuel cells: in contrast to the Pd electrode that produced a small amount of gas during these tests, no gas evolution was observed on the Au electrode. The OCP for hypochlorite reduction was measured to 0.38 V (Au) and 0.46 V (Pd). The oxidation of water to oxygen can occur above 0.38 V at pH 14.4, the nominal pH of this solution, explaining the gas evolution in the case of Pd. The measured OCP was again within 0.2 V of the standard reduction potential (0.57 V). While not ideal for this reaction, the alkaline electrolyte is required to stabilize the hypochlorite solution. The ohmic resistance of the cathodes was measured by EIS as 3.0 Ω (Au) and 2.9 Ω (Pd). The electrical resistance of the Au coated electrodes was thus reduced by more than 50% compared to the bare carbon strip electrodes (7-9 Ω). Overall, these half-cell experiments indicate that the alkaline formate anodic half-cell and the hypochlorite cathodic half-cell are well-suited to implementation in a fuel cell.

An additional half-cell test was performed with the ACS-grade hypochlorite solution replaced with a low-cost household bleach product (Javex-5; Colgate-Palmolive), containing 5.25% sodium hypochlorite. The obtained cyclic voltammograms closely matched those in Figure 4.

3.4. Microfluidic fuel cell implementation

A microfluidic fuel cell with flow-through porous electrode architecture was fabricated, incorporating an electrodeposited porous Au electrode as cathode and an electrodeposited porous Pd/Au electrode as anode. The assembled cell is shown in Figure 5. The transparency of the PDMS enables observation of the flow, and detection of any intermittent disturbances. As gaseous products can destabilize the co-laminar flow [13], the Au cathode was chosen over the Pd cathode (that produced a small amount of gas in the *ex situ* experiments) for implementation in the fuel cell. The fuel and oxidant streams enter the microfluidic fuel cell device (Figure 5) through separate inlets and approach the electrodes via the deep (300 μm) distribution channels. From the distribution channels, the flow is directed orthogonally into the porous electrodes. The cross-flow through the porous media has two orders of magnitude higher pressure drop than the flow in the distribution channels [15], and is therefore expected to be uniformly distributed throughout the available cross-sectional area of the electrodes. In addition, the high cross-sectional area open to the cross-flow provides low mean velocities inside the porous electrodes, which enables ample opportunity for high coulombic fuel utilization. Both anodic and cathodic streams enter the center channel through the electrodes on both sides at the same flow rate. The two streams are directed towards the outlet in a co-laminar format. The center channel is relatively shallow (150 µm) and has a small cross-sectional area in order to provide high mean velocities and reliable co-laminar flow. In this way mixing of the waste streams is limited to a relatively small diffusion width in the centre, while the electrolyte provides effective ionic transport. The flow-through electrode architecture thus achieves utilization of the full depth of the electrode and associated active area, which is 20-30 times larger than the vertically projected area of the electrode [16], and provides enhanced species transport from the bulk to the active sites as well as effective ionic transport in a membraneless configuration.

3.5. Microfluidic fuel cell performance

The assembled microfluidic fuel cell device with flow-through porous electrodes was operated at flow rates ranging from 2 to 300 µL min^{-1} per stream, using formate anolyte and hypochlorite catholyte. The cell exhibited very stable co-laminar flow without any gas evolution or other disturbances and the open circuit cell potential was steady between 1.37 and 1.42 V, depending on the flow rate used. These cell potential levels are similar to the estimated cell potential from the *ex situ* experiments (1.37 V), calculated as the difference in OCP between the Pd anode and the Au cathode. The combined ohmic resistance of the cell was measured using EIS at open circuit and 60 µL min^{-1} as 24.1 Ω. This resistance measurement includes the solution resistance with respect to ionic transport in the co-laminar center channel and the electrical resistance in electrodes, contacts and wires. By incorporation of an external reference electrode (SCE) in the outlet reservoir, we were also able to measure the ohmic resistance of the individual electrodes *in situ* using the same technique, resulting in 7.0 Ω for the anode and 12.8 Ω for the cathode. These values are somewhat higher than the corresponding *ex situ* measurements (3.6 Ω and 3.0 Ω, respectively), primarily attributed to high electrical contact resistance on the chip. The solution resistance was estimated to 4.3 Ω by subtracting the electrical resistance from the combined ohmic cell resistance, which is in agreement with previous studies using acidic electrolyte [14].

Room-temperature polarization data were obtained under potentiostatic control at steady state conditions. Figure 6 presents three different polarization curves obtained at 2, 10 and 60 μL min^{-1}. The current densities increased with flow rate up to a maximum 230 mA cm^{-2} at 60 μL min^{-1}, indicating partial mass transport control and relatively fast electrochemical kinetics; however, increasing the flow rate above 60 μL min^{-1} (polarization curves not shown here) resulted in no significant performance improvements. Based on these observations, electrochemical kinetics and ohmic resistance were dominating at high flow rates. The parasitic combined ohmic resistance of the cell contributed almost 50% to the average slope of the polarization curve (51 Ω) at 60 μL min^{-1}, and about 70% to the linear part of the curve at practical cell voltages of 0.8 V and below. At low flow rates, the potential loss associated with ohmic resistance was not as severe: it was less than 30% at 10 μL min^{-1} and only about 8% at 2 μL min^{-1}. At these flow rates, the current densities were primarily controlled by the rate of reactant supply. The cell was not operated below 2 μL min^{-1}, although the stability of the co-laminar flow is expected to be maintained at least down to 0.3 μL min^{-1} [15].

The relatively low current densities produced in the high cell voltage range (1.0-1.4 V) indicate significant activation overpotential for the electrochemical reactions, which is common to most fuel cell systems. This effect was further analyzed by employing the external reference electrode (SCE) to measure the performance of the individual electrodes *in situ* under the same flow conditions, using the opposite electrode as counter electrode. Separate anodic and cathodic polarization curves are presented in Figure 7. This type of analysis is often used to diagnose overall fuel cell performance and to identify half-cell-specific limitations. Given the significant differences related to the electrochemistry of the formate oxidation and hypochlorite reduction reactions, the anodic and cathodic polarization curves are surprisingly well-balanced. The symmetry outlined by the two curves justifies the viability of the formate/hypochlorite fuel and oxidant combination and also confirms the uniform transport characteristics of the flow-through architecture. Both electrodes responded well to fuel cell operation at cell voltages below 1.0 V, where neither of them caused an overall restriction to the cell. The activation overpotential was shared by the two half-cells but dominated by the cathode. These results are in good agreement with the *ex situ* measurements, where the activation overpotential was quite high on the Au cathode.

Power density curves calculated based on the polarization data at 2, 10 and 60 μL min^{-1} are provided in Figure 8. The overall power density increased significantly with flow rate, which again confirms the partial mass transport control. The highest power density measured in this study was 52 mW cm^{-2} at 0.4 V and 60 μL min^{-1}. This level of power density compares favorably to most other microfluidic fuel cells reported to date and demonstrates the high capacity of the proposed formate/hypochlorite fuel and oxidant combination. The power densities measured here did not however reach the levels obtained with the vanadium redox system in the same cell architecture [15] due to the lower cell voltages and reactant concentrations. The feasibility of the formate/hypochlorite system in the flow-through electrode architecture is more evident in the low flow rate regime. Even at the lowest flow rate (2 μL min^{-1}), a useful peak power density of 18 mW cm^{-2} was generated at 0.6 V cell voltage. Fuel cell operation in this regime is very efficient due to the high levels of fuel utilization enabled by the flow-through electrode architecture and practical cell voltages achieved concurrently. The fuel utilization with respect to the hypochlorite component, which had a lower molar concentration (0.67 M) than the formate solution (1.2 M), was as high as 85% at the point of peak power and effectively 100% at low cell voltages. Based on the theoretical standard cell potential of 1.74 V, the overall energy conversion efficiency at 0.6 V was ~30% per single pass. The highly energy efficient microfluidic fuel cell performance previously demonstrated with the vanadium redox system was thus maintained with the new formate/hypochlorite system.

The fuel cell performance measured here can also be compared to the *ex situ* half-cell characterizations provided by the cyclic voltammograms in Figure 4. In contrast to the steady state fuel cell data, these predictions are based on unsteady operation (50 mV s^{-1} scan rate) without flow, and the ohmic resistance was only about 3 **Ω** per electrode. A fuel cell based on the performance measured in the *ex situ* experiments would theoretically have an open circuit voltage of 1.37 V (Au cathode) or 1.45 V (Pd cathode), and would produce peak power densities of 81 mW cm^{-2} (Au cathode) and 143 mW cm^{-2} (Pd cathode) at 0.35 V and 0.55 V cell voltage, respectively. These power density levels are much higher than those obtained in the microfluidic fuel cell, despite the lack of convective transport. This comparison indicates that the high capacity inherent to the formate/hypochlorite system was not fully exploited in the proof-of-concept microfluidic fuel cell, primarily due to its high parasitic ohmic resistance. While electrode contamination from the carbonate species is a possibility at high fuel concentrations, no detectable deterioration was observed in these tests.

Finally, we also assembled a prototype microfluidic fuel cell with a Pd cathode, to evaluate the performance gains compared to the cell with a Au cathode, envisaged by the *ex situ* measurements. The cell generated an initial peak power density of 59 mW cm^{-2} (at a flow rate of 60 μL min^{-1}), 13% higher than the previous cell, but the gas bubbles growing on the Pd cathode made its operation unstable shortly thereafter. To enable reliable fuel cell operation with a Pd cathode, some design modifications need to be undertaken. Potentially a grooved channel geometry for gas removal could be incorporated, as previously demonstrated [13]. An alternative strategy is to evaluate other catalysts for the hypochlorite reduction that do not produce gas. Both platinum [27] and a combination of palladium and iridium [28] have been used effectively for hypochlorite reduction but their application in microfluidic fuel cells needs to be assessed.

4. Conclusions

This work demonstrated the feasibility of an alkaline formic acid-based anode coupled with an alkaline hypochlorite cathode in a microfluidic fuel cell architecture with flow-through porous electrodes. Both half-cells were unique in terms of fuel cell implementation. In contrast to the vanadium redox system, formic acid and sodium hypochlorite are both available as highly concentrated liquids, thereby enabling a microfluidic fuel cell system with high overall energy density. The proof-of-concept formate/hypochlorite microfluidic fuel cell concurrently achieved high power densities and near-complete fuel utilization at relatively high cell voltages, and therefore enabled high overall energy conversion efficiency. The performance would be enhanced further by reducing the combined ohmic resistance of the cell, specifically the on-chip electrical contact resistance, and by performing a catalyst screening study for hypochlorite reduction to reduce the activation overpotential and enhance the electrochemical kinetics while preventing gas evolution. Other advancements under investigation include employing higher fuel and oxidant concentrations in the fuel cell, switching to potassium hydroxide electrolyte and optimizing its concentration, and evaluating other liquid hydrocarbon fuels such as methanol. The new alkaline formate and hypochlorite fuel cell concept demonstrated here, or either one of its individual half-cells, may also find applications using conventional membrane-based fuel cell designs.

Acknowledgment

The authors would like to acknowledge project funding by the Natural Sciences and Engineering Research Council of Canada (NSERC) and Angstrom Power Inc., and infrastructure funding from Canada Foundation for Innovation (CFI) and British Columbia Knowledge Development Fund (BCKDF).

References

[1] A. Bazylak, D. Sinton, N. Djilali, Journal of Power Sources 143 (2005) 57-66.
[2] M.H. Chang, F. Chen, N.S. Fang, Journal of Power Sources 159 (2006) 810-816.
[3] F.L. Chen, M.H. Chang, M.K. Lin, Electrochimica Acta 52 (2007) 2506-2514.
[4] E.R. Choban, L.J. Markoski, A. Wieckowski, P.J.A. Kenis, Journal of Power Sources 128 (2004) 54-60.
[5] E.R. Choban, J.S. Spendelow, L. Gancs, A. Wieckowski, P.J.A. Kenis, Electrochimica Acta 50 (2005) 5390-5398.
[6] E.R. Choban, P. Waszczuk, P.J.A. Kenis, Electrochemical and Solid State Letters 8 (2005) A348-A352.
[7] J.L. Cohen, D.J. Volpe, D.A. Westly, A. Pechenik, H.D. Abruna, Langmuir 21 (2005) 3544-3550.
[8] J.L. Cohen, D.A. Westly, A. Pechenik, H.D. Abruna, Journal of Power Sources 139 (2005) 96-105.
[9] R. Ferrigno, A.D. Stroock, T.D. Clark, M. Mayer, G.M. Whitesides, Journal of the American Chemical Society 124 (2002) 12930-12931.
[10] S. Hasegawa, K. Shimotani, K. Kishi, H. Watanabe, Electrochemical and Solid State Letters 8 (2005) A119-A121.
[11] R.S. Jayashree, D. Egas, J.S. Spendelow, D. Natarajan, L.J. Markoski, P.J.A. Kenis, Electrochemical and Solid State Letters 9 (2006) A252-A256.
[12] R.S. Jayashree, L. Gancs, E.R. Choban, A. Primak, D. Natarajan, L.J. Markoski, P.J.A. Kenis, Journal of the American Chemical Society 127 (2005) 16758-16759.
[13] E. Kjeang, A.G. Brolo, D.A. Harrington, N. Djilali, D. Sinton, Journal of the Electrochemical Society 154 (in press)
[14] E. Kjeang, J. McKechnie, D. Sinton, N. Djilali, Journal of Power Sources 168 (2007) 379-390.
[15] E. Kjeang, R. Michel, N. Djilali, D. Sinton, Manuscript in preparation)
[16] E. Kjeang, B.T. Proctor, A.G. Brolo, D.A. Harrington, N. Djilali, D. Sinton, Electrochimica Acta 52 (2007) 4942-4946.
[17] E. Kjeang, D. Sinton, D.A. Harrington, Journal of Power Sources 158 (2006) 1-12.
[18] S.M. Mitrovski, L.C.C. Elliott, R.G. Nuzzo, Langmuir 20 (2004) 6974-6976.
[19] S.M. Mitrovski, R.G. Nuzzo, Lab on a Chip 6 (2006) 353-361.
[20] K.G. Lim, G.T.R. Palmore, Biosensors & Bioelectronics 22 (2007) 941-947.
[21] C.M. Moore, S.D. Minteer, R.S. Martin, Lab on a Chip 5 (2005) 218-225.
[22] M. Togo, A. Takamura, T. Asai, H. Kaji, M. Nishizawa, Electrochimica Acta 52 (2007) 4669-4674.
[23] A. Kundu, J.H. Jang, J.H. Gil, C.R. Jung, H.R. Lee, S.H. Kim, B. Ku, Y.S. Oh, Journal of Power Sources 170 (2007) 67-78.
[24] J.D. Morse, International Journal of Energy Research 31 (2007) 576-602.

[25] Y.M. Zhu, Z. Khan, R.I. Masel, Journal of Power Sources 139 (2005) 15-20.
[26] S. Licht, Electrochemistry Communications 1 (1999) 33-36.
[27] A.M. Cardenas-Valencia, C.J. Biver, L. Langebrake, Journal of Power Sources 166 (2007) 273-283.
[28] M.G. Medeiros, E.G. Dow, Journal of Power Sources 80 (1999) 78-82.
[29] S.J. You, Q.L. Zhao, J.N. Zhang, J.Q. Jiang, S.Q. Zhao, Journal of Power Sources 162 (2006) 1409-1415.
[30] J.J. Whalen, J.D. Weiland, P.C. Searson, Journal of the Electrochemical Society 152 (2005) C738-C743.
[31] D.D. Wagman, W.H. Evans, V.B. Parker, R.H. Schumm, I. Halow, S.M. Bailey, K.L. Churney, R.L. Nuttall, Journal of Physical and Chemical Reference Data 11 (1982) 1-&.
[32] CRC Handbook of Chemistry and Physics, CRC Press, Boca Raton, FL, 2002.

Figure Captions

Figure 1. Electrodeposition of gold on porous carbon electrodes: (a) cyclic voltammogram of a bare substrate in gold plating solution measured at 50 mV s^{-1}, and (b) potentiostatic deposition curves at three different potentials (as indicated vs. SCE).

Figure 2. Scanning electron micrographs showing the microstructure of the porous gold electrodes electrodeposited on carbon paper substrates at (a) -0.7 V, (b) -0.9 V and (c) -1.1 V (SCE), captured at 2000x magnification.

Figure 3. Scanning electron micrographs of a porous gold electrode electrodeposited at -1.1 V (SCE), captured at (a) 60x, (b) 800x and (c) 6000x magnification.

Figure 4. Cyclic voltammograms measured *ex situ* for formate oxidation on a porous palladium anode and hypochlorite reduction on porous gold and palladium cathodes in a stationary three-electrode electrochemical cell. The anolyte

and catholyte consisted of 1.2 M formate and 0.67 M hypochlorite, respectively, in alkaline solution. The scan rate was 50 mV s^{-1}.

Figure 5. Labeled images of the assembled microfluidic fuel cell with flow-through porous palladium and gold electrodes.

Figure 6. Fuel cell polarization curves measured experimentally at steady state and room temperature, for operation at three different flow rates (as indicated).

Figure 7. Fuel cell polarization data of anode and cathode measured *in situ* at room temperature and 60 μL min^{-1} flow rate, using the opposite fuel cell electrode as counter electrode and an external reference electrode (SCE).

Figure 8. Power density curves for formate/hypochlorite fuel cell operation at steady state and room temperature, measured at three different flow rates (as indicated).

List of figures

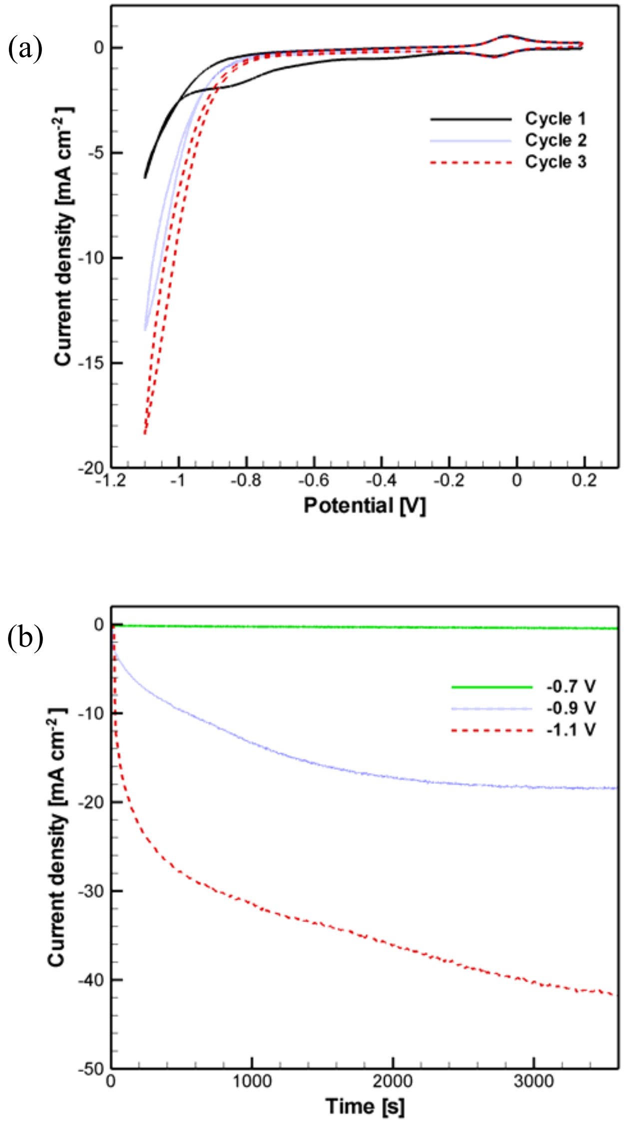

Figure 1. Electrodeposition of gold on porous carbon electrodes: (a) cyclic voltammogram of a bare substrate in gold plating solution measured at 50 mV s^{-1}, and (b) potentiostatic deposition curves at three different potentials (as indicated vs. SCE).

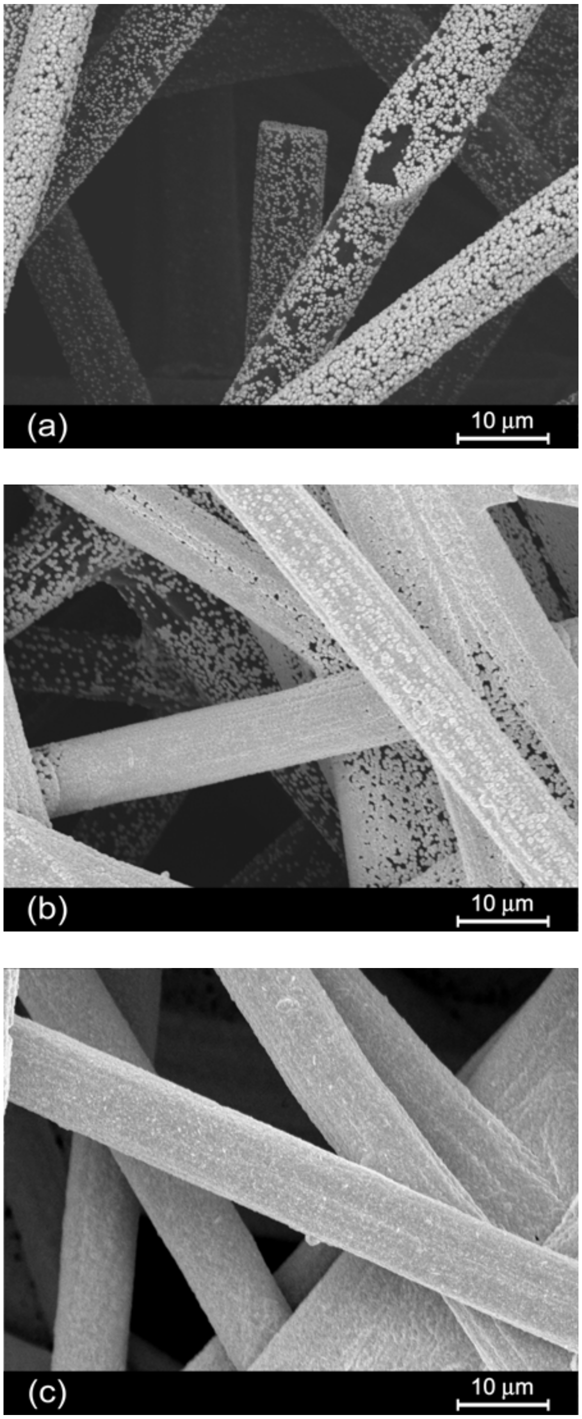

Figure 2. Scanning electron micrographs showing the microstructure of the porous gold electrodes electrodeposited on carbon paper substrates at (a) -0.7 V, (b) -0.9 V and (c) -1.1 V (SCE), captured at 2000x magnification.

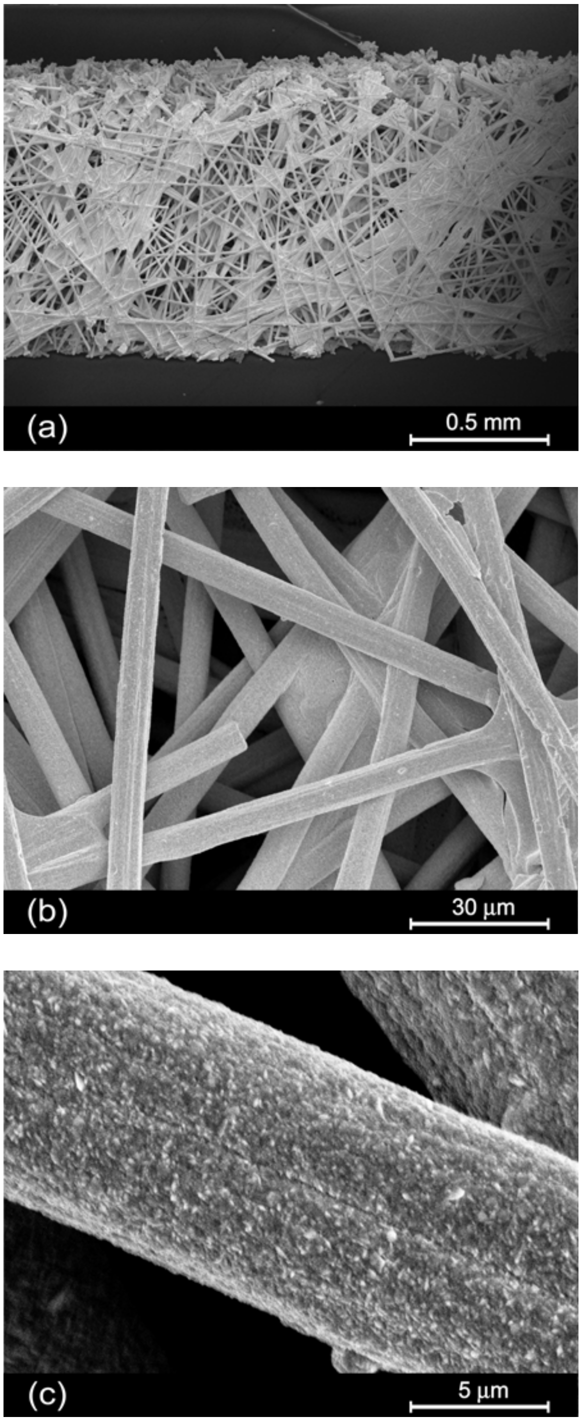

Figure 3. Scanning electron micrographs of a porous gold electrode electrodeposited at -1.1 V (SCE), captured at (a) 60x, (b) 800x and (c) 6000x magnification.

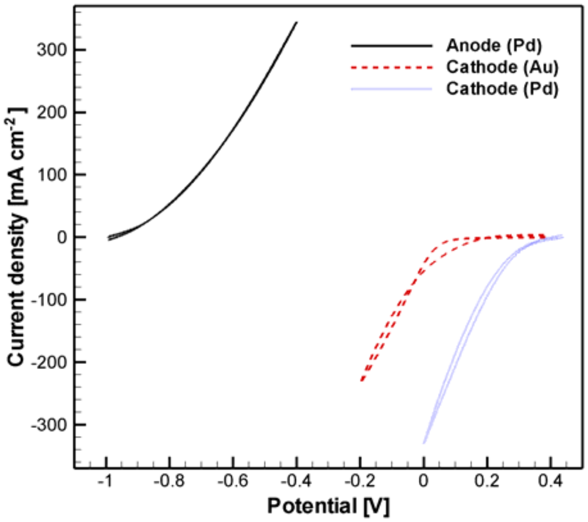

Figure 4. Cyclic voltammograms measured *ex situ* for formate oxidation on a porous palladium anode and hypochlorite reduction on porous gold and palladium cathodes in a stationary three-electrode electrochemical cell. The anolyte and catholyte consisted of 1.2 M formate and 0.67 M hypochlorite, respectively, in alkaline solution. The scan rate was 50 mV s^{-1}.

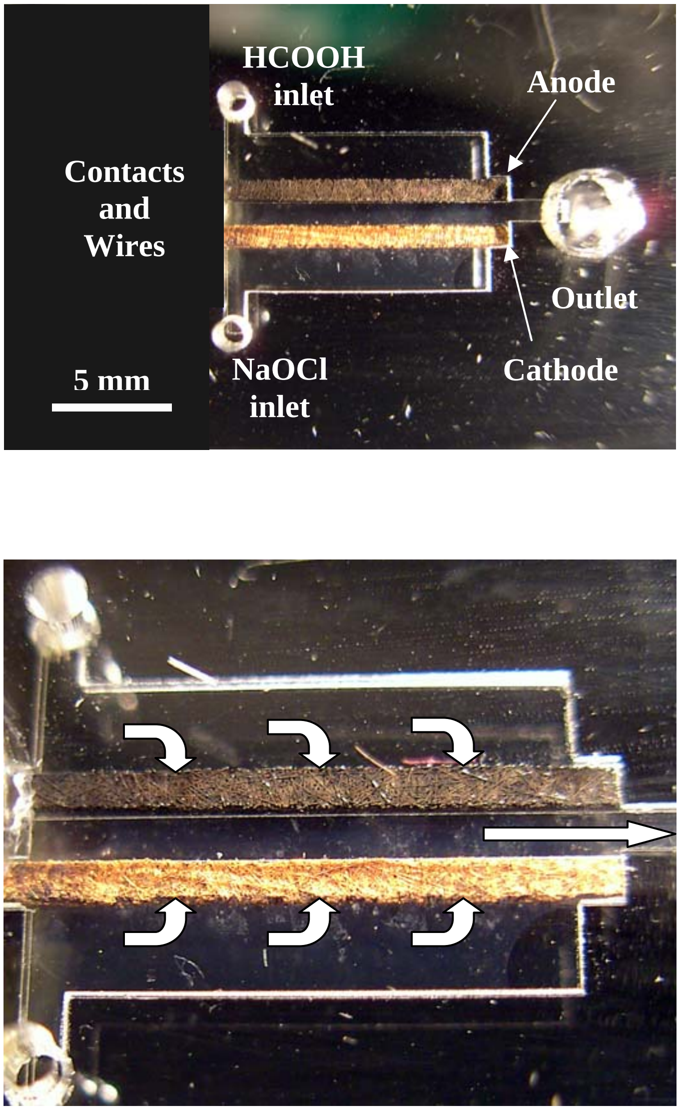

Figure 5. Labeled images of the assembled microfluidic fuel cell with flow-through porous palladium and gold electrodes.

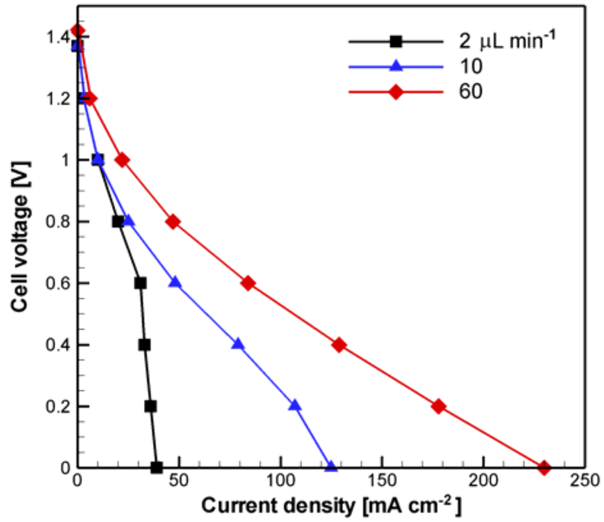

Figure 6. Fuel cell polarization curves measured experimentally at steady state and room temperature, for operation at three different flow rates (as indicated).

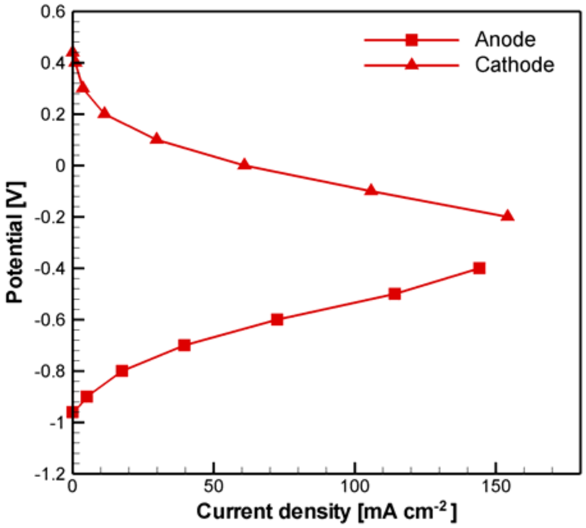

Figure 7. Fuel cell polarization data of anode and cathode measured *in situ* at room temperature and 60 μL min^{-1} flow rate, using the opposite fuel cell electrode as counter electrode and an external reference electrode (SCE).

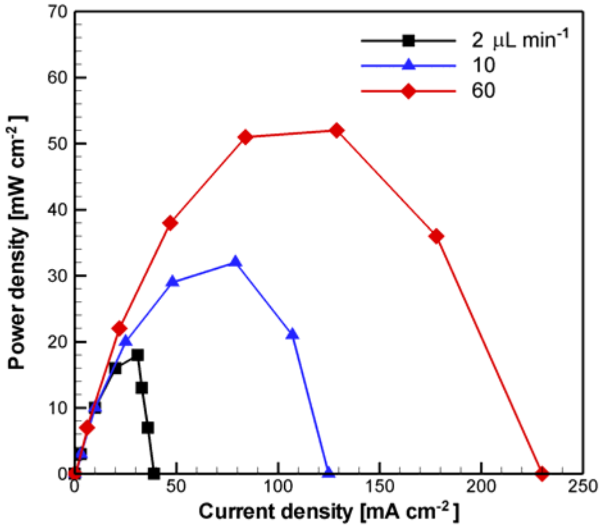

Figure 8. Power density curves for formate/hypochlorite fuel cell operation at steady state and room temperature, measured at three different flow rates (as indicated).

Appendix G

Strategic Enzyme Patterning for Microfluidic Biofuel Cells

Reproduced by permission of Elsevier

Available online at www.sciencedirect.com

SCIENCE DIRECT®

Journal of Power Sources 158 (2006) 1–12

JOURNAL OF POWER SOURCES

www.elsevier.com/locate/jpowsour

Strategic enzyme patterning for microfluidic biofuel cells

E. Kjeang [a], D. Sinton [a,*], D.A. Harrington [b]

[a] *Department of Mechanical Engineering, Institute for Integrated Energy Systems (IESVic), University of Victoria,*
P.O. Box 3055 STN CSC, Vic., BC, Canada V8W 3P6
[b] *Department of Chemistry, Institute for Integrated Energy Systems (IESVic), University of Victoria,*
P.O. Box 3055 STN CSC, Vic., BC, Canada V8W 3P6

Received 12 July 2005; accepted 30 July 2005
Available online 1 December 2005

Abstract

The specific character of biological enzyme catalysts enables combined fuel and oxidant channels and simplified non-compartmentalized fuel cell assemblies. In this work, a microstructured enzymatic biofuel cell architecture is proposed, and species transport phenomena combined with consecutive chemical reactions are studied computationally in order to provide guidelines for optimization. This is the first computational study of this technology, and a 2D CFD model for species transport coupled with laminar fluid flow and Michaelis–Menten enzyme kinetics is established. It is shown that the system is reaction rate limited, indicating that enzyme specific turnover numbers are key parameters for biofuel cell performance. Separated and mixed enzyme patterns in different proportions are analyzed for various Peclet numbers. High fuel utilization is achieved in the diffusion dominated and mixed species transport regimes with separated enzymes arranged in relation to individual turnover rates. However, the Peclet number has to be above a certain threshold value to obtain satisfying current densities. The mixed transport regime is particularly attractive while current densities are maintained close to maximum levels. Optimum performance is achieved by mixed enzyme patterning tailored with respect to individual turnover rates, enabling high current densities combined with nearly complete fuel utilization.

Keywords: Biofuel cell; Enzyme kinetics; Biocatalysis; Microfluidics; Numerical modeling; Consecutive reactions

---

1. Introduction

In recent years, the demand on the power supplies of portable electronic equipment such as laptops and cellular phones has substantially increased due to additional technical features and miniaturization efforts. Well-developed lithium ion battery technology currently powers most of these applications. It is unlikely, however, that improvements in battery technology will keep pace with the accelerating power demand [1]. In order to enable further advances, other alternatives such as fuel cells have to be considered. The high cost associated with the development of new small-scale fuel cell power supplies are surpassed by the growing portable power needs of the mobile workforce and the major industries that now support them [2]. Direct methanol fuel cells exhibit relatively high power and energy densities [3], but there are several problems associated with these, for instance methanol crossover and slow anode kinetics reduce efficiency and open-circuit voltage [4-5]. Recently, this technology has been challenged by emerging microscale biofuel cell designs.

A biofuel cell is not necessarily a fuel cell that uses a biological fuel, although that might very well be the case. Biofuel cells always involve biological molecules or living cells to catalyze the chemical reactions, replacing conventional transition metal catalysts such as platinum. The underlying concept is to control electrochemical processes occurring in nature to provide useful electrical current. Chemical energy can be converted to electrical energy by coupling the biocatalytic oxidation of organic or inorganic compounds to the chemical reduction of an oxidant in a controlled environment. There are two main types of biofuel cells; microbial biofuel cells and enzymatic biofuel cells. Microbial fuel cells utilize entire living cells or microorganisms combined with redox intermediates to catalyze the oxidation of a fuel. Microbe catalyzed processes involve several fairly complex steps with various intermediates [6] and are quite inefficient [7]. In an enzymatic biofuel cell, the chemical reactions are catalyzed by biological redox enzymes that can be separated and

---

[*] Corresponding author. Tel.: +1 250 721 8623; fax: +1 250 721 6051.
E-mail address: dsinton@me.uvic.ca (D. Sinton).

0378-7753/$ – see front matter © 2005 Elsevier B.V. All rights reserved.
doi:10.1016/j.jpowsour.2005.07.092

Nomenclature

A_c	cross-sectional area (m^2)
c	concentration ($mol\,m^{-3}$)
D	solute diffusivity ($m^2\,s^{-1}$)
D_h	hydraulic diameter (m)
Da	Damköhler number
F	Faraday's constant ($C\,mol^{-1}$)
FU	fuel utilization
g	constant of gravity ($m\,s^{-2}$)
h	channel height (m)
i	current density ($A\,m^{-2}$)
J	species molar flux ($mol\,s^{-1}\,m^{-2}$)
k	rate constant (s^{-1})
k_{cat}	turnover number (s^{-1})
K_m	sensitivity ($mol\,m^{-3}$)
L	axial length of electrode (m)
L_c	characteristic length (m)
M	molar mass ($kg\,mol^{-1}$)
N_A	Avogadro's number (mol^{-1})
p	pressure (Pa)
Pe	Peclet number
R	turnover rate ($mol\,s^{-1}\,m^{-2}$)
Re	Reynolds number
t	time (s)
T	temperature (K)
u	bulk velocity ($m\,s^{-1}$)
$\bar{u}$	mean bulk velocity ($m\,s^{-1}$)
V_{out}	output voltage (V)
$\dot{V}$	volumetric flow rate ($m^3\,s^{-1}$)
v	specific activity ($mol\,kg^{-1}\,s^{-1}$)
w	channel width (m)
$\dot{W}_{out}$	output power (W)
$\dot{W}_p$	pumping power (W)
x	direction of main flow (axial)
y	direction across channel (transverse)
z	number of electrons

Greek letters

μ	kinematic viscosity ($kg\,m^{-1}s^{-1}$)
ρ	density ($kg\,m^{-3}$)

Subscripts

in	inlet value
max	maximum value
out	outlet value
ref	reference value
0	bulk value

Superscripts

A	methanol dehydrogenase (MDH)
ADH	alcohol dehydrogenase
B	formaldehyde dehydrogenase (FalDH)
C	formate dehydrogenase (FDH)

purified from suitable organisms, thus extracting the actual part of the cell that enables catalytic operation [8]. Enzyme catalysts are specific to particular substances (fuels) and the presence of other substances does not, in general, impact the rate of catalysis. This specificity of enzyme catalysis enables the combination of fuel and oxidant streams in a single manifold [8], with multiple benefits in the context of fuel cell design and operation: no proton exchange membrane is needed, sealing, manifolding and fluid delivery requirements are greatly reduced, ohmic losses and water management issues associated with proton exchange membrane fuel cell (PEMFC) technologies are eliminated [9], as are two-phase transport issues associated with gas diffusion layers [10]. With fuel and oxidant streams fully mixed in the same channel, fuel crossover is also not a problem. Cost reduction is possibly the main aspect that can make biological fuel cells competitive for small-scale power supplies. Firstly, the proton exchange membrane is a costly component of conventional fuel cell assemblies [11]. Secondly, the cost of platinum, which is already high, is expected to increase further with increased demand and production [12]. Biological enzymes, on the other hand, are derived from naturally abundant organisms and can be produced using low-cost fermentation techniques [13]. Other benefits are operation near or at room temperature and compact units produced by inexpensive and well-established microfabrication methods. Channels down to 10 μm in diameter can be fabricated, greatly improving the active surface-to-volume ratio of the device and consequently its power density, which remains quite limited with current biofuel cell designs. As with all fuel cell technologies, however, stability is a key issue for biofuel cells [13]. Enzymatic biofuel cells must withstand extended use, varied duty cycles, a range of environmental conditions and must reach lifetimes satisfying the demands of advanced applications, preferably on the order of years. Possible applications range from miniaturized portable electronic equipment [2] and sensors to integrated lab-on-chip power supplies [14] and advanced in vivo diagnostic medical devices with reactants available in the ambient environment [13].

In most enzymatic biofuel cells developed to date, enzymes are placed in solution and the electron transfer from the enzyme biocatalysts to the electrode is mediated by a redox couple. The rate of electron transfer is generally limited by the ability of the redox species to diffuse back and forth. Several methods to improve electron transfer rates by immobilization of enzymes on electrode surfaces have been presented, for example: covalent enzyme–electrode polymer linkages, layered electrodes obtained by functional monolayers and non-covalent coupling by hydrophobic/hydrophillic or affinity interactions [15]. Electron mediators (co-factors) extracting electrons from the active sites of the enzymes are necessary for efficient flow of electrical current [8]. Alcohol dehydrogenase enzymes were immobilized in Nafion by Moore et al. [14] and their ethanol fuelled anode reached an open-circuit voltage of 0.34 V and current densities of 53 $\mu A\,cm^{-2}$ using an external platinum cathode. The highest open-circuit voltage (0.71 V) and power density (1.5 $mW\,cm^{-2}$) for a methanol/oxygen biofuel cell was observed when the biocatalyst was immobilized close to the anode and utilized its electron mediator [16]. To achieve this, complete oxidation of

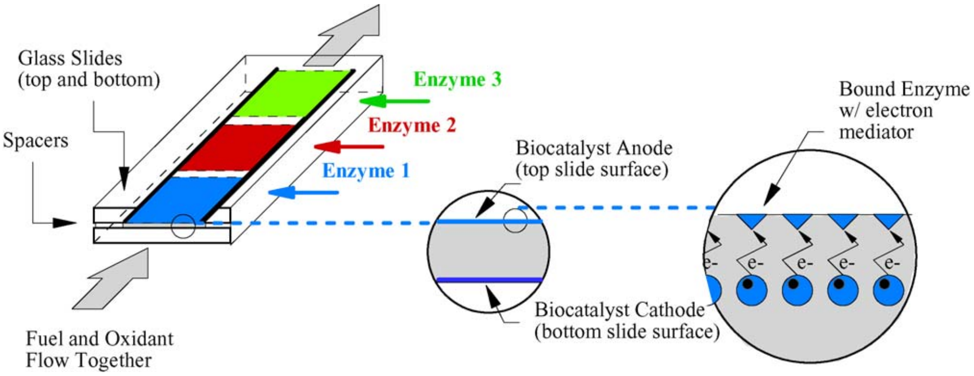

Fig. 1. Proof-of-concept microfluidic biofuel cell design.

methanol to carbon dioxide by three different enzymes was engaged. Patterning multiple enzyme electrodes to harness consecutive reactions represents a significant opportunity for biofuel cell technologies, particularly with respect to fuel utilization.

The biocatalysts of interest here are covalently linked directly to the electrode surface via electron mediators (cofactor) that are immobilized in contact with the active enzyme sites. Biomimetic dyes are used as electron mediators; they insert into the binding site on the enzyme and bind specifically and irreversibly without interfering with the catalytic activity of the enzyme. An illustration of the proof-of-concept microfluidic biofuel cell is shown in Fig. 1, with a schematic depiction of the surface-bound biocatalysts. The simple flat-plate microchannel design facilitates a high surface-to-volume ratio, effectively one-dimensional flow behavior, rapid cross-stream diffusion and straightforward surface preparation. Prior to assembly, an electrically conducting material is deposited on the interior surfaces to form the anode and cathode, and the enzymes are tethered directly to these layers.

The focus of this study is to model species transfer associated with heterogeneous chemical reactions and enzyme kinetics based on the microchannel geometry in Fig. 1. The first aim is to determine whether the process is diffusion limited or reaction rate limited. Secondly, various enzyme-electrode patterns coupled with coherent bulk velocities are investigated in order to realize efficient fuel cell operation. This is the first computational study of this technology, and the results are intended to provide guidelines for the design and fabrication of microfluidic biofuel cells exploiting consecutive reactions. The long-term objective is to integrate the forefront of molecular biology with advanced microfabrication techniques to produce practical biofuel cell systems with novel architectures that result in advanced functionality.

2. Method

2.1. Enzyme kinetics

An enzyme converts one chemical species (the substrate) into another one (the product). The substrate concentration distribution in the combined fuel and oxidant feed stream of a microfluidic biofuel cell depends on the rate of the heterogeneous chemical reactions taking place on the biocatalytic electrode surfaces. For now, we ignore the coupled effects of oxidant transport and cathode kinetics and instead focus on the anodic process. The Damköhler number represents the ratio of reaction velocity to diffusive velocity defined as

$$Da = \frac{k c_0^{\upsilon-1}}{D/L_c} \qquad (1)$$

In this equation, k is a rate constant for heterogeneous reactions, c_0 the bulk concentration, υ the overall order of reaction, D the diffusion coefficient and L_c is a characteristic length. There are two common scenarios:

(1) $Da \gg 1$: diffusion limited scenario
The reaction rate is fast compared to substrate diffusion to the catalyst site. Substrate transport is occurring at its maximum rate with approximately zero concentration at the reaction surface.

(2) $Da \ll 1$: reaction rate limited scenario
Diffusion of species is fast compared to the reaction rate. The concentration of substrate at the reaction surface is approximately equal to the bulk concentration.

To determine if the biofuel cell is diffusion limited or reaction rate limited, an appropriate system to model is the well-known horse liver alcohol dehydrogenase (ADH) enzyme kinetics for ethanol oxidation to acetaldehyde. The ADH catalyzed reaction is a one-step process, namely

$$CH_3CH_2OH \xrightarrow{ADH} CH_3CHO + 2H^+ + 2e^-$$

Wild type horse liver ADH has a maximum turnover number for catalytic ethanol oxidation of $k_{cat}^{ADH} = 155\,s^{-1}$ for pH from 8 to 10 [17]. It is a dimer with an irregular shape which makes it difficult to measure its size. The unit cell of a $P2_1$ space group of a crystal structured form of ADH is reported to be $55.05 \times 73.63 \times 92.49$ Å ($\beta = 102.6°$) [18]. As a rule-of-thumb, its molecular cross-sectional area can be estimated to be around $A_c = 10^{-16}\,m^2$. If we assume that the electrode surface coverage of enzymes is complete, the maximum turnover rate for the heterogeneous reaction can be calculated as

$$R_{\max} = k_{\text{cat}}[\text{E}] = \frac{k_{\text{cat}}}{A_{\text{c}} N_{\text{A}}} \tag{2}$$

The surface concentration of enzymes is in our case equal to $[\text{E}] = (A_{\text{c}} N_{\text{A}})^{-1}$. Thus, we get

$$R_{\max}^{\text{ADH}} = \frac{k_{\text{cat}}^{\text{ADH}}}{A_{\text{c}} N_{\text{A}}} = \frac{155}{10^{-16} \times 6.02 \times 10^{23}} = 2.6 \times 10^{-6} \text{mol m}^{-2}\,\text{s}^{-1}$$

The one-dimensional diffusive species flux is defined as

$$J = -D \frac{\partial c}{\partial x} \tag{3}$$

If we consider a microchannel $h = 20\ \mu\text{m}$ in height with a bulk ethanol concentration of 500 mM, the maximum diffusive flux of ethanol becomes

$$J = -D \frac{c_0}{h} \cong 10^{-9} \frac{0.5 \times 10^3}{20 \times 10^{-6}} = 2.5 \times 10^{-2}\ \text{mol m}^{-2}\,\text{s}^{-1}$$

Thus, species diffusion is about four orders of magnitude faster than the reaction rate, indicating that the system is reaction rate limited ($Da \ll 1$). Even if the turnover rate was improved by a factor of 100, the anodic process would still be reaction rate limited.

The methanol fuelled biofuel cell oxidizes methanol to carbon dioxide via the simplified three-step process

$$\text{CH}_3\text{OH} \xrightarrow{\text{MDH}} \text{HCHO} + 2\text{H}^+ + 2\text{e}^-$$

$$\text{HCHO} + \text{H}_2\text{O} \xrightarrow{\text{FalDH}} \text{HCOO}^- + 3\text{H}^+ + 2\text{e}^-$$

$$\text{HCOO}^- \xrightarrow{\text{FDH}} \text{CO}_2 + \text{H}^+ + 2\text{e}^-$$

The turnover numbers and average sizes of the three catalytic enzymes participating in this process are expected to be of the same order of magnitude as for ADH, and all systems are therefore expected to be reaction rate limited. These new enzymes appear less frequently in the literature and there is relatively little appropriate data. Table 1 presents a summary of the information available in enzyme databases. The relatively low MDH activity is strongly enhanced by a 50 kDa activator protein from the same organism, resulting in a 40-fold increase in the MDH turnover rate (included in the tabulated value) [20]. A protein purified from *Methylococcus capsulatus* has been shown to improve the specific activity of FalDH [23]. There are also higher specific activities available for FDH purified from *Pseudomonas oxalaticus* with cofactor methylene blue or NAD [24]. Turnover numbers are normally not available in the literature, but can be calculated based on the specific activity, v, as described by the Michaelis–Menten model for first-order, steady-state enzyme kinetics [25],

$$v = \frac{v_{\max} c_0}{K_{\text{m}} + c_0} \tag{4}$$

The sensitivity K_{m} is a measure of the changes in reaction velocity when the substrate availability is reduced, in fact, K_{m} represents the substrate concentration value at which the reaction velocity is half-maximum, $v = v_{\max}/2$. Catalytic oxidation of primary alcohols by alcohol dehydrogenases using cofactors in fact resembles two-substrate reactions described by the Theorell–Chance mechanism, where a ternary complex is presumably formed but its breakdown to yield the first product is very fast so that the ternary complex is kinetically insignificant [26]. With the cofactor bound to the enzyme, one can assume that the binding of substrate is the rate-limiting step as in an ordinary one-substrate mechanism, expressed in the classic Michaelis–Menten model of two-stage enzyme–substrate action,

$$\text{E} + \text{S} \underset{k_{-1}}{\overset{k_1}{\rightleftarrows}} \text{ES} \xrightarrow{k_2} \text{E} + \text{P}$$

The single substrate S binds reversibly to the enzyme E in the first stage, and the single product P is formed in the second stage. The sensitivity in Eq. (4) combines the effects of forward rate constant k_1, back rate constant k_{-1} and product formation rate constant k_2. Fig. 2 shows a typical Michaelis–Menten curve with normalized variables $v/v_{\max}$ and c_0/K_{m}. If the sensitivity is small relative to the bulk concentration, c_0, the specific activity is close to its maximum value. This implies that fuel cell

Table 1
Enzyme data valid for enzymes in solution

	MDH [20]	FalDH [21]	FDH [22]	ADH [17–19]
EC number	1.1.1.244	1.2.1.46	1.2.1.2	1.1.1.1
Organism	*B. methanolicus*	*P. putida*	*P. putida* sp. 101	*E. caballus*
Substrate	Methanol	Formaldehyde	Formate	Ethanol
Product	Formaldehyde	Formate	CO_2	Acetaldehyde
Cofactor	NAD	NAD	NAD	NAD
Number of subunits	10	4	6	2
Molecular weight (kDa)	430	250	280	–
Specific activity (μmol min^{-1} mg^{-1})	10.4	8.3	2.43	–
Max substrate conc. (M)	0.5	–	–	–
Required ions	Mg^{2+}, Zn^{2+}	–	–	–
Optimum temperature (°C)	–	30–40	40	–
Optimum pH	–	8.5	8	8–10
Sensitivity (mM)	0.99	0.2	0.62	7
Diameter (nm)	15			10

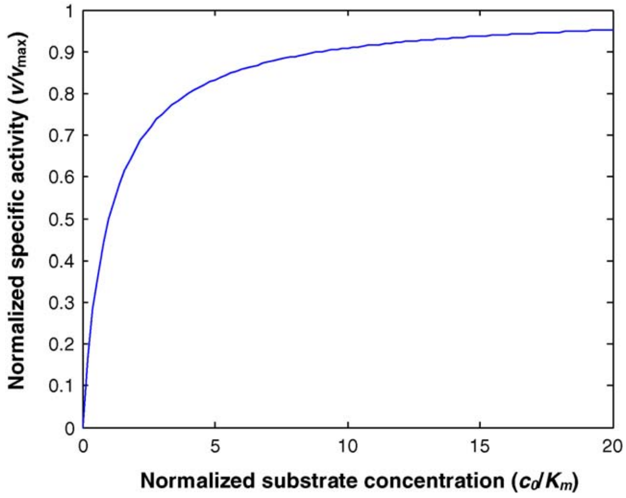

Fig. 2. Normalized Michaelis–Menten curve for enzyme kinetics.

operation near maximum specific activity is possible even with concentrations almost as low as K_m. For example if $c_0 = 5K_m$, we get $v = 0.83v_{max}$, which is only 17% short of the maximum value.

Specific activities found in the literature are often given in terms of catalytic turnover numbers per unit mass of protein in the enzyme sample. Assuming that the enzymes are fully purified, the actual molecular turnover number can be calculated as

$$k_{cat} = vM \tag{5}$$

The enzyme molecular mass, M, is also available in enzyme databases. Using Eq. (5) the maximum turnover numbers may be estimated as follows,

$$\text{MDH}: \quad k^{A}_{cat,max} = \frac{10.4 \times 10^{-6}}{60} \times 430 \times 10^{6} = 75\,\text{s}^{-1}$$

$$\text{FalDH}: \quad k^{B}_{cat,max} = \frac{8.3 \times 10^{-6}}{60} \times 250 \times 10^{6} = 35\,\text{s}^{-1}$$

$$\text{FDH}: \quad k^{C}_{cat,max} = \frac{2.43 \times 10^{-6}}{60} \times 280 \times 10^{6} = 11\,\text{s}^{-1}$$

We denote methanol, formaldehyde and formate oxidation with superscripts A, B and C, respectively. Note that the use of tabulated values for these calculations can be treacherous, as the values vary depending on variations in molecular structure and ambient conditions such as temperature and pH. Although these turnover numbers are expected to be order-of-magnitude correct, a targeted experimental study in this area would be very beneficial. To determine the flux of substrate and product to and from the electrode surface for a reaction rate limited system, we require estimates of the average size of the enzyme molecules and the average surface coverage. For an order-of-magnitude estimate we assume complete monolayer surface coverage and size equivalent to the cross-sectional area used for ADH, $A_c = 10^{-16}\,\text{m}^2$, for all three enzymes. The turnover rates are then

$$\text{MDH}: \quad R^{A}_{max} = \frac{75}{10^{-16} \times 6.02 \times 10^{23}} = 1.2 \times 10^{-6}\,\text{mol}\,\text{m}^{-2}\,\text{s}^{-1}$$

$$\text{FalDH}: \quad R^{B}_{max} = \frac{35}{10^{-16} \times 6.02 \times 10^{23}} = 5.7 \times 10^{-7}\,\text{mol}\,\text{m}^{-2}\,\text{s}^{-1}$$

$$\text{FDH}: \quad R^{C}_{max} = \frac{11}{10^{-16} \times 6.02 \times 10^{23}} = 1.9 \times 10^{-7}\,\text{mol}\,\text{m}^{-2}\,\text{s}^{-1}$$

If all the electrons released by the chemical reactions are captured by the electron mediators, the maximum current density at each enzyme patch is obtained by

$$i_{max} = \text{zFR}_{max} \tag{6}$$

Here, z represents the number of electrons released by oxidation of one substrate molecule. Note that all turnover parameters and current densities also depend on bulk concentration and enzyme sensitivity via the Michaelis–Menten model for first-order enzyme catalysis given in Eq. (4). The actual turnover rates and current densities are thus written as

$$R = R_{max}\frac{c_0}{K_m + c_0} \tag{7}$$

$$i = i_{max}\frac{c_0}{K_m + c_0} \tag{8}$$

As before, if the substrate concentration is high compared to the sensitivity ($c_0 \gg K_m$), the Michaelis–Menten kinetic effects can be neglected. This is not always the case in consecutive chemical processes, as some concentrations will approach zero, especially if effectively complete fuel utilization is achieved.

A complete biofuel cell must also contain a cathode, where the protons and electrons released at the anode are captured in order to provide a closed electrical circuit. The need for high pressures and temperatures make conventional O_2-reducing cathodes incompatible with biocatalytic anodes. For consistency with the specificity of the biofuel cell concept, the cathodic chemical reaction should also be catalyzed by suitable redox enzymes. Two options are considered in this work, either reduction of oxygen to water catalyzed by the bilirubin oxidase enzyme or peroxide reduction to water catalyzed by the catalase–peroxidase enzyme. Peroxide is preferable from an oxidant supply point-of-view given that it is miscible with water in all proportions and can easily be added to the liquid mixture in the microchannel. Oxygen for the cathodic reaction can also be dissolved in water, but only in relatively low concentrations. Alternatively, using a gas permeable backing material such as poly(dimethylsiloxane) (PDMS) [27], oxygen from the ambient air could diffuse through the backing layer to supplement the dissolved oxygen for the cathodic reaction. Oxygen has the advantage of being available in the ambient air whereas peroxide must be continuously supplied from a reservoir. The overall cell potential is however limited by the potential difference between the anode and cathode redox couples, and it appears that the theoretical potential difference achievable with peroxide is somewhat higher than for oxygen. Moreover, the single enzyme cathodic reactions described here are expected to be faster than the anodic reactions [28,29]. The focus of this study is the biofuel cell anode, and its inherent kinetics are assumed to be independent of the cathode characteristics.

2.2. Species transport

The diffusion coefficient of small molecules in water at room temperature is normally around $D \approx 10^{-9}\ \mathrm{m^2\,s^{-1}}$, but increases exponentially with temperature. An enzymatic biofuel cell operating at its optimum temperature, say 40 °C, is likely to experience somewhat faster diffusion. Kulikovsky [30] recommends a reference value of $D_{\mathrm{ref}} = 1.58 \times 10^{-9}\ \mathrm{m^2\,s^{-1}}$ at $T_{\mathrm{ref}} = 298\ \mathrm{K}$ for methanol in water in void pores, and use the temperature dependence

$$D_{\mathrm{MeOH/H_2O}}(T) = D_{\mathrm{ref}} \exp(0.026236(T - T_{\mathrm{ref}})) \tag{9}$$

At optimum temperature (40 °C) we get $D = 2.34 \times 10^{-9}\ \mathrm{m^2\,s^{-1}}$. This value is assumed to be valid for all solutes.

Total species flux by diffusion and advection is described by

$$\vec{J} = -D\vec{\nabla} c + c\vec{u} \tag{10}$$

The ratio of advection to diffusion is defined by the Peclet number

$$Pe = \frac{L_{\mathrm{c}}\bar{u}}{D} \tag{11}$$

The average bulk velocity is denoted by $\bar{u}$, and L_{c} is a characteristic length. For high Peclet numbers, we may neglect diffusive flux at the inlet and outlet, and species transport becomes proportional to the local concentration. With this assumption, a useful analytical expression for the species concentration distribution may be derived. Taking heterogeneous chemical reactions into account and assuming maximum reaction rates, the species balance in a channel with rectangular cross-section can be written as

$$c_{\mathrm{in}}\bar{u}hw = \sum_j R^j_{\max} L^j w + c_{\mathrm{out}}\bar{u}hw \tag{12}$$

In this relationship, c_{in} is the inlet concentration, $\bar{u}$ the average velocity, h the channel height, w the channel width, L the length of each active enzyme patch and c_{out} the outlet concentration. For a single reaction process with only one type of enzyme fully covering the anode surface, the species balance at downstream position x in the microchannel becomes

$$c_{\mathrm{in}}\bar{u}h = R_{\max}x + c(x)\bar{u}h \tag{13}$$

Solving for the concentration, we get

$$c(x) = c_{\mathrm{in}} - \frac{R_{\max}}{\bar{u}h}x \tag{14}$$

This analytical result will be used to assess the accuracy of the numerical model.

The biofuel cell system is expected to exhibit low Damköhler numbers (reaction rate limited) and therefore essentially constant substrate concentration in the cross-stream direction. In order to get complete fuel utilization, we can then design the microchannel to match zero concentration at the outlet. But because of degrading enzyme kinetics it is rather inefficient to use concentrations close to zero. Moreover, the advective flux is reduced for near-zero concentrations and the diffusive part should again be added. Thus a 2D computational model incorporating diffusive flux and concentration dependent enzyme kinetics is required. Fuel utilization based on total flux for a single reaction process is calculated as

$$\mathrm{FU} = 1 - \frac{J_{\mathrm{out}}}{J_{\mathrm{in}}} \tag{15}$$

To determine overall fuel utilization for a consecutive process we need to include the other reaction steps as well. For methanol, two electrons are released in each step, so for complete fuel utilization we get six electrons per methanol molecule. Overall fuel utilization in terms of electrons doing actual work can therefore be defined as

$$\mathrm{FU} = 1 - \frac{6J^{\mathrm{A}}_{\mathrm{out}} + 4J^{\mathrm{B}}_{\mathrm{out}} + 2J^{\mathrm{C}}_{\mathrm{out}}}{6J^{\mathrm{A}}_{\mathrm{in}}} \tag{16}$$

For instance, 100% FU for the first step in a three-step process with 0% FU for the secondary steps would result in an overall FU of 33% using this equation.

In electrochemical devices, cross-stream transport may appear due to water involvement in the chemical reactions and electro-osmotic drag. But in microscale biofuel cells where diffusion is fast compared to reaction rates such effects do not intervene with substrate transport and may readily be neglected.

2.3. CFD model

A numerical model that solves the Navier–Stokes equations for the laminar velocity profile of the bulk flow and the convective diffusion equation for solute species transport is implemented in the commercially available software package FEMLAB 3.1. The 2D channel geometry under study is $h = 20\ \mu\mathrm{m}$ in height and $L = 30\ \mathrm{mm}$ long, which is considered fixed throughout the analysis. The continuum assumption is appropriate for liquid flows in microchannels of this scale, justifying the use of continuous flow theory and established computational fluid dynamics methods [31]. The Navier–Stokes equations for conservation of mass and momentum for steady incompressible flow are given as

$$\nabla \cdot \vec{u} = 0 \tag{17}$$

$$\rho\vec{g} - \nabla p + \mu\nabla^2\vec{u} = 0 \tag{18}$$

No-slip boundary conditions are applied at the channel walls with uniform inlet velocity $\bar{u}$ and constant outlet pressure. The flows modeled here exhibit low Reynolds numbers ($Re \approx 10^{-3}$), and are steady and fully developed over the majority of the computational domain. Gravity effects are neglected, and the flow is assumed to be isotropic and isothermal throughout the domain. The convective diffusion equation for solute species conservation, with passive scalar treatment and the assumption of infinite dilution, is written as

$$\rho\frac{\partial c^i}{\partial t}+\rho\vec{u}\cdot\nabla c^i=\nabla(\rho D\nabla c^i) \tag{19}$$

c^i represents molar concentration of solute, and one separate convective diffusion equation is needed for each of the participating species. Source terms can readily be ignored since there are no homogeneous chemical reactions. Dirichlet boundary conditions are used at the inlet, that is, constant primary substrate concentration $c_{\text{in}} = 500\,\text{mM}$ representing a fuel reservoir and zero secondary species concentrations. Neumann boundary conditions are assigned to the cathode surface at $y = h$, describing an impermeable wall with zero concentration gradients $(\partial c^i/\partial y)|_{y=h}=0$. At the anode surface at $y = 0$ we have concentration dependent flux due to the heterogeneous chemical reactions. Incorporating Michaelis–Menten kinetics for the enzyme catalyzed reactions, the boundary conditions can be written as $D(\partial c^i/\partial y)|_{y=0}=R^i_{\text{max}}(c^i/(K^i_{\text{m}}+c^i))$ for sinks and $D(\partial c^i/\partial y)|_{y=0}=-R^j_{\text{max}}(c^j/(K^j_{\text{m}}+c^j))$ for sources with $i \neq j$. Purely advective flux is applied for all solutes at the outlet, $(\partial c^i/\partial x)|_{x=L}=0$.

The governing equations are coupled through velocity and chemical reactions, and can be solved either sequentially or simultaneously. The boundary conditions for the species conservation equations depend on concentration, which is one of the outputs of each iteration, and must be updated accordingly. For a consecutive process the anode boundary conditions may also depend on the concentration of other species. For example, the second species in a two-step process is produced at the same rate as the first species is consumed, i.e. its boundary condition at the production site will depend on the reaction kinetics of the first species. To solve all the governing equations of a consecutive system simultaneously thereby becomes very memory intensive. For improved efficiency, it is preferable to solve the equations sequentially as follows:

(1) Navier–Stokes equations → u, p
(2) u, c^{A} → convective diffusion eq. for species A → c^{A} (iterate)
(3) u, c^{A}, c^{B} → convective diffusion eq. for species B → c^{B} (iterate)
(4) u, c^{B}, c^{C} → convective diffusion equation for species C → c^{C} (iterate)

These types of multiphysics problems are conveniently tackled using a finite element based methodology, which can handle a wide range of coupled non-linear physical problems with dependent boundary conditions. A direct solver type that converts the non-linear governing equations to linear systems is applied, using a non-iterative, fast and unconditionally stable (always converging) approach.

Mesh optimization is an important part of problem solving using CFD. Simple elongated unstructured triangular elements with manually refined sections are used for this study, mostly because of their flexibility. A thorough mesh convergence analysis was performed for simple one-step ethanol oxidation catalyzed by ADH enzymes. The substrate concentration was intentionally kept high such that Michaelis–Menten kinetics can be ignored. Mesh control was assessed by comparing numerical results to the analytical solution derived in Section 2.2. The selected mesh, including local mesh refinements in regions with high gradients, showed an accurate concentration profile as compared to the analytical result in Eq. (14) and was also computationally viable in the context of direct solver memory limitations.

3. Results and discussion

Maximum current densities obtained from Eq. (6) are $i^{\text{C}}_{\text{max}} = 4\,\mu\text{A}\,\text{cm}^{-2}$ for FDH, $i^{\text{B}}_{\text{max}} = 11\,\mu\text{A}\,\text{cm}^{-2}$ for FalDH and $i^{\text{A}}_{\text{max}} = 24\,\mu\text{A}\,\text{cm}^{-2}$ for MDH. Ethanol oxidation by ADH can reach a maximum current density of $i^{\text{ADH}}_{\text{max}} = 50\,\mu\text{A}\,\text{cm}^{-2}$, which is close to the value reported by Moore et al. [14], $53\,\mu\text{A}\,\text{cm}^{-2}$ for Nafion immobilized enzymes. However, Moore's group points out that their biofuel cell anode is mass transfer limited because of slow species transfer through the pore network of the Nafion structure, and does not fully utilize its feasible kinetics. With electron mediator cross-linking as in our case, enzymes exposed directly to the fuel facilitate much faster mass transfer and consequently higher current densities. Using enzyme kinetics data for enzymes in solution, as in this model, is therefore likely to underestimate reaction rates, and provide a conservative estimate of fuel cell performance.

Fig. 3 presents the concentration distribution in the channel for an ethanol fuelled ADH anode with the selected mesh, and also shows the extremely large aspect ratio of the geometry (1500:1). The inlet velocity is in this case tailored for 50% theoretical fuel utilization. The substrate concentration decreases linearly with axial length, with an outlet value of 254 mM, near the predicted 250 mM for ~50% fuel utilization. The discrepancy from the analytically predicted value appears when Michalis–Menten kinetics with relatively high sensitivity are introduced; marginally reducing the reaction rates even at high substrate concentrations. The average current density, determined by boundary integration, is approximately equal to $i^{\text{ADH}}_{\text{max}}$. As shown by the contours in Fig. 3, the substrate concentration

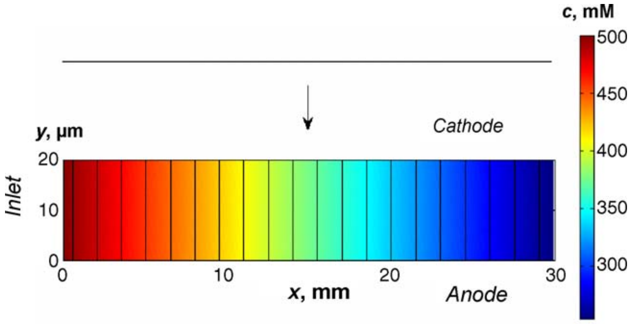

Fig. 3. Ethanol concentration in the microchannel with an ADH catalyzed anode at $y = 0$, plotted with magnified channel height. True channel geometry is shown above (aspect ratio 1500:1). Conditions: $c_{\text{in}} = 500\,\text{mM}$, $\bar{u} = 1.56 \times 10^{-5}\,\text{m}\,\text{s}^{-1}$, $h = 20 \times 10^{-6}\,\text{m}$, $L = 0.03\,\text{m}$.

is roughly constant in the cross-stream direction, indicating a reaction rate limited process.

To estimate the required pumping power for the microchannel flow, we calculate the pressure drop given from laminar flow theory [32] as

$$\Delta p = \frac{32\mu L\bar{u}}{D_\mathrm{h}^2} \tag{20}$$

With hydraulic diameter $D_\mathrm{h} = 2\,\mathrm{h}$ the pressure drop becomes $\Delta p = 5.9\,\mathrm{Pa}$. The pumping power is equal to the pressure drop multiplied by the volumetric flow rate

$$\dot{W}_\mathrm{p} = \dot{V}\Delta p = \bar{u}hw\Delta p \tag{21}$$

Furthermore, the overall power output of the fuel cell can be estimated as

$$\dot{W}_\mathrm{out} = IV_\mathrm{out} \cong iLwV_\mathrm{out} \tag{22}$$

Per unit width, we get $\dot{W}_\mathrm{p}/w \cong 10^{-9}\,\mathrm{W\,m^{-1}}$ and $\dot{W}_\mathrm{out}/w \cong 10^{-2}\,\mathrm{W\,m^{-1}}$ ($V_\mathrm{out} \cong 1\,\mathrm{V}$). The pumping power is thereby negligible.

A similar anode model is also established for three-step consecutive methanol oxidation to carbon dioxide. Six useful electrons are released in this process as opposed to only two for the one-step ethanol process. Considering the molecular mass of methanol and ethanol, respectively, the energy density of methanol is much higher. In fact, 4–5 times more useful electrons can be captured per unit mass of fuel. The methanol inlet concentration is set to 500 mM and the velocity is reduced relative to the ADH model because of additional steps and slower kinetics. As a starting point, the enzymes are distributed along the anode surface in three discrete, equally sized zones of 10 mm in length (case 1). The anode surface boundary is therefore divided into three parts and the turnover rates of MDH, FalDH and FDH are implemented in a stepwise fashion and assumed to be completely substrate specific. One electrical contact is required for each enzyme zone to avoid potential losses, and the zones have to be sufficiently separated to prevent leak currents. We assume this spacing to be thin compared to the zone lengths and apply the same microchannel geometry, material properties and other boundary conditions as in the ADH study. The solid lines of Fig. 4 present the resulting concentration distributions for a 50% methanol fuel utilization predictive inlet velocity. This figure effectively illustrates the reaction rate limited consecutive anodic process in a microchannel. The methanol concentration decreases linearly over the MDH enzyme zone, allowing the formaldehyde product concentration to increase at the same rate. Downstream of the MDH zone, the leftover methanol concentration remains constant. On the FalDH enzyme surface, formaldehyde is consumed to create formate on a one-to-one basis. The slope of the concentration curves is less steep, indicating slower kinetics than for MDH. Formate is slowly consumed on the FDH surface while the other concentrations are constant. Carbon dioxide formed on this surface is assumed to be dissolved or vented off in a way that does not disturb the kinetics of the FDH enzymes. The substrate concentrations at the outlet are $c_\mathrm{out}^\mathrm{A} = 277\,\mathrm{mM}$, $c_\mathrm{out}^\mathrm{B} = 104\,\mathrm{mM}$ and $c_\mathrm{out}^\mathrm{C} = 80\,\mathrm{mM}$ for the initial case without an extended inlet section (solid lines). The average current density is close to the maximum values for the individual enzymes, but ideally, the outlet concentrations should all be zero. Nonzero quantities indicate unused fuel and incomplete fuel utilization, which in this case is FU = 25%. The reason why $c_\mathrm{out}^\mathrm{A}$ is much larger than the predicted 250 mM is that there is a significant diffusive flux (about 5%) entering the domain at the inlet. To isolate this effect, an extended 1 cm long non-catalyzed section is added to the inlet region in the numerical model. Results with an extended inlet region are shown as dashed lines in Fig. 4 and compared to the previous results. The outlet concentrations are now $c_\mathrm{out}^\mathrm{A} = 252\,\mathrm{mM}$, $c_\mathrm{out}^\mathrm{B} = 128\,\mathrm{mM}$ and $c_\mathrm{out}^\mathrm{C} = 80\,\mathrm{mM}$ with overall fuel utilization FU = 27%. The main difference is that all species are allowed to diffuse across the interior boundary at $x = 0$, even though the methanol flux entering the domain at $x = -0.001\,\mathrm{m}$ is purely advective. In reality, the fuel reservoir and electrodes ought to be separated

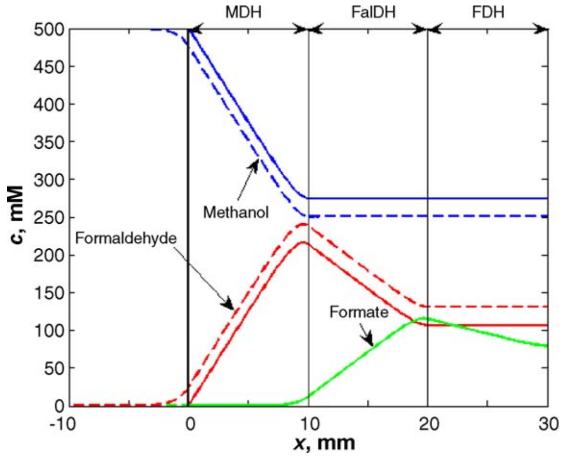

Fig. 4. Species concentration at the anode surface from inlet to outlet. Solid lines indicate results for an inlet at $x = 0$, whereas dashed lines correspond to results for an extended inlet section ($-0.01 < x < 0\,\mathrm{m}$). Conditions: $c_\mathrm{in}^\mathrm{A} = 500\,\mathrm{mM}$, $c_\mathrm{in}^\mathrm{B} = 0\,\mathrm{mM}$, $c_\mathrm{in}^\mathrm{C} = 0\,\mathrm{mM}$, $\bar{u} = 2.4 \times 10^{-6}\,\mathrm{m\,s^{-1}}$, $h = 20 \times 10^{-6}\,\mathrm{m}$. Enzyme patterning: $L^\mathrm{A} = L^\mathrm{B} = L^\mathrm{C} = 0.01\,\mathrm{m}$ (case 1).

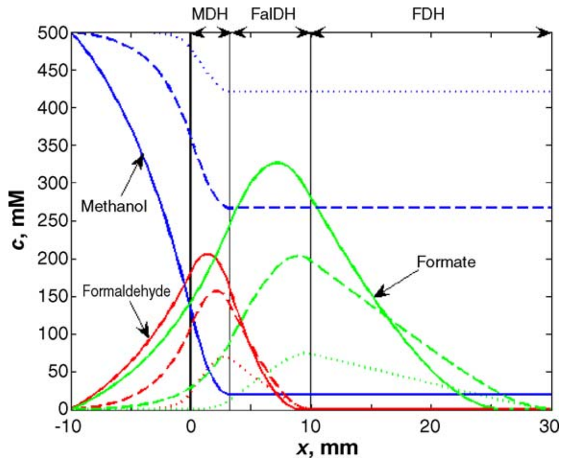

Fig. 5. Species concentration at the anode surface from inlet to outlet for various average velocities ($\bar{u} = 2.4 \times 10^{-6}\,\mathrm{m\,s^{-1}}$ for dotted lines, $\bar{u} = 0.8 \times 10^{-6}\,\mathrm{m\,s^{-1}}$ for dashed lines and $\bar{u} = 0.3 \times 10^{-6}\,\mathrm{m\,s^{-1}}$ for solid lines). Enzyme patterning: $L^\mathrm{A} = 3.2\,\mathrm{mm}$, $L^\mathrm{B} = 6.7\,\mathrm{mm}$, $L^\mathrm{C} = 20.1\,\mathrm{mm}$ (case 2).

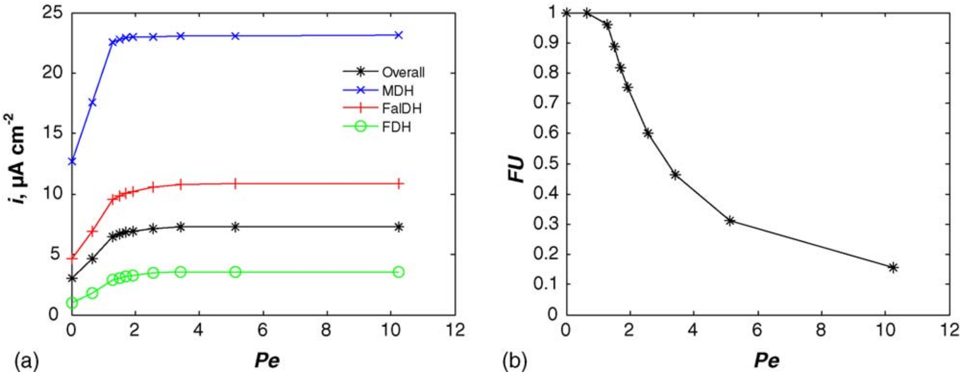

Fig. 6. Current densities (a) and fuel utilization (b) vs. Peclet number. Enzyme patterning: $L^A = 3.2$ mm, $L^B = 6.7$ mm, $L^C = 20.1$ mm (case 2).

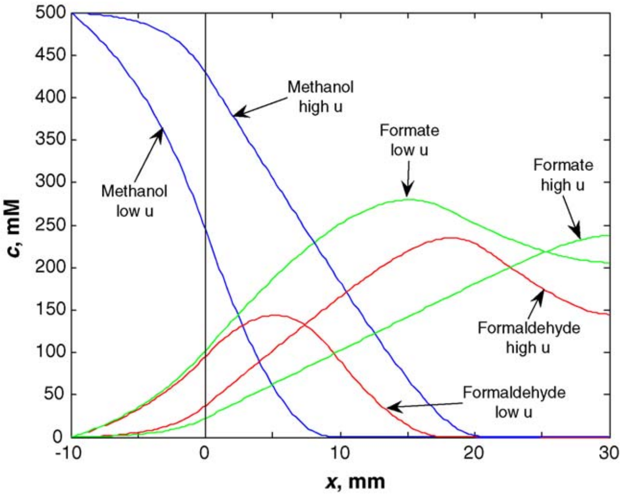

Fig. 7. Concentration distributions at the anode surface for two bulk velocities; high ($\bar{u} = 8 \times 10^{-7}\ \mathrm{m\,s^{-1}}$) and low ($\bar{u} = 3 \times 10^{-7}\ \mathrm{m\,s^{-1}}$). Enzyme patterning: mixed 1:1:1 (case 3).

in this manner by some inlet feed section with no chemical reactions.

In order to improve fuel utilization, we have to take advantage of the difference in turnover rates for the various enzymes. The zones with low turnover rates should be extended at the expense of the high rate zones. Since each reaction generates an equivalent number of electrons, the optimal lengths of the zones correspond to the ratio $1/R^A$:$1/R^B$:$1/R^C$. Assuming that $R = R_{\max}$ everywhere, we get

$$L^i = \frac{(R^i_{\max})^{-1}}{\sum_j (R^j_{\max})^{-1}} L, \quad i = \mathrm{A, B, C}, \quad j = \mathrm{A, B, C} \qquad (23)$$

For the three-step methanol process, the optimal lengths become $L^A = 3.2$ mm, $L^B = 6.7$ mm and $L^C = 20.1$ mm, which are applied in case 2. Fig. 5 shows concentration profiles with respect to these zone lengths, obtained for three different bulk velocities. Again, an extended inlet section is used. For the same velocity as in case 1 (dotted lines), the methanol concentration remains high and the other concentrations are low throughout. Case 1 does actually perform better than case 2 at high velocities. In order to reach high fuel utilization the velocity must be reduced, as can be seen by the improved methanol concentration drop as the velocity is cut down. Simultaneously, as we reduce the velocity, *Pe* numbers approach unity and an increased fraction of diffusive flux enters the non-catalyzed inlet section. An important issue to note in the case of low *Pe* is that the secondary species are able to diffuse back into the inlet section. For the lowest velocity ($\bar{u} = 0.3 \times 10^{-6}\ \mathrm{m\,s^{-1}}$), both formaldehyde and formate are able to diffuse back all the way to the fuel reservoir. Back diffusion of secondary species will in principle have no effect on fuel utilization, but it can reduce current densities due

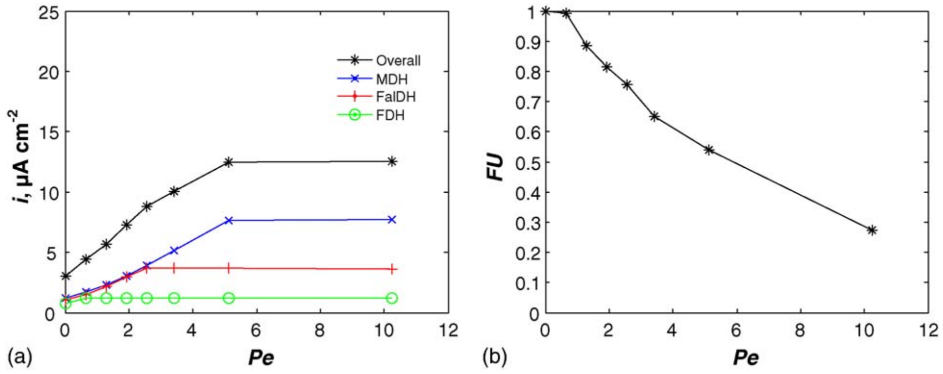

Fig. 8. Current densities (a) and fuel utilization (b) vs. Peclet number. Enzyme patterning: mixed 1:1:1 (case 3).

to a lack of secondary fuel at the enzyme sites. Current densities at the individual enzyme zones as well as the overall current density are shown in Fig. 6a, where the Peclet numbers are based on the characteristic length scale for streamwise diffusion, $L_c = 0.01$ m. The current densities decrease rapidly as the rate of diffusion overrides the rate of advection ($Pe < 1$). On the other hand, all current densities are remarkably stable in the advection dominated regime. Fuel utilization is near 100% in the diffusion dominated and mixed regimes, as indicated in Fig. 6b, unaffected by back diffusion. It is also shown that the enzyme turnover rates cannot keep up with the species transport as the velocity reaches some threshold value, causing less fuel efficient operation with unused fuel at the outlet.

Another option for the anode enzyme patterning is to mix all three types throughout the entire electrode surface using only one electrical contact, which is preferable from a fabrication point-of-view. The simplest option is to mix the enzymes on a 1:1:1 molecular basis, denoted by case 3, such that each enzyme covers one third of the surface area and the turnover rates become

$$R = \frac{1}{3} R_{\max} \frac{c}{K_m + c} \tag{24}$$

Concentration profiles for case 3 are presented in Fig. 7 for two different bulk velocities. In general, the concentration distributions are similar to the results of case 1, where a large flux of secondary species is leaving the domain at the outlet. To measure this effect, current densities (a) and overall fuel utilization (b) are given in Fig. 8 as functions of the Peclet number. High current densities are obtained in the advection dominated regime but the fuel utilization for high Pe is poor. The fuel efficiency is only sufficient in the diffusion dominated regime. It is therefore difficult to find an appropriate balance between these two parameters for the mixed enzyme electrode design, unless the individual enzyme surface coverage ratios are modified. Matching the surface coverage to the turnover rates, as in case 2, we utilize the ratios $1/R^A$:$1/R^B$:$1/R^C$. The new turnover rates adopted in case 4 are calculated by

$$R = \frac{(R_{\max})^{-1}}{\sum_j (R^j_{\max})^{-1}} R_{\max} \frac{c}{K_m + c}, \qquad j = \mathrm{A, B, C} \tag{25}$$

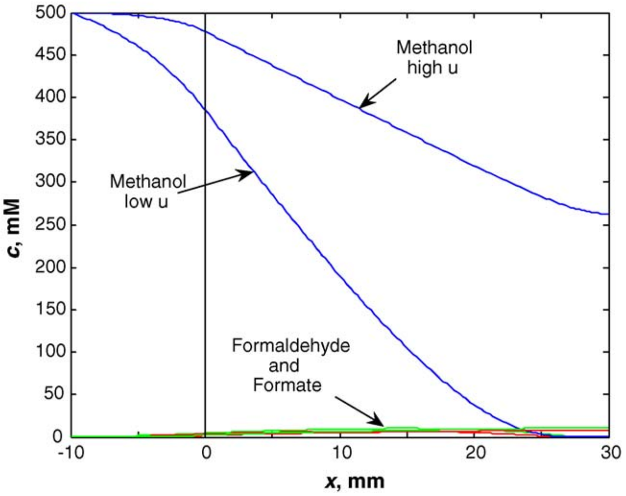

Fig. 9. Concentration distributions at the anode surface for two bulk velocities; high ($\bar{u} = 8 \times 10^{-7}$ m s^{-1}) and low ($\bar{u} = 3 \times 10^{-7}$ m s^{-1}). Enzyme patterning: mixed $1/R^A$:$1/R^B$:$1/R^C$ (case 4).

The concentration profiles obtained for case 4 are shown in Fig. 9 for the same velocities as in Fig. 7. The rate of methanol consumption is slower than in case 3 as the MDH fraction is reduced, but significant improvements are attained in terms of secondary species outlet concentrations. Fig. 10 presents current densities and fuel utilization for case 4. In this case, fuel utilization remains high and steady for a wider range of Peclet numbers. Maximum current densities are lower than for case 3 but can be realized for most Pe above unity. It is possible to combine high current densities with high fuel usage for this enzyme patterning strategy. For example, $Pe = 1.5$ provides 7.0 μA cm^{-2}, which is 99% of the maximum current density for case 4, at 99% fuel utilization.

To summarize the results obtained for the anodic three-step methanol oxidation process, Fig. 11 presents a comparison of current densities and fuel utilization for cases 1–4 at low Peclet numbers. The diffusion dominated regime ($Pe < 1$) is not recommended due to low current densities. Fuel cell performance is generally better in the mixed regime ($1 < Pe < 2$) where reasonably high current densities are met by nearly complete fuel utilization, with case 4 showing superior characteristics. In the

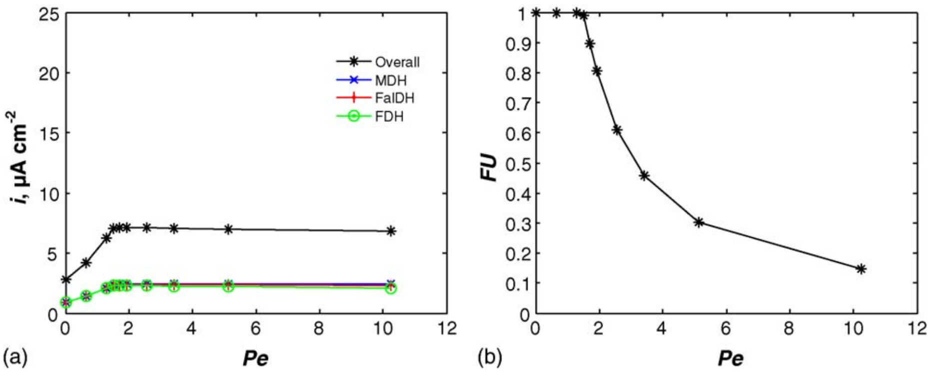

Fig. 10. Current densities (a) and fuel utilization (b) vs. Peclet number. Enzyme patterning: mixed $1/R^A$:$1/R^B$:$1/R^C$ (case 4).

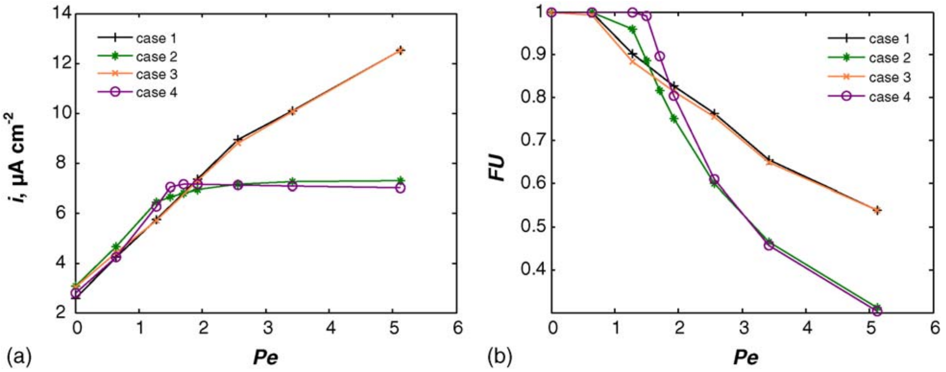

Fig. 11. Current density (a) and fuel utilization (b) comparison for enzyme arrangements according to cases 1–4.

advection dominated regime, cases 1 and 3 are the preferable choices although fuel utilization is poor.

4. Conclusions

A microstructured enzymatic biofuel cell architecture for consecutive chemical reactions was proposed, and species transport coupled with laminar flow and Michaelis–Menten kinetics was studied in 2D using a numerical approach. Biofuel cell performance was shown to be limited by the reaction rates associated with enzyme kinetics. Turnover rates for individual enzymes were key parameters throughout this analysis and directly determined the realizable current densities. The pumping power required for the microchannel flow was determined to be negligible compared to the predicted output power of the unit cell.

The current densities obtained for one-step enzyme catalyzed ethanol oxidation were generally higher than for consecutive methanol oxidation. If maximum current density is the only target, one-step ethanol oxidation is thereby recommended. Methanol is, however, the more attractive fuel in terms of energy density, as 4–5 times more electrons can be captured per unit mass of fuel. Four separated and mixed electrode enzyme patterning strategies were presented, and tested with various bulk velocities to optimize overall current density and fuel utilization. Nearly complete fuel utilization was accomplished in the diffusion dominated and mixed species transport regimes. Local current densities are high and steady in the advection dominated regime, but become significantly reduced for low velocities because of back diffusion and fuel supply shortcomings. The mixed transport regime is therefore particularly attractive for biofuel cell operation, with particularly superior characteristics shown for mixed enzyme patterning that accounts for individual turnover rates. Overall current density is mainly limited by the slow turnover rates for formate and formaldehyde oxidation by FalDH and FDH. Finding new or modified enzymes with higher turnover numbers is a sound strategy to improve the performance of this technology. Inclusion of proper enzyme–electrode tethering is expected to enhance current densities, and accurate measurements of individual turnover numbers for tethered enzymes are desired for further advancements.

Acknowledgements

The funding for this research provided by a Natural Sciences and Engineering Research Council (NSERC) strategic grant and by Angstrom Power Inc. is highly appreciated. The authors also thank Dr. Ned Djilali for helpful comments.

References

[1] J. Larminie, A. Dicks, Fuel Cell Systems Explained, 2nd ed., John Wiley & Sons Ltd., Chichester, England, 2003.
[2] C.K. Dyer, J. Power Sources 106 (2002) 31–34.
[3] E. Kjeang, J. Goldak, M.R. Golriz, J. Gu, D. James, K. Kordesch, Fuel Cells, in press.
[4] S. Wasmus, A. Küver, J. Electroanal. Chem. 461 (1999) 14–31.
[5] E. Kjeang, J. Goldak, M.R. Golriz, J. Gu, D. James, K. Kordesch, J. Power Sources 153 (2006) 89–99.
[6] H.P. Bennetto, Biotechnol. Educ. 1 (4) (1990) 163–168.
[7] D.H. Park, J.G. Zeikus, Appl. Environ. Microbiol. 66 (4) (2000) 1292–1297.
[8] E. Katz, A.N. Shipway, I. Willner, in: W. Vielstich, H.A. Gasteiger, A. Lamm (Eds.), Biochemical Fuel Cells, Handbook of Fuel Cells—Fundamentals, Technology and Applications, vol. 1, John Wiley & Sons, Ltd., New York, 2003.
[9] A. Bazylak, D. Sinton, N. Djilali, J. Power Sources 143 (1–2) (2005) 57–66.
[10] S. Litster, D. Sinton, N. Djilali, J. Power Sources 154 (2006) 95–105.
[11] C. Ma, L. Zhang, S. Mukerjee, D. Ofer, B. Nair, J. Membr. Sci. 219 (1–2) (2003) 123–136.
[12] R.H. Borgwardt, Transport. Res. Part D 6 (2001) 199–207.
[13] S.C. Barton, J. Gallaway, P. Atanassov, Chem. Rev. 104 (2004) 4867–4886.
[14] C.M. Moore, S.D. Minteer, R.S. Martin, Lab on a Chip 5 (2005) 218–225.
[15] I. Willner, E. Katz, Angew. Chem. Int. Ed. 39 (2000) 1180–1218.
[16] C.M. Moore, N.L. Akers, S.D. Minteer, Proceedings of the 204th Meeting of The Electrochemical Society, 2003 (Abs. 1225).
[17] L.A. LeBrun, D.H. Park, S. Ramaswamy, B.V. Plapp, Biochemistry 43 (11) (2004) 3014–3026.
[18] H.W. Adolph, P. Zwart, R. Meijers, E.S. Cedergren-Zeppezauer, Annual Report 1998. EMBL Hamburg Outstation at Deutsches Elektronensynchrotron DESY, Hamburg, 1999, pp. 345–346.
[19] R. Pietruszko, Meth. Enzymol. 89 (1982) 429–435.
[20] H.J. Hektor, H. Kloosterman, L. Dijkhuizen, J. Biol. Chem. 277 (49) (2002) 46966–46973.
[21] W. Hohnloser, B. Osswald, F. Lingens, Hoppe Seylers Z. Physiol. Chem. 361 (12) (1980) 1763–1766.

[22] V.V. Karzanov, Y.A. Bogatsky, V.I. Tishkov, A.M. Egorov, FEMS Microbiol. Lett. 60 (1989) 197–200.
[23] S. Tate, H. Dalton, Microbiology 145 (1999) 159–167.
[24] T. Hopner, U. Ruschig, U. Muller, P. Willnow, Meth. Enzymol. 89 (1982) 531–537, Pt D.
[25] R.A. Copeland, Enzymes: A Practical Introduction to Structure, Mechanism and Data Analysis, 2nd ed., Wiley-VCH Inc., New York, 2000.
[26] N.C. Price, L. Stevens, Fundamentals of Enzymology: The Cell and Molecular Biology of Catalytic Proteins, 3rd ed., Oxford University Press Inc., New York, 1999.
[27] J.C. McDonald, D.C. Duffy, J.R. Anderson, D.T. Chiu, H. Wu, O.J.A. Schueller, G.M. Whitesides, Electrophoresis 21 (2000) 27–40.
[28] K. Johnsson, W.A. Froland, P.G. Schultz, J. Biol. Chem. 272 (5) (1997) 2834–2840.
[29] J.P. Chen, H.Y. Wang, Biotechnol. Tech. 12 (1998) 851–853.
[30] A.A. Kulikovsky, J. Appl. Electrochem. 30 (2000) 1005–1014.
[31] N.T. Nguyen, S.T. Wereley, Fundamentals and Applications of Microfluidics, Artech House, Boston, MA, 2002.
[32] C.T. Crowe, D.F. Elger, J.A. Roberson, Engineering Fluid Mechanics, 7th ed., John Wiley & Sons Inc., New York, 2001.